LARGE-EDDY SIMULATION OF TRANSITION AND TURBULENCE IN WALL-BOUNDED SHEAR FLOW
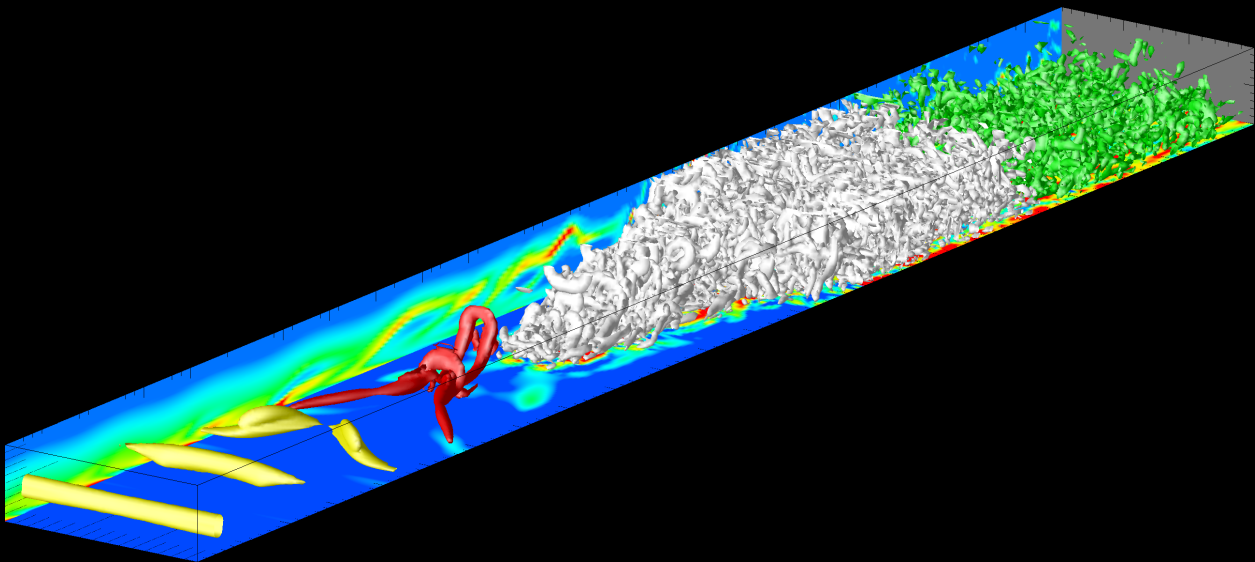
Philipp Schlatter

Visualisation taken from a large-eddy simulation (LES) of spatial K-type transition in plane channel flow. Shown are isosurfaces of the negative-λ_2 vortex-identification criterion. The two-dimensional wave disturbances (yellow isosurfaces) at the inlet break down to turbulence through the formation of Λ-vortices and hairpin vortices (red isosurfaces). A turbulent spot (white) is formed which evolves into fully developed turbulent channel flow further downstream (green). The colored bottom wall shows the skin friction, the rear side wall displays the spanwise vorticity in the valley plane.

Diss. ETH No. 16000

LARGE-EDDY SIMULATION OF TRANSITION AND TURBULENCE IN WALL-BOUNDED SHEAR FLOW

A dissertation submitted to the
SWISS FEDERAL INSTITUTE OF TECHNOLOGY
ZÜRICH

for the degree of
Doctor of Technical Sciences

presented by

Philipp Christian Schlatter

Dipl. Ing. ETH (Swiss Federal Institute of Technology Zürich)
born on May 21, 1975
citizen of Zürich (ZH)

accepted on the recommendation of

Prof. Dr. L. Kleiser, examiner
Prof. Dr. N. D. Sandham, co-examiner

2005

Abstract

Large-eddy simulations (LES) of transitional and turbulent wall-bounded incompressible flow have been performed. A special focus has been on the reliable and efficient modelling of laminar-turbulent transition in plane channel flow at low resolutions, for which several subgrid-scale (SGS) models have been evaluated, including the approximate deconvolution model (ADM) and related approaches, classical and high-pass filtered (HPF) eddy-viscosity models, and dynamic models. The simulations have been performed in both the temporal and spatial transition framework.

The results show that a direct modelling involving a relaxation regularisation (ADM-RT model) provides the most accurate results for both transitional quantities and turbulent statistics. By use of three-dimensional visualisation of instantaneous flow structures it is investigated how well the SGS models on coarse grids are able to predict the physically relevant mechanisms at successive stages of transition: Λ-vortices, rollup of shear layers, and hairpin vortices. The results show that the ADM-RT model predicts similar transitional structures as present in fully resolved direct numerical simulation (DNS) data, however using less than one percent of the numerical resolution of the latter. Other SGS models are not capable of predicting these physical structures at the chosen coarse resolution.

Additionally, the different SGS models have been examined in homogeneous isotropic turbulence. The models provide an accurate prediction of the energy and dissipation spectra even for high Reynolds numbers.

A Fourier method based on a windowing approach to prescribe non-periodic inflow and outflow boundary conditions has been formulated and evaluated. Test cases involving a travelling vortex core and a spatially developing jet have shown very good outflow damping properties. The spectral accuracy of the underlying numerical scheme is retained. The windowing approach has been compared to the well-established fringe method.

Kurzfassung

Large-Eddy-Simulationen (LES) von transitionellen und turbulenten wandbegrenzten inkompressiblen Strömungen wurden durchgeführt. Spezielle Beachtung fand dabei die verlässliche und effiziente Modellierung der laminar-turbulenten Transition in ebener Kanalströmung bei geringer Auflösung. Es wurden verschiedene Turbulenzmodelle untersucht, insbesondere das "Approximate Deconvolution Model" (ADM) und verwandte Ansätze, klassische und hochpassgefilterte Wirbelviskositätsmodelle (eddy-viscosity models), einschliesslich des bekannten dynamischen Modells. Die Simulationen wurden sowohl in räumlicher als auch zeitlicher Betrachtungsweise der Transition durchgeführt.

Die Resultate zeigen, dass eine direkte Modellierung basierend auf einer Regularisierung mittels eines Relaxationsterms die genauesten Resultate sowohl für transitionelle Grössen als auch für turbulente Statistiken liefert. Dreidimensionale Visualisierungen zeigen ausserdem, ob und wie die verschiedenen Modelle die charakteristischen Stufen der Transition wiedergeben: Λ-Wirbel, Aufrollen der Scherschichten und Haarnadelwirbel. Die Resultate zeigen weiter, dass das ADM-RT-Modell sehr ähnliche Strukturen wie die vollaufgelösten Daten der direkten numerischen Simulation (DNS) vorhersagt, obwohl weniger als ein Prozent der Gitterauflösung verwendet wurde. Andere Modelle waren hingegen bei der gewählten niedrigen Auflösung nicht in der Lage, diese Strukturen vorherzusagen.

Zusätzlich wurden die verschiedenen Modelle auch in homogener isotroper Turbulenz untersucht. Es zeigte sich, dass sie eine genaue Voraussage der Energie- als auch der Dissipationsspektren auch für hohe Reynoldszahlen erlauben.

Eine Fouriermethode basierend auf einem Windowing-Ansatz wurde zur Aufprägung von Ein- und Ausflussbedingungen formuliert und bewertet. Testfälle mit einem Wirbel und einem sich räumlich entwickelnden Freistrahl (Jet) zeigten gute Dämpfungseigenschaften am Ausflussrand. Die spektrale Genauigkeit des zugrundeliegenden numerischen Verfahrens bleibt erhalten. Die Windowing-Methode wurde verglichen mit der etablierten Fringe-Methode.

Acknowledgements

Contents

Nomenclature

Roman symbols

c	wave speed
C	model coefficient
C_K	Kolmogorov constant
$\mathbf{e}_i$	unit vector in direction i
$E, \overline{E}$	total kinetic energy, kinetic energy of mean flow
$E(k)$	energy spectrum
$E_1(k_1, x_3)$	one-dimensional Fourier spectrum
$E_1^{\mathrm{int}}(k_1)$	integrated one-dimensional Fourier spectrum
$E_3(k_3)$	Chebyshev spectrum
$E_3'(k_3)$	Chebyshev spectrum of the fluctuations
$F(x)$	fringe function
F_2	second-order structure function
F_i^F	fringe-forcing term
G^P	primary spatial LES filter
G	low-pass filter for ADM
G_{ex}	explicit low-pass filter for ADM
G_2	secondary filter for ADM
$G^{(2)}$	second-order filter
G_{test}	test filter for dynamic Smagorinsky model
h	channel half-width
H	generic high-pass filter
H_N	high-order high-pass filter for ADM
H_{12}	shape factor
i	imaginary unit $\sqrt{-1}$
i, j, k	frequently used indices
I	identity
k	integer wavenumber
k_{max}	maximum resolved integer wavenumber
L	reference length
L_i, L_x, L_y, L_z, L	computational box dimensions (in direction i)
N	deconvolution order
N_i, N_x, N_y, N_z, N	number of grid points (in direction i)
p	pressure
r	filter order
Q_N	approximate deconvolution filter

Re	Reynolds number
Re_τ	Reynolds number based on the friction velocity
Re_λ	Reynolds number based on the Taylor microscale
S_{ij}	strain rate
$S(x)$	smooth step function
t	time
T_{k_3}	Chebyshev polynomial of order k_3
TKE, k	turbulent kinetic energy
u_i, u, v, w	velocity component (in direction i)
$u_i^\star$	deconvolved velocity component
u_τ	friction velocity
$\mathbf{u}$	velocity vector
U	reference velocity
x, y, z, x_i	streamwise, spanwise, and wall-normal direction
x_start, x_end	extent of the fringe domain
$\mathbf{x}$	spatial position vector

Greek symbols

α, β	streamwise and spanwise wavenumbers
χ	relaxation parameter
δ_{ij}	Kronecker symbol
Δ	grid spacing, characteristic length scale
Δx, Δy, Δz	grid spacing in direction x, y, z
Δ_rise, Δ_fall	parameters defining the fringe function
ε, $\varepsilon_\mathrm{visc}$, ε_SGS	dissipation, viscous and SGS dissipation
$\mathcal{E}_\mathrm{visc}$, $\mathcal{E}_\mathrm{SGS}$	wavenumber-dependent viscous and SGS dissipation
$\varepsilon_\mathrm{SGS}^-$, $\varepsilon_\mathrm{SGS}^+$	forward, backward SGS dissipation
η	Kolmogorov length
η	wall-normal vorticity
λ	wave length
λ_2	second eigenvalue used in vortex-identification criterion
$\lambda(x)$, λ_f	fringe function, fringe strength
ν	kinematic viscosity
ν_t	eddy viscosity
ω	wavenumber
ω_c (ω_c^test)	cutoff wavenumber of filter (of test filter)
ω_i	vorticity component in direction i
τ_{ij}	subgrid-scale model stresses
τ_w	skin friction

Other symbols and operators

$\mathcal{U}_i$	base flow
$\mathcal{V}$	computational domain
$\mathcal{P}$	turbulent production
$\mathcal{O}$	Landau symbol (order of)
$\lvert \cdot \rvert$	absolute value
$\lVert \cdot \rVert$	Euclidian norm
$\hat{(\cdot)}$	Fourier transformed quantity, spectral component
$\mathcal{F}$	Fourier transform
∇	Nabla operator
$\propto$	proportional to
$(\cdot) * (\cdot)$	convolution
$\langle \cdot \rangle$	statistical Reynolds average
$\overline{(\cdot)}$	filtered with primary LES filter G^P

Subscripts

$(\cdot)_b$	based on bulk velocity
$(\cdot)_{CL}$	based on centre-line velocity
$(\cdot)_\tau$	based on friction velocity
$(\cdot)_{\mathrm{lam}}$	laminar
$(\cdot)_S$	belonging to the Smagorinsky model
$(\cdot)_{SF}$	belonging to the structure-function model
$(\cdot)_{FSF}$	belonging to the filtered structure-function model

Superscripts

$(\cdot)^{\mathrm{HPF}}$	belonging to high-pass filtered model
$(\cdot)^{\mathrm{VMS}}$	belonging to variational multiscale model
$(\cdot)'$	fluctuating part of Reynolds average or disturbance
$(\cdot)^*$	complex conjugate
$(\cdot)^\star$	approximately deconvolved quantity
$(\cdot)^\circ$	dimensional quantity
$(\cdot)^+$	scaling in viscous (wall) units

Abbreviations

2D, 3D	two- and three-dimensional
ADM, ADM-3D	approximate deconvolution model (three-dimensional formulation)
ADM-2D	approximate deconvolution model (two-dimensional formulation)
ADM-RT	relaxation-term model
CFD	computational fluid dynamics
CPU	central processing unit
DNS	direct numerical simulation
DS, DS-3D	dynamic Smagorinsky model (three-dimensional test filter)
DS, DS-2D	dynamic Smagorinsky model (two-dimensional test filter)
FFT	fast Fourier transform
FSF	filtered structure-function model
GFlops	10^9 floating-point operations per second
HPF	high-pass filtered
LES	large-eddy simulation
rms	root-mean-square
RT	relaxation term
SF	structure-function model
SGS	subgrid scale
SSM	scale-similarity model
SVV	spectral vanishing viscosity
TKE	turbulent kinetic energy
TS	Tollmien-Schlichting
VMS	variational multiscale

Papers

The content of this thesis is based on the following publications which have been published or have been accepted for publication during the course of the PhD project.

P. Schlatter, S. Stolz, and L. Kleiser. Evaluation of high-pass filtered eddy-viscosity models for large-eddy simulation of turbulent flows. *J. Turbulence*, 2005. Accepted.

S. Stolz, P. Schlatter, and L. Kleiser. High-pass filtered eddy-viscosity models for LES of transitional and turbulent flow. *Phys. Fluids*, 2005. Accepted.[†]

P. Schlatter, N. A. Adams, and L. Kleiser. A windowing method for periodic inflow/outflow boundary treatment of non-periodic flows. *J. Comput. Phys.*, 2005. To appear.

P. Schlatter, S. Stolz, and L. Kleiser. LES of transitional flows using the approximate deconvolution model. *Int. J. Heat Fluid Flow*, 25(3), pages 549–558, 2004.

P. Schlatter, S. Stolz, and L. Kleiser. LES of spatial transition in plane channel flow. In *Turbulence and Shear Flow Phenomena 4*, 2005. To appear.

P. Schlatter, S. Stolz, and L. Kleiser. Computational simulation of transitional and turbulent shear flows. In J. Peinke, A. Kittel, S. Barth, and M. Oberlack, editors, *Progress in Turbulence*, vol. 101 of *Springer Proceedings in Physics*, pages 207–214. Springer, Berlin, Germany, 2005.

P. Schlatter, S. Stolz, and L. Kleiser. Applicability of LES models for prediction of transitional flow structures. In *Laminar-Turbulent Transition*, sixth IUTAM Symposium 2004 (Bangalore, India), 2004. To appear.

P. Schlatter, S. Stolz, and L. Kleiser. High-pass filtered eddy-viscosity models in incompressible high-Reynolds number flows. In H. I. Andersson and P.-Å. Krogstad, editors, *Advances in Turbulence X*, pages 303–306. CIMNE, Barcelona, Spain, 2004.

P. Schlatter, S. Stolz, and L. Kleiser. Numerical simulation of transitional and turbulent shear flows. In R. Jeltsch, K. Nipp, and W. van Gunsteren, editors, *CSE Annual Report 2002/2003*, pages 18–25. ETH Zürich, Switzerland, 2003.

P. Schlatter, S. Stolz, and L. Kleiser. Relaxation-term models for LES of transitional/turbulent flows and the effect of aliasing errors. In R. Friedrich, B. J. Geurts, and O. Métais, editors, *Direct and Large-Eddy Simulation V*, pages 65–72. Kluwer, Dordrecht, The Netherlands, 2004.

S. Stolz, P. Schlatter, D. Meyer, and L. Kleiser. High-pass filtered eddy-viscosity models for LES. In R. Friedrich, B. J. Geurts, and O. Métais, editors, *Direct and Large-Eddy Simulation V*, pages 81–88. Kluwer, Dordrecht, The Netherlands, 2004.[†]

P. Schlatter, S. Stolz, and L. Kleiser. LES of transitional flows using approximate deconvolution. In N. Kasagi, J. K. Eaton, R. Friedrich, J. A. C. Humphrey, M. A. Leschziner, and T. Miyauchi, editors, *Turbulence and Shear Flow Phenomena 3*, pages 923–928, 2003.

[†] These papers are not directly included in the thesis. However, their main ideas and conclusions are important for the work presented here.

Chapter 1

Introduction

1.1 Laminar-turbulent transition

The behaviour and properties of fluid flows are important in many different technical applications of today's industrial world. One of the most relevant characteristics of a fluid is the flow state in which it is moving: laminar, turbulent, or the transitional state in between. Laminar flow is a well predictable, structured and layered flow (Latin *lamina*: layer, sheet, leaf), which usually exercises significantly less frictional resistance to solid bodies and much lower mixing rates than the chaotic, swirly and fluctuating state of fluid in turbulent motion. Understanding and predicting both turbulent and laminar flow is crucial in a variety of technical applications, *e.g.* flows in boundary layers on aircraft wings, around cars, intermittent flows around turbine blades, and flows in chemical reactors or combustion engines. The evolution of an initially laminar flow into a fully developed turbulent flow is called *laminar-turbulent transition*. This process and specifically the triggering mechanisms of transition are not fully understood even today, after more than a century of research.

The crucial non-dimensional parameter determining whether a flow will likely be laminar or turbulent is the Reynolds number Re, which can be defined as the ratio of inertial to viscous forces acting on the fluid particles. Flows at low Re are laminar. Flow through a pipe with circular cross-section, for example, will be turbulent above Reynolds numbers of a few thousands, with the precise value depending mainly on the level of disturbances at the inlet and the wall roughness within the pipe. Reynolds numbers of practically important flows may be as high as millions or even billions. This behaviour is generic: Although the laminar flow remains a solution of the governing Navier-Stokes equations at all Reynolds numbers, this solution becomes unstable to disturbances at some finite *critical* Reynolds number Re_{crit}. Under controlled circumstances, a sequence of linear and nonlinear (primary, secondary, higher-order) instabilities leads, through a more or less extended transitional state, to the *fully developed* turbulent state.

The history of transition research dates back to the classical experi-

ments made by Osborne Reynolds already in the 19th century (Reynolds, 1883). By injecting ink into the flow in a glass tube, he discovered that the change-over from laminar to turbulent flow is basically dependent upon the above-mentioned non-dimensional Reynolds number $Re = \frac{UD}{\nu}$ with U denoting the fluid velocity, D the tube diameter, and ν the kinematic viscosity of the fluid.

Later, Orr (1907a,b) and Sommerfeld (1908) independently derived the linearised stability equations. The *Orr-Sommerfeld equations* are still fundamental in transition research. After the theoretical description of the linear stages of transition by Tollmien (1929) and Schlichting (1933), the experimental verification of artificially excited *Tollmien-Schlichting* (TS) wave disturbances in a flat-plate boundary layer by Schubauer & Skramstad (1947) marked a major breakthrough towards understanding transition phenomena. The introduction of the secondary instability theory by Herbert (1988) allowed a theoretical approach to transition into the early three-dimensional stages of transition.
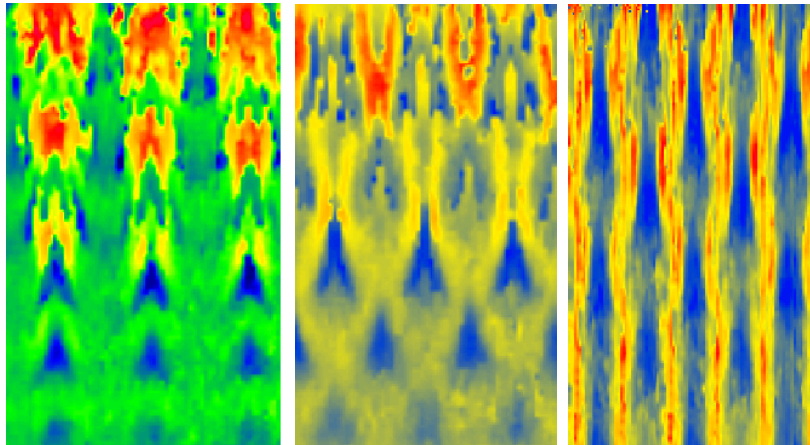
Figure 1.1: Different transition types in a boundary layer: aligned Λ-vortices (K-type), staggered Λ-vortices (H-type), laminar streaks (O-type). Flow is from bottom to top (from Berlin et al. *(1999))*

The classical mechanisms of disturbance growth of modal instability solutions are sketched in figure 1.1 displaying experimental PIV measurements. In this figure, the classical fundamental K- (Klebanoff) and subharmonic H- (Herbert) or N- (Novosibirsk) type breakdowns are shown (Kachanov, 1994). These scenarios are usually called forced transition and are the most dominant breakdown types for low levels of ambient turbulence (turbulence intensity $Tu < 1\%$).

Many additional transition scenarios have been proposed and veri-
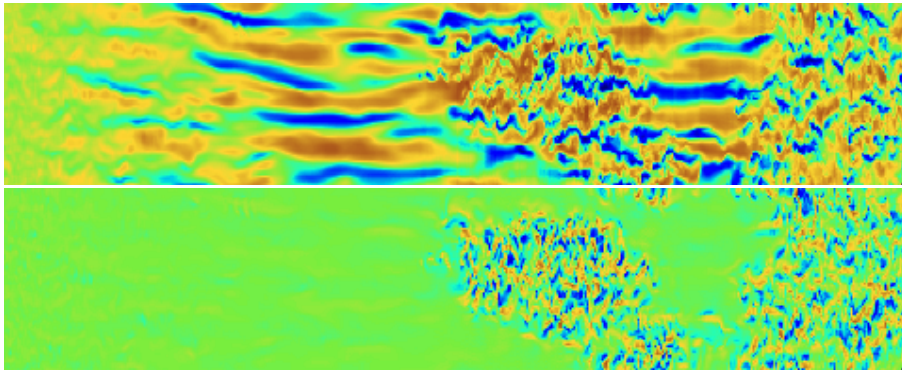
Figure 1.2: Visualisation of an instantaneous flow field displaying the stream-wise and wall-normal velocity components in a plane parallel to the wall (Schlatter, 2001; Brandt et al., *2004) for free-stream induced turbulence over a flat plate.* Top: *Streamwise velocity component.* Below: *Wall-normal velocity component. The formation of a turbulent spot embedded in a streaky laminar base flow is clearly visible.*

fied, *e.g.* oblique transition (O-type) (Schmid & Henningson, 1992) and bypass transition triggered by ambient high-level turbulence, see figure 1.2 and Morkovin (1969). In bypass transition, a process different from the exponential growth of modal waves is causing transition. Transient algebraic growth of disturbances can lead to turbulence at much lower Re, bypassing the exponential growth altogether, see the review by Reshotko (2001). Figure 1.2 shows a snapshot of bypass transition taken from Schlatter (2001); Brandt *et al.* (2004).

A summary of developments in transition research is given in the review article by Kachanov (1994) on boundary layer flow and in the recent monograph by Schmid & Henningson (2001). Specifically for engineering flows, Mayle (1991) reviews important transition results in the field of turbine engines.

An overview of laminar-turbulent transition is sketched in figure 1.3 for the canonical case of the flow over a flat plate (boundary-layer transition). Figure 1.4 shows the corresponding vortical structures observed during transition in plane channel flow (taken from the simulations presented in chapter 5). The fluid flows along the plate (position ①) until at a certain downstream position, indicated by Re_{crit}, it becomes unstable. Further downstream, two-dimensional disturbances are generated within the boundary layer (pos. ②), which rapidly evolve into three-dimensional perturbations of triangular shape (Λ-vortices, pos. ③). These vortical structures in turn tend to break down into local turbulent spots through
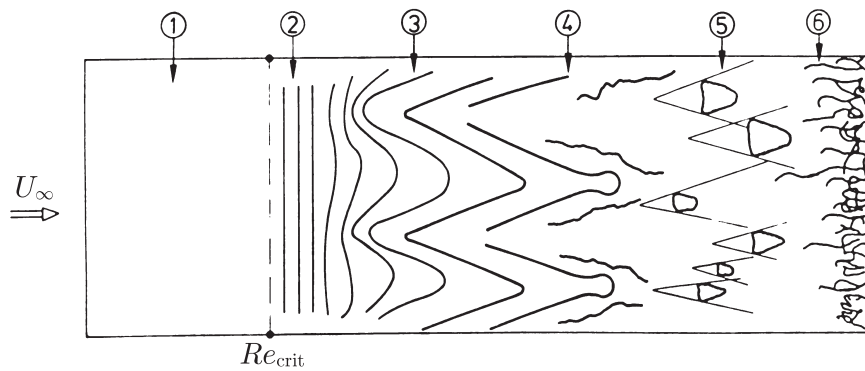
Figure 1.3: Schematic view of laminar-turbulent transition in a flat-plate boundary layer.
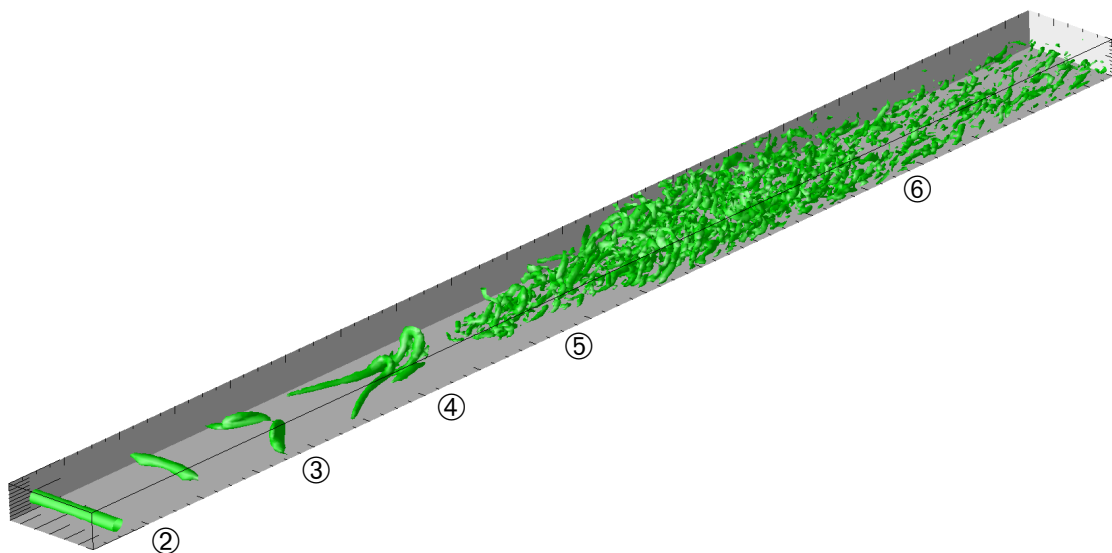
Figure 1.4: Visualisation of spatial K-type transition in plane channel flow obtained from a large-eddy simulation (LES, see chapter 5). The vortical structures are visualised by the λ_2 criterion (Jeong & Hussain, 1995).

the formation of pronounced hairpin vortices (pos. ④), which grow and merge together to form a fully turbulent boundary layer (pos. ⑤-⑥), indicated by the downstream position Re_{tr}.

1.2 Numerical simulation: DNS and LES

The governing equations for laminar, transitional and turbulent flows are the *Navier-Stokes* equations (see section 2.1), which have been known for almost 200 years. Except for a few simple laminar flow cases, no closed analytical solutions to these nonlinear equations are known. Therefore, one needs to resort to numerical simulation techniques in order to get at least an approximate solution of a given fluid dynamics problem. Increasing the Reynolds number Re leads to the excitation of smaller and smaller turbulent scales down to a lower limit. These smallest, so-called *Kolmogorov scales* need to be resolved in numerical simulations based on the Navier-Stokes equations; the simulation accuracy strongly depends on the spatial and temporal resolution employed. The fully resolved direct solution of the Navier-Stokes equations, referred to as *direct numerical simulation* (DNS, see the review by *e.g.* Moin & Mahesh (1998)), is in general extremely expensive even for moderate Re, since the required CPU time roughly scales as Re^3. Practical high Reynolds-number calculations thus need to be performed using simplified turbulence models. One commonly used possibility is to solve the Reynolds-averaged Navier-Stokes equations (RANS) (Wilcox, 1998). Although this technique may require a number of *ad-hoc* adjustments of the turbulence model to a particular flow situation, quite satisfactory results can often be obtained for practical applications.

A technique with a level of generality in between DNS and RANS is the *large-eddy simulation* (LES). The first successful LES was performed in the pioneering work by Deardorff (1970). His simulations of turbulent channel flow were based on the eddy-viscosity model proposed some years earlier by Smagorinsky (1963). He in turn devised his model mainly in order to stabilise his meteorological simulation code; the Smagorinsky model therefore closely resembles the von Neumann-Richtmyer artificial diffusion (Richtmyer & Morton, 1965) to which it reduces in the one-dimensional case.

In an LES, the eddies (turbulent vortices) above a certain size are completely resolved on the numerical grid, whereas the effect of the smaller scales needs to be only modelled. The idea behind this scale-separation is that the smaller eddies are more homogeneous and isotropic than the large ones and depend little on the specific flow situation, whereas the energy-carrying large-scale vortices are strongly affected by the particular flow conditions (geometry, inflow, etc.). Moreover, the

self-similarity of the small scales is often supposed to allow an easier modelling. Since for LES not all scales have to be resolved on the computational grid, only a fraction of the computational cost compared to fully resolved DNS (typically of order 1%) is required.

The success of an LES is essentially dependent on the quality of the underlying *subgrid scale* (SGS) model and the applied numerical solution scheme. Substantial research efforts during the past 30 years have led to more universal SGS models. The main benchmark cases for new SGS models were, due to their geometrical and implementational simplicity, homogeneous isotropic turbulence and turbulent channel flow in the incompressible case. It soon became clear that especially the near-wall behaviour of SGS models deserves special attention. Moin & Kim (1982) used a van-Driest-type wall-damping function (van Driest, 1956). A major generalisation of SGS modelling was achieved by Germano *et al.* (1991) who proposed an algorithm which allows for dynamically adjusting the model coefficient to the local flow conditions, *e.g.* reducing the model contribution in the vicinity of walls or in laminar or transitional flow regions. The dynamic procedure is based on the algebraic identity, known as the Germano identity, which relates the energy fluxes over a test filter level to the corresponding fluxes at the grid-filter level. An additional transport equation for the kinetic energy is employed in the more general dynamic model proposed by Ghosal *et al.* (1995).

An alternative approach was presented by Schumann (1975), who split the model terms for his channel flow simulations into an isotropic and an inhomogeneous part. Only the model contributions arising from the inhomogeneous part were added to the momentum equations, which were complemented with an additional transport equation for the SGS energy. Similarly, in the variational multiscale approach (Hughes *et al.*, 2000) the SGS terms are computed by standard eddy-viscosity closures from a velocity field which only contains the high-frequency oscillations.

The concept of spectral eddy viscosity, derived by Kraichnan (1976) and yielding excellent results for homogeneous isotropic turbulence, was transferred to physical space as of the structure-function model by Métais & Lesieur (1992). The local kinetic energy near the numerical cutoff is expressed through the second-order velocity structure function (Batchelor, 1953), which can easily be computed locally in physical space, thus allowing its application to inhomogeneous flow with general, not necessarily spectral numerics.

A new class of models has been introduced by Bardina *et al.* (1980,

1983) based on the scale-similarity assumption. As the eddy-viscosity closure assumes a one-to-one correlation between the SGS stresses and the large-scale strain rate, the scale-similarity model (SSM) is based upon the idea that the important interactions between the resolved and subgrid scales involve the smallest resolved eddies and the largest SGS eddies. In practise, this idea is realised by a double filtering of the unclosed nonlinear terms. Although excellent correlations between the real and the modelled SGS stresses were found in *a-priori* tests (see *e.g.* Liu *et al.* (1994)), an application of the SSM in real applications does not incorporate a correct SGS energy transfer. As a remedy, usually an eddy-viscosity term is added to provide the necessary energy dissipation yielding the so-called mixed model. Zang *et al.* (1993) introduced the dynamic mixed model which includes a dynamic determination of the model coefficient similar to Germano *et al.* (1991).

Considerable research effort has recently been devoted to the development of SGS models of velocity estimation or deconvolution type, see *e.g.* the review by Domaradzki & Adams (2002). These models can be considered as a generalisation of the scale-similarity approach. Variants include *e.g.* the subgrid estimation model (Domaradzki & Saiki, 1997), the truncated Navier-Stokes simulations (Domaradzki *et al.*, 2002) and the approximate deconvolution model (ADM) developed by Stolz & Adams (1999). ADM has been applied successfully to a number of compressible and incompressible cases (Stolz *et al.*, 2001*a,b*). With the deconvolution-type models, it is tried to extract some information about the SGS stresses from the resolved field, thus providing a better approximation of the unknown model terms.

Without using an explicit expression for the subgrid-scale stresses, Boris *et al.* (1992) introduced the MILES concept (for monotonically integrated large-eddy simulation) for the simulation of compressible turbulence. The SGS stresses are incorporated into the inherent artificial dissipation of the underlying numerical discretisation. However, it was found that different numerical schemes produce very different SGS stresses which are not always able to predict the correct SGS dissipation. Recent progress on MILES modelling is summarised in Grinstein & Fureby (2002). An interesting extension of the MILES concept combining the LES formalism with an adapted numerical method is discussed in Adams *et al.* (2004).

Concise reviews about different strategies for LES and SGS modelling are given in Lesieur & Métais (1996); Domaradzki & Adams (2002); Men-

eveau & Katz (2000); Piomelli (2001) and in the recent text books by Sagaut (2002) and Pope (2000). A detailed description of some important LES techniques is given in chapter 2 below.

It is expected that LES will play a major role in the future for prediction and analysis of certain complex turbulent flows in which a representation of unsteady turbulent fluctuations is important, such as laminar-turbulent transition, large-scale flow separation in aerodynamics, coupled fluid-structure interaction, turbulent flow control, aeroacoustics and turbulent combustion (Piomelli, 1999). However, LES applied to complete configurations (*e.g.* airplanes) at high Reynolds numbers still requires an immense computational effort, mostly due to the fine resolution necessary to resolve the boundary layers at the walls. There are new strategies to circumvent these problems, *e.g.* the concept of detached eddy simulation (DES) which uses a combination of the LES and RANS approaches, see *e.g.* the review by Squires (2004).

1.3   Simulation of transitional flows

Transitional flows have been the subject of intense experimental and numerical research. Since the beginning of the 1980s, with the increasing power of computers, and reliability and efficiency of numerical algorithms, several researchers began to consider the simulation of the breakdown to turbulence in simple incompressible shear flows. Pioneering work was performed by Fasel (1976), who concentrated on small disturbance amplitudes in two-dimensional DNS. Fasel & Bestek (1980) investigated the nonlinear disturbance development in plane Poiseuille flow for both subcritical and supercritical Reynolds numbers. Kleiser (1982) used very accurate spectral methods to calculate through the first linear and nonlinear stages of three-dimensional channel flow transition reproducing the experiment of Nishioka *et al.* (1975). One of the first well-resolved simulations to actually compute three-dimensional temporal transition and the following fully developed turbulence was presented in the DNS work of Gilbert (1988); Gilbert & Kleiser (1990), who simulated fundamental K-type transition in plane Poiseuille flow. The three-dimensional vortical structures of channel flow transition have also been considered by DNS in Biringen (1987). A summary of early results on spatial transition simulations is given in Fasel (1990).

Due to its simplicity and the availability of reliable experimental results and highly resolved simulation data, the case of forced modal

transition is still an important benchmark case for turbulence models (see e.g. Gilbert & Kleiser (1991); Zang *et al.* (1990); Germano *et al.* (1991); Schlatter *et al.* (2004*c*)). Comprehensive review articles on the numerical simulation of transition can be found in Kleiser & Zang (1991) and Rempfer (2003).

1.3.1 Numerical requirements for simulation of transitional flows

In transitional flows one is typically dealing with stability problems where small initial disturbances with energies many orders of magnitude smaller than the energy of the steady base flow may evolve into turbulent fluctuations. After disturbance growth and breakdown the resulting energy of the turbulent fluctuations may be of the same order as that of the base flow. Moreover, the spatial and temporal evolution of various sorts of wave disturbances and their nonlinear interaction needs to be computed accurately over many disturbance cycles. For these reasons high-order numerical schemes which can accurately capture small disturbances and wave propagation have to be employed (Rempfer, 2003). These specific challenges have to be addressed when accurately simulating laminar-turbulent transition and make it one of the most demanding problems of computational fluid dynamics. High accuracy and stability of the underlying numerical scheme is mandatory to obtain meaningful results.

Numerical schemes that are used for transition simulations often rely on spectral methods (Canuto *et al.*, 1988) or high-order finite-difference methods (Lele, 1992). All methods currently in use work with spatial discretisations that are at least fourth-order accurate. For time integration, typically third- and fourth-order schemes are used.

Numerical simulations always introduce modelling and discretisation errors due to truncation of the physical domain and the discrete representation of the solution and its derivatives. Moreover, aliasing errors due to misrepresentation of high-frequency components which cannot be resolved on the computational grid are present if no special dealiasing treatment is employed. As in large-eddy simulations the computational grid is much coarser than that of a corresponding DNS, the numerical errors are more severe (Chow & Moin, 2003). Numerical errors mainly contaminate the small-scale content of the resolved solution which in an LES is the range of scales interacting with the non-resolved scales.

In spectral simulations it is possible to minimise the derivative errors and to eliminate the aliasing errors by employing the 3/2-rule with additional computational effort (see Canuto *et al.* (1988)). On the other hand, most LES simulations of flows in complex geometries are performed with non-spectral discretisation (usually finite-difference methods) where these numerical errors are inherently present (Ghosal, 1996; Kravchenko & Moin, 1997). Although strategies for the reduction of errors with such methods exist, *e.g.* filtering (Lele, 1992), increased filter-width-to-grid-ratio (Chow & Moin, 2003) and the skew-symmetric form of the nonlinear terms in the Navier-Stokes equations (Kravchenko & Moin, 1997), they are not commonly employed. For this reason, it seems important to examine both the influence of dealiasing on the LES results and the usability of SGS models minimising the effects of aliasing errors.

1.3.2 LES of transition

The use of large-eddy simulations (LES) to predict transitional and turbulent flows is appealing as they promise to provide accurate results at greatly reduced computational cost in comparison with fully resolved direct numerical simulations (DNS). However, transitional flows are substantially different from turbulent flows in many respects. Not only is there no fully developed energy cascade, but also slow growth and subtly complex interactions between the base flow and various instability modes can affect the physical changeover from the laminar to the turbulent state and must thus be resolved or modelled reliably.

An SGS model suitable to simulate transition should be able to deal equally well with laminar, various stages of transitional, and turbulent flow states. The model should leave the laminar base flow unaffected and only be effective, in an appropriate way, when nonlinear interactions between the resolved modes and the non-resolved scales become important. The initial slow growth of the instability waves is mostly sufficiently resolved even on a coarse LES grid. Due to the usually spatially intermittent character of transitional flows (*e.g.* spatial simulations, bypass transition), spatial averaging of the model coefficients should be avoided. Furthermore, for the sake of generality and extendability to more complex geometries, a three-dimensional formulation of the model without any preferred directions is required. Another troublesome problem for SGS models is to avoid any singularity when dealing with laminar flows (*e.g.* a singularity in the midplane of laminar channel

flow for the dynamic Smagorinsky model, see section B.4). Moreover, symmetries present in the initial conditions should be preserved as long as they are physically justified.

While a number of different LES subgrid-scale (SGS) models with applications to turbulent flows have been reported in the literature (see *e.g.* the review of Lesieur & Métais (1996)), large-eddy simulations of transitional flows have become an active field of research only recently. Nevertheless, a number of successful applications of LES to transitional flows are available, most of them based on an eddy-viscosity assumption using the Smagorinsky model (Smagorinsky, 1963). It is well known that Smagorinsky's model in its original formulation is too dissipative and usually, in addition to distorting laminar flows, relaminarises transitional flows (see *e.g.* Piomelli & Zang (1991)). The eddy-viscosity closure, in general, assumes a one-to-one correlation between the SGS stresses and the large-scale strain rate tensor. For this reason, a dynamic or adaptive determination of the model coefficient is of vital importance when simulating transitional flows. Consequently, Piomelli *et al.* (1990) introduced, in addition to the van Driest wall-damping function (van Driest, 1956), an intermittency correction in the eddy-viscosity to decrease the dissipation in (nearly-) laminar regions for their channel flow simulation. By properly designing the transition function, good agreement to temporal DNS results has been attained. Voke & Yang (1995) employed the fixed-coefficient Smagorinsky model in conjunction with a low-Reynolds number correction to simulate bypass transition. These authors attribute their excellent results to the specific case of bypass transition, which is characterised by relatively rapid growth of disturbances and is therefore less susceptible to the specific SGS model. Piomelli *et al.* (1991) studied the energy budget including the SGS terms from DNS data of transitional and turbulent channel flow. They concluded that for an appropriate modelling of both transitional and turbulent channel flow backscatter effects (energy transfer from subgrid scales to resolved scales) are important.

The class of dynamic SGS models proposed by Germano *et al.* (1991) calculate their model coefficient during the simulation. The computation of the model coefficient was subsequently refined by Lilly (1992). This class of models is mainly used together with the Smagorinsky model, however, the methodology can be transferred to other models. The dynamic Smagorinsky model has been successfully applied to, *e.g.*, temporal transition in channel flow (Germano *et al.*, 1991) and spatial transi-

tion in incompressible boundary layers (Huai *et al.*, 1997) and on a swept wedge (Huai *et al.*, 1999) using the localised dynamic version of Piomelli & Liu (1995). Nevertheless, clipping of negative values and an averaging in homogeneous directions needed to determine the dynamic model coefficient has usually to be employed in order to minimise the occurrence of singularities. Several remedies for this problem have been proposed, *e.g.* the Lagrangian dynamic SGS model (Meneveau *et al.*, 1996) in which the evolution of the SGS stresses is tracked in a Lagrangian way. This model has been applied to transitional channel flow with good results.

Ducros *et al.* (1996) introduced the filtered structure function (FSF) model, which is also based on an eddy-viscosity assumption. In its original form, the structure-function model (Métais & Lesieur, 1992) was found to be too dissipative for transitional flows, similarly to the classical fixed-coefficient Smagorinsky model. In the FSF model, on the other hand, the high-pass filter used for the computation of the structure function decreases the influence of low-frequency oscillations in the calculation of the SGS terms. As a consequence, the model influence is reduced in regions of the flow which are mainly dominated by mean strain, *e.g.* in the vicinity of walls or in laminar regions. The FSF model was successfully applied to weakly compressible spatial transition in boundary layer flow. The formation of Λ-vortices and hairpin vortices could clearly be detected, however, no quantitative comparison to experiments or DNS data is given. A related approach is the selective structure function (SSF) model, developed by David (1993) and recently modified by Ackermann & Métais (2001). Basically, the eddy-viscosity is turned on as soon as the flow is considered to be three-dimensional. Otherwise, if the turbulence is not three-dimensional enough, *e.g.* in laminar or near-wall regions, the model contributions are switched off reducing the energy dissipation in such regions.

The combination of the dynamic Smagorinsky model in conjunction with the scale-similarity approach (mixed dynamic model, Zang *et al.* (1993)) yielded very accurate results for the case of a compressible transitional boundary layer at high Mach number (El-Hadi & Zang, 1995). The same model in incompressible formulation was applied to the simulation of bypass transition (Péneau *et al.*, 2004) and was able to capture the growth of laminar streaks and subsequently the appearance of turbulent spots within the boundary layer.

Krishnan & Sandham (2004) simulated the highly intermittent evolution of turbulent spots in an otherwise laminar supersonic channel em-

ploying the mixed-time-scale (MTS) model of Inagaki *et al.* (2002, 2005). The eddy viscosity for the MTS model is constructed as a combination of a time and velocity scale, and guarantees the disappearance of the eddy viscosity in laminar flow regions even with fixed model coefficients.

The variational multiscale (VMS) method (Hughes *et al.*, 2000) providing a scale separation between the large-scale fluctuations and the high-frequency oscillations has been used for the simulation of incompressible bypass transition along a flat plate (Calo, 2004; Hughes *et al.*, 2004). Reasonable agreement with the corresponding DNS (Jacobs & Durbin, 2001; Brandt *et al.*, 2004) has been attained. The high-pass filtered (HPF) eddy-viscosity models, which are closely related to the VMS approach, and their application to transitional and turbulent channel flow will be discussed in chapters 4 and 5, see also Stolz *et al.* (2004).

The approximate deconvolution model (ADM) has been applied for a transitional and turbulent jet (Rembold *et al.*, 2002). Recently, for the present thesis work incompressible K-type transition in channel flow has been simulated successfully using ADM and related modelling strategies (Schlatter *et al.*, 2004c), and the transitional vortical structures have been closely examined and visualised (Schlatter *et al.*, 2004a). These findings will be detailed in chapters 4 and 5 of this monograph. Stolz (2005b) used ADM and the HPF Smagorinsky model to simulate subharmonic transition along a supersonic flat plate boundary layer in good agreement with available DNS data.

Most of the above references show that, *e.g.* for the model problem of temporal transition in channel flow, spatially averaged integral flow quantities like the skin friction Reynolds number Re_τ or the shape factor H_{12} can be predicted reasonably well by LES even on comparably coarse meshes, see *e.g.* Germano *et al.* (1991); Schlatter *et al.* (2004c). However, for a reliable SGS modelling strategy it is equally important to faithfully represent the physically dominant transitional flow mechanisms and their three-dimensional vortical structure such as the formation of Λ-vortices and hairpin vortices. A successful SGS model needs to predict those structures well even at low numerical resolution, as demonstrated by Schlatter *et al.* (2004a).

1.4   Objectives and outline of the present work

This thesis aims at contributing to the development of appropriate subgrid-scale modelling approaches for large-eddy simulations of tran-

sitional and turbulent shear flows. Classical and newly devised SGS models are tested in the canonical case of K-type transition in incompressible plane channel flow. This standard test case is appealing since detailed experimental data (Nishioka *et al.*, 1975) and accurate results from direct numerical simulations (Gilbert & Kleiser, 1990) are available. Moreover, the physical processes of this transition scenario are already well understood and thus allow a better validation of the SGS models. It is believed that many physical and modelling issues present in transitional flows can be studied by considering this canonical flow.

The thesis is organised as follows. In chapter 2, the governing equations and the different SGS models are introduced and characterised. Chapter 3 presents the numerical method for the channel flow simulations. The simulation results obtained for temporal channel-flow transition and turbulence are discussed in chapter 4. In particular, integral quantities and instantaneous flow structures are analysed for forced K-type transition and fully developed turbulent channel flow at a friction Reynolds number Re_τ of up to 590.

The temporal transition study is then extended to spatial simulations in chapter 5. In the spatial framework the disturbances grow in in the streamwise direction rather than in time. Whereas the similarity of the spatial and temporal approach is well-established for the early transitional and the turbulent phases (Kleiser & Zang, 1991), there are differences during the highly intermittent later transitional stages concerning the evolution of the physical flow structure and, possibly, the effect of appropriate subgrid-scale (SGS) modelling.

Additionally, the high-pass filtered eddy-viscosity models and ADM have been tested in homogeneous isotropic turbulence at a Taylor microscale Reynolds number of up to $Re_\lambda \approx 5500$ (chapter 6). For those cases detailed analysis including energy and dissipation spectra is shown. A summary and conclusions of this thesis are given in chapter 7 together with an outlook.

In the appendix A a new Fourier method to prescribe non-periodic boundary conditions while retaining periodic discretisation of the computational domain is summarised (a full description is given in Schlatter *et al.* (2005*a*)). Appendix B describes some general implementation details of the SGS models used throughout this thesis.

Chapter 2

Large-eddy simulation

2.1 Governing equations

The governing equations for laminar, transitional, and turbulent flows are the Navier-Stokes equations for the velocity components u_i ($i = 1, 2, 3$) and the pressure p, given here in non-dimensional form for an incompressible flow,

$$\frac{\partial u_i}{\partial t} + \frac{\partial u_i u_j}{\partial x_j} = -\frac{\partial p}{\partial x_i} + \frac{1}{Re}\frac{\partial^2 u_i}{\partial x_j \partial x_j} \; , \tag{2.1}$$

complemented with the incompressibility constraint,

$$\frac{\partial u_i}{\partial x_i} = 0 \; . \tag{2.2}$$

The summation convention over repeated indices is used throughout this thesis unless stated otherwise. The Reynolds number Re is defined as

$$Re = \frac{U^\circ L^\circ}{\nu^\circ} \tag{2.3}$$

with some dimensional reference quantities U°, L° and the kinematic viscosity ν°. In the traditional LES approach (Leonard, 1974), the equations (2.1) and (2.2) are spatially filtered by a low-pass filter G^P (*primary LES filter*) with some filter width Δ. The primary low-pass filtered velocity is given by

$$\overline{u}_i(x) := G^P * u_i := \int_{\mathcal{V}} G^P(x, x', \Delta) u_i(x') dx' \; , \tag{2.4}$$

where $\mathcal{V}$ is the computational domain. The filtering operation yields the LES equations

$$\frac{\partial \overline{u}_i}{\partial t} + \frac{\partial \overline{u}_i \overline{u}_j}{\partial x_j} = -\frac{\partial \overline{p}}{\partial x_i} - \frac{\partial \tau_{ij}}{\partial x_j} + \frac{1}{Re}\frac{\partial^2 \overline{u}_i}{\partial x_j \partial x_j} \tag{2.5}$$

and the filtered continuity equation

$$\frac{\partial \overline{u}_i}{\partial x_i} = 0 \ . \tag{2.6}$$

The LES equations govern the evolution of the large, energy-carrying scales of motion. Note that the primary filter G^P may have a continuous transfer function (graded filter, see below) or be the implicit grid filter due to the discretisation of the LES equations (see *e.g.* Domaradzki & Adams (2002)).

The effect of the non-resolved small scales enters in (2.5) through the subgrid-scale (SGS) term

$$\tau_{ij} := \overline{u_i u_j} - \overline{u}_i \overline{u}_j \ , \tag{2.7}$$

which is not closed since $\overline{u_i u_j}$ cannot be obtained from the filtered quantities $\overline{u}_i$ alone. τ_{ij} must thus be modelled by an appropriate SGS model. The energy dissipation due to the SGS stresses τ_{ij} is (see section B.3)

$$\varepsilon_{\mathrm{SGS}} = \tau_{ij} \overline{S}_{ij} \ , \tag{2.8}$$

with the large-scale strain rate

$$\overline{S}_{ij} = \frac{1}{2} \left(\frac{\partial \overline{u}_i}{\partial x_j} + \frac{\partial \overline{u}_j}{\partial x_i} \right) \ . \tag{2.9}$$

$\varepsilon_{\mathrm{SGS}}$ describes the amount of kinetic energy which is dissipated by the SGS model in addition to the (physical) viscous dissipation. It is often argued that a correct prediction of the SGS dissipation is one of the crucial statistical features of a successful LES (see *e.g.* Meneveau & Katz (2000)).

2.1.1   Filtering

The conceptually most important operation in the derivation of the LES equations (2.5) and (2.6) is the spatial low-pass filtering of the velocity field (and related quantities) according to equation (2.4). The primary filter G^P provides the scale separation between the large scales, which are to be discretised and resolved on the numerical grid, and the small scales, which are only modelled through τ_{ij}. Depending on this primary filter and its shape and cutoff frequency the modelling strategy has to

be chosen accordingly. A rough distinction of SGS models can be made depending on the nature of the primary filter G^P. The primary filter can simply be the implicit grid filter due to the discretisation on the coarse LES grid, *e.g.* in a spectral context a spectral cutoff filter at the highest resolved wavenumber. Classical eddy-viscosity models usually employ the implicit grid filter as primary filter G^P. Conversely, explicitly filtered LES, *e.g.* the approximate deconvolution model (ADM) (Stolz & Adams, 1999), make use of a graded primary filter. A comparison of some explicitly filtered models is given in Gullbrand & Chow (2003).

Graded filters

For the SGS models which will be introduced in the following section 2.2 the definition of a graded high-order filter (*i.e.* one having a continuous transfer function in spectral space) is necessary. Here, we adopt the filter definition by Stolz *et al.* (2001*a*) for a low-pass filter G which is defined for arbitrary grids and has been used with great success in the approximate deconvolution model (see section 2.2.3). On non-equidistant grids, *e.g.* the Gauss-Lobatto collocation points used in the wall-normal direction of the channel flow simulations, the filter is implemented in physical space on an implicit five-point stencil. Derivation details and the filter weights can be found in Stolz *et al.* (2001*a*).

For discretisations on equidistant grids in Fourier space, the transfer function $\hat{G}$ of the filter G (see figure 2.2) can be written as

$$\hat{G}(\omega) = \frac{\hat{G}_{ex}(\omega)}{1 + K[\hat{G}_{ex}(\omega) - 1]} \ , \quad K = \frac{2\hat{G}_{ex}(\omega_c) - 1}{\hat{G}_{ex}(\omega_c) - 1} \ , \qquad (2.10)$$

with the explicit filter $\hat{G}_{ex}$

$$\hat{G}_{ex}(\omega) = 0.625 + 0.5\cos\omega - 0.125\cos 2\omega \ . \qquad (2.11)$$

The cutoff wavenumber ω_c is defined by $\hat{G}(\omega_c) = 1/2$ and can be chosen freely. Based on the low-pass filter G a class of corresponding high-pass filters

$$H_N(\omega) = [I - G(\omega)]^{N+1} \qquad (2.12)$$

can be defined with their order increasing with N. The high-pass filter H_N is at least of order $\mathcal{O}(\Delta^{r(N+1)})$ with Δ being the grid spacing and r the order of the filter G (Stolz *et al.*, 2001*a*). The latter is at least $r = 3$ on arbitrary grids for the filter G introduced above. Figure 2.2 shows
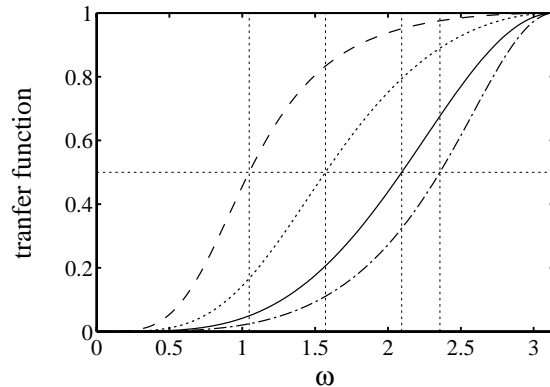
Figure 2.1: Filter transfer functions $\hat{H}_0(\omega, \omega_c) = 1 - \hat{G}(\omega, \omega_c)$ for the cutoff wavenumbers $\omega_c \in \left\{ \frac{\pi}{3}, \frac{\pi}{2}, \frac{2\pi}{3}, \frac{3\pi}{4} \right\}$.

the transfer function of the high-pass filters H_0 and H_5 with a chosen cutoff frequency $\omega_c = 2\pi/3$. In figure 2.1, $\hat{H}_0$ is depicted for different ω_c. Note that $\hat{H}_N$ is equivalent to the high-pass filter used in ADM (Stolz *et al.* (2001*a*)), see section 2.2.3,

$$H_N(\omega) = [I - G(\omega)]^{N+1} = I - Q_N(\omega) * G(\omega) , \qquad (2.13)$$

with

$$Q_N(\omega) = \sum_{\nu=0}^{N} [I - G(\omega)]^{\nu} \approx G^{-1}(\omega) \qquad (2.14)$$

being the approximate deconvolution filter.

The formulation of the filters in physical space allows greater flexibility, *e.g.* the extension to non-spectral discretisations such as finite differences. Note that for spectral discretisations in directions with non-equidistant grids a filtering in spectral space can alternatively be performed, see *e.g.* Boyd (1998). This approach has been tested yielding similar results as the filtering in physical space.

The three-dimensional high-pass filter is derived from the one-dimensional filter by a tensor product, *i.e.*

$$G * \overline{u} = G_1 * G_2 * G_3 * \overline{u} \qquad (2.15)$$

and *e.g.*

$$H_0 * \overline{u} = \overline{u} - G * \overline{u} = \overline{u} - G_1 * G_2 * G_3 * \overline{u} \qquad (2.16)$$
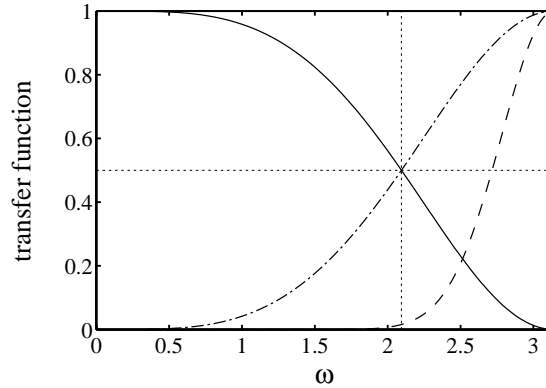
Figure 2.2: Transfer function of the primary and secondary filters used for the ADM and related models: —— Primary low-pass filter $\hat{G}$ eq. (2.10), —·— high-pass filter $\hat{H}_0 = 1 - \hat{G}$, ---- high-pass filter $\hat{H}_5 = (1 - \hat{G})^6$. Cutoff wavenumber $\omega_c = 2\pi/3$.

with G_i being the one-dimensional low-pass filter in the direction x_i. Note that the tensor product introduces a slight anisotropy of the filters. This issue will be discussed further in the context of homogeneous isotropic turbulence (chapter 6).

With a suitable filter H_N with $N \geq 0$, high-pass filtered quantities $H_N * \overline{u}_i$ are effectively vanishing for smooth velocity profiles (*e.g.* low-order polynomial) which represent laminar and flows such as those occuring, *e.g.*, in the near-wall and early transitional flow regions. It is therefore readily possible to use a high-pass filtering operation to separate the large scales from the small-scale fluctuations, which are, as will be discussed further down, important for SGS modelling.

Test filter for the dynamic Smagorinsky model

The dynamic Smagorinsky model (Germano *et al.* (1991), see also section B.4) requires a test filter at a lower cutoff wavenumber than the implicit grid filter. For our calculations using this model, different test filters have been evaluated with the cutoff wavenumber fixed at $\omega_c = \pi/2$ (Germano *et al.*, 1991), see also the discussion in Stolz *et al.* (2005). These filters are shown in figure 2.3 and include G (equation (2.10), $I - H_1$ (see equation (2.12)) and the second-order filter $G^{(2)}$. This filter is defined in physical space as

$$\alpha \tilde{u}_{i-1} + \tilde{u}_i + \alpha \tilde{u}_{i+1} = \left(\frac{1}{2} + \alpha\right) \left[\frac{1}{2} u_{i-1} + u_i + \frac{1}{2} u_{i+1}\right] \; , \qquad (2.17)$$
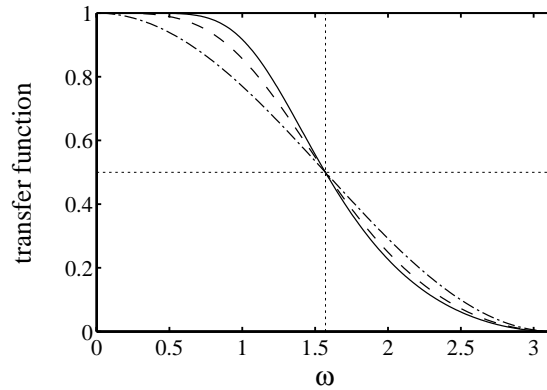
Figure 2.3: Filter transfer functions used as test filter $\hat{G}_{\text{test}}$ for the dynamic Smagorinsky model, cutoff wavenumber $\omega_c = \frac{\pi}{2}$. ——— $1 - \hat{H}_1 = 2\hat{G} - \hat{G}^2$, ----- $\hat{G}$, —·—·— *second-order filter* $\hat{G}^{(2)} = \frac{1}{2}(1 + \cos(\omega))$.

with $\alpha = -(1/2)\cos(\omega_c)$ and the filtered and unfiltered grid functions $\tilde{u}_i$, u_i, respectively. The corresponding transfer function reads

$$\hat{G}^{(2)} = \frac{\left(\frac{1}{2} + \alpha\right)[1 + \cos\omega]}{1 + 2\alpha\cos\omega} \quad . \tag{2.18}$$

For $\omega_c = \pi/2$ the transfer function reduces to

$$\hat{G}^{(2)} = \frac{1}{2}\left(1 + \cos(\omega)\right) . \tag{2.19}$$

The filter $I - H_1 = Q_1 G = 2G - G^2$ is based on the filter G defined in equation (2.10). To obtain a cutoff wavenumber $\omega_c = \pi/2$ for the filter $I - H_1$, a cutoff wavenumber

$$\omega_c = \arccos\left(1 - \sqrt{-8 + 6\sqrt{2}}\right) \approx 1.2626 \tag{2.20}$$

has to be chosen to evaluate G. Note that $I - H_1$ is at least of sixth order on arbitrary grids.

Simulation results using the different test filters for the dynamic Smagorinsky model are presented in section 4.3.

2.2 Subgrid-scale modelling

In this section, we present the SGS models which have been employed to obtain the results presented in chapters 4-6. For a more general overview

of various SGS models and their application we refer to the introduction in sections 1.2 and 1.3 and the review articles by Lesieur & Métais (1996); Meneveau & Katz (2000); Piomelli (2001); Domaradzki & Adams (2002).

2.2.1   Classical eddy-viscosity models

The most widely-used SGS models are the eddy-viscosity models, given by

$$\tau_{ij} - \frac{\delta_{ij}}{3}\tau_{kk} = -2\nu_t \overline{S}_{ij} \ , \tag{2.21}$$

where $\overline{S}_{ij}$ is the large-scale strain-rate tensor defined in equation (2.9). The eddy viscosity ν_t is usually modelled according to Smagorinsky (1963) yielding the popular Smagorinsky model

$$\nu_t = (C_S \Delta)^2 |\overline{S}| \ , \tag{2.22}$$

with the definition

$$|\overline{S}| = (2\overline{S}_{ij}\overline{S}_{ij})^{1/2} \ . \tag{2.23}$$

Δ denotes a typical length scale of the spatial filter generally computed from the grid size as $\Delta = (\Delta x \Delta y \Delta z)^{1/3}$. The model coefficient C_S ("Smagorinsky constant") has to be determined empirically and is dependent on the particular flow situation. Assuming that the cutoff frequency lies within a $k^{-5/3}$ Kolmogorov cascade, an approximate value for the Smagorinsky coefficient can be derived (Lilly, 1992)

$$C_S = \frac{1}{\pi}\left(\frac{3C_K}{2}\right)^{-3/4} \approx 0.18 \ , \tag{2.24}$$

assuming a Kolmogorov constant $C_K \approx 1.4$. However, as reported by Deardorff (1970) and Moin & Kim (1982), in practise the coefficient has to be reduced to values $C_S \approx 0.1$ to sustain turbulence in a channel flow.

Another approach is the structure function (SF) model (Métais & Lesieur, 1992) in which the eddy viscosity is given by

$$\nu_t = C_{SF} C_K^{-3/2} \Delta \sqrt{F_2(\overline{\mathbf{u}}, \mathbf{x}, \Delta)} \tag{2.25}$$

with the Kolmogorov constant $C_K \approx 1.4$ and F_2 being the second-order velocity structure function which is computed from the values of $\overline{\mathbf{u}}$ at the six neighbouring grid points surrounding $\mathbf{x}$ (see appendix B.1). In the filtered structure function (FSF) model (Ducros *et al.*, 1996), the

argument of F_2 in equation (2.25) is high-pass filtered with a suitable filter. However, in the original formulation for inhomogeneous flows the structure function is computed in a two-dimensional formulation including the four neighbouring points only.

Classical variants of eddy-viscosity models with constant model coefficients, *e.g.* the above-mentioned Smagorinsky model and the structure-function model, are quite successful in certain flow situations. Nevertheless, for some flows, *e.g.* wall-bounded shear flows, transitional or intermittent flows, *ad-hoc* remedies have to be used to obtain acceptable results, *e.g.* a van-Driest wall-damping function (van Driest, 1956) or a low-Reynolds number correction (Voke & Yang, 1995).

Another widely-used option is to resort to dynamic SGS models, which were introduced by Germano *et al.* (1991) and further refined by Lilly (1992), see also chapter 1. These models, in particular the dynamic Smagorinsky (DS) model (see section B.4), attempt to use a spatially and temporally varying local model coefficient $C_S(\mathbf{x}, t)$ which is adapted dynamically to different flow situations, *e.g.* laminar, transitional, and turbulent flow. In principle, a second test filter level is introduced, usually with cutoff wavenumber $\omega_c^{\text{test}} = \pi/2$ (see section 2.1.1). The energy flux across this wavenumber band is then measured and is related to the exchange of energy between the resolved and the subgrid scales by use of the Germano identity (Germano *et al.*, 1991).

The dynamic models, however, in general do not correctly predict a laminar base flow depending on the test filter used. Moreover, clipping possible negative values and averaging in homogeneous directions during the computation of the dynamic model coefficient has usually to be employed for turbulent flows in order to minimise the occurrence of instabilities (see section B.4). Several remedies to this problem have been proposed, *e.g.* the Lagrangian dynamic SGS model (Meneveau *et al.*, 1996) in which the evolution of the SGS stresses is tracked in a Lagrangian way.

2.2.2   High-pass filtered eddy-viscosity models

Alternatively, high-pass filtered (HPF) velocities can be used instead of the full LES velocity field for the computation of the subgrid-scale model terms. In Sagaut *et al.* (2000) a high-pass filter has been employed for the computation of the eddy viscosity, comparable to the filtered Smagorinsky model (Nicoud & Ducros, 1999). Similarly, Ducros *et al.*

(1996) extended the structure-function model, see previous section 2.2.1.

In laminar flow regions and in the viscous sublayer of turbulent wall-bounded flows, the SGS model contributions should vanish or at least be very small. Using the classical Smagorinsky or the SF model, this condition is not necessarily fulfilled since the strain rate $S_{ij}(\overline{\mathbf{u}})$ actually peaks at the walls. Therefore, van-Driest-type wall-damping functions are usually employed to reduce the model influence close to the walls. The FSF model and the dynamic Smagorinsky model aim at directly reducing the eddy viscosity in the vicinity of the walls by computing a spatially varying value of the model coefficient C_S. However, truly vanishing SGS stresses are not attained for both of these SGS models in their three-dimensional formulation which is necessary for inhomogeneous flows.

In addition to filtering the arguments of the eddy viscosity, it is also possible to compute the strain rate from the high-pass filtered LES velocity field too. This type of models, henceforth called HPF models, has been proposed independently by Vreman (2003) and Stolz *et al.* (2004); Meyer (2003). The approach can be considered a generalisation of the variational multiscale (VMS) method presented by Hughes *et al.* (2000). Therein, the scale separation is performed by projection onto disjunct functional spaces, whereas in our methodology, a filtering approach with graded (as opposed to sharp cutoff) filters has been chosen.

The HPF eddy-viscosity models employ high-pass filtered quantities $H * \overline{\mathbf{u}}$ instead of the LES quantities $\overline{\mathbf{u}}$ for the computation of both the strain rate and the turbulent eddy viscosity,

$$\tau_{ij} - \frac{\delta_{ij}}{3}\tau_{kk} \approx -2\nu_t^{\mathrm{HPF}} S_{ij}(H * \overline{\mathbf{u}}) \qquad (2.26)$$

with the high-pass filtered strain rate

$$S_{ij}(H * \overline{\mathbf{u}}) = \frac{1}{2}\left(\frac{\partial H * \overline{u}_i}{\partial x_j} + \frac{\partial H * \overline{u}_j}{\partial x_i}\right) , \qquad (2.27)$$

and a suitable high-pass filter H. The fixed-coefficient HPF Smagorinsky model for the SGS stresses τ_{ij} is thus given by

$$\nu_t^{\mathrm{HPF}} = (C_S^{\mathrm{HPF}}\Delta)^2 |S(H * \overline{\mathbf{u}})| . \qquad (2.28)$$

Similarly, from the structure-function model an expression for the HPF-SF model can be derived by employing high-pass filtering for both

the strain rate $S_{ij}(H * \overline{\mathbf{u}})$ and the structure function $F_2(H * \overline{\mathbf{u}})$

$$\nu_t^{\text{HPF}} = C_{SF}^{\text{HPF}} C_K^{-3/2} \Delta \sqrt{F_2(H * \overline{\mathbf{u}}, \mathbf{x}, \Delta)} \; . \qquad (2.29)$$

Results obtained with the HPF models defined above will be presented in chapters 4 and 6. In particular, the models have been employed successfully to incompressible turbulent channel flow at $Re_\tau \approx 180$ (Stolz *et al.*, 2004, 2005) and $Re_\tau \approx 590$ (Schlatter *et al.*, 2005*c*). Furthermore, different high-pass filters were evaluated. The HPF models were also applied to simulate forced temporal K-type transition in channel flow (Stolz *et al.*, 2004, 2005) and in the spatial approach (Schlatter *et al.*, 2005*d*). It turned out that the high-pass filtering in fact reduces the SGS dissipation in the transitional flow regions, allowing the simulation of such flows even with a fixed model coefficient.

The extension of the HPF Smagorinsky model to compressible flows has been studied and applied to a spatial supersonic turbulent boundary layer by Stolz (2004, 2005*c*) and to supersonic boundary-layer transition (Stolz, 2005*b*). Additionally, the behaviour of the models in homogeneous isotropic turbulence is examined in chapter 6, see also Schlatter *et al.* (2005*c*).

A close relation to the variational multiscale (VMS) method (Hughes *et al.*, 2000, 2001) can be established, see also Vreman (2003). The "small-small" models presented therein can be recovered by our methodology, equations (2.26)-(2.29), by using the spectral cutoff filter as high-pass filter H which guarantees that the model contributions are computed from the high-frequency velocity field only. Note that for an exact representation of the "small-small" VMS method, τ_{ij} has to be restricted to the "small" wavenumber range, *i.e.* $\tau_{ij}^{\text{VMS}} = H * \tau_{ij}^{\text{HPF}}$. However, this difference is minor as shown by Vreman (2003).

The SGS model proposed by Schumann (1975) separating the locally isotropic part from the inhomogeneous part of the flow can be reproduced with our methodology by filtering out only the respective mean quantities, *e.g.* in the wall-parallel directions. Schumann's model is also included in the study of the turbulent channel flow presented in chapter 4.

High-pass filter and model coeffient

The performance of the high-pass filtered eddy-viscosity models strongly depends on the high-pass filter H used for the scale separation. It is

therefore advisable to use a filter which can be applied in three dimensions even on non-equidistant grids and in the presence of solid walls, in order to comply with the requirement for LES of transitional flows discussed section 1.3.1. Moreover, the filter should be of high order in such a way that model contributions from smooth velocity profiles (near-wall region, laminar base flow) are evanescent (Stolz *et al.*, 2005; Schlatter *et al.*, 2005*c*). However, to allow for an extension to non-spectral, *e.g.* finite-difference methods, the cutoff frequency of the filter should not be too high due to the misrepresentation of the high-frequency content in finite-difference methods (Lele, 1992). It therefore seems natural to use the filter G (equation (2.10)) and its corresponding high-pass filter $H_0 = I - G$ (equation (2.12)) to perform the high-pass filtering for these models. A comparison of different filters, including the one used by Vreman (2004), has been made by Stolz *et al.* (2005).

As detailed in section 2.1.1, the cutoff wavenumber ω_c of H_0 can be chosen and adapted to specific requirements. The influence of ω_c on the simulation results (refer to chapter 4) can be minimised by adapting the model coefficient according to the empirical relation (Stolz *et al.*, 2004)

$$C_S^{\text{HPF}} = \frac{1}{1 - \frac{1}{\pi}\omega_c} \cdot C_0 \qquad (2.30)$$

for the HPF Smagorinsky model with the recommended value $C_0 = 0.1/3$. Similar relations are given for the HPF-SF model and the FSF model (Schlatter *et al.*, 2004*b*) (see figure 2.4),

$$C_{SF}^{\text{HPF}} = \frac{1}{112 - 41.7\omega_c} \qquad (2.31)$$

and

$$C_{FSF} = \frac{1}{58.8 - 15.2\omega_c} \ . \qquad (2.32)$$

The corresponding filter transfer functions $\hat{H}_0(\omega, \omega_c) = 1 - \hat{G}(\omega, \omega_c)$ for the cutoff wavenumbers $\omega_c \in \{\frac{\pi}{3}, \frac{\pi}{2}, \frac{2\pi}{3}, \frac{3\pi}{4}\}$ have already been shown in figure 2.1.

The relations (2.31) and (2.32) have been found by performing several LES of turbulent channel flow at $Re_\tau \approx 180$ with different coefficients C_{FSF}, C_{SF}^{HPF} and cutoff wavenumbers ω_c and optimising for the most accurate value of the averaged skin friction Re_τ. However, the results presented in section 4.7 indicate that the optimised model coefficients C_S^{HPF}, C_{FSF}, C_{SF}^{HPF} are applicable for other Reynolds numbers.
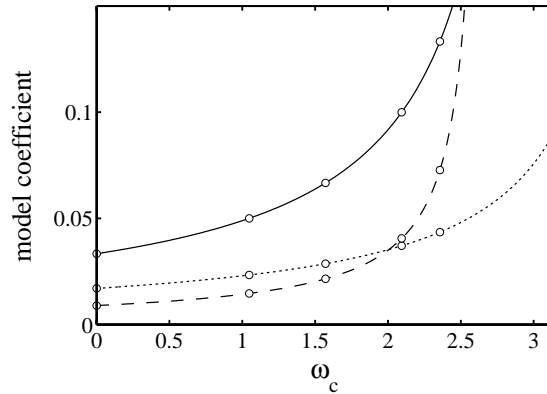
Figure 2.4: Adaptation of the model coefficient to the filter cutoff wavenumber ω_c: ——— C_S^{HPF} *for the HPF Smagorinsky model,* ········· C_{FSF} *for the FSF model, and* - - - - C_{SF}^{HPF} *for the HPF-SF model.*

Additionally, transitional channel flow was also predicted well by using these model coefficients (Stolz *et al.*, 2004). Moreover, for homogeneous isotropic turbulence (see chapter 6) only a slight adaptation of the coefficients was necessary.

2.2.3 Approximate deconvolution model (ADM)

Another recent modelling approach is the approximate deconvolution model (ADM) which was proposed by Stolz & Adams (1999) for the LES of incompressible and compressible flows. The model is based on an approximate defiltering of the explicitly filtered LES data by a truncated series expansion of the inverse filter. Furthermore, a relaxation regularisation which acts only on the scales close to the numerical cutoff is used to model the interaction of the resolved and represented scales with those not represented numerically.

The ADM SGS model to close equation (2.5) can be written as follows (Stolz *et al.*, 2001*a*)

$$\frac{\partial \tau_{ij}}{\partial x_j} = \frac{\partial \overline{u_i^\star u_j^\star}}{\partial x_j} - \frac{\partial \overline{u}_i \overline{u}_j}{\partial x_j} + \chi (I - Q_N * G) * \overline{u}_i \ . \qquad (2.33)$$

Note that the LES filter operation (2.4) is performed using G as the primary filter G^P. In equation (2.33), a star denotes the approximately deconvolved quantities

$$u_i^\star := Q_N * \overline{u}_i \ . \qquad (2.34)$$

G is the graded discrete primary low-pass filter defined in equation (2.10) and Q_N its approximate inverse (refer to equation (2.14))

$$Q_N = \sum_{\nu=0}^{N} (I - G)^\nu \approx G^{-1} \ .$$

The transfer functions of G and $H_N = I - Q_N * G$ are shown in figure 2.2.

The relaxation term $-\chi(I - Q_N * G) * \overline{u}_i = -\chi H_N * \overline{u}_i$ (see equation (2.13)) provides the necessary drain of energy out of the coarsely discretised system. In case of constant χ, it can be interpreted as a secondary filter operation with the filter $Q_N * G$ applied every $1/(\chi\Delta t)$ time steps with Δt being the time step of the numerical integration (Stolz *et al.*, 2001*a*). This secondary filter operation is similar to the "truncated Navier-Stokes dynamics" approach presented by Domaradzki *et al.* (2002). Furthermore, the relaxation regularisation is related to the spectral vanishing viscosity (SVV) concept first introduced by Tadmor (1989) to suppress oscillations in the spectral solution of the inviscid Burgers equation. Recently, the SVV was extended to the Navier-Stokes equations by Karamanos & Karniadakis (2000). In section 4.7.3 a formal comparison of the ADM relaxation term to the SGS model term introduced by the HPF eddy-viscosity model (section 2.2.2) is presented.

The complete ADM equations combining the equations (2.5) and (2.33) can be written as

$$\frac{\partial \overline{u}_i}{\partial t} + \frac{\partial \overline{u_i^\star u_j^\star}}{\partial x_j} = -\frac{\partial \overline{p}}{\partial x_i} + \frac{1}{Re}\frac{\partial^2 \overline{u}_i}{\partial x_j \partial x_j} - \chi(I - Q_N * G) * \overline{u}_i \ . \quad (2.35)$$

The actual implementation of ADM in numerical codes is based on this equation (2.35). A drawback of the ADM formulation is that the resulting equation (2.35) is not Galilean-invariant (see Speziale (1985); Stolz (2005*a*)). The additional term appearing in a coordinate system moving with the constant velocity V_j is

$$V_j \frac{\partial(\overline{u}_i - \overline{u_i^\star})}{\partial x_j} \ . \quad (2.36)$$

This term is proportional to the difference between the filtered velocity $\overline{u}_i$ and the filtered approximately deconvolved velocity $\overline{u_i^\star}$ which is presumably small but not exactly vanishing. However, due to the filter properties, only the high-wavenumber range is affected. Related

SGS models, *e.g.* the dynamic reconstruction (DRM) model proposed by Gullbrand (2003), are also not Galilean-invariant. However, by introducing a slight modification in the ADM equations, a Galilean-invariant formulation can be obtained (Stolz *et al.*, 2001*a*)

$$\frac{\partial \tau_{ij}}{\partial x_j} = \frac{\partial \overline{u_i^\star u_j^\star}}{\partial x_j} - \frac{\partial \overline{u_i^\star}\,\overline{u_j^\star}}{\partial x_j} + \chi(I - Q_N * G) * \overline{u}_i \ , \qquad (2.37)$$

which can be considered a scale-similarity approach based on the deconvolved velocities. Compared to equation (2.35), this modified ADM model using equation (2.37) is considerably more expensive to evaluate in numerical codes since the nonlinear product has to be evaluated three times instead of only once as in equation (2.35).

It is instructive to consider an alternative notation of the approximate deconvolution model by using the approximately deconvolved quantities as dependent variables. After convolution of equation (2.35) with Q_N and neglecting commutation errors (for a discussion on commutation errors see Stolz (2001)) one obtains for constant χ (Stolz, 2005*a*)

$$\frac{\partial u_i^\star}{\partial t} + \frac{\partial Q_N * (\overline{u_i^\star u_j^\star})}{\partial x_j} = -\frac{\partial p^\star}{\partial x_i} + \frac{1}{Re}\frac{\partial^2 u_i^\star}{\partial x_j \partial x_j} - \chi(I - Q_N * G) * u_i^\star \ . \quad (2.38)$$

By replacing $u_i^\star$ with $\overline{u}_i$ and defining the primary LES filter G^P (equation (2.4)) as $Q_N * G$, *i.e.*

$$\overline{u}_i = Q_N * G * u_i \ ,$$

the previous equation (2.38) can be rewritten as

$$\frac{\partial \overline{u}_i}{\partial t} + \frac{\partial \overline{u}_i \overline{u}_j}{\partial x_j} = -\frac{\partial \overline{p}}{\partial x_i} + \frac{1}{Re}\frac{\partial^2 \overline{u}_i}{\partial x_j \partial x_j} - \chi(\overline{u}_i - \overline{\overline{u}}_i) \ , \qquad (2.39)$$

which is equivalent to the ADM formulation given in equation (2.35) under the given assumptions. Note that in the context of equation (2.39) the primary LES filter to obtain the quantities $\overline{u}_i$, $\overline{p}$ is $G^P = Q_N * G$ and not G as in the ADM formulation of equations (2.33) and (2.35). From equation (2.39) it becomes evident that the ADM formalism corresponds to an explicit high-order low-pass filtering of the nonlinear terms together with the relaxation regularisation

$$-\chi H_N * \overline{u}_i = -\chi(\overline{u}_i - \overline{\overline{u}}_i) \ ,$$

which acts on high-frequency components of the solution $\overline{u}_i$ only. The explicit high-pass filtering of the nonlinear term reduces numerical errors present in the solution, *e.g.* aliasing errors and differentiation errors (the latter evidenced by the modified wavenumber concept). A discussion of these numerical effects is given in *e.g.* Gullbrand (2003); Gullbrand & Chow (2003).

The advantage of the formulation (2.39) compared to (2.35) is that only one filter level is needed, which simplifies the model implementation. Moreover, the filter shape and cutoff wavenumber of the primary LES filter can be easily adapted to the properties of the underlying numerical discretisation scheme (see *e.g.* the adaptive deconvolution order used by von Kaenel *et al.* (2004)). In particular, the primary filter $\overline{(\cdot)}$ is now the same as the secondary filter implied by the relaxation term (see discussion above). Moreover, due to the higher cutoff wavenumber of the primary filter more realistic comparisons to DNS results are possible.

Similarly to equation (2.35), the new notation used for equation (2.39) yields a non-Galilean-invariant model. The error term is (compare to equation (2.36))

$$V_j \frac{\partial(\overline{u}_i - \overline{\overline{u}}_i)}{\partial x_j} \; , \tag{2.40}$$

i.e. proportional to the same velocity difference also used in the relaxation term. In the new notation, the subgrid-scale force of the deconvolution is written as

$$\frac{\partial \tau_{ij}}{\partial x_j} = \frac{\partial \overline{\overline{u}_i \overline{u}_j}}{\partial x_j} - \frac{\partial \overline{u}_i \overline{u}_j}{\partial x_j} \; , \tag{2.41}$$

which is strikingly similar to the scale-similarity model by Bardina *et al.* (1980)

$$\frac{\partial \tau_{ij}^{\mathrm{SS}}}{\partial x_j} = \frac{\partial \overline{\overline{u}_i \overline{u}_j}}{\partial x_j} - \frac{\partial \overline{\overline{u}}_i \overline{\overline{u}}_j}{\partial x_j} \; . \tag{2.42}$$

The difference of the singly filtered velocities $\overline{u}_i$ and the doubly filtered quantities $\overline{\overline{u}}_i$ is vanishing for low wavenumbers and is small for higher frequencies. Note also that the scale-similarity model in the formulation (2.42) is Galilean invariant (Speziale, 1985), however it is known to amplify the high-wavenumber content of the solution (Lund, 1997). Note that the models described in equations (2.37) and (2.42) are not equivalent, but their difference is minor.

Relaxation parameter χ

If $\chi > 0$ is constant on equidistant grids, the relaxation term is purely dissipative. However, with spatially varying χ and filter H_N, also non-dissipative (backscatter) effects are possible (Stolz & Adams, 2003). Note that this low-order relaxation regularisation is not equivalent to the use of an eddy-viscosity-type dissipation (used *e.g.* in the Smagorinsky and the structure-function model) because the affected spectral components are different.

The local model coefficient $\chi(\mathbf{x}, t)$ of the relaxation term can be estimated from the instantaneous LES solution by a dynamic procedure (Stolz *et al.*, 2001*a,b*)

$$\chi(\mathbf{x}, t+\Delta t) = \chi(\mathbf{x}, t) \frac{F_2(\mathbf{x}, t+\Delta t)|_{\chi=0} - F_2(\mathbf{x}, t)}{F_2(\mathbf{x}, t+\Delta t)|_{\chi=0} - F_2(\mathbf{x}, t+\Delta t)|_{\chi=\chi(\mathbf{x},t)}} , \quad (2.43)$$

where $F_2(t) = F_2(H_N * \overline{\mathbf{u}}, t)$ is the second-order velocity structure function (see section B.1) computed from the high-pass filtered velocity field $H_N * \overline{\mathbf{u}}$. This dynamic determination of χ aims at keeping the energy at small scales constant, for which $F_2(H_N * \overline{\mathbf{u}})$ is a measure. Usually, χ is updated only every couple of time steps, but changing this interval somewhat was found to have negligible influence in developed flows. In order to ascertain numerical stability, χ is clipped to

$$0 \le \chi \le 1/\Delta t , \quad (2.44)$$

or else the time step Δt could be reduced accordingly. Moreover, a filter operation has to be applied to smoothen χ in regions where it strongly varies in space. A second-order Padé filter is used for this purpose with cutoff wavenumber $\omega_c = \pi/8$ (Stolz *et al.*, 2001*b*), see the definition in equations (2.17) and (2.18). The computation of F_2 is performed with the six-point formulation on all grid points according to Lesieur & Métais (1996) to account for non-equidistant grid spacing.

The dynamic procedure (2.43) is in principle parameter-free. However, numerical tests in channel flow showed that the dynamically computed model coefficient $\chi(\mathbf{x}, t)$ strongly depends on the clipping bounds (2.44) and thus leads to a dependence of χ on the actual time step Δt of the simulation. In particular, for the fully developed turbulent channel flow at $Re_\tau \approx 180$ presented in Stolz *et al.* (2001*a*), at about 12% of the grid points χ had to be clipped. Moreover, during the early stages

of transition in channel flow (see section 4.4), the determination equation (2.43) for χ is ill-posed since the values for F_2 are very small due to the (nearly) laminar flow field. On the other hand, as shown in Stolz et al. (2001b), the above dynamic algorithm detects the appearance of shocks in compressible flow and increases χ accordingly in such regions. Moreover, χ also correctly reacts to the presence of aliasing errors at small scales and acts to damp such artefacts (Schlatter et al., 2004d).

Therefore, additional LES have been performed with simplified definitions of χ as an alternative to the dynamic procedure (2.43). In particular, the following choices have been tested: simulations with fixed $\chi > 0$,

$$\chi = C_1 = \text{constant} , \tag{2.45}$$

χ based on the velocity gradient tensor,

$$\chi = C_2 \|\nabla \overline{\mathbf{u}}\| , \tag{2.46}$$

and χ based on the high-pass filtered velocity gradient tensor,

$$\chi = C_3 \|\nabla (H_N * \overline{\mathbf{u}})\| . \tag{2.47}$$

The term $\|\nabla (H_N * \overline{\mathbf{u}})\|$ is closely related to $\sqrt{F_2(H_N * \overline{\mathbf{u}})}/\Delta$ (see appendix B.2) with the grid spacing Δ (Lesieur & Métais, 1996). Since the structure function is easier to evaluate in physical space, the definition

$$\chi = C_4 \sqrt{F_2(H_N * \overline{\mathbf{u}})}/\Delta \tag{2.48}$$

was also implemented and evaluated. A similar approach was also studied by Müller et al. (2004) for isotropic homogeneous turbulence. In principle, the coefficients C_i can be derived from energy considerations similar to Ducros et al. (1996) for homogeneous isotropic flow. No additional artificial bounds (clipping) or filter operations were found to be necessary. Results obtained for the different variants of χ are reported in chapter 4 and in Schlatter et al. (2004d).

ADM for turbulent and transitional flows

Large-eddy simulations using ADM as SGS model in the fully turbulent regime have shown very good agreement with filtered DNS data for a wide range of flows, e.g. for incompressible channel flow (Stolz et al., 2001a), shock/turbulent-boundary-layer interaction (Stolz et al., 2001b),

and high-Reynolds-number supersonic boundary layer flow (Stolz & Adams, 2003). A transitional/turbulent rectangular jet has been simulated successfully by Rembold *et al.* (2002). Müller *et al.* (2002) used ADM for the simulation of forced and decaying homogeneous isotropic turbulence. The application of ADM in a semi-industrial finite-volume CFD code has been demonstrated by von Kaenel *et al.* (2003).

ADM-2D and the relaxation-term model (ADM-RT)

In addition to the standard ADM (also denoted as ADM-3D) methodology described above, two alternative variants have been analysed, both of which were found to be suitable for LES of transitional and turbulent channel flow on very coarse grids, as demonstrated in Schlatter *et al.* (2004*c*) and chapter 4. The reason for introducing these new models is that with the standard ADM methodology destabilising properties of the deconvolution operation on coarse grids have been observed in the wall-normal direction. The problem arises mainly due to the use of explicit filtering within the ADM approach with deconvolution used for the nonlinear terms and subsequent filtering. This further reduces the range of resolved wavenumbers (see details in section 4.4.1 in chapter 4).

The first variant uses, instead of three-dimensional filtering and deconvolution, only two-dimensional filtering in the homogeneous wall-parallel directions. Similarly, the relaxation term is also applied only in a two-dimensional formulation. Consequently, this model is termed ADM-2D. The two-dimensional deconvolution operator is maintained all the way through the transitional and turbulent phases. Herewith the advantages of the ADM technique are retained, although this model is not as general as the original formulation since it is restricted to filtering in the two homogeneous directions only while in principle the third direction requires full DNS-like resolution. However, for LES of transitional and turbulent channel flow a special treatment of the inhomogeneous wall-normal direction is common practise, *e.g.* in the four-point formulation of F_2 in the filtered structure-function model (Ducros *et al.*, 1996) or the two-dimensional spectral cutoff test filter in the dynamic Smagorinsky model (Germano *et al.*, 1991). Results of the ADM-2D model are presented in section 4.4.

As will be demonstrated in chapters 4 and 5, the most promising alternative to the standard ADM formalism (2.33) turned out to be the relaxation-term model (ADM-RT). For this model, the three-dimensional

filter definition is used to evaluate the relaxation term (RT), but the nonlinear terms are evaluated as

$$\frac{\partial \overline{u}_i \overline{u}_j}{\partial x_j} \ , \tag{2.49}$$

i.e. computed from the LES quantities without approximate deconvolution as in a no-model calculation. Different from ADM-3D and ADM-2D, within this procedure the quantities $\overline{u}_i$ have to be considered as filtered by the grid filter only, G^P in equation (2.4). This modification is still as general as the standard ADM procedure but does not use deconvolved quantities for the nonlinear terms (see also Schlatter *et al.* (2004*d*)). Note that the high-pass filter still involves the approximate deconvolution operator Q_N in the definition of the relaxation term, however no actual deconvolution of the convection terms is performed. The SGS forces thus simply read

$$\frac{\partial \tau_{ij}}{\partial x_j} = \chi(I - Q_N * G) * \overline{u}_i = \chi(I - G)^{N+1} * \overline{u}_i = \chi H_N * \overline{u}_i \ , \tag{2.50}$$

leading to the LES equations for the ADM-RT model

$$\frac{\partial \overline{u}_i}{\partial t} + \frac{\partial \overline{u}_i \overline{u}_j}{\partial x_j} = -\frac{\partial \overline{p}}{\partial x_i} + \frac{1}{Re}\frac{\partial^2 \overline{u}_i}{\partial x_j \partial x_j} - \chi H_N * \overline{u}_i \ . \tag{2.51}$$

The ADM-RT model has been shown to produce very accurate results in spectral simulations of fully turbulent channel flow even on rather coarse grids. These results are presented in this thesis in chapter 4 and Schlatter *et al.* (2004*c*,*d*). Moreover, for temporal and spatial transition, the ADM-RT model was able to produce excellent results including the prediction of the correct transition location together with the dominant vortical structures, see section 4.6 and chapter 5 (Schlatter *et al.*, 2004*a*, 2005*d*).

Note however that for LES of compressible boundary-layer flow using finite-difference discretisation, the deconvolution was found to be beneficial (Stolz & Adams, 2003), which is mainly due to a reduction of aliasing and discretisation errors. This will further be discussed in section 4.5.

For all of the models ADM-2D, ADM-3D and ADM-RT the different definitions of the relaxation parameter χ detailed in the previous section can be used.

Chapter 3

Numerical method

3.1 Geometry and simulation method

The geometry for the simulation of transitional and turbulent channel flow is given in figure 3.1. The streamwise direction is denoted by $x = x_1$, the spanwise direction by $y = x_2$ and the wall-normal direction by $z = x_3$. Similarly, the non-dimensional extents of the domain are denoted by L_1, L_2 and $L_3 = 2$, respectively. Periodic (homogeneous) boundary conditions are applied in both the spanwise and the streamwise direction. No-slip conditions are prescribed at the solid walls ($z = \pm 1$).
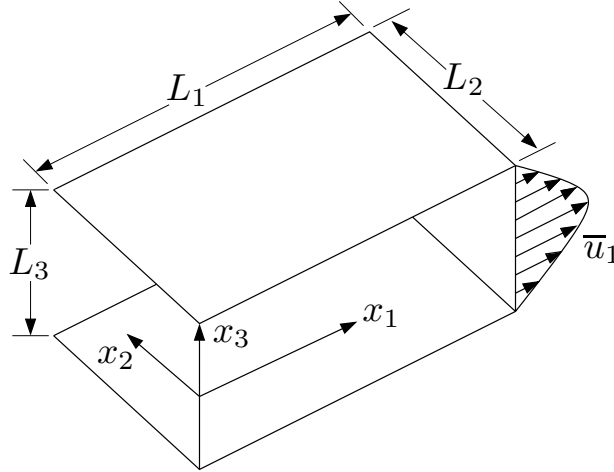
Figure 3.1: Sketch of the channel flow configuration. The coordinates $x = x_1$ denote the streamwise, $y = x_2$ the spanwise, and $z = x_3$ the wall-normal direction, respectively.

The incompressible Navier-Stokes equations (2.5) are discretised by a fully spectral method with Fourier representation in the periodic wall-parallel directions and by Chebyshev expansions in the wall-normal direction. The approximation of the velocities is thus given by

$$\overline{u}_i(x_1, x_2, x_3, t) = \sum_{k_1} \sum_{k_2} \sum_{k_3} \hat{\overline{u}}_i(k_1, k_2, k_3, t) e^{2\pi \mathrm{i} \left(\frac{k_1 x_1}{L_1} + \frac{k_2 x_2}{L_2} \right)} T_{k_3}(x_3) \ ,$$

$$(3.1)$$

with the imaginary unit $\mathrm{i} = \sqrt{-1}$ and wavenumbers k_j. The spectral velocity is denoted by $\hat{\bar{u}}_i$. The Chebyshev polynomials $T_{k_3}(x_3)$ are given by

$$T_{k_3}(x_3) = \cos(k_3 \arccos(x_3)) . \qquad (3.2)$$

In the wall-parallel directions $N_1 \times N_2$ computational nodes are used with equidistant grid spacing $\Delta x = L_1/N_1$ and $\Delta y = L_2/N_2$. The wall-normal direction x_3 is discretised on the N_3 non-equidistantly distributed Gauss-Lobatto collocation points (Canuto *et al.*, 1988)

$$x_{3,j} = \cos(j\pi/N_3) , \quad 0 \le j \le N_3 - 1 . \qquad (3.3)$$

In the Fourier directions periodic boundary conditions are fulfilled. Therefore, the Galerkin method for the minimisation of the residuals can be chosen. In the wall-normal direction, the tau method (see Canuto *et al.* (1988)) has been applied since the Chebyshev polynomials $T_{k_3}(x_3)$ do not statisfy the no-slip conditions individually. The equations for the two highest Chebyshev modes T_{N_3-2} and T_{N_3-1} are replaced by the boundary conditions (see Canuto *et al.* (1988)).

The divergence-free condition is enforced exactly up to machine accuracy in the discretised velocity field by an influence-matrix technique (Kleiser & Schumann, 1980; Kleiser, 1982; Kleiser & Schumann, 1984) with appropriate correction of the tau errors (Kleiser *et al.*, 1998). Time advancement is achieved by a semi-implicit low-storage second-order Runge-Kutta/Crank-Nicolson scheme (Wray, 1987; Sandham & Kleiser, 1992). A constant time step has been used which was always lower than half of the stability limit of the explicit Runge-Kutta scheme. The nonlinear advection terms of the Navier-Stokes equations are computed pseudospectrally with full dealiasing employing the 3/2-rule in all spatial directions (see Canuto *et al.* (1988)). The odd-ball modes in the wall-parallel planes $|k_j| = N_j/2$, $j = 1, 2$ arising from the use of even-numbered fast Fourier transform (FFT) routines are explicitly set to zero. During the simulation, a constant flow rate is maintained through a forcing term (Gilbert, 1988).

3.2 Implementation

The actual code implementation is based on the work by Gilbert (1988); Gilbert & Kleiser (1990) and written in Fortran 77 with some Fortran 90/95 extensions to allow for dynamic memory management. The programme is entirely controlled by the use of parameter files.
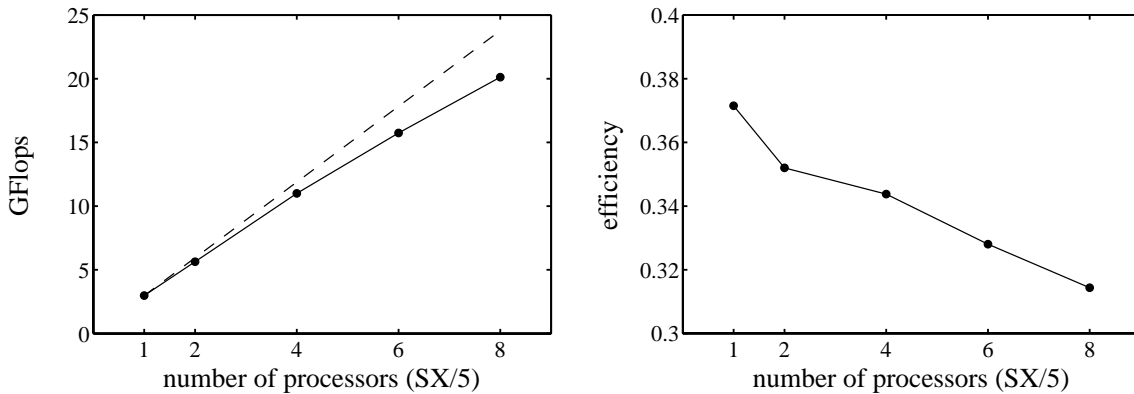
Figure 3.2: Performance of the spectral code used for channel flow simulations for a fixed problem size of $N_1 \times N_2 \times N_3 = 160 \times 160 \times 161$ grid points. Performance data for shared-memory version on the NEC SX-5. Left: ● Measured sustained performance, – – – – linear speed-up. Right: Sustained efficiency of the code in relation to the theoretical peak performance.

Moreover, the code has been completely parallelised using the shared-memory approach with standard and portable OpenMP compiler directives (Dagum & Menon, 1998; Chandra *et al.*, 2001) based on explicit loop-level parallelism. 70% of the CPU time of a typical run is spent in the FFT routines for which the self-adapting FFTW library has been adopted (Frigo & Johnson, 1999). Alternatively, for simulations performed on vector computers, the FFT library by Temperton (1983, 1985) and the machine-optimised NEC Advanced Scientific Library (ASL) are preferred.

Performance data for the NEC SX-5 vector supercomputer, located at the Swiss National Supercomputing Centre (CSCS), Manno (Switzerland), are shown in figure 3.2. The theoretical peak performance per processor for this machine is 8 GFlops. For a direct numerical simulation (DNS) on $160 \times 160 \times 161$ grid points (with dealiasing, problem size 1700 MB), nearly linear speed-up for up to 8 processors could be attained. The efficiency compared to the peak performance is about 38% on a single processor and drops to approximately 32% on 8 processors for this fixed problem size. This measured performance can be considered quite reasonable for this moderate problem size.

In figure 3.3, different computer architectures are compared for DNS at two resolutions, $160 \times 160 \times 161$ and $32 \times 32 \times 33$ grid points. The efficiency of the vector computer (NEC SX-5) strongly degrades for the smaller problem size (compare to figure 3.2) due to the un-
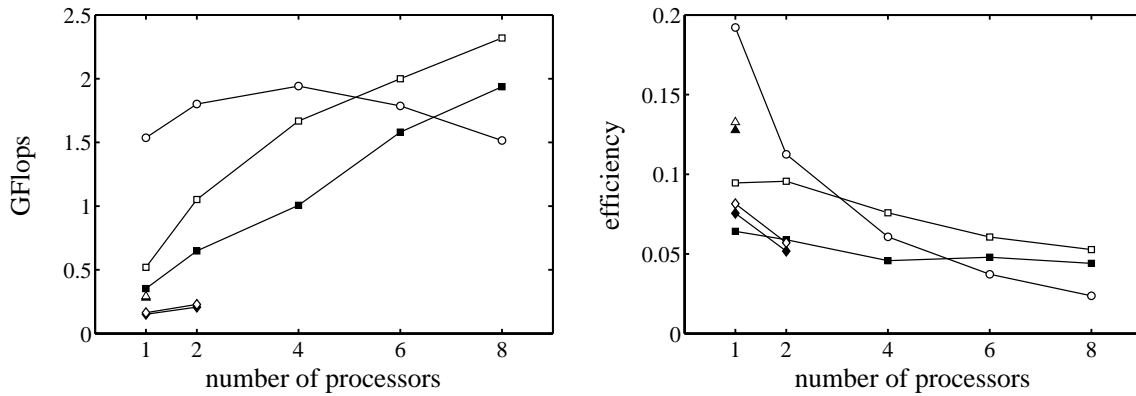
Figure 3.3: Performance of the spectral code for different resolutions, full symbols correspond to resolution $N_1 \times N_2 \times N_3 = 160 \times 160 \times 161$, open symbols $N_1 \times N_2 \times N_3 = 32 \times 32 \times 33$. ○ NEC SX-5 (peak performance per processor 8 GFlops), □ and ■ IBM SP-4 (5.5 GFlops), ◇ and ♦ Linux dual-CPU PC (2 GFlops, 32 bit), △ and ▲ Linux PC (2.2 GFlops, 64 bit). Left: *Measured sustained performance.* Right: *Sustained efficiency of the code compared to the respective peak performance.*

favourably small vector length. On the other hand, the efficiency for the (super-)scalar architectures (IBM SP-4 and Linux PC) is similar for both resolutions, and it is only slightly decreasing with increasing number of processors. However, for the bigger case the actual speed of the scalar machines is substantially smaller than for the vector computer, *e.g.* roughly 8 processors of the IBM SP-4 are needed to equal the performance of one NEC SX-5 processor.

The GFlops numbers presented in figure 3.3 have been computed based on the hardware counter on the SX-5 and the measured wall-clock time on the different architectures. It is therefore not accounted for the possibly varying number of floating-point operations of the different FFT libraries. The GFlops numbers of figure 3.2 thus have to be interpreted with some caution.

It is expected that by using a combination of shared-memory parallelism (OpenMP) and the distributed-memory approach (using the message passing interface MPI, see *e.g.* Pacheco (1997)) an additional increase in performance could be gained especially on massively-parallel architectures.

Chapter 4

Temporal transition and turbulence

The temporal simulation framework provides a simplified way to perform simulations of transition and turbulence. In contrast to the physical flow situation, periodic boundary conditions are imposed in the streamwise direction, which avoid the need for prescribing well-posed inflow and outflow boundary conditions. Especially in the channel geometry, where the mean flow is not spatially evolving in either the laminar or the turbulent phase, the temporal approach is a popular alternative to the more costly spatial simulation (see chapter 5).

In the present chapter, results of large-eddy simulations using the various models introduced in chapter 2 are compared to fully resolved direct numerical simulations at different Reynolds numbers. The parameter settings of the DNS are based on the simulations by Gilbert (1988); Kim *et al.* (1987); Moser *et al.* (1999). However, all the data have been recomputed in the course of this work to provide a database of fully resolved simulation results and to allow detailed analysis of those data.

Section 4.1 describes the initial conditions and the parameter settings used for the channel simulations. Results of an evaluation of the subgrid-scale stresses from a DNS of K-type transition are presented in section 4.2. Large-eddy simulation results are given in section 4.3 using the dynamic Smagorinsky model applying different test filters for transitional and turbulent channel flow. The approximate deconvolution model (ADM) is examined in section 4.4, and the ADM relaxation-term model in section 4.5. Visualisations of temporal K-type transition computed with LES are presented in section 4.6. Turbulent channel flow results at higher Reynolds number $Re_\tau \approx 590$ are given in section 4.7 for the high-pass filtered eddy-viscosity models and ADM-RT.

4.1 Initial conditions and parameter settings

4.1.1 Initial conditions for K-type transition

The initial disturbances for the transition simulations consist of a two-dimensional (stable) Tollmien-Schlichting (TS) wave with maximum streamwise velocity amplitude of 3% of the laminar centre-line velocity
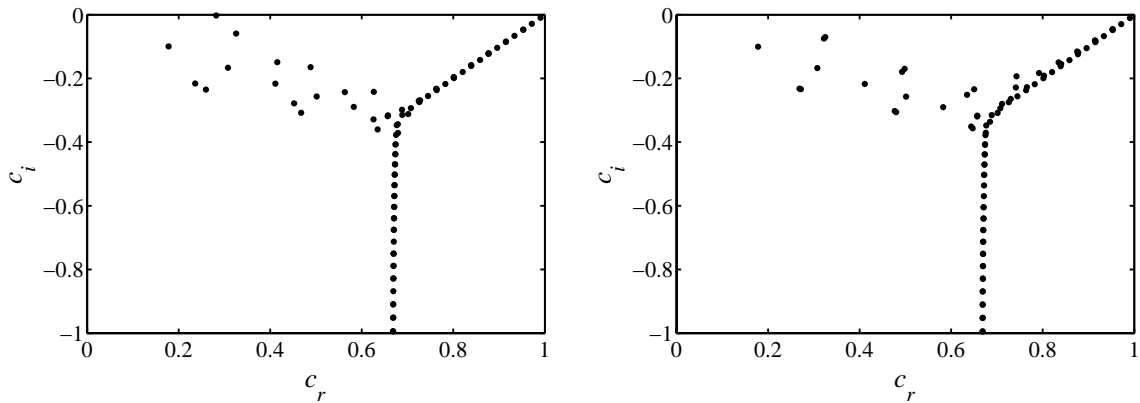
Figure 4.1: Spectrum of the eigenvalues $c = c_r + c_i$i (wave speed $c = \omega/\alpha$) to the coupled Orr-Sommerfeld/Squire equations with parabolic base flow, $Re_b = 3333$, $\alpha = 1.12$. Left: Two-dimensional waves, $\beta = 0$. Right: Three-dimensional waves, $\beta = \pm 2.1$.
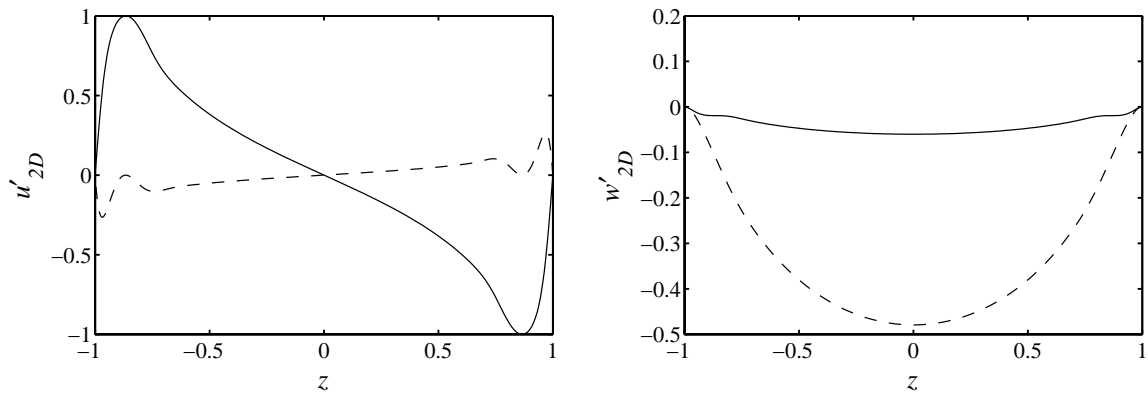
Figure 4.2: Two-dimensional eigenfunction for the eigenvalue $c = 0.28 - 2.5 \cdot 10^{-3}$i, $Re_b = 3333$, $\alpha = 1.12$, $\beta = 0$. ——— *Real part,* ---- *imaginary part. Left: Streamwise velocity disturbance u'_{2D}. Right: Wall-normal velocity disturbance w'_{2D}.*

and two superimposed weak oblique (stable) three-dimensional waves with amplitude 0.1% with the same fundamental streamwise wavelength as the two-dimensional disturbance. The superposition of the three waves is such that the maximum amplitude of the disturbance occurs at $y = L_y/2$ (spanwise "peak position"). The computation of the TS waves was performed using a standard Chebyshev collocation method involving the solution to the Orr-Sommerfeld and Squire equations (see *e.g.* Schmid & Henningson (2001)). The eigenvalue spectra for the two-dimensional and three-dimensional waves are shown in figure 4.1. In
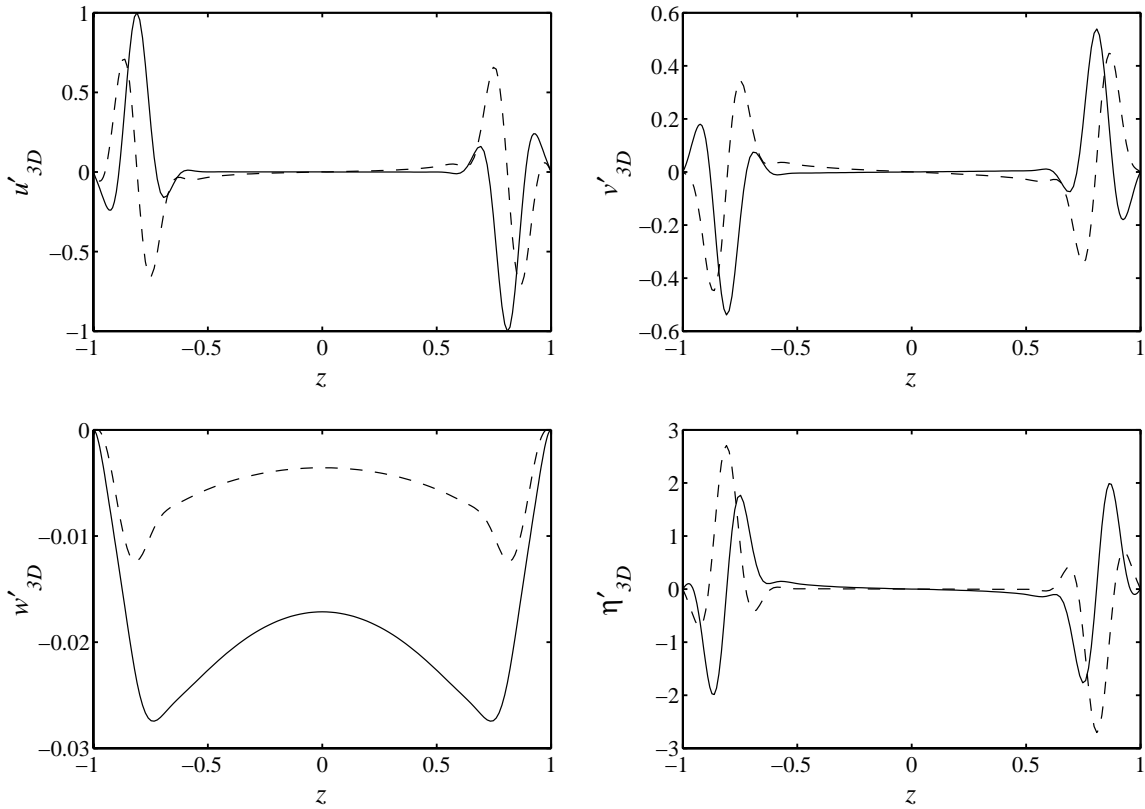
Figure 4.3: *Three-dimensional eigenfunction for the eigenvalue* $c = 0.32 - 7.0 \cdot 10^{-2}$i, $Re_b = 3333$, $\alpha = 1.12$, $\beta = 2.1$. ——— *Real part,* - - - - *imaginary part. From* left *to* right *and* top *to* bottom: *Streamwise velocity disturbance* u'_{3D}, *spanwise velocity disturbance* v'_{3D}, *wall-normal velocity disturbance* w'_{3D}, *and wall-normal vorticity disturbance* η'_{3D}.

figures 4.2 and 4.3, the eigenfunctions of the disturbances included in the initial conditions are displayed.

This type of initial disturbance promotes the growth of an aligned pattern of Λ-vortices leading to standard K-type breakdown (see *e.g.* Kachanov (1994)). The above initial conditions are chosen similar to the experiments by Nishioka *et al.* (1975). The Reynolds number based on bulk velocity and channel half-width is $Re_b = 3333$. The non-dimensional box dimensions are $5.61 \times 2.99 \times 2$, non-dimensionalised by the channel half-width (see also table 4.1). Moreover, the same parameters have been used in the fully resolved DNS by Gilbert (1988) and Gilbert & Kleiser (1990). These authors used a resolution of up to $128^2 \times 129$ grid points, however for the present work the simulation was recomputed on $160^2 \times 161$ grid points. However, no significant differences
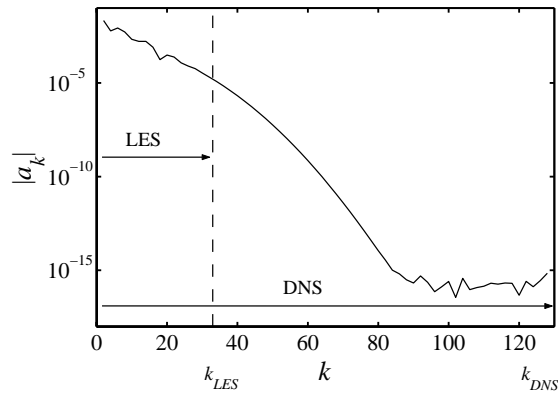
Figure 4.4: Chebyshev spectrum $|a_k|$ of the streamwise velocity component of the initial disturbance. The vertical dashed line indicates a wall-normal resolution of $N = 33$ used for some of the results presented herein.

in the results could be observed.

In figure 4.4, the Chebyshev spectrum of the streamwise velocity component of the initial disturbance for the K-type transition is shown. As it can be inferred from the figure, the disturbances are fully resolved (up to machine precision $\mathcal{O}(10^{-16})$) at $k \approx 90$. For $k > 25$ the energy content of the modes decreases monotonically, indicating that the minimum resolution to resolve the initial disturbance lies above $k = 25$. For this reason a minimum wall-normal resolution of about $k = 33$ will be chosen for an LES using those initial conditions.

To further validate this point, two simulations with sufficiently fine resolution ($128^2 \times 129$ grid points) were conducted starting from fields with resolution $32^2 \times 33$ at $t = 0$ and $t = 80$, respectively. Both showed no significant differences in the integral quantities such as skin friction and shape factor during transition compared to the reference DNS calculation ($160^2 \times 161$ grid points for simulation and initial condition). Moreover, it can be concluded that the early transitional phase of the saturated Tollmien-Schlichting wave is sufficiently resolved with only 33 points across the channel. Further test calculations were conducted to confirm the accuracy of the results with respect to the choice of the time step which is limited by the usual CFL condition, indicating that the results presented herein are not affected by the choice of the time step of the numerical integration.

4.1.2 Parameter settings

The parameters for the various simulations in channel geometry are given in tables 4.1 and 4.2. The parameters are chosen to match standard cases found in the literature. The simulation of turbulent channel flow at the parameters of case A was first performed by Kim *et al.* (1987) and later revisited by Moser *et al.* (1999) together with case C at an increased Reynolds number. The simulations of standard fundamental (K-type) transition is performed using the parameter settings of Kleiser (1982); Gilbert (1988); Gilbert & Kleiser (1990) (case B), which were chosen to reproduce the experimental setup of Nishioka *et al.* (1975). Note that all DNS results for cases A, B and C have been recomputed in the course of the present work in order to allow detailed analysis of the fully resolved data, in particular to be able to obtain filtered DNS data (filtered to the respective LES resolution). Note that for case A the streamwise resolution of the DNS is lower than for cases B and C, however as reported in Kim *et al.* (1987) no significant differences in the averaged results could be observed. The LES resolution for case A was thus chosen rather coarse in the streamwise direction. Case D denotes the spatial simulation presented in chapter 5, included here for reference.

All statistical quantities have been averaged over the wall-parallel planes x, y and, as appropriate, over time t, for which the notation according to the Reynolds decomposition

$$u_i = \langle u_i \rangle + u_i' = \langle u_i \rangle_{x,y,t} + u_i' \tag{4.1}$$

is used.

For the non-dimensionalisation of the velocity and length scales the channel half-width h° and the laminar streamwise velocity in the channel centre $(z = 0)$ $u_{CL}^\circ|_{\mathrm{lam}}$ have been used, see section 2.1. The non-dimensional bulk velocity is defined as

$$u_b = \frac{1}{2} \int_{-1}^{1} \langle \overline{u} \rangle \, \mathrm{d}z = \frac{2}{3} \; . \tag{4.2}$$

u_b and the respective Reynolds number $Re_b = u_b^\circ h^\circ / \nu^\circ = (2/3) Re_{CL}|_{\mathrm{lam}}$ are held constant during the simulations (see chapter 3). The Reynolds number based on the centre-line velocity is given by

$$Re_{CL} = \frac{u_{CL}^\circ h^\circ}{\nu^\circ} = Re_{CL}|_{\mathrm{lam}} \overline{u}_{CL} \; . \tag{4.3}$$

Table 4.1: Parameters for the simulations in plane channel geometry.

	$L_x \times L_y \times L_z$	Re_τ	Re_{CL}	H_{12}	Re_b	$Re_{CL}|_{\mathrm{lam}}$
A	$4\pi \times 4\pi/3 \times 2$	179	3262	1.655	2800	4200
B	$2\pi/1.12 \times 2\pi/2.1 \times 2$	208	3857	1.637	3333	5000
C	$2\pi \times \pi \times 2$	587	12576	1.574	10935	16403
D	$100 \times 3 \times 2$	208	3857	1.637	3333	5000

The shape factor is calculated as

$$H_{12} = \int_{-1}^{1} (1 - \langle \overline{u} \rangle)\, \mathrm{d}z / \int_{-1}^{1} \langle \overline{u} \rangle\, (1 - \langle \overline{u} \rangle)\, \mathrm{d}z \ . \qquad (4.4)$$

The Reynolds number based on the friction velocity is defined as

$$Re_\tau = \frac{u_\tau^\circ h^\circ}{\nu^\circ} = \sqrt{Re_{CL}|_{\mathrm{lam}} \left| \frac{\partial \langle \overline{u} \rangle}{\partial z} \right|_{\mathrm{wall}}} \ . \qquad (4.5)$$

The friction velocity is given as

$$u_\tau^\circ = \sqrt{\frac{\tau_w^\circ}{\rho^\circ}} \ , \qquad (4.6)$$

using the dimensional density ρ° and the skin friction

$$\tau_w^\circ = \nu^\circ \rho^\circ \left| \frac{\partial \langle u^\circ \rangle}{\partial z^\circ} \right|_{\mathrm{wall}} \ . \qquad (4.7)$$

The values given in table 4.1 are statistically averaged results taken from the DNS. In figures 4.5 and 4.6 the results for the DNS at the different Reynolds numbers are summarised together with the corresponding no-model LES (coarse-grid DNS). The averaged Reynolds stresses $\langle \overline{u}_1' \overline{u}_1' \rangle^{1/2}/u_\tau$, $\langle \overline{u}_2' \overline{u}_2' \rangle^{1/2}/u_\tau$, $\langle \overline{u}_3' \overline{u}_3' \rangle^{1/2}/u_\tau$, $\langle \overline{u}_1' \overline{u}_3' \rangle/u_\tau^2$ and the mean streamwise velocity profile $\langle \overline{u}(z^+) \rangle^+$ are depicted in figure 4.5. For the fully resolved DNS data, it can be seen that with increasing Reynolds number the peak of the turbulent kinetic energy moves closer to the wall, whereas in the mean streamwise velocity profile the formation of a distinct logarithmic layer can be observed, see the discussion in Moser *et al.* (1999). The data of the no-model calculations deviate

Table 4.2: Resolution of the simulations of table 4.1. For LES the data using a typical resolution is given.

		$N_x \times N_y \times N_z$	$\Delta x^+ \times \Delta y^+ \times \Delta z^+|_{\text{wall}}/\Delta z^+|_{\text{centre}}$
A	DNS	$128 \times 128 \times 129$	$18 \times 5.8 \times 0.044/5.4$
	LES	$32 \times 32 \times 33$	$70 \times 23 \times 0.86/18$
B	DNS	$160 \times 160 \times 161$	$7.3 \times 3.9 \times 0.040/4.1$
	LES	$32 \times 32 \times 33$	$37 \times 20 \times 1.0/21$
C	DNS	$384 \times 384 \times 257$	$9.7 \times 4.8 \times 0.044/7.2$
	LES	$64 \times 64 \times 65$	$58 \times 29 \times 0.7/29$
D	LES	$1024 \times 32 \times 33$	$41 \times 20 \times 1.0/21$
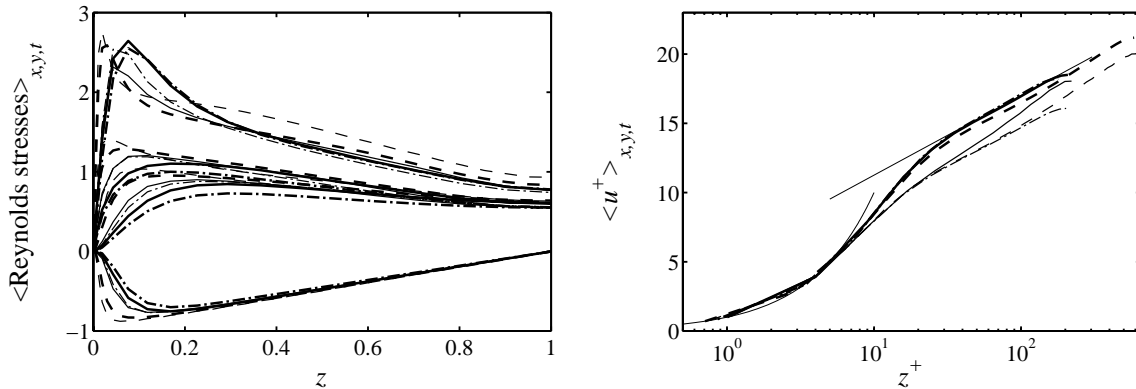
Figure 4.5: Comparison of turbulent channel flow results for the cases given in table 4.1. $-\cdot-\, Re_\tau = 179$, $\underline{\hspace{1cm}}\, Re_\tau = 208$, $----\, Re_\tau = 587$. Thick lines: Fully resolved DNS. Thin lines: LES resolution (no-model LES). Parameters see tables 4.1 and 4.2. Left: *Reynolds stresses.* Right: *Mean velocity profile.*

clearly from the reference DNS data, indicating that the LES resolution is indeed not sufficient without an appropriate SGS model. The analytical correlations

$$u^+ \;=\; y^+ \tag{4.8}$$

$$u^+ \;=\; 2.5\log(y^+) + 5.5 \tag{4.9}$$

are included in the plots of the mean streamwise velocity profile for reference.

The energy budget for the DNS and the no-model LES is displayed in figure 4.6. Shown are the turbulent production $\mathcal{P}$, the viscous dissipation due to mean-flow strain $\varepsilon_{\text{visc,mean}}$ and the viscous dissipation due to
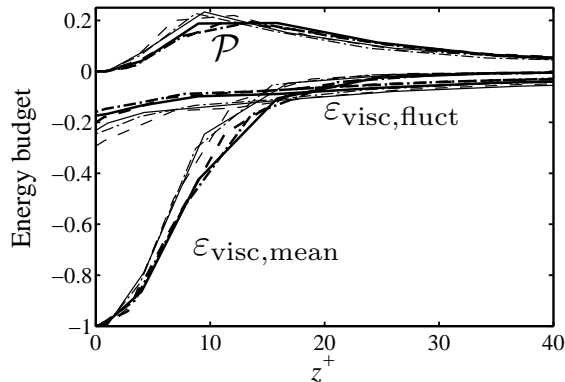
Figure 4.6: Energy budget normalised by viscous wall units, $(u_\tau^\circ)^4/\nu^\circ$: Production $\mathcal{P}$, viscous dissipation due to mean-flow strain $\varepsilon_{\mathrm{visc,mean}}$, viscous dissipation due to strain of fluctuations $\varepsilon_{\mathrm{visc,fluct}}$. Line caption see figure 4.5.

strain of fluctuations $\varepsilon_{\mathrm{visc,fluct}}$. These quantities are defined in section B.3 in the appendix, see also section 4.7.4. Due to the scaling in viscous units, the influence of the Reynolds number is small. However, again a distinct difference between the fully resolved DNS and the coarse-grid simulations can be observed.

4.2 Analysis of DNS results during transition

During the temporal evolution of K-type transition, a saturated TS wave is formed ($t < 100$), which undergoes secondary instability with the formation of strong shear layers and pronounced open Λ-vortices ($t \approx 130$) (Gilbert & Kleiser, 1990; Sandham & Kleiser, 1992). These vortices in turn provoke the appearance of hairpin vortices (roll-up of shear layer, $t \approx 136$) first in the peak plane ($y = L_y/2$), which are also visible in the streamwise velocity signal as sharp low-velocity "spikes". The roll-up of the shear layer then proceeds to more complex flow states and eventually the whole flow domain is affected ($t \approx 155$).

During the transitional processes, the resolution requirements for a fully resolved simulation naturally increase with the growing complexity of the flow field. By an examination of the DNS data similar to an *a-priori* analysis, quantitative information important for an LES can be obtained, see also Schlatter *et al.* (2004*a*). Figure 4.7a shows the excited computational modes during transition taken from the respective DNS. In the wall-parallel directions, a threshold of 10^{-15} has been
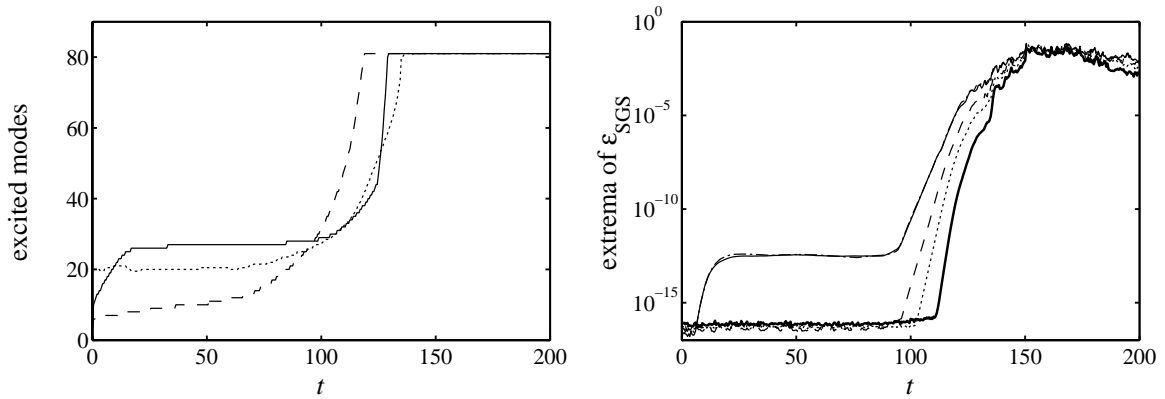
Figure 4.7: Left: *Excited modes of the DNS (resolution $160^2 \times 161$ grid points).* ———— *Streamwise direction,* ———— *spanwise direction,* ········ *wall-normal direction (number of Chebyshev modes is halved to allow comparison with Fourier modes). In the Fourier directions a threshold of 10^{-15} is used whereas the threshold value in the wall-normal direction is 10^{-6}.* Right: *Maximum of SGS dissipation* $\max_{x,y,z} \varepsilon_{\mathrm{SGS}}$. ———— $32^2 \times 33$, —·— $32^2 \times 49$ *(almost coinciding with $32^2 \times 33$),* ———— $48^2 \times 49$, ········ $64^2 \times 65$, ———— $96^2 \times 97$.

chosen, whereas in the wall-normal direction due to the full Chebyshev spectrum (see figure 4.4) a threshold of 10^{-6} has been used. It can be seen that at first higher and higher Fourier harmonics in the streamwise direction are excited, which is attributed to the formation of the saturated two-dimensional Tollmien-Schlichting wave (Kleiser, 1982; Gilbert, 1988). Starting from $t \approx 80$ the flow undergoes secondary instability due to the three-dimensional disturbance (Herbert, 1988), which leads to an increased resolution requirement in both the spanwise and the wall-normal directions.

By choosing a resolution of only $32^2 \times 33$ grid points (16 Fourier modes), the simulation is underresolved in all directions for at least $t > 70$. In figure 4.7b, the SGS dissipation $\varepsilon_{\mathrm{SGS}}$ (see section B.3) was computed from DNS data, *i.e.* (see equations (2.7) and (2.8))

$$\tau_{ij} := \overline{u_i u_j} - \overline{u}_i \overline{u}_j$$

and

$$\varepsilon_{\mathrm{SGS}} = \tau_{ij} \overline{S}_{ij} \ ,$$

for a number of LES grids with full dealiasing. The spatial filtering implied by the overbar was performed by a spectral truncation of the wall-parallel Fourier components and an interpolation in physical space

for the wall-normal direction. The physical-space interpolation was chosen in order to leave the mean velocity profile unchanged between the high-resolution data and the truncated data and to maintain the wall boundary conditions (see also section 4.7).

Similarly to figure 4.7, the resolution $32^2 \times 33$ indicates the necessity of an SGS model even for the early laminar stages prior to transition, mainly due to the underresolved 2D saturated TS wave. Based on these findings, for the following an LES resolution of $32^2 \times 33$ grid points was chosen in order to assess the ability of the SGS model to predict laminar, transitional and turbulent flows (see the following sections and Schlatter *et al.* (2004*c,d*)). The choice of this resolution has also been prompted by the examination of the intial disturbances, see section 4.1.1.

4.3   Dynamic Smagorinsky model

The dynamic Smagorinsky model, introduced by Germano *et al.* (1991) and slightly modified by Lilly (1992), is one of the most popular SGS models for LES. A description of the algorithm is given in section B.4. As mentioned in section 2.1.1 the computation of the dynamic model coefficient relies on a low-pass test filtering of the turbulent stresses. For the results presented in this section, four different test filters have been examined with fixed cutoff wavenumber $\omega_c = \pi/2$. The filters are $I - H_1 = Q_1 G$ (equation (2.12)), G (equation (2.10)), a second-order filter (2.19) and the spectral cutoff filter (acting only on the wall-parallel Fourier modes). The filter transfer functions are depicted in figure 2.3.

Results obtained using the dynamic Smagorinsky model with the different test filters are shown in figures 4.8-4.11. The Reynolds stresses $\langle \overline{u}_1' \overline{u}_1' \rangle^{1/2}/u_\tau$, $\langle \overline{u}_2' \overline{u}_2' \rangle^{1/2}/u_\tau$, $\langle \overline{u}_3' \overline{u}_3' \rangle^{1/2}/u_\tau$, $\langle \overline{u}_1' \overline{u}_3' \rangle/u_\tau^2$ and the mean streamwise velocity profile $\langle \overline{u}(z^+) \rangle^+$ in wall scaling are shown in figure 4.8 for the three different Reynolds numbers at the resolutions given in table 4.2. It is evident from the figure that for all Reynolds numbers the dependence of the model on the test filter is similar. The use of the second-order filter leads to a too dissipative model behaviour resulting in an overprediction of the mean velocity profile $\langle \overline{u} \rangle^+$ and of $\langle \overline{u}_1' \overline{u}_1' \rangle^{1/2}/u_\tau$. Moreover, the restriction of the second-order filter to two dimensions (filtering in wall-parallel directions only) gives similar results as with the three-dimensional formulation. The filter G (equation (2.10)) as test filter is also too dissipative for all Reynolds numbers. The spectral cutoff filter (acting in two dimensions only) provides an increased accuracy in

Figure 4.8: Turbulent channel flow simulated by the dynamic Smagorinsky model using different test filters. From top *to* bottom*: $Re_\tau \approx 180$, $Re_\tau \approx 210$, $Re_\tau \approx 590$. Left: Mean streamwise velocity profile. Right: Averaged Reynolds stresses.* —— *Second-order filter (3D),* − − − − G, ········ $I - H_1$, −·−·− *spectral cutoff filter (only 2D),* —— *second-order filter (only 2D),* ∘ *no-model LES,* • *DNS interpolated onto LES grid.*

the prediction of both the Reynolds stresses and the velocity profile, however this filter is restricted to spectral numerics. Moreover, its generality is limited since the filtering is performed in the wall-parallel directions

only. Note that the original paper of Germano *et al.* (1991) was based on this filter. Similar or slightly improved accuracy as with the cutoff filter can however been obtained by using the three-dimensional high-order filter $I - H_1 = Q_1 G$ (sixth order), see also Stolz *et al.* (2005).

Figure 4.9 shows the energy budget and the different contributions to the SGS dissipation for the three Reynolds numbers. No major differences between the various test filters and Reynolds numbers can be observed for the energy budget including production and viscous dissipation, and all LES show a significant improvement over the no-model calculation. To the contrary, the SGS dissipation, however, is strongly dependent on the test filter used. In particular, the contribution to the SGS dissipation $\varepsilon_{\mathrm{SGS,mean}}$ due to the mean flow is nearly twice as high for the second-order filter compared to *e.g.* the spectral cutoff filter. This is certainly one reason that the dynamic Smagorinsky model with the second-order test filter is too dissipative. Similar conclusions can also be drawn for the other filter types.

Using the dynamic Smagorinsky model it is possible to simulate laminar-turbulent transition (Germano *et al.*, 1991). In the laminar and early transitional regions, the algorithm computes a vanishing or at least small value for the model coefficient such that the (usually weak) disturbances present in the flow are not overly affected. Figure 4.10 shows the evolution of Re_τ during temporal K-type transition. It can be observed that the higher-order filters ($I - H_1$ and spectral cutoff filter) are predicting transition too early similar to the no-model calculation. More dissipation during the early stages of transition is provided by the second-order test filter providing a good prediction of the transition location compared to the fully resolved DNS.

In figure 4.11 the model coefficient C_S^2 is shown, both for the temporal evolution during transition and averaged during the fully turbulent phase well after transition. The dynamic determination algorithm indeed predicts a negligible C_S for early times $t < 100$ with all test filters. As transition proceeds, the model coefficient rises according to the increased turbulent activity within the flow field. In the fully turbulent channel flow, all test filters predict a vanishing coefficient at the solid walls ($z = \pm 1$) and thus a vanishing eddy viscosity. The asymptotic behaviour for all filters is $\propto (z^+)^3$ as predicted by theory (see *e.g.* Piomelli (1993)). However, a drastic difference in the magnitude of the model coefficient (and hence in the eddy viscosity) can be observed for the different filters. The lowest coefficient is obtained for the spectral cutoff filter, whereas
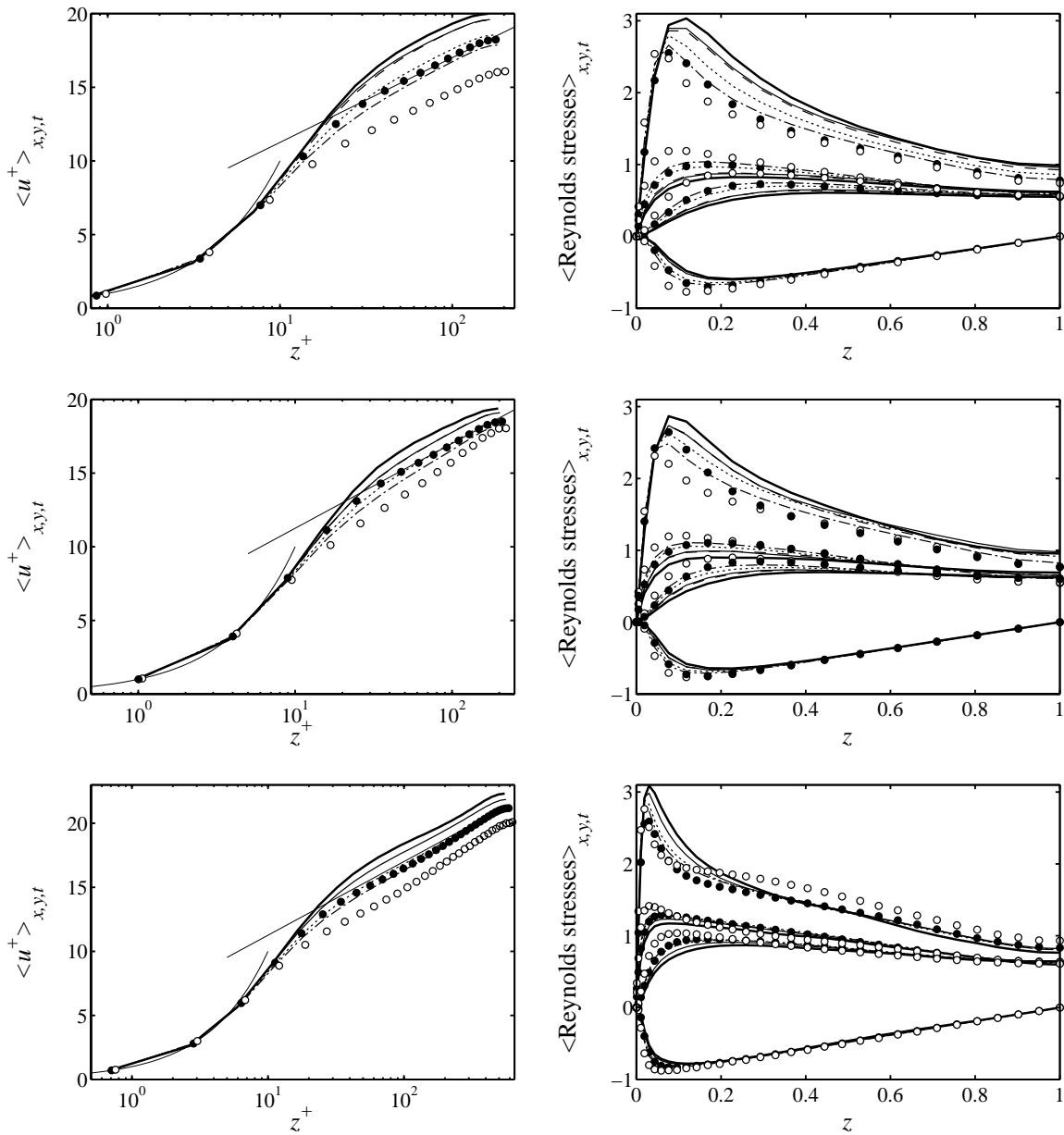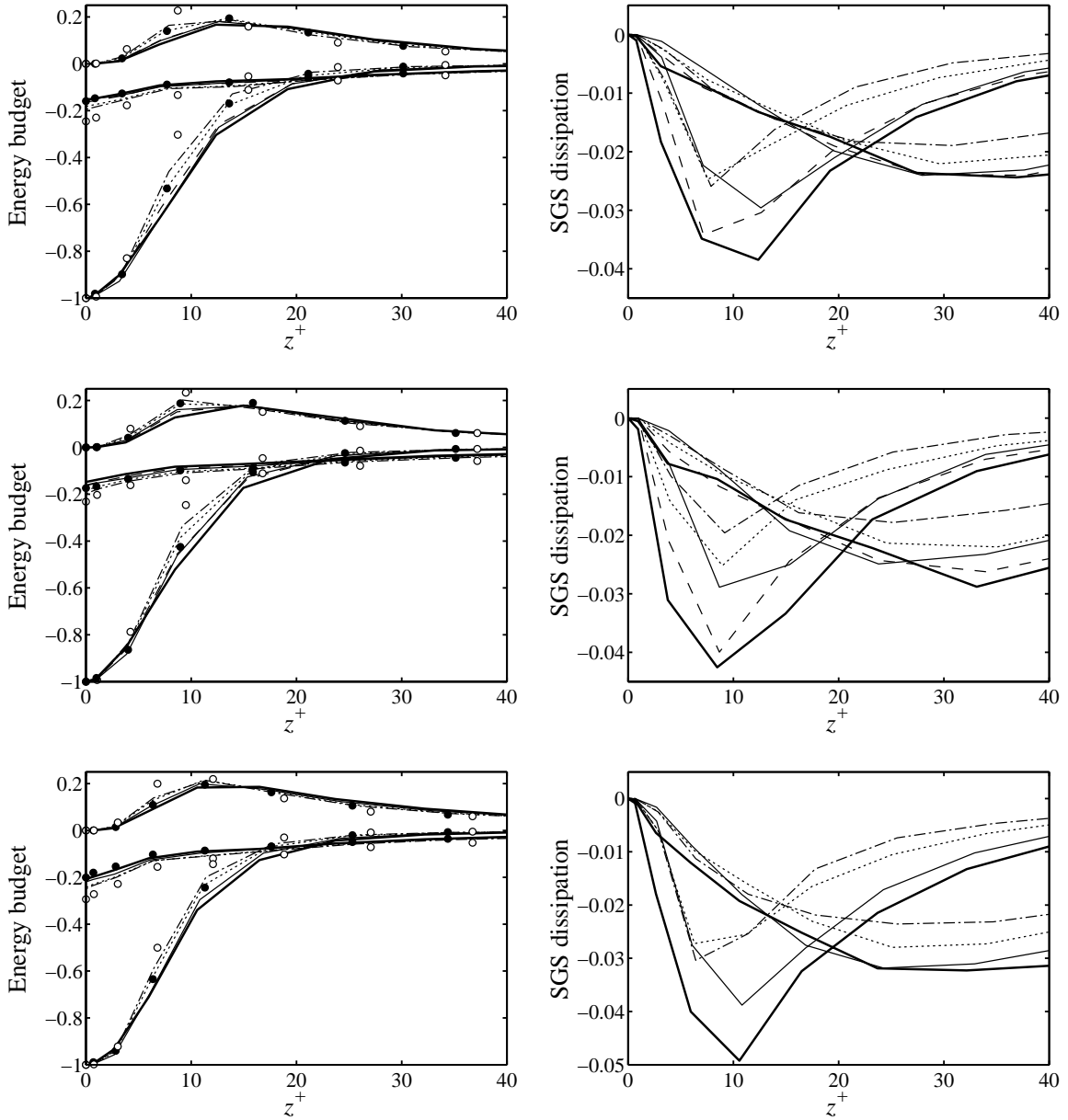
Figure 4.9: Turbulent channel flow simulated by the dynamic Smagorinsky model using different test filters. From top *to* bottom*:* $Re_\tau \approx 180$*,* $Re_\tau \approx 210$*,* $Re_\tau \approx 590$*.* Left: *Production* $\mathcal{P}$*, viscous dissipation due to mean-flow strain* $\varepsilon_{\text{visc,mean}}$*, viscous dissipation due to strain of fluctuations* $\varepsilon_{\text{visc,fluct}}$*.* Right: *SGS dissipation due to mean flow* $\varepsilon_{\text{SGS,mean}}$*, SGS dissipation due to fluctuations* $\varepsilon_{\text{SGS,fluct}}$ *(note that for all models* $\varepsilon_{\text{SGS,mean}} > \varepsilon_{\text{SGS,fluct}}$ *close to the wall).* —— *Second-order filter (3D),* −−−− *G,* ········· $I - H_1$*,* −·−· *spectral cutoff filter (only 2D),* —— *second-order filter (only 2D),* ○ *no-model LES,* • *DNS interpolated onto LES grid.*
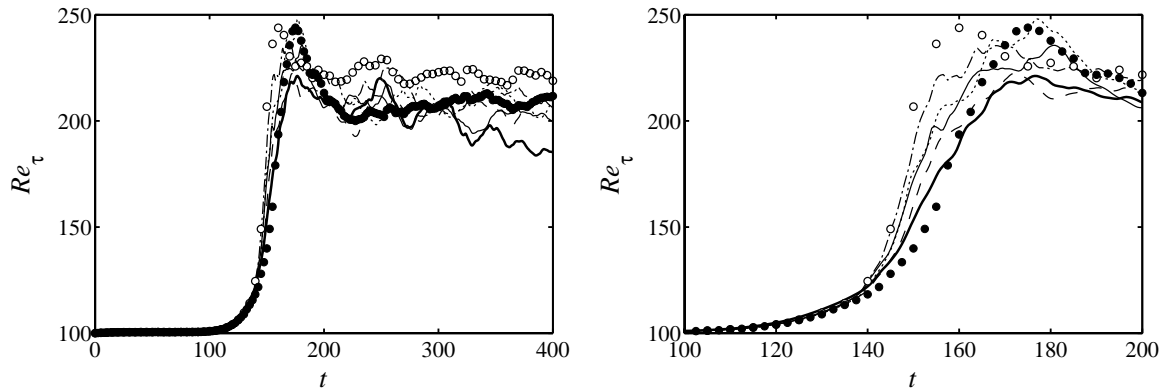
Figure 4.10: Time evolution of Re_τ for temporal K-type transition at $Re_b = 3333$ using the dynamic Smagorinsky model with different test filters. ——— *Second-order filter (3D),* - - - - *G,* ········ *$I - H_1$,* —·— *spectral cutoff filter (only 2D),* ——— *second-order filter (only 2D),* ○ *no-model LES,* ● *DNS interpolated onto LES grid.*
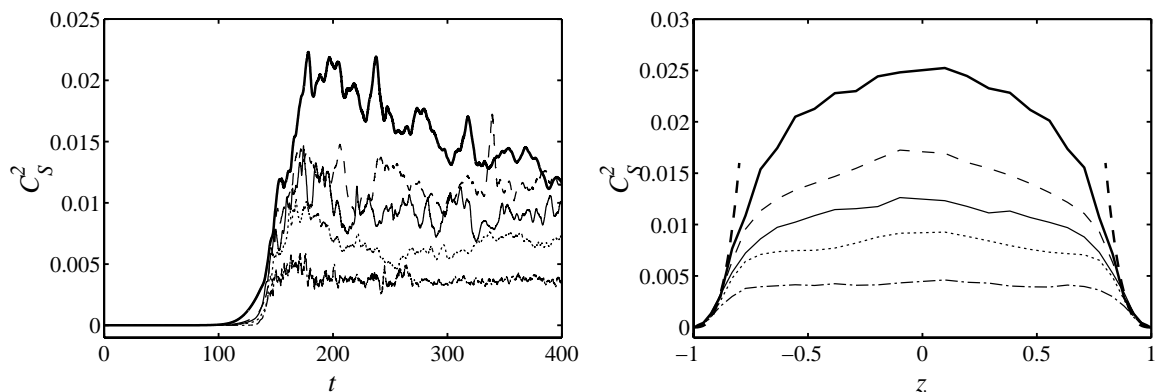
Figure 4.11: Smagorinsky coefficient C_S^2 as computed by the dynamic Smagorinsky model for temporal K-type transition, $Re_b = 3333$, $Re_\tau \approx 210$. Left: *Time evolution of C_S^2 during transition.* Right: *Averaged model coefficient well after transition for turbulent channel flow at $Re_\tau \approx 210$.* ——— *Second-order filter (3D),* - - - - *G,* ········ *$I - H_1$,* —·— *spectral cutoff filter (only 2D),* ——— *second-order filter (only 2D). Thick dashed line indicates asymptotic progression $\propto (z^+)^3$ close to the walls (Piomelli, 1993).*

the largest value is computed with the second-order filter, which results in an increased SGS dissipation (see figure 4.9). However, the general three-dimensional formulation using the high-order filter $I - H_1$ as test filter is predicting a comparably low value for the model coefficient.

To conclude, the dynamic Smagorinsky model allows the simulation

of laminar, transitional, and turbulent channel flow with all the mentioned test filters, however the influence of the filter type on the results is significant. For the following considerations and the results presented in chapter 5 we will routinely compare to the dynamic Smagorinsky model evaluated using the three-dimensional second-order test filter, since this filter seems to provide the most accurate description of transitional flows. Additionally, this filter is general in formulation (three-dimensional) and straightforward to implement in simulation codes with other than spectral numerics.

4.4 Temporal transition and turbulence using the approximate deconvolution model

In this section, the approximate deconvolution model (ADM, equation (2.35)) and related LES strategies like the SGS model based on relaxation regularisation (ADM-RT, equation (2.51)) are considered for transitional and turbulent channel flow at $Re_\tau \approx 210$ and $Re_\tau \approx 180$, see also Schlatter *et al.* (2004*c*, 2003*a*). The description of the ADM model is given in section 2.2.3 and is based on the original formulation provided in Stolz & Adams (1999); Stolz *et al.* (2001*a*).

4.4.1 ADM for transitional flows

For both laminar and turbulent flow, the standard ADM formulation with deconvolution and relaxation in three dimensions, equation (2.33), henceforth denoted as ADM-3D, gives very accurate results as reported in Stolz *et al.* (2001*a*) for turbulent channel flow at Re_τ up to 590. However, initial tests on very coarse grids (*i.e.* only 33 points in the wall-normal direction, see section 4.1) using ADM-3D in its original form (Stolz *et al.*, 2001*a*) have indicated that for this resolution it cannot directly be applied to simulate transitional flows in which the initial state consists of a laminar base flow with superimposed small-amplitude disturbances. However, with increased resolution the transitional process is predicted well. The problem arises mainly due to the use of explicit filtering within the ADM approach with deconvolution used for the nonlinear terms and subsequent filtering. This further reduces the range of resolved wavenumbers from $[0, \pi]$ to $[0, \omega_c]$, *e.g.* $[0, 2\pi/3]$.

Figure 4.12 shows the evolution of the 2D Fourier modes with vanishing relaxation term, *i.e.* $\chi = 0$ and only deconvolution and explicit
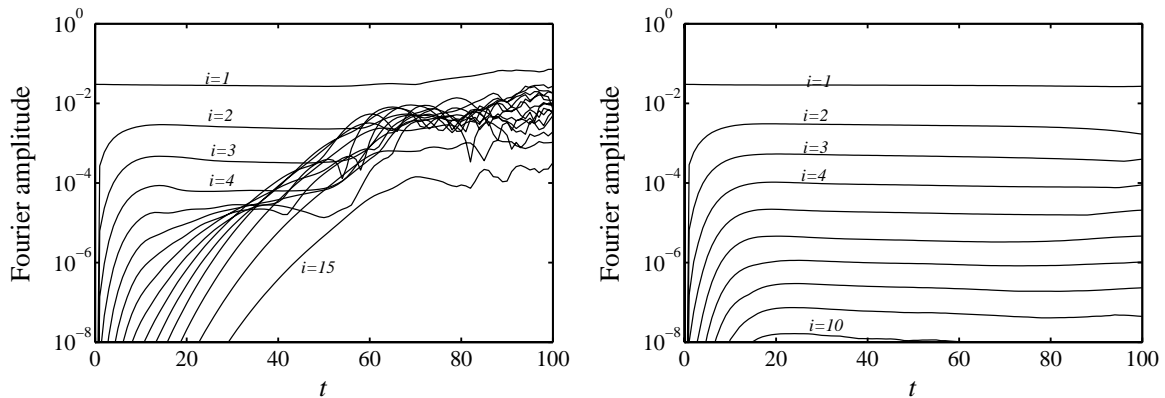
Figure 4.12: Evolution of the wall-normal maximum of the 2D Fourier amplitudes $\max_{x_3} |\hat{\bar{u}}_1(k_i, 0, x_3, t)|$ *during the initial phase of transition. The standard ADM-3D SGS model is used with deconvolution, but without relaxation (i.e.* $\chi = 0$*). Left: Resolution* $32^2 \times 33$*. Right: Resolution* $32^2 \times 49$*.*

filtering used for the nonlinear terms. The physical solution at this stage of development ($t < 100$) consists of a saturated 2D wave, the harmonics of which exhibit a geometric progression with increasing wavenumbers, with each of the Fourier modes slowly decaying in time (Gilbert & Kleiser, 1990), see also figure 4.16. However, with 33 points only in the wall-normal direction the influence of deconvolution on the laminar solution is such that small-scale perturbations are amplified until they are dominating the flow field. The reason for this is the repeated application of the filter G in regions close to the wall. Fulfilling the wall boundary conditions can lead to oscillations in the near-wall region. Note that this phenomenon only occurs if wall-normal (three-dimensional) filtering and deconvolution is used and the wall-normal resolution is fairly coarse. As also shown in figure 4.12 (see also section 4.4.5), when using 49 or more points in the wall-normal direction the deconvolution gives acceptable results even close to the wall due to the lower energy content of the modes near the cutoff (see figure 4.4).

Applying the filter operation in Chebyshev spectral space instead of a real-space implementation does not remedy the described difficulties, which are inherent to such coarse grids. It should be noted again that the grid was deliberately chosen very coarse and furthermore, explicit filtering was employed.

To overcome the above-mentioned difficulties of the standard ADM procedure on very coarse grids, the modified ADM versions, *i.e.* ADM-2D and ADM-RT, have been investigated, for which simulation results are

summarised in table 4.3. The formal definition of those models has been given in section 2.2.3.

All computations were started at $t = 0$ with the initial condition described in section 4.1 and integrated up to at least a non-dimensional time $t = 1000$. For the statistically stationary results of fully developed turbulent channel flow the data is averaged over the time period $t = 500$ to $t = 1000$ well after the transitional phase. At resolution $32^2 \times 33$, the grid spacing is

$$\Delta x^+ \times \Delta y^+ \times \Delta z^+|_{\text{wall}}/\Delta z^+|_{\text{centre}} = 36.6 \times 19.5 \times 1.01/20.5 \ ,$$

see also tables 4.1 and 4.2. For ADM-2D and ADM-RT the relaxation term $-\chi \cdot (I - Q_N * G) * \overline{u}_i$ was computed in real space. The use of a dealiasing procedure (see Canuto *et al.* (1988)) to calculate the nonlinear product in the relaxation term was tested but found not necessary, due to a sufficiently smooth relaxation coefficient χ. For the simulations presented in this section, the model coefficient χ has been determined dynamically using the procedure explained in equation (2.43) (section 2.2.3). However, tests have shown that using a constant χ produces similar results, see also section 4.5 below.

DS-3D denotes the dynamic Smagorinsky model (Germano *et al.*, 1991; Lilly, 1992), included for reference. The test filter used for the dynamic Smagorinsky model is the three-dimensional filter of second order with $\omega_c = \pi/2$, equation (2.19), see also previous section 4.3. No significant differences between two and three-dimensional test filtering have been observed for the dynamic Smagorinsky model.

4.4.2   Transitional phase

During the initial phase of transition ($t < 100$) the saturated two-dimensional Tollmien-Schlichting wave is dominant, and thus all integral quantities like Re_τ remain at their laminar values. In the secondary instability phase (Herbert, 1988), the onset of transition becomes visible (at $t \approx 100$) by the typical Λ-shaped vortices which evolve with their own dynamics ($t \approx 120$). This leads to the distinct spanwise "peak-valley splitting" (Nishioka *et al.*, 1975; Gilbert & Kleiser, 1990). In the following "spike stage" the flow is dominated by strong wall-normal shear layers which rapidly break down to turbulence, first in the peak plane ($y = L_y/2$) and shortly thereafter in the valley region ($y = 0$). Although the Λ-vortices can be identified in all the different simulations, the time

Table 4.3: Temporally and spatially averaged Reynolds number Re_τ obtained for the different simulations of fully developed turbulent channel flow at $Re_b = 2800$ and $Re_b = 3333$.

Re_τ for $Re_b =$	2800	3333	
ADM-2D $32^2 \times 33$, 2D filt./deconv.	180.8	214.0	- - - -
ADM-3D $32^2 \times 33$, 3D filt./deconv.	170.8	n/a	
ADM-RT $32^2 \times 33$, only 3D relax.	177.5	208.9	——
DS-3D $32^2 \times 33$, dyn. Smagorinsky	165.8	195.1	········
no-model LES $32^2 \times 33$	202.7	220.0	——
no-model LES $32^2 \times 48$	203.1	219.9	
fully resolved DNS $160^2 \times 161$	178.6	208.2	
grid-filtered to $32^2 \times 33$	178.9	208.4	●
filtered with G (2D)	178.9	208.4	○
filtered with G (3D)	176.8	206.2	

of breakdown is different for the various computations. This is shown in figure 4.13 which depicts the temporal evolution of the Reynolds number Re_τ based on the friction velocity and the channel half-width, averaged over the two walls. The onset of transition and the initial growth of Re_τ is still comparable for all simulations, while they begin to separate during the spike stage ($t \approx 140$). Furthermore, the peak value of the skin friction is similar and the well-known overshoot of Re_τ of about 15% is visible for DNS, ADM-2D and ADM-RT. The formation of fully developed turbulence seems to proceed on the same time scale. The stationary values of Re_τ after transition are given in table 4.3 ($Re_b = 3333$).

The shape factor H_{12} is a measure which indicates a reorganisation of the mean velocity profile (figure 4.14). Starting from the value $H_{12} = 2.5$ of the laminar base flow profile all simulations reach the turbulent value at around the same time $t \approx 170$. The mean-velocity reduction in the middle of the channel, seen from Re_{CL} in figure 4.14, shows again at least two different paths from the laminar to the turbulent values, which are more distinct than a slight translation in time.

It is common to all these results that the no-model LES and the two-dimensionally filtered ADM-2D go through transition at earlier times than the fully resolved DNS, see Figures 4.13 and 4.14. Conversely, ADM-RT on coarse grids undergoes transition slightly later than the reference data. Note that due to the two-dimensional formulation of
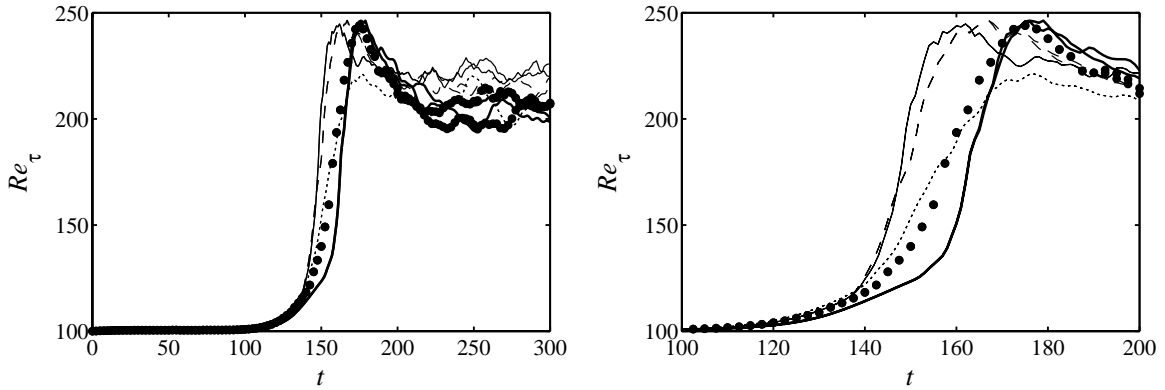
Figure 4.13: Evolution of Re_τ averaged in a wall-parallel plane during the transitional phase ($Re_b = 3333$). Line caption see table 4.3. Multiple values indicate lower/upper channel wall.
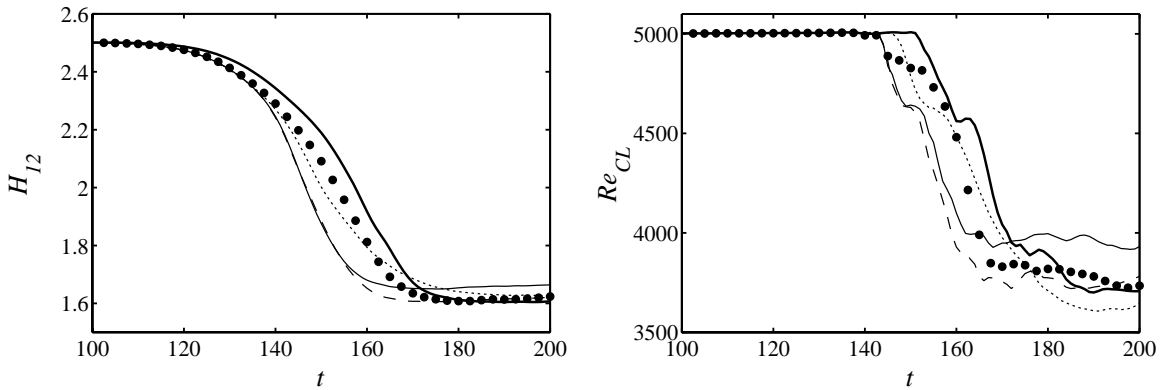
Figure 4.14: Left: *Evolution of the shape factor H_{12} averaged in a wall-parallel plane during the transitional phase ($Re_b = 3333$).* Right: *Evolution of Re_{CL} averaged in a wall-parallel plane during the transitional phase ($Re_b = 3333$). Line caption see table 4.3.*

the SGS model in ADM-2D, actually no SGS model is employed in the wall-normal direction. DS-3D seems to first follow the evolution of the no-model LES and then to change to the path of the fine-grid DNS.

Better insight can be gained by looking at the velocity fluctuations, *e.g.* the wall-normal maximum, $u_{rms,max}$, of the streamwise u_{rms}, given for the "valley" plane (Gilbert & Kleiser, 1990) in figure 4.15. It is obvious that the no-model LES and ADM-2D are close together, indicating that the SGS model is still inactive until $t \approx 150$. For ADM-RT at $t \approx 120$ some minor differences can already be observed and due to SGS influence the u_{rms} peak at $t = 160$ is accurately predicted. The dynamic
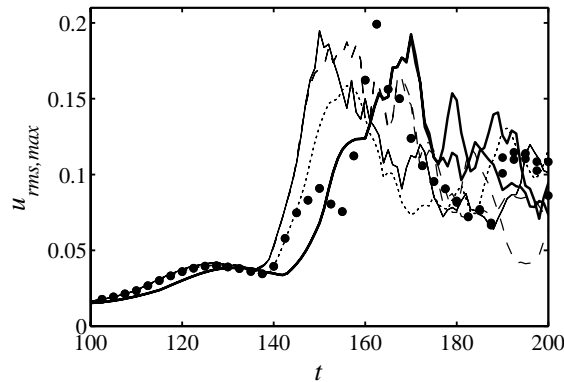
Figure 4.15: Evolution of $u_{rms,max}$ during the transitional phase ($Re_b = 3333$). The wall-normal maximum $u_{rms,max}$ of the streamwise u_{rms} in the "valley" plane is shown. Line caption see table 4.3.

Smagorinsky model again follows a route in between the no-model LES and the fully resolved DNS calculation. In the peak plane (not shown here), the phase of intense fluctuations is observed at the same time ($t \approx 150$) for all simulations.

4.4.3   Detailed analysis of ADM-RT results

From the results presented in figures 4.13-4.15 it can be concluded that ADM-RT (see equation (2.51)) is quite accurate despite its formal simplicity. It is therefore interesting to take a closer look at the evolution of the Fourier components that correspond to the 2D saturated Tollmien-Schlichting wave. Figure 4.16 shows results of both the DNS and the ADM-RT calculation (in figure 4.26 in section 4.5 the spectrum of the no-model LES is also shown). The modes with an amplitude level above 10^{-6} for the LES are approximately on the respective DNS level. The higher modes are on a lower level in the LES due to dissipation introduced by the relaxation term. The higher modes are somewhat noisy, which must clearly be attributed to the SGS model. As will be shown in section 4.5, using a constant relaxation parameter χ these oscillations are not present, see figure 4.26. On the other hand, these perturbations appearing using the dynamically determined χ do not grow in time and do not lead to inaccurate integral results. They originate close to the wall boundaries where the three-dimensional high-pass filter used in the dynamic procedure is difficult to apply.

The temporal evolution and the spatial distribution of the dynamic
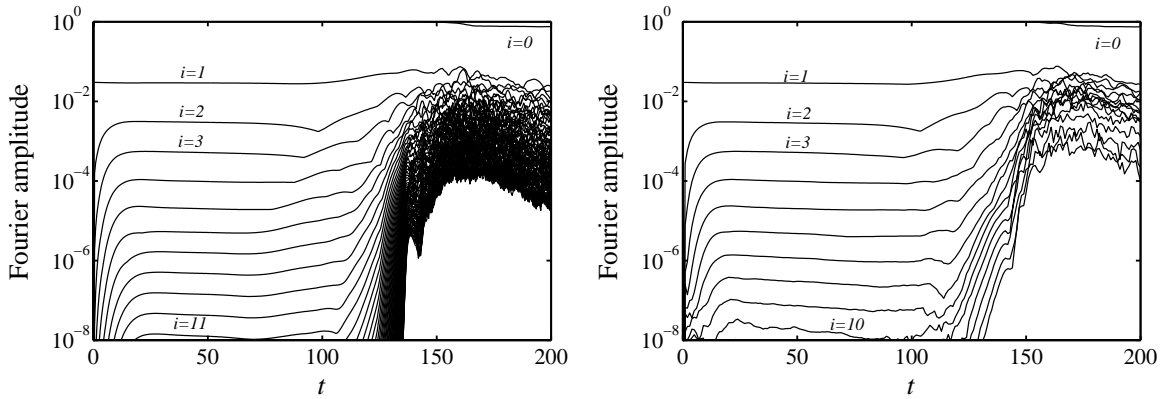
Figure 4.16: Evolution of the wall-normal maximum of the 2D Fourier amplitudes $\max_{x_3} |\hat{\overline{u}}_1(k_i, 0, x_3, t)|$ *corresponding to two-dimensional waves during the transitional phase* $(Re_b = 3333)$. *Left:* fully resolved DNS $160^2 \times 161$. *Right:* ADM-RT $32^2 \times 33$, $\chi = \chi_{\mathrm{dyn}}$.

coefficient χ for the relaxation term is shown in figure 4.17. Every full Runge-Kutta time step, χ is updated according to equation (2.43). This definition was derived aiming at keeping the energy content of the small scales in equilibrium, which holds, *e.g.*, for fully turbulent flows. The consequence can be seen in figure 4.17 for $t < 135$: Since the energy of the smallest scales is growing at these times due to physical interactions, the relaxation term is growing as well to counteract the generation of small-scale energy. The total influence of the relaxation term $-\chi(H * \overline{u}_i)$ is still very limited because $H * \overline{u}_i$ is small. However, during the secondary instability phase, a broad range of modes is excited which increases the effect of the relaxation term (growing $H * \overline{u}_i$) and in turn reduces χ accordingly. Only when the flow shows a full (developed) energy spectrum the equilibrium between production and dissipation becomes relevant, indicated by the statistically constant values of χ ($t > 160$).

In figure 4.17, also wall-normal profiles of χ are shown. During the saturated TS-wave phase a flat maximum is visible close to the wall ($t = 60$), whereas during the secondary instability phase ($t = 100$) χ is on a high level and evenly distributed over the channel height. In the fully developed turbulent flow, χ is fairly constant across the channel; a slight decrease close to the wall can be observed. This is actually desired as the influence of the model close to the wall should be smaller.

Note that using a constant relaxation parameter χ all the way from $t = 0$ through transition and in the fully turbulent phase yields results as accurate as with the dynamically determined χ. This will be discussed
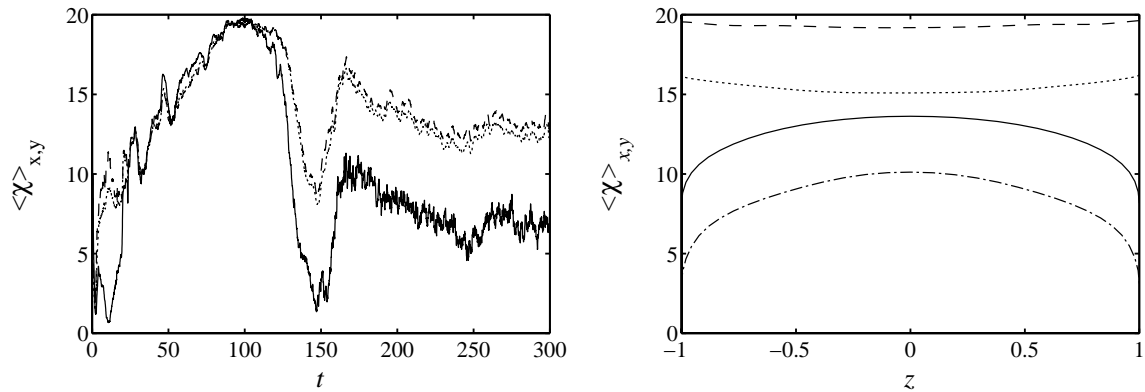
Figure 4.17: Left: *Evolution of χ averaged over wall-parallel planes during the transitional phase ($Re_b = 3333$, ADM-RT).* ——— $z = 1$ *(at wall),* ---- $z = 0$ *(centre),* ········ $z = 0.55$. Right: *Wall-normal distribution of χ averaged over wall-parallel planes during the transitional phase ($Re_b = 3333$, ADM-RT).* ········ $t = 60$, ---- $t = 100$, —·— $t = 150$, ——— *averaged $t = 500 - 1000$.*

further in section 4.5, see also section 2.2.3.

4.4.4   Fully turbulent phase

In table 4.3, the averaged values for Re_τ are also given for $Re_b = 2800$ (see Moser *et al.* (1999)). For the cases with $Re_b = 3333$, statistical averaging is performed from $t = 500$ to $t = 1000$. It is obvious that the no-model LES overpredicts the stationary value of Re_τ by approximately 10% compared to the fully resolved DNS. Both model calculations ADM-2D and ADM-RT provide a much better prediction of the wall friction. The dynamic Smagorinsky model (DS-3D) does similarly, although it seems to be too dissipative.

A similar conclusion can be drawn from the mean velocity profile; especially ADM-RT agrees very well with the fully resolved DNS, see figure 4.18.

The prediction of the velocity fluctuations (figure 4.19) for the dynamic Smagorinsky model is not very accurate, whereas the ADM variants ADM-2D and ADM-RT show a substantial improvement. The simulation ADM-RT is very close to the values of the fine-grid reference DNS calculation. ADM-2D is slightly less accurate, leading to the conclusion that capturing of three-dimensional effects in the relaxation and deconvolution are important during both transition and in the fully developed turbulence (compare also the three-dimensional filtering and deconvolu-
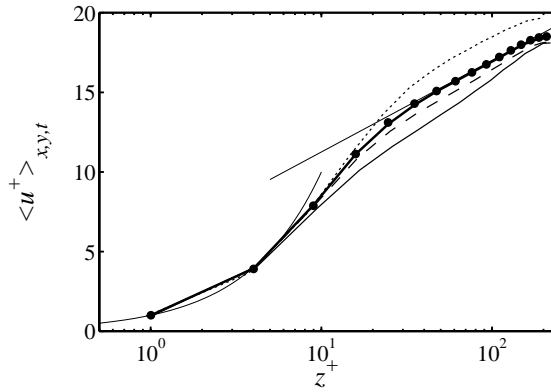
Figure 4.18: Averaged velocity profile $\langle \overline{u} \rangle^+$ scaled in wall units in the fully turbulent regime ($Re_b = 3333$). Line caption see table 4.3.
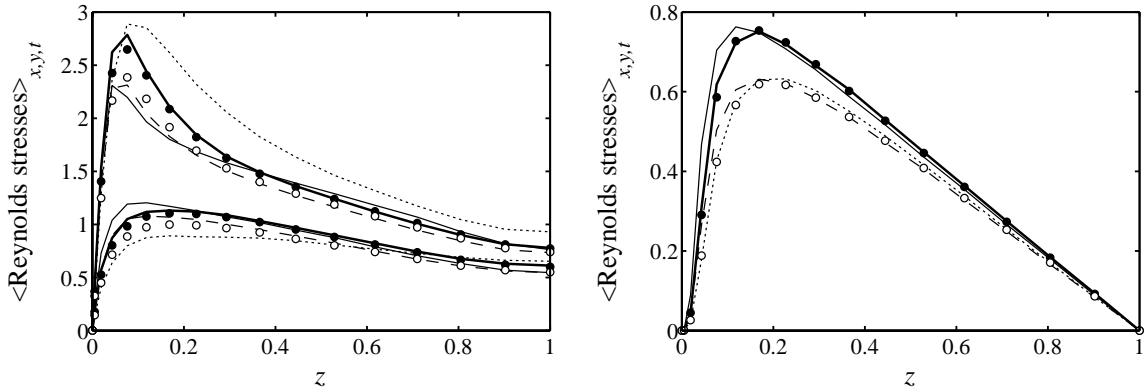
Figure 4.19: Averaged velocity fluctuations in the fully turbulent case ($Re_b = 3333$). Line caption see table 4.3. Left: $\langle \overline{u}_1' \overline{u}_1' \rangle^{1/2}/u_\tau$ and $\langle \overline{u}_2' \overline{u}_2' \rangle^{1/2}/u_\tau$. Right: $\langle \overline{u}_1' \overline{u}_3' \rangle/u_\tau^2$.

tion in Stolz *et al.* (2001*a*) at $Re_b = 2800$).

One-dimensional energy spectra are displayed in figure 4.20. The one-dimensional Fourier spectra in the streamwise direction averaged in time and the spanwise direction are defined as

$$E_1(k_1, x_3) = \langle \hat{\overline{u}}_1(k_1, x_2, x_3, t) \hat{\overline{u}}_1(k_1, x_2, x_3, t)^* \rangle_{x_2,t} \ , \qquad (4.10)$$

with a star denoting the complex conjugate. Alternatively, these spectra can be integrated in the wall-normal direction yielding

$$E_1^{\text{int}}(k_1) = \int_{-1}^{1} \langle \hat{\overline{u}}_1(k_1, x_2, x_3, t) \hat{\overline{u}}_1(k_1, x_2, x_3, t)^* \rangle_{x_2,t} \mathrm{d}x_3 \ . \qquad (4.11)$$
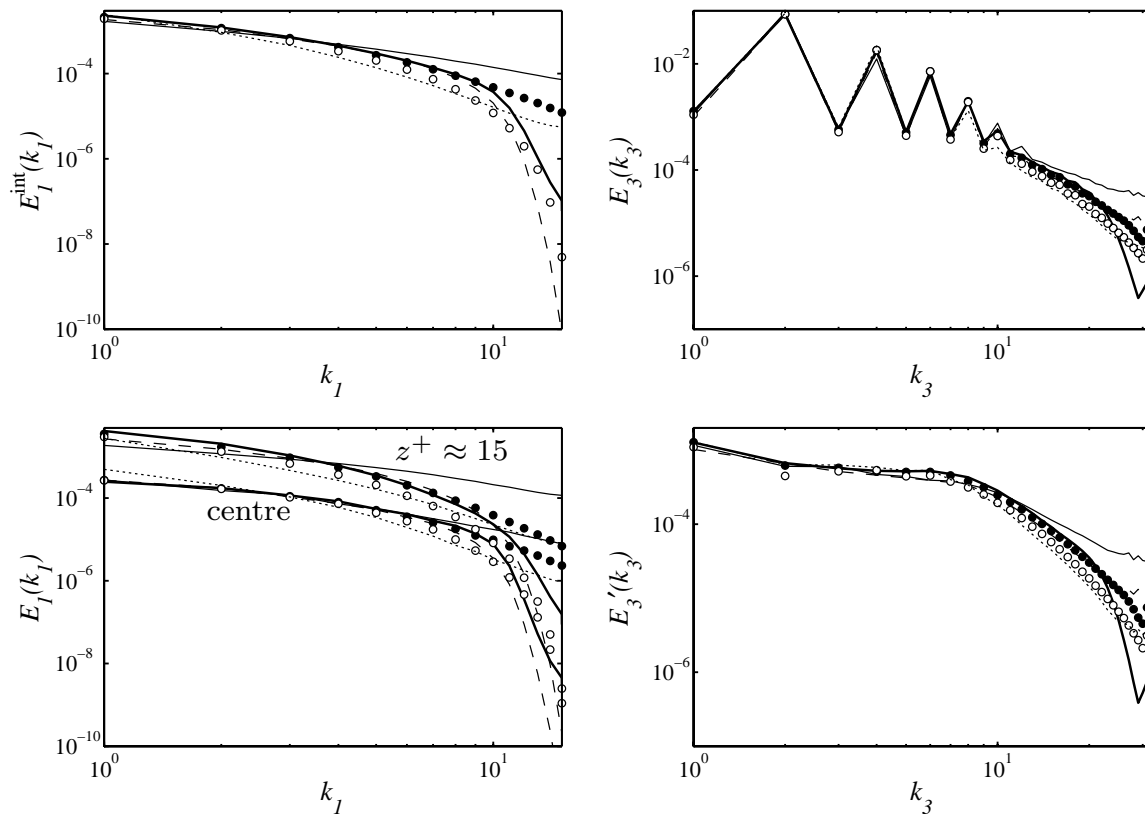
Figure 4.20: Spectra in the fully turbulent case ($Re_b = 3333$). Line caption see table 4.3. Left: *Integrated streamwise Fourier spectra $E_1^{\mathrm{int}}(k_1)$ (top) and $E_1(k_1, x_3)$ at two wall-normal positions (bottom).* Right: *Wall-normal Chebyshev spectra $E_3(k_3)$ (top) and $E_3'(k_3)$ (bottom). Definition of the spectra see equations (4.10)-(4.13).*

The spectrum of the Chebyshev expansion is defined as

$$E_3(k_3) = \langle |\hat{\bar{u}}_1(x_1, x_2, k_3, t)|^2 \rangle_{x_1, x_2, t} \, . \tag{4.12}$$

Its zigzag appearance at lower k_3 is caused by the wall-normal symmetry of the mean-flow profile which is represented by the even Chebyshev modes. Removing the mean flow, a Chebyshev spectrum of the fluctuations can be defined as

$$E_3'(k_3) = \langle |\hat{\bar{u}}_1 - \langle \hat{\bar{u}}_1 \rangle_{x_1, x_2, t}|^2 \rangle_{x_1, x_2, t} \, . \tag{4.13}$$

It is visible in figure 4.20 that the no-model LES clearly overpredicts all spectra. On the other hand, the ADM-RT model closely follows the interpolated DNS for low wavenumbers, and is strongly damped for smaller scales ($k_1 > 11$, $k_3 > 25$). This is caused by the relaxation

Table 4.4: Temporally and spatially averaged skin friction Reynolds number Re_τ obtained for the different simulations of fully developed turbulent channel flow at various resolutions. The DNS value is $Re_\tau = 208.2$, see table 4.1.

Re_τ	$32^2 \times 33$	$32^2 \times 49$	$48^2 \times 49$	$64^2 \times 65$
ADM-2D	214.0	210.4	211.5	209.6
ADM-3D	n/a	198.4	196.6	204.2
ADM-RT	208.9	210.7	210.0	207.8
DS-3D	195.1	192.4	194.0	198.8
no-model LES	220.0	219.9	212.2	209.7

acting as a secondary filter operation by the filter $I - H_N$ as explained in section 2.2.3. ADM-2D is also strongly damped in the wall-parallel directions whereas in the wall-normal direction no decline is observed, since no explicit filtering in this direction is used. The data obtained by the dynamic Smagorinsky model is slighly too dissipative for all spectra shown, *i.e.* the spectrum is lower than the reference DNS data.

Results of ADM-RT for turbulent channel flow at a higher Reynolds number $Re_\tau \approx 590$ are presented in section 4.7.3 below together with a comparison to high-pass filtered eddy-viscosity models.

4.4.5 Convergence study

In order to assess the dependence of the LES results on grid refinement, calculations at different resolution have been performed for the SGS models previously discussed. In table 4.4, results for Re_τ in the turbulent phase at $Re_b = 3333$ are given. Figure 4.21 depicts the results for ADM-2D, ADM-3D and ADM-RT, whereas in figure 4.22 the respective data for the dynamic Smagorinsky model and the no-model LES are shown. All the models show convergence towards the unfiltered reference DNS in both the turbulent Reynolds stresses and the temporal evolution of Re_τ.

ADM-2D is clearly converging towards the DNS results. As mentioned earlier, the flow undergoes transition somewhat too early, because during the initial phases of transition ($t < 150$, see also figure 4.13) the model contributions are negligible due to the two-dimensional filtering and the disturbance nature at this stage. Simulations using ADM-3D are only possible with a resolution equal or above $32^2 \times 49$ grid points
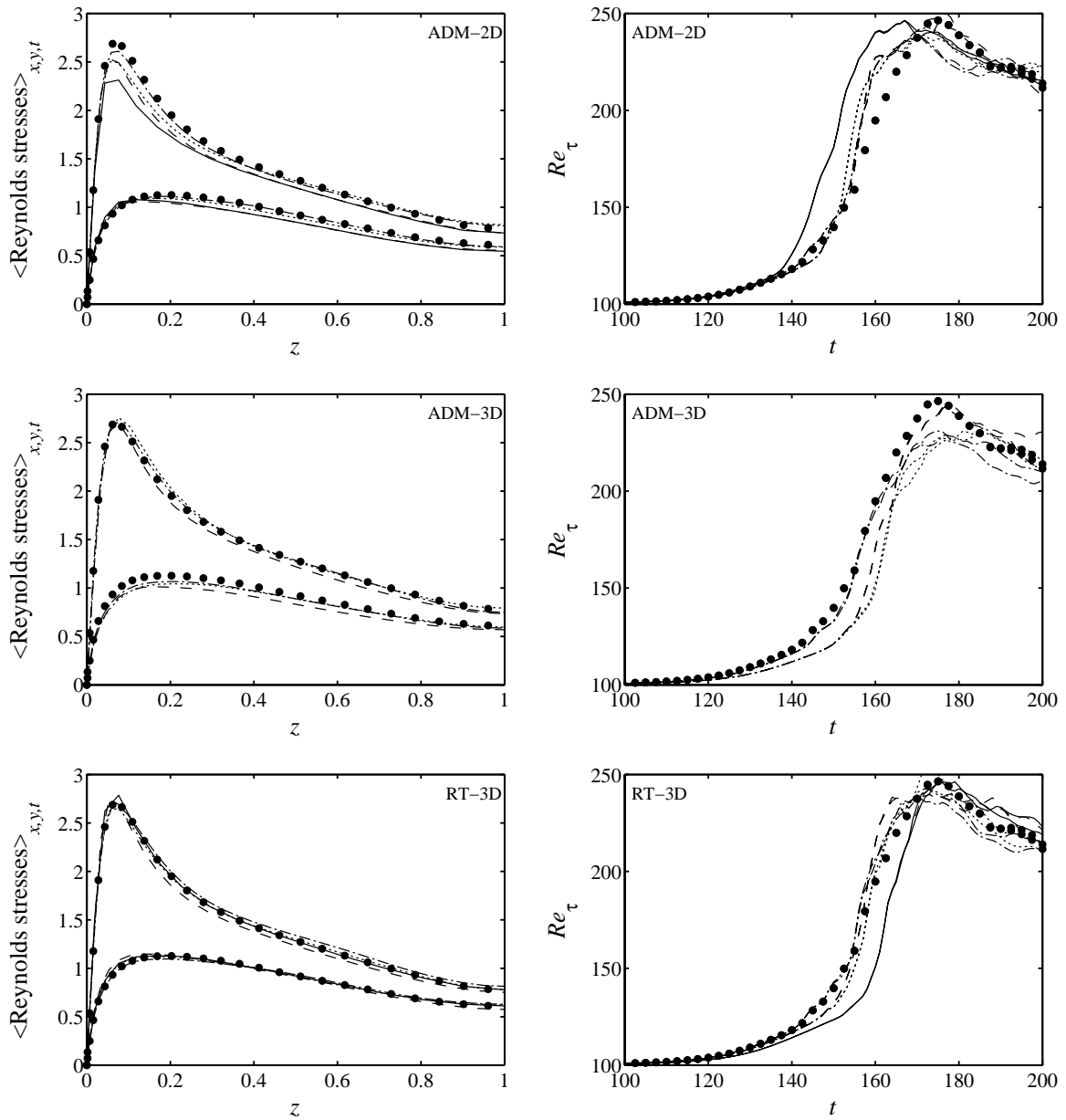
Figure 4.21: Convergence study showing the Reynolds stresses $\langle \overline{u}_1' \overline{u}_1' \rangle^{1/2} / u_\tau$ and $\langle \overline{u}_2' \overline{u}_2' \rangle^{1/2} / u_\tau$, and Re_τ during transition, see also continuation in figure 4.22. Top: ADM-2D. Middle: ADM-3D. Bottom: ADM-RT. —— $32^2 \times 33$, ---- $32^2 \times 49$, ········ $48^2 \times 49$, -·-·- $64^2 \times 65$, • DNS $160^2 \times 161$ (unfiltered, every third data point shown).

due to the oscillations created by the deconvolution at lower resolution (see figure 4.12). The value of Re_τ and its peak at $t \approx 175$ are slightly underpredicted.

Considering ADM-RT, in the fully turbulent regime all simulations,
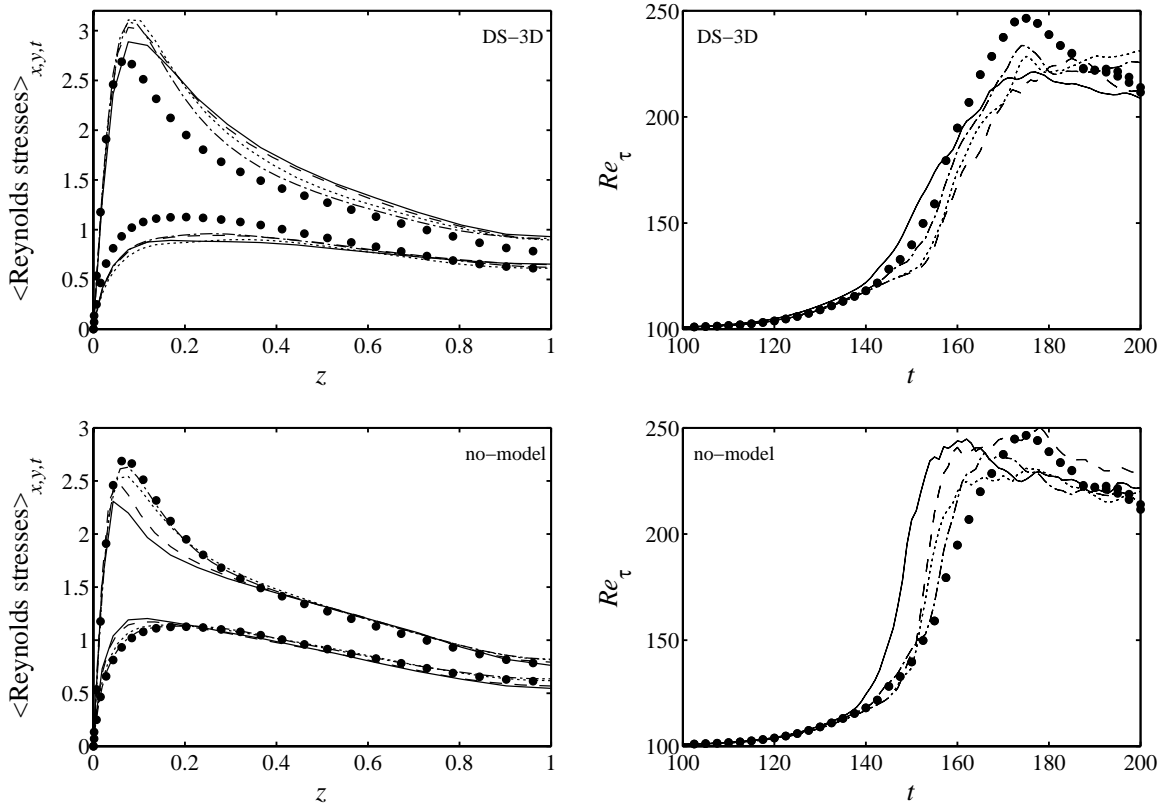
Figure 4.22: Convergence study showing the Reynolds stresses $\langle \overline{u}'_1 \overline{u}'_1 \rangle^{1/2}/u_\tau$ *and* $\langle \overline{u}'_2 \overline{u}'_2 \rangle^{1/2}/u_\tau$, *and* Re_τ *during transition, continued from figure 4.21.* Top: *Dynamic Smagorinsky model DS-3D.* Bottom: *DNS (no-model LES).* ——— $32^2 \times 33$, ‒ ‒ ‒ ‒ $32^2 \times 49$, ······· $48^2 \times 49$, —·— $64^2 \times 65$, • *DNS* $160^2 \times 161$ *(unfiltered, every third data point shown).*

starting already with $32^2 \times 33$ grid points, collapse on the reference data. With a resolution of $32^2 \times 49$ grid points and higher, also the transition time is predicted accurately, whereas a slight delay is visible in the data of the coarsest resolution. As already mentioned in section 4.1.1, a resolution of 33 points in the wall-normal direction is a lower limit for accurate LES at the present parameters. It is important to note that the evolution of Re_τ shown in figure 4.21 for ADM-RT on the $32^2 \times 49$ grid is quite similar to that of ADM-3D with $48^2 \times 49$ grid points: As mentioned earlier, the deconvolution reduces the range of resolved wavenumbers.

4.5 Detailed analysis of relaxation-term models (ADM-RT)

The results of the previous section 4.4 have shown that for ADM with deconvolution applied for the computation of the nonlinear terms a certain minimum resolution in the wall-normal direction has to be maintained. It was shown further that an ADM-type SGS model without deconvolution yielded very appealing results for incompressible channel flow using spectral numerics at even lower resolution. In this section we will extend the analysis of these relaxation-term models (ADM-RT, see equation (2.51) in section 2.2.3 and Schlatter *et al.* (2004*d*)). The influence of the determination procedure of the relaxation parameter χ is examined (see equations (2.43)-(2.48)) and, additionally, the necessity of a dealiasing procedure using the 3/2-rule (see Canuto *et al.* (1988)) for the computation of the nonlinear terms is discussed.

Two different incompressible flow situations are considered, see tables 4.1 and 4.2 in section 4.1: Subcritical temporal K-type transition with the Reynolds number based on bulk velocity and channel half-width $Re_b = 3333$ ($Re_\tau \approx 210$ in fully developed turbulence) and fully turbulent channel flow with $Re_\tau \approx 180$ ($Re_b = 2800$, Kim *et al.* (1987); Moser *et al.* (1999)). For the LES a deliberately chosen coarse resolution of $32^2 \times 33$ points is used (see previous section 4.4 for a discussion). The same LES resolution was also used for the turbulent case with $Re_b = 2800$. At this resolution, a computation without any model is significantly underresolved (except for the laminar case) in all three spatial directions, see the comments in section 4.2.

Figure 4.23 shows different calculations of turbulent channel flow, both with aliasing errors and with full dealiasing. It can be seen that for the simulations involving a relaxation term of the form (2.50), the lack of dealiasing does not produce inferior results. On the other hand, the calculations using the dynamic Smagorinsky model (three-dimensional second-order test filter with $\omega_c = \pi/2$, equation (2.19)) and the no-model calculations are much worse without the dealiasing procedure. It should be noted that the computational effort without dealiasing is reduced by at least a factor of two for the present spectral code. Moreover, proper dealiasing can usually be performed with spectral numerics only (Chow & Moin, 2003). However, as shown here, the effects of aliasing errors can be reduced significantly in an LES using a relaxation term. An interesting observation is that with the dynamic estimation χ_{dyn},
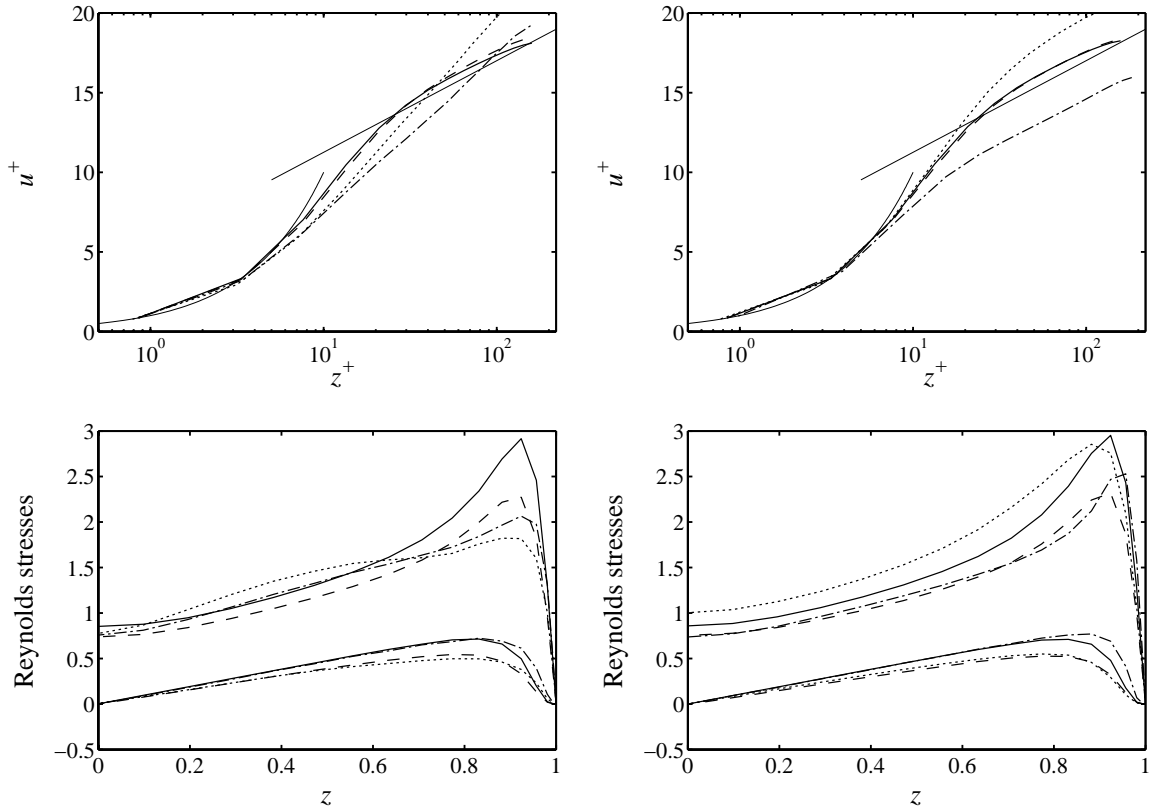
Figure 4.23: Turbulent statistics for $Re_b = 2800$. Left column: *Calculations without dealiasing.* Right column: *Calculations using 3/2-rule for dealiasing.* Top row: *Mean velocity profile in wall units.* Bottom row: *Reynolds stresses $\langle \overline{u}'_1 \overline{u}'_1 \rangle^{1/2}/u_\tau$ and $\langle \overline{u}'_1 \overline{u}'_3 \rangle/u_\tau^2$:* ——— $\chi = \chi_{\mathrm{dyn}}$, $----$ *ADM-3D (with deconvolution),* $-\cdot-$ *no-model LES $32^2 \times 33$,* $\cdots\cdots$ *dynamic Smagorinsky model.*

equation (2.43), is automatically increased if no dealiasing is employed. This is mainly due to increased energy in the tail of the energy spectra causing the dynamic procedure to increase the model coefficient.

Furthermore, the different variants of determining the relaxation parameter χ as detailed in section 2.2.3 (see also appendix B) have been investigated for transitional and fully turbulent channel flow with $Re_b = 3333$. The dynamic determination of χ based on the description in Stolz *et al.* (2001*a,b*) has been examined, equation (2.43). Additionally, substantially simplified definitions are also included, in particular a constant χ, equation (2.45), χ based on the velocity gradient tensor, (2.46), on the high-pass filtered velocity gradient tensor, (2.47), and computed from the second-order velocity structure function, (2.48). For the present results, $C_1 = 10$, $C_2 = 1$, $C_3 = 10$ have been chosen as model
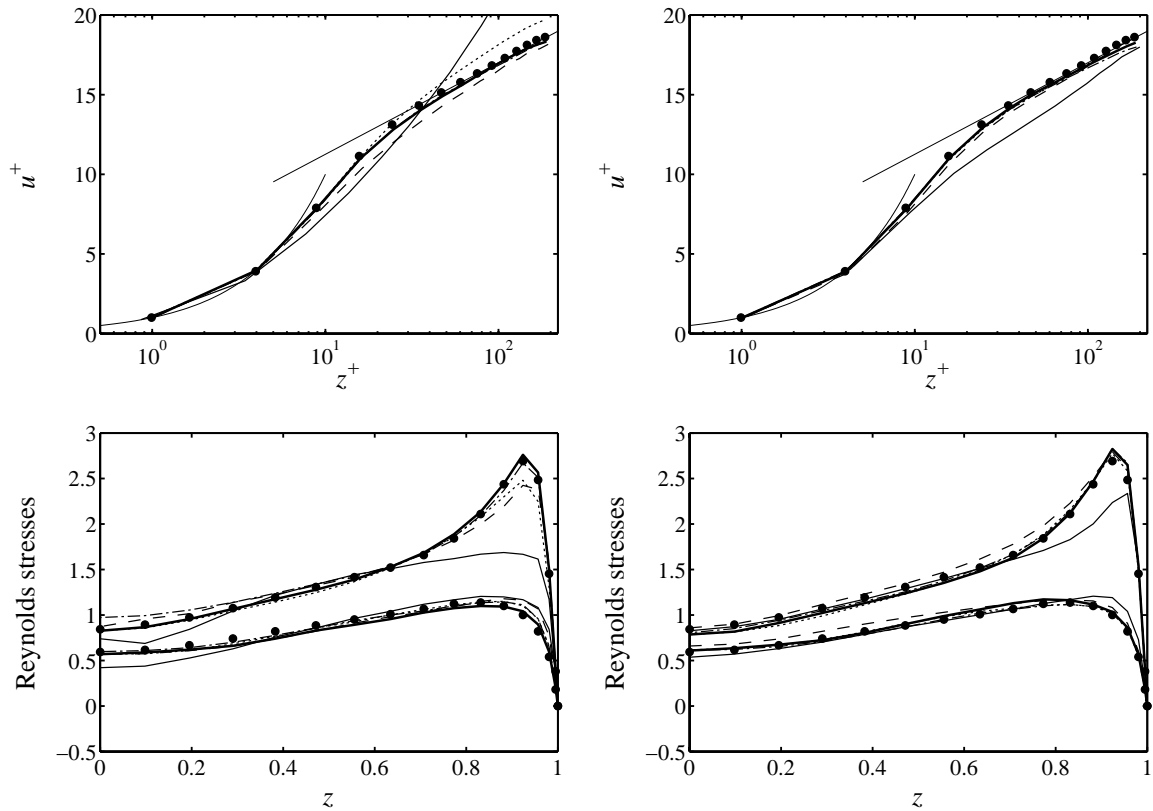
Figure 4.24: Turbulent statistics for $Re_b = 3333$ for ADM-RT using different definitions of the relaxation parameter χ. Left column: *Calculations without dealiasing.* Right column: *Calculations using 3/2-rule for dealiasing.* Top row: *Mean velocity profile in wall units.* Bottom row: *Reynolds stresses* $\langle \overline{u}_1' \overline{u}_1' \rangle^{1/2}/u_\tau$ *and* $\langle \overline{u}_2' \overline{u}_2' \rangle^{1/2}/u_\tau$: ——— $\chi = \chi_{\text{dyn}}$, —·—$\chi = C_1 = \text{const.}$, - - - -$\chi = C_2 \|\nabla \overline{u}\|$, ········ $\chi = C_3 \|\nabla H * \overline{u}\|$, ——— *no-model LES* $32^2 \times 33$, • *grid-filtered DNS* $160^2 \times 161$

coefficients. A statistical evaluation of the dynamic determination of χ is given in figure 4.17 in the previous section.

In figure 4.24, statistical quantities of the fully turbulent simulations with and without dealiasing are depicted. It is evident that the no-model LES (coarse-grid DNS) deviates significantly from the fine-grid DNS. However, all LES results agree better with the fully resolved DNS data. The simulations without dealiasing depicted on the left confirm the above-mentioned findings and show that it is possible to reduce the effects of aliasing errors significantly even when using a constant χ.

It is interesting to note that the results of the three LES are similar, although different definitions of the model coefficient χ were used. It can
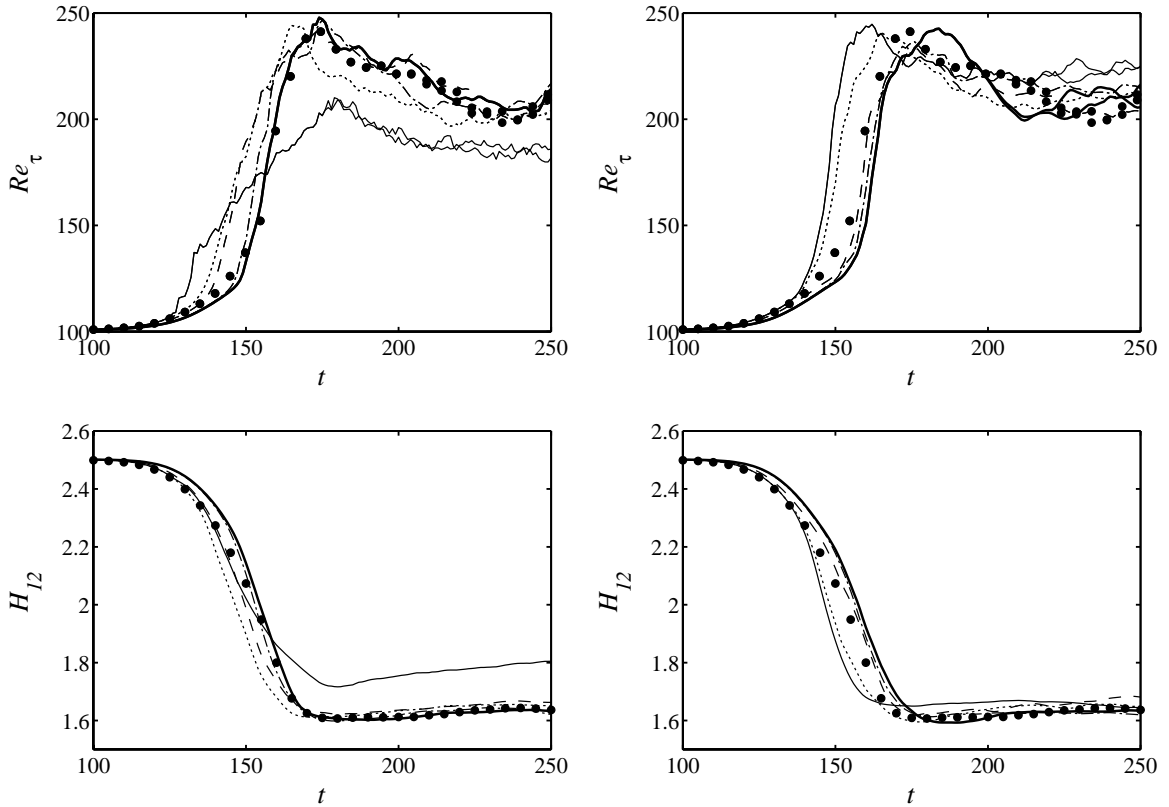
Figure 4.25: Time evolution of the shape factor H_{12} and the Reynolds number Re_τ based on the skin friction for simulations of K-type transition. Left column: *Calculations without dealiasing.* Right column: *Calculations using 3/2-rule for dealiasing. Line captions see figure 4.24. Multiple values indicate lower/upper channel wall.*

therefore be concluded that for fully turbulent channel flow the specific form of χ is less important as long as an appropriate amount of energy is dissipated and, additionally, effects of aliasing errors are reduced.

The evolution of the shape factor H_{12} and Re_τ during the transitional phase is shown in figure 4.25. The underresolved DNS (no-model LES) shows premature transition compared to the fully resolved DNS for the dealiased simulation whereas it completely fails in the presence of aliasing errors ($H_{12} \approx 1.8$ after transition). Generally, the effects of aliasing errors lead to slightly earlier transition for the LES. Nevertheless, all LES with the relaxation term as model produce acceptable results for transition, *i.e.* showing correct onset of transition and the well-known overshoot of Re_τ of approximately 15%.

In figure 4.26 the evolution of the Fourier components
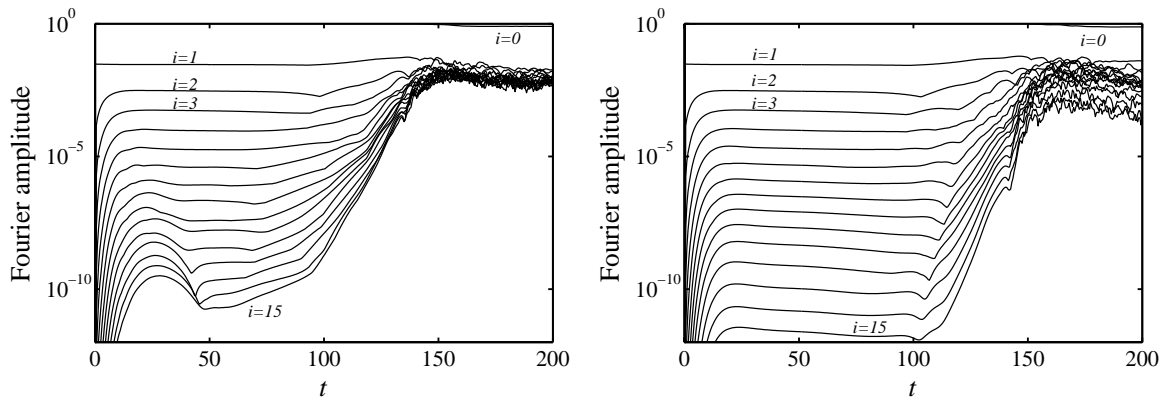
Figure 4.26: Evolution of the wall-normal maximum of the 2D Fourier amplitudes $\max_{x_3} |\hat{\bar{u}}_1(k_i, 0, x_3, t)|$ *corresponding to two-dimensional waves during the transitional phase (Re$_b$ = 3333). Left: No-model LES $32^2 \times 33$ (with dealiasing). Right: ADM-RT $32^2 \times 33$, $\chi = C_1 =$ const. (with dealiasing). Compare also to figure 4.16 depicting the spectrum of the fully resolved DNS.*

$\max_{x_3} |\hat{\bar{u}}_1(k_i, 0, x_3, t)|$ is displayed (compare to figure 4.16). These modes correspond to the 2D saturated Tollmien-Schlichting wave. Shown in the figure are results for the no-model LES and the ADM-RT model with constant χ, both obtained with dealiasing of the nonlinear terms. The no-model LES shows a distinct kink in the higher Fourier modes ($i > 10$) at $t \approx 30$. This feature is clearly an artefact of the insufficient resolution especially in the wall-normal direction, since the kink is not present in the fully resolved calculation, see figure 4.16, and in simulations using 49 points in the wall-normal direction (not shown). For the LES using ADM-RT with constant relaxation parameter χ on $32^2 \times 33$ grid points the kink is also not present, the two-dimensional Fourier modes slowly decay as in the fully resolved DNS (figure 4.16). The modes with an amplitude level above 10^{-6} for the ADM-RT model are approximately on the respective DNS level. The higher LES modes are on a lower level due to SGS dissipation introduced by the relaxation term (secondary filtering). In particular, the spectra obtained using a constant $\chi = 10$ are clearly less noisy than those obtained using the ADM-RT model with dynamic χ_{dyn}, see figure 4.16.

In general, the inclusion of high-pass filtering in the model coefficient, *e.g.* χ, seems to lead to more accurate results. This is also true for transitional flows, see Stolz *et al.* (2004). On the other hand, assuming constant $\chi = C_1$ gives very appealing results, only slightly less accurate than the dynamic determination $\chi = \chi_{\mathrm{dyn}}$. Similar observations can

also be made for the HPF eddy-viscosity models (section 2.2.2) for which results are shown in section 4.7.

4.6 Visualisation of transitional structures

Transitional flows are dominated by the growth of disturbances and the subsequent formation and evolution of typical vortical structures which in turn break down into turbulent flow. In this section, visualisations of those transitional structures are presented for the case of forced fundamental K-type transition in channel flow with the initial conditions given in section 4.1 ($Re_b = 3333$).

Results of LES using the dynamic Smagorinsky (DS) model (section 2.2.1) the ADM-RT model (equation (2.51) in section 2.2.3) together with a no-model LES (coarse-grid DNS) are presented. Note that for the dynamic Smagorinsky model a three-dimensional graded filter of second order ($\omega_c = \pi/2$, equation (2.19)) has been used as test filter (see section 4.3). The SGS stresses for the ADM-RT model are given by (see equation (2.50) in section 2.2.3),

$$\frac{\partial \tau_{ij}}{\partial x_j} = \chi H_5 * \overline{u}_i \ ,$$

i.e. a relaxation regularisation (relaxation term, RT) has been added to the momentum equations. H_5 denotes the three-dimensional high-pass filter defined by equation (2.12) in section 2.1.1 and χ is the model coefficient, set constant in the present section, motivated by the findings of the previous section 4.5. A value $\chi = 10$ has been chosen, compare to figure 4.17. The model contribution of the ADM-RT model are thus confined to the smallest scales.

Three-dimensional visualisations of the breakdown process for the different models are depicted in figure 4.27 for the times $t_{\mathrm{DNS}} = 136$, $t_{\mathrm{DNS}} = 140$ and $t_{\mathrm{DNS}} = 154.5$ using the negative-λ_2 vortex-identification criterion by Jeong & Hussain (1995). To allow a direct comparison of the LES and the DNS, the selected times for the LES were slightly shifted such that the stage of transition development is matched at $t_{\mathrm{DNS}} \approx 128$. Note that the DNS results have been coarsened to the LES grid prior to plotting in order to allow for a more meaningful comparison.

The results for the ADM-RT model show a similar behaviour as the DNS: Hairpin vortices ($t_{\mathrm{DNS}} = 136$) and the related roll-up ($t_{\mathrm{DNS}} = 140$) of the shear layer are clearly visible and their position, convection speed

DNS (interpolated onto LES grid)

No-model LES

Dynamic Smagorinsky model

ADM-RT model
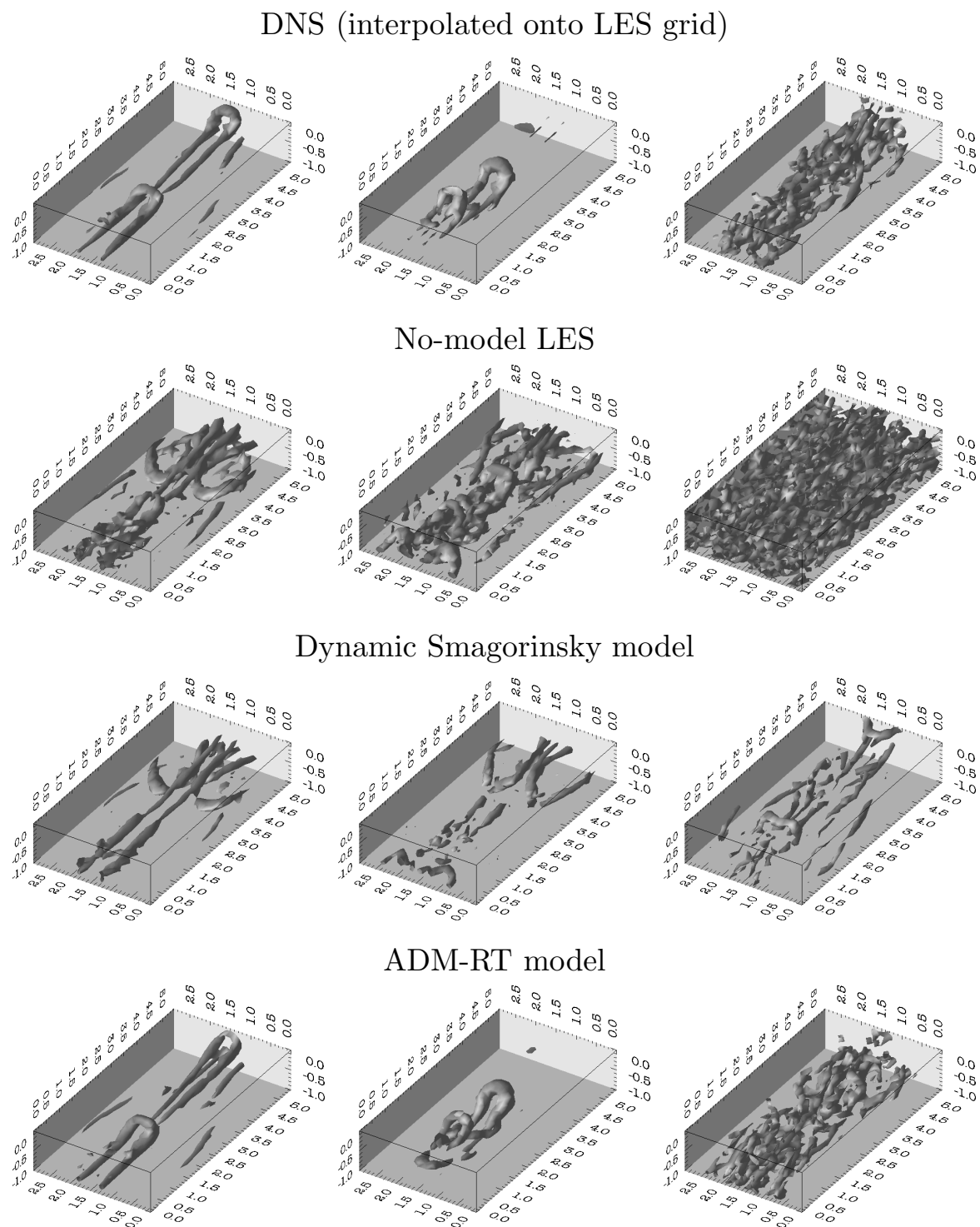
Figure 4.27: Three-dimensional visualisation of the transitional structures for the different simulations by isocontours of the negative-λ_2 criterion (same isolevel for respective times). From left *to* right*: $t_{\mathrm{DNS}} = 136$, $t_{\mathrm{DNS}} = 140$, $t_{\mathrm{DNS}} = 154.5$.*

DNS (interpolated onto LES grid)

No-model LES

Dynamic Smagorinsky model

ADM-RT model
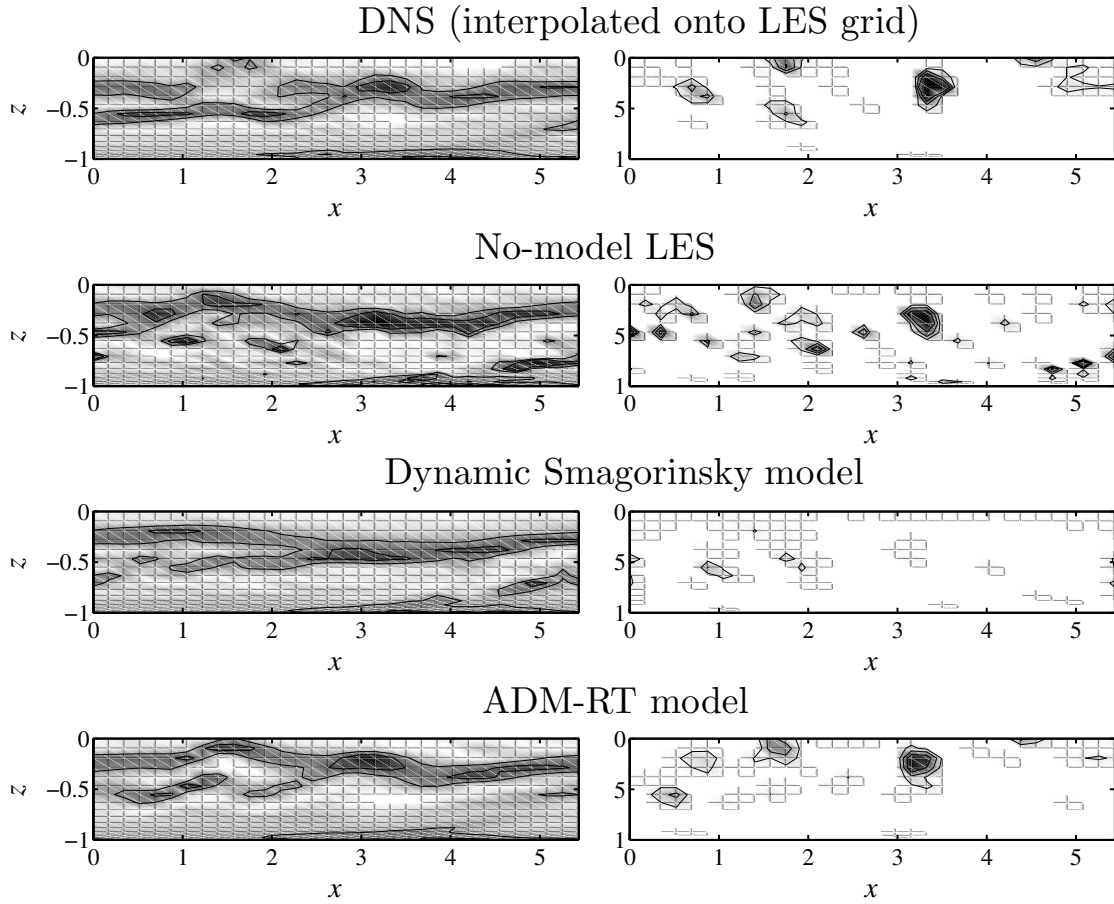
Figure 4.28: Contour plots in the peak plane ($y = L_y/2$) for the different simulations at $t_{\mathrm{DNS}} = 140$ (three-spike stage). Left column: Shear $\partial \overline{u}/\partial z$. Right column: Vortices identified by the negative-λ_2 criterion.

and growth rate are similar to the DNS. Moreover, the initial stages of the turbulent breakdown are confined to a region close to the peak plane ($t_{\mathrm{DNS}} = 154.5$). The no-model LES shows fragments of hairpin vortices, but these are disguised by a high level of ambient high-frequency oscillations (noise) which is attributed to missing SGS dissipation. Unlike the DNS data, at the latest time shown ($t_{\mathrm{DNS}} = 154.5$) already the whole span of the channel is turbulent. The simulation using the dynamic Smagorinsky model does not show a proper roll-up of the shear layer. Vortices are generated, but these are not so pronounced, closer to the wall, and spread further away from the peak plane. Moreover, no hairpin vortex can be detected.

In figure 4.28, the wall-normal shear $\partial \overline{u}/\partial z$ and λ_2 are shown in the peak plane ($y = L_y/2$) at the early three-spike stage ($t_{\mathrm{DNS}} = 140$). Similar visualisations have alread been presented by Sandham & Kleiser
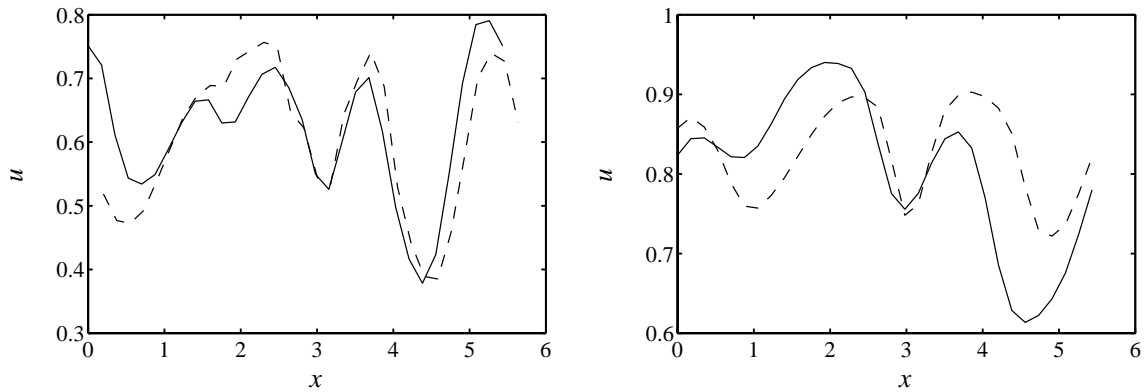
Figure 4.29: Streamwise velocity $\overline{u}$ for the three spike stage at $z = -0.3$. ----DNS, ——— ADM-RT. Left: $t_{\text{DNS}} = 143$, peak plane $(y = L_y/2)$. Right: $t_{\text{DNS}} = 154.5$, valley plane $(y = 0)$.

(1992). The "kinks" in the shear layer $(x \approx 1.5)$ coincide with the hairpin vortices, clearly detectable by the λ_2 criterion (figure 4.28, right column). Again, the results obtained with the ADM-RT model compare favourably to the DNS data. The no-model LES also shows the roll-up of the shear layer in an overall more noisy environment. The DS model, however, does not predict the physically correct transitional flow structure.

A quantitative comparison of the streamwise velocity component during the three-spike stage at both the peak and the valley position is given in figure 4.29 for the DNS and the ADM-RT model only since these stages could not be identified properly in either the DS or the no-model simulation. It is evident that the three-spike stage is captured quite accurately by the ADM-RT model. Note that at $t_{\text{DNS}} = 154.5$ transition at the peak position is already well advanced (see also figure 4.27), but the ADM-RT model is still able to accurately predict the roll-up at the valley position.

4.7   High-pass filtered eddy-viscosity models

In this section, the high-pass filtered (HPF) eddy-viscosity models as introduced in section 2.2.2 are employed for the simulation of turbulent channel flow at moderate Reynolds numbers (see also Schlatter *et al.* (2005c)). Results using the HPF models applied to transitional and turbulent channel flow at lower Reynolds numbers are presented in Stolz

et al. (2004) and Stolz *et al.* (2005), while homogeneous isotropic turbulence is considered in chapter 6 of this thesis.

4.7.1   Parameter settings

The Reynolds number based on the bulk velocity is set to $Re_b = 10935$ resulting in $Re_\tau \approx 590$ (see table 4.1). The corresponding DNS was performed on $384^2 \times 257$ grid points using the same parameters as in Moser *et al.* (1999). The LES results reported here were obtained with a resolution of $N_1 \times N_2 \times N_3 = 64^2 \times 65$ grid points. For all cases, the physical dimensions of the simulation box are $2\pi \times \pi \times 2$ resulting in a resolution in wall units of

$$\Delta x^+ \times \Delta y^+ \times \Delta z^+\big|_{\text{wall}}/\Delta z^+\big|_{\text{centre}} = 9.65 \times 4.83 \times 0.0444/7.24$$

for the DNS and approximately

$$\Delta x^+ \times \Delta y^+ \times \Delta z^+\big|_{\text{wall}}/\Delta z^+\big|_{\text{centre}} = 58 \times 29 \times 0.7/29$$

for an LES. All simulations were continued until $t \approx 1000$ when fully converged statistics were reached.

Simulations for the high-pass filtered eddy-viscosity models with different cutoff wavenumbers $w_c \in \{0, \pi/3, \pi/2, 2\pi/3, 3\pi/4\}$ are compared to calculations using the filtered structure-function model at the same cutoff wavenumbers. Note that the filter is applied in three dimensions as defined in section 2.1.1.

Reference calculations have been performed using the Smagorinsky model with $C_S = 0.05$ and without wall-damping, the dynamic Smagorinsky model (DS), and a simulation on the LES grid without model (no-model LES). Furthermore, the data of the high-resolution DNS was interpolated onto the LES grid. This reduction included a spectral truncation of the wall-parallel Fourier components and an interpolation in physical space for the wall-normal direction. The physical-space interpolation was used in order to leave the mean velocity profile and all boundary values unchanged between the high-resolution data and the truncated data. The same interpolation algorithm has been used in the analysis of the DNS data presented in section 4.2.

For the dynamic Smagorinsky model (Germano *et al.*, 1991) the formulation of Lilly (1992) was used, see section B.4. As test filter a three-dimensional second-order filter defined in equation (2.19) with $\omega_c = \pi/2$

was used. The averaging needed for the computation of the dynamic co-efficient was performed in wall-parallel planes and negative values of C_S were clipped, see equation (B.47). For the FSF model and the HPF-SF model, the structure function F_2 was evaluated in three dimensions (*i.e.* using the six-point formulation), see section B.1. The high-pass filter H_0 defined in equation (2.16) was used for the argument of F_2 and for the evaluation of the strain rate S_{ij}.

The filter G, given by equation (2.10) in section 2.1.1, is not defined for a cutoff frequency $\omega_c = 0$. High-pass filtering with $\omega_c = 0$ is thus defined as subtracting the mean flow $\langle \overline{u}_i \rangle_{x,y}(z,t)$, *i.e.*

$$H * \overline{u}_i = \overline{u}_i - \langle \overline{u}_i \rangle_{x,y}(z,t) \ . \tag{4.14}$$

This definition is identical to the one used by Schumann (1975) for his channel flow simulations. In the following, we include results for $\omega_c = 0$ because this modification to the classical eddy-viscosity models is strikingly simple, but turns out to have a significant positive effect on the quality of the results.

4.7.2   Turbulence statistics

The parameters and scalar results of the simulations are presented in tables 4.5-4.8. The quantities A and B in these tables are defined as

$$A \ = \ \int \langle \varepsilon_{\text{SGS}} \rangle \mathrm{d}z / \int \langle \varepsilon_{\text{visc}} \rangle \mathrm{d}z \ , \tag{4.15}$$

$$B \ = \ \int \varepsilon_{\text{SGS,fluct}} \mathrm{d}z / \int \langle \varepsilon_{\text{SGS}} \rangle \mathrm{d}z \ , \tag{4.16}$$

which will be further discussed in section 4.7.4. For the HPF eddy-viscosity models using the formulae for the model coefficient C given in section 2.2.2, the averaged Re_τ varies by approximately 2% around the DNS value, $Re_\tau = 587$. The no-model LES, as anticipated for spectral numerics, features too little viscous dissipation to compensate for the low resolution leading to an overprediction of the skin friction, $Re_\tau \approx 630$. On the other hand, the dynamic Smagorinsky model is too dissipative leading to an underprediction of the skin friction, $Re_\tau \approx 550$. Similar results have also been obtained for lower Reynolds number (see Stolz *et al.* (2004) and previous sections).

The mean velocity profile $\langle \overline{u} \rangle^+$ and the different Reynolds stresses are shown in figure 4.30 for the HPF Smagorinsky model, in figure 4.31

Table 4.5: *Parameters and results for the channel-flow simulations performed using the HPF Smagorinsky model. A and B are defined in equations (4.15) and (4.16).*

ω_c	C_S^{HPF}	Re_τ	$\int\langle\varepsilon_{\mathrm{visc}}\rangle\mathrm{d}z$	A	B
0	0.0333	598	$-5.70\cdot10^{-2}$	0.097	0.941
$\pi/3$	0.05	587	$-5.47\cdot10^{-2}$	0.146	0.918
$\pi/2$	0.0667	580	$-5.73\cdot10^{-2}$	0.146	0.956
$2\pi/3$	0.1	574	$-5.78\cdot10^{-2}$	0.158	0.977
$3\pi/4$	0.133	588	$-5.74\cdot10^{-2}$	0.161	0.985

Table 4.6: *Parameters and results for the channel-flow simulations performed using the HPF-SF model. A and B are defined in equations (4.15) and (4.16).*

ω_c	C_{SF}^{HPF}	Re_τ	$\int\langle\varepsilon_{\mathrm{visc}}\rangle\mathrm{d}z$	A	B
0	0.0089	582	$-5.68\cdot10^{-2}$	0.138	0.965
$\pi/3$	0.0146	578	$-5.65\cdot10^{-2}$	0.159	0.953
$\pi/2$	0.0215	582	$-5.60\cdot10^{-2}$	0.147	0.973
$2\pi/3$	0.0405	584	$-5.58\cdot10^{-2}$	0.147	0.985
$3\pi/4$	0.0727	583	$-5.60\cdot10^{-2}$	0.151	0.990

Table 4.7: *Parameters and results for the channel-flow simulations performed using the FSF model. A and B are defined in equations (4.15) and (4.16).*

ω_c	C_{FSF}	Re_τ	$\int\langle\varepsilon_{\mathrm{visc}}\rangle\mathrm{d}z$	A	B
0	0.017	596	$-4.60\cdot10^{-2}$	0.399	0.591
$\pi/3$	0.0233	594	$-4.54\cdot10^{-2}$	0.433	0.585
$\pi/2$	0.0286	592	$-4.57\cdot10^{-2}$	0.416	0.577
$2\pi/3$	0.0371	592	$-4.60\cdot10^{-2}$	0.407	0.591
$3\pi/4$	0.0435	592	$-4.61\cdot10^{-2}$	0.398	0.560

for the HPF-SF model and in figure 4.32 for the FSF model, each using a cutoff wavenumber $\omega_c \in \{0, \frac{\pi}{3}, \frac{\pi}{2}, \frac{2\pi}{3}, \frac{3\pi}{4}\}$. A very close agreement of the data with the fully resolved DNS can be observed for the HPF models. Note also that the proposed adaptation of the model coefficient (section 2.2.2) is indeed able to virtually eliminate the influence of the cutoff wavenumber ω_c: The velocity profiles and the Reynolds stresses

Table 4.8: Parameters and results for the various reference channel flow simulations. A and B are defined in equations (4.15) and (4.16). ν_t denotes the eddy viscosity, see section 4.7.3 and equation (2.26).
† *DNS data interpolated onto LES grid ($64 \times 64 \times 65$).*
‡ *DNS with $384^2 \times 257$ grid points.*

Model	Re_τ	$\int \langle \varepsilon_{\text{visc}} \rangle \mathrm{d}z$	A	B
Smag. $C_S = 0.05$	577	$-5.61 \cdot 10^{-2}$	0.558	0.504
dyn. Smagorinsky	550	$-5.40 \cdot 10^{-2}$	0.343	0.753
HPF $\nu_t = 3 \cdot 10^{-5}$	585	$-5.80 \cdot 10^{-2}$	0.114	0.993
ADM-RT $\chi = 2$	586	$-5.41 \cdot 10^{-2}$	0.186	0.998
no-model LES	628	$-5.65 \cdot 10^{-2}$		
DNS (interp.)†	588	$-5.05 \cdot 10^{-2}$		
DNS‡	587	n/a		

Figure 4.30: HPF Smagorinsky model. Left: *Mean streamwise velocity profile $\langle \overline{u}_1 \rangle^+$ in wall units.* Right: *Reynolds stresses $\langle \overline{u}_1' \overline{u}_1' \rangle^{1/2}/u_\tau$, $\langle \overline{u}_2' \overline{u}_2' \rangle^{1/2}/u_\tau$, $\langle \overline{u}_3' \overline{u}_3' \rangle^{1/2}/u_\tau$, $\langle \overline{u}_1' \overline{u}_3' \rangle/u_\tau^2$.* ---·--- $\omega_c = 0$, - - - - $\omega_c = \pi/3$, ········ $\omega_c = \pi/2$, ——— $\omega_c = 2\pi/3$, ——— $\omega_c = 3\pi/4$, • *DNS (interpolated onto LES grid).*

nearly collapse onto each other. This is also true for the FSF model, figure 4.32, but this model seems to be too dissipative close to the wall around $z^+ \approx 15$, which is clearly visible by an underprediction of $\langle \overline{u} \rangle^+$ and in $\langle \overline{u}_1' \overline{u}_1' \rangle$ by a slight shift of the peak away from the wall.

Data for the reference calculations are shown in figures 4.33 and 4.34 allowing a comparison of the present HPF results to those of previous

Figure 4.31: HPF-SF model. Left: *Mean streamwise velocity profile* $\langle \overline{u}_1 \rangle^+$ *in wall units.* Right: *Reynolds stresses* $\langle \overline{u}_1' \overline{u}_1' \rangle^{1/2}/u_\tau$, $\langle \overline{u}_2' \overline{u}_2' \rangle^{1/2}/u_\tau$, $\langle \overline{u}_3' \overline{u}_3' \rangle^{1/2}/u_\tau$, $\langle \overline{u}_1' \overline{u}_3' \rangle/u_\tau^2$. — · — $\omega_c = 0$, — — — $\omega_c = \pi/3$, · · · · · · · $\omega_c = \pi/2$, —— $\omega_c = 2\pi/3$, ——— $\omega_c = 3\pi/4$, ● *DNS (interpolated onto LES grid).*
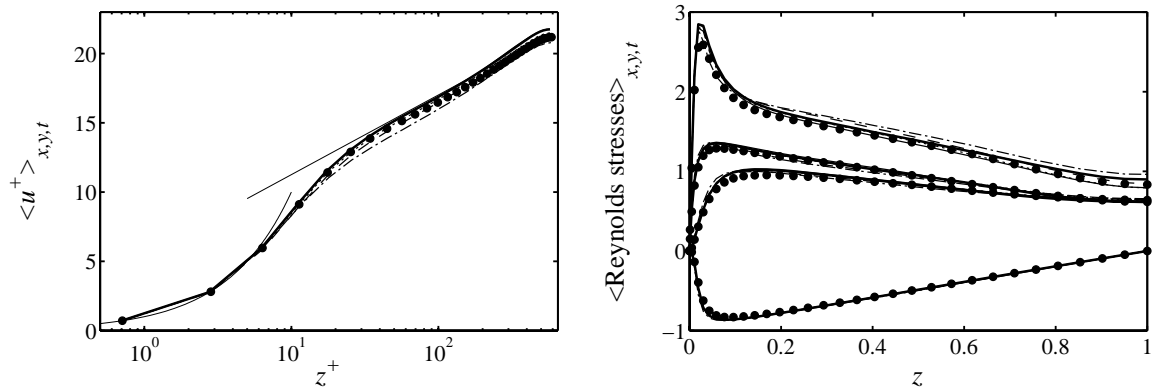

Figure 4.32: FSF model. Left: *Mean streamwise velocity profile* $\langle \overline{u}_1 \rangle^+$ *in wall units.* Right: *Reynolds stresses* $\langle \overline{u}_1' \overline{u}_1' \rangle^{1/2}/u_\tau$, $\langle \overline{u}_2' \overline{u}_2' \rangle^{1/2}/u_\tau$, $\langle \overline{u}_3' \overline{u}_3' \rangle^{1/2}/u_\tau$, $\langle \overline{u}_1' \overline{u}_3' \rangle/u_\tau^2$. — · — $\omega_c = 0$, — — — $\omega_c = \pi/3$, · · · · · · · $\omega_c = \pi/2$, —— $\omega_c = 2\pi/3$, ——— $\omega_c = 3\pi/4$, ● *DNS (interpolated onto LES grid).*

SGS models. The velocity profiles displayed in figure 4.33 show that the dynamic Smagorinsky model is too dissipative, in contrast to the no-model calculation, which clearly underpredicts the dissipation, see also table 4.8. Except for the vicinity of the wall, the classical Smagorinsky model correctly predicts the mean streamwise velocity profile but the Reynolds stresses are not approximated accurately.

It is interesting to compare the near-wall region $z^+ \approx 15$ of the velocity profile $\langle \overline{u} \rangle^+$ for the various SGS models (figure 4.34). Unlike the fixed-coefficient eddy-viscosity models, the HPF models achieve an accu-
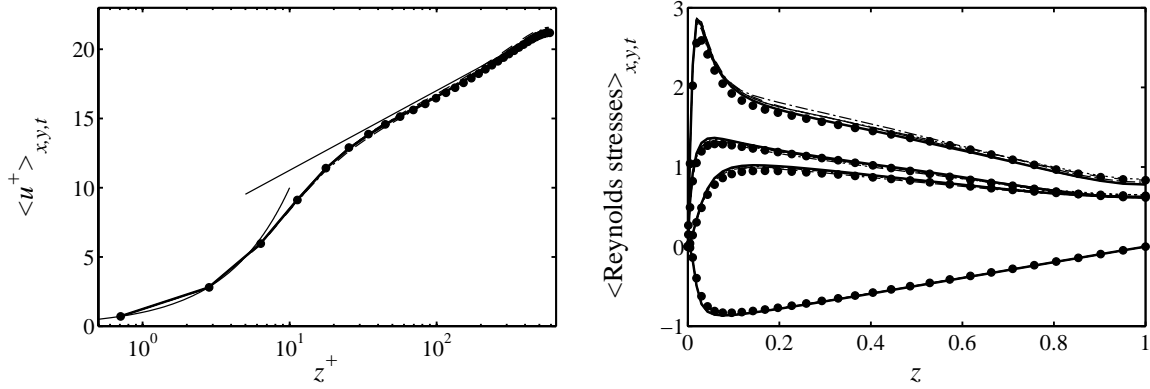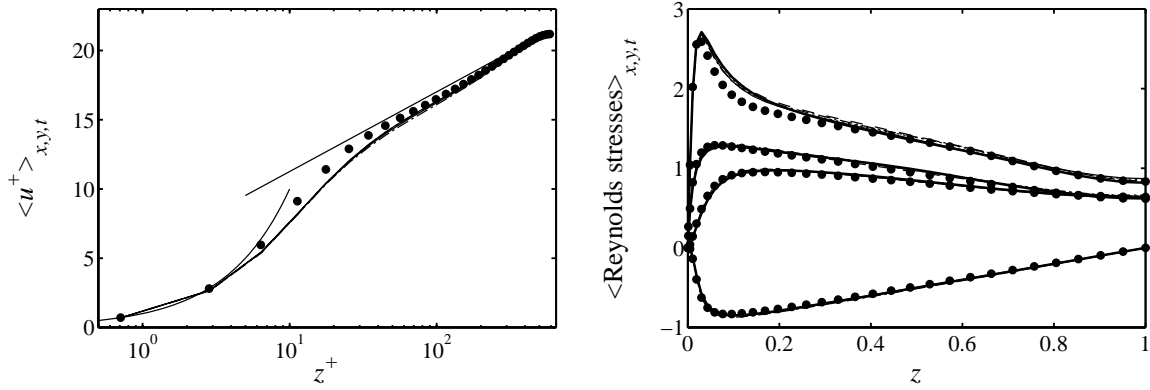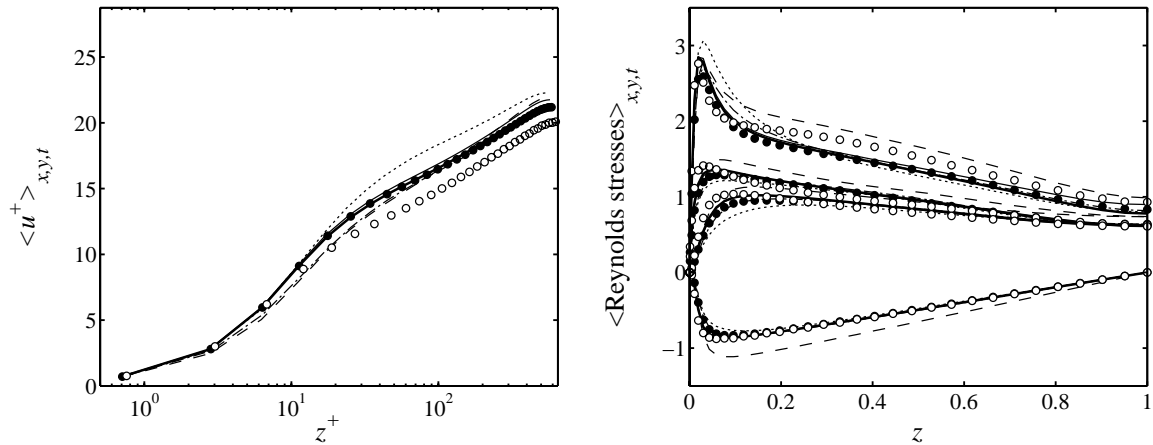
Figure 4.33: Left: *Mean streamwise velocity profile* $\langle \overline{u}_1 \rangle^+$ *in wall units.* Right: *Reynolds stresses* $\langle \overline{u}_1' \overline{u}_1' \rangle^{1/2}/u_\tau$, $\langle \overline{u}_2' \overline{u}_2' \rangle^{1/2}/u_\tau$, $\langle \overline{u}_3' \overline{u}_3' \rangle^{1/2}/u_\tau$, $\langle \overline{u}_1' \overline{u}_3' \rangle/u_\tau^2$. ——— *HPF-SF model* ($\omega_c = 2\pi/3$), ——— *HPF Smagorinsky model* ($\omega_c = 2\pi/3$), – – – *Smagorinsky model* ($C_S = 0.05$), ⋯⋯ *dynamic Smagorinsky model,* –·– *FSF model* ($\omega_c = 2\pi/3$), • *DNS (interpolated onto LES grid),* ∘ *no-model LES. See also enlargement in figure 4.34.*
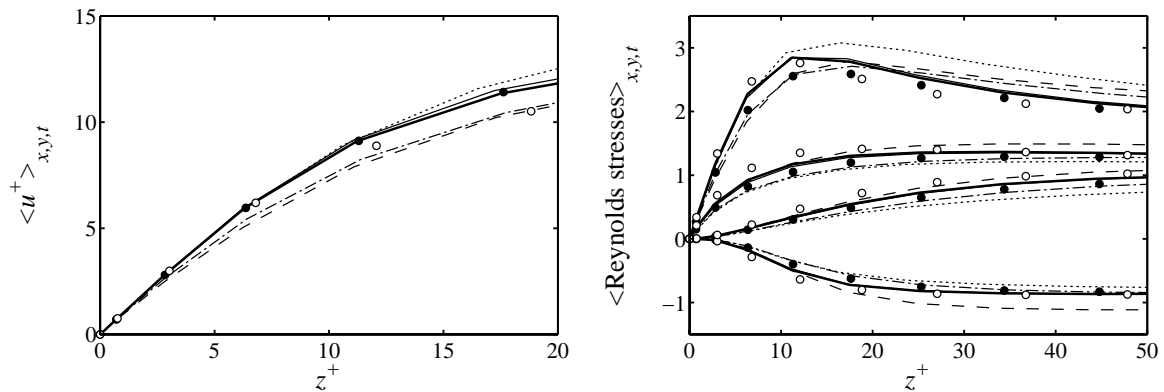
Figure 4.34: Enlargement of the data given in figure 4.33 depicting the near-wall region. Left: *Mean streamwise velocity profile.* Right: *Reynolds stresses. Line captions see figure 4.33.*

rate prediction of the velocity profile without the need for *ad-hoc* wall-damping functions, whereas the classical Smagorinsky model and the FSF model show a distinct departure from the DNS results. Similar results have already been found for the lower Reynolds number $Re_\tau \approx 180$ by Stolz *et al.* (2004).

One-dimensional energy spectra are displayed in figures 4.35 and 4.36.

In particular, the one-dimensional Fourier spectra in the streamwise direction averaged in time and the spanwise direction $E_1(k_1, x_3)$ (see equation (4.10)), the Fourier spectra integrated in the wall-normal direction $E_1^{\mathrm{int}}(k_1)$ (4.11), the Chebyshev spectrum $E_3(k_3)$ (4.12) and the Chebyshev spectrum of the fluctuations $E_3'(k_3)$ (4.13) are shown. Note that the zigzag appearance of $E_3(k_3)$ is caused by the wall-normal symmetry of the mean-flow profile which is represented by the even Chebyshev modes.

For the HPF-SF model, figure 4.35, a minor overprediction of the spectra at higher wavenumbers is seen for low ω_c, improving continuously with increasing ω_c. This behaviour is visible for both the streamwise Fourier spectra and the Chebyshev spectra. As can be inferred from figure 4.36, the data for the LES with the Smagorinsky, dynamic Smagorinsky and FSF model deviate from the DNS results already at lower wavenumbers $k_1 < 4$, overpredicting the integrated spectrum $E_1^{\mathrm{int}}(k_1)$. For the smaller scales, the FSF model shows a very accurate approximation of the DNS data, whereas the dynamic Smagorinsky model clearly underpredicts the energy content at high wavenumbers. The streamwise spectrum of the Smagorinsky model in the centre of the channel is significantly overpredicted and nearly collapses with the no-model data.

4.7.3 Comparison to ADM/ADM-RT

Averaged results of LES using the ADM-RT model (see section 2.2.3, equation (2.51)) are presented in figure 4.37. Note that in the figure the lines for ADM-RT model and the HPF-SF model virtually collapse. It can be concluded that the performance of the HPF eddy-viscosity models is similar to those of the ADM-RT model for turbulent channel flow.

In order to determine the influence of the exact shape of the eddy viscosity ν_t on the quality of the statistical results, an additional LES has been performed using the HPF eddy-viscosity methodology with a constant value of ν_t, *i.e.* $\nu_t(x, y, z, t) = \nu_t = 3 \cdot 10^{-5}$. The numerical value for ν_t was chosen empirically corresponding approximately to the spatially averaged ν_t in the calculations with the HPF-SF and HPF Smagorinsky models. The results of the simulation with constant ν_t are compared to those of the HPF Smagorinsky model and the HPF-SF model in figure 4.38. It is interesting to note that the data basically coincide for both the mean velocity profile and the Reynolds stresses. It can there-
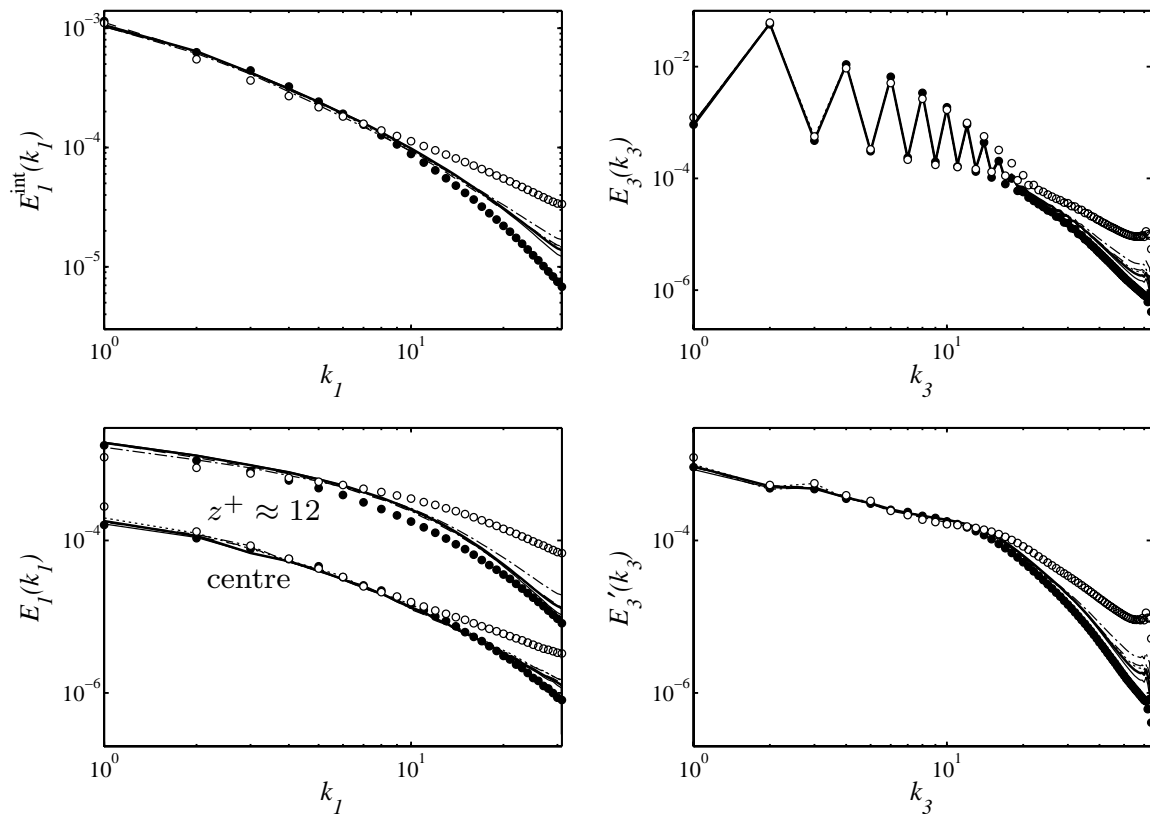
Figure 4.35: Spectra of the HPF-SF model. Left: *Integrated streamwise Fourier spectra $E_1^{\mathrm{int}}(k_1)$ (top) and $E_1(k_1, x_3)$ at two wall-normal positions* (bottom). Right: *Wall-normal Chebyshev spectra $E_3(k_3)$ (top) and $E_3'(k_3)$* (bottom). $— \cdot — \omega_c = 0$, $- - - - \omega_c = \pi/3$, $\cdots\cdots \omega_c = \pi/2$, $\longrightarrow \omega_c = 2\pi/3$, $\longrightarrow \omega_c = 3\pi/4$, $\bullet$ *DNS (interpolated onto LES grid)*, $\circ$ *no-model LES. Definition of the spectra see equations (4.10)-(4.13).*

fore be concluded that the shape of ν_t, *i.e.* which closure methodology is applied for determining ν_t, is not of particular importance when using HPF models. However, it is of course crucial to use a correct estimate for the magnitude of ν_t. A similar conclusion was also drawn in section 4.5 concerning the determination of the relaxation parameter χ for the ADM-RT model.

It is instructive to pay attention to the similarity of the model term with constant ν_t to the relaxation term used in the approximate deconvolution model (ADM) and the relaxation-term model (ADM-RT), see section 2.2.3. From equations (2.5) and (2.26) the HPF model terms occurring in the i-th momentum equation assuming constant ν_t read in
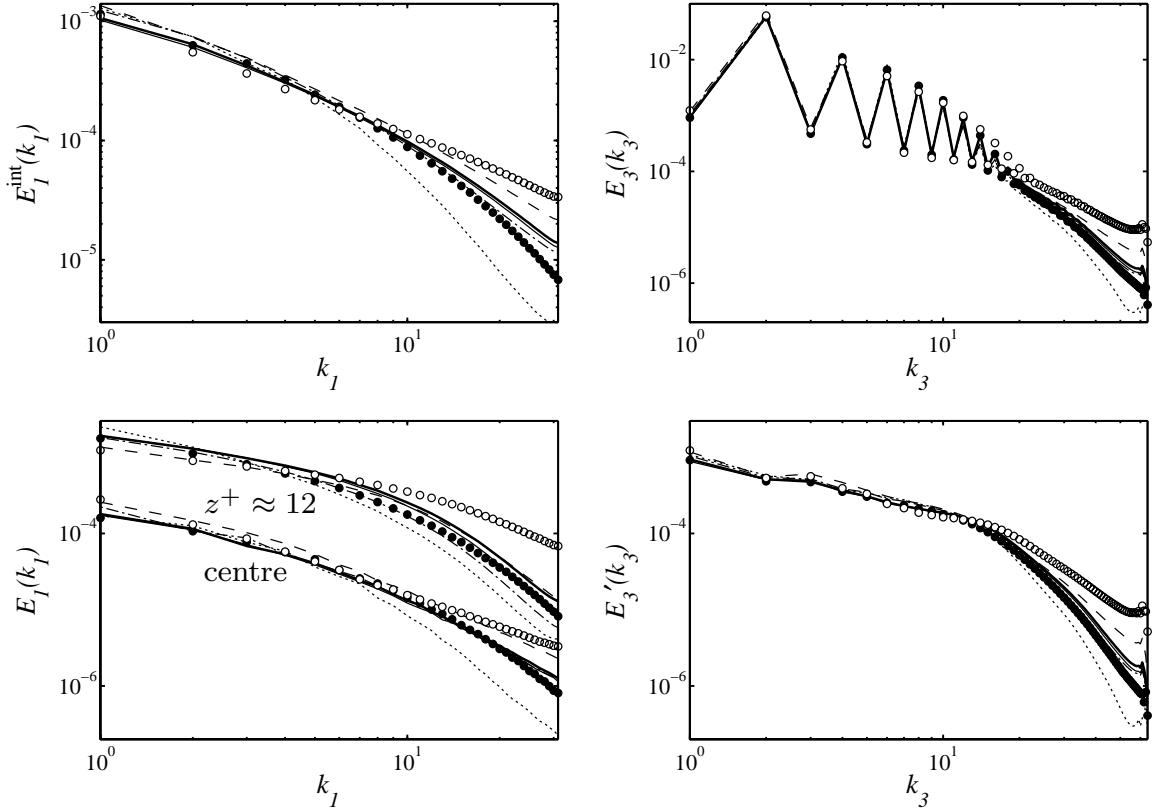
Figure 4.36: Left: *Integrated streamwise Fourier spectra $E_1^{\mathrm{int}}(k_1)$ (*top*) and $E_1(k_1, x_3)$ at two wall-normal positions (*bottom*). Right: Wall-normal Chebyshev spectra $E_3(k_3)$ (*top*) and $E_3'(k_3)$ (*bottom*).* ——— *HPF-SF model ($\omega_c = 2\pi/3$),* ——— *HPF Smagorinsky model ($\omega_c = 2\pi/3$),* - - - - *Smagorinsky model ($C_S = 0.05$),* ······· *dynamic Smagorinsky model,* —·—·*FSF model ($\omega_c = 2\pi/3$),* • *DNS (interpolated onto LES grid),* ∘ *no-model LES. Definition of the spectra see equations (4.10)-(4.13).*

Fourier space ($\mathcal{F}$ denoting the Fourier transform)

$$\mathcal{F}\left\{-2\frac{\partial}{\partial x_j}\left[\nu_t S_{ij}(H * \overline{\mathbf{u}})\right]\right\} = \nu_t |\mathbf{k}|^2 \hat{H} \cdot \hat{\overline{u}}_i \ . \tag{4.17}$$

Similarly, from equations (2.35) and (2.51) the relaxation term of ADM and ADM-RT is defined, assuming a constant model coefficient χ as well, as

$$\mathcal{F}\left\{\chi H_{\mathrm{ADM}} * \overline{\mathbf{u}}\right\} = \chi \hat{H}_{\mathrm{ADM}} \cdot \hat{\overline{u}}_i \ , \tag{4.18}$$

with a high-pass filter $\hat{H}_{\mathrm{ADM}}$. Equating the right-hand sides now yields

$$\nu_t \hat{H} = \chi \frac{\hat{H}_{\mathrm{ADM}}}{|\mathbf{k}|^2} \ . \tag{4.19}$$
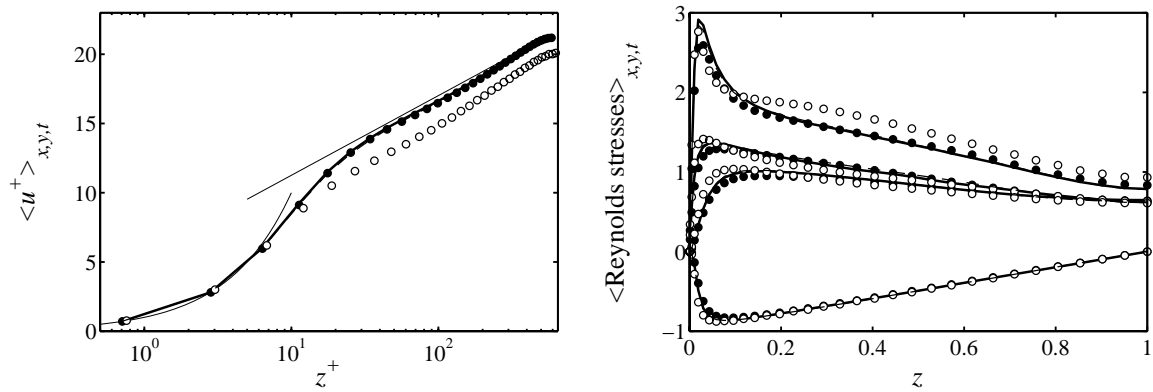
Figure 4.37: Left: *Mean streamwise velocity profile* $\langle \overline{u}_1 \rangle^+$ *in wall units.* Right: *Reynolds stresses* $\langle \overline{u}_1' \overline{u}_1' \rangle^{1/2}/u_\tau$, $\langle \overline{u}_2' \overline{u}_2' \rangle^{1/2}/u_\tau$, $\langle \overline{u}_3' \overline{u}_3' \rangle^{1/2}/u_\tau$, $\langle \overline{u}_1' \overline{u}_3' \rangle/u_\tau^2$. ———— *HPF-SF model* ($\omega_c = 2\pi/3$), ---- *ADM-RT model* ($\chi = 2$), • *DNS (interpolated onto LES grid),* ○ *no-model LES. Note that the solid and the dashed line virtually collapse.*
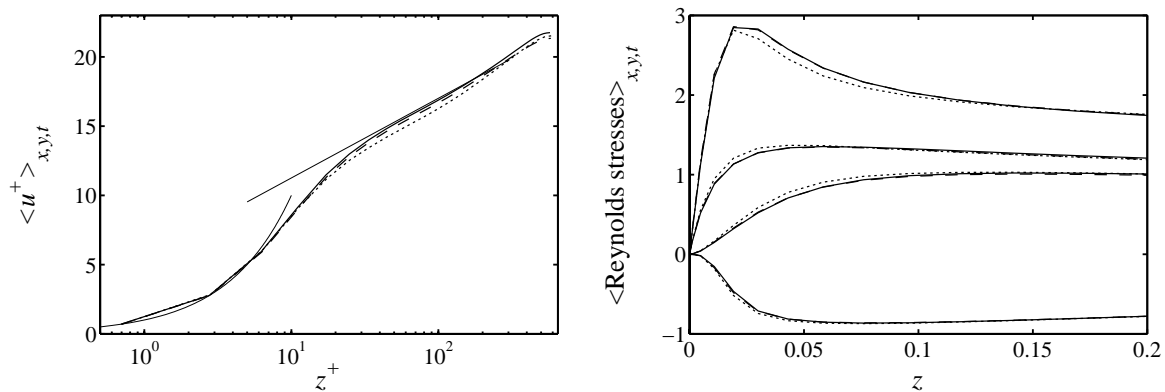
Figure 4.38: Left: *Mean streamwise velocity profile* $\langle \overline{u}_1 \rangle^+$ *in wall units.* Right: *Reynolds stresses* $\langle \overline{u}_1' \overline{u}_1' \rangle^{1/2}/u_\tau$, $\langle \overline{u}_2' \overline{u}_2' \rangle^{1/2}/u_\tau$, $\langle \overline{u}_3' \overline{u}_3' \rangle^{1/2}/u_\tau$, $\langle \overline{u}_1' \overline{u}_3' \rangle/u_\tau^2$. ———— *HPF Smagorinsky model* ($\omega_c = 2\pi/3$), ---- *HPF-SF model* ($\omega_c = 2\pi/3$), ········ *HPF eddy-viscosity model* ($\omega_c = 2\pi/3$) *with* $\nu_t(x, y, z, t) = \text{const.} = 3 \cdot 10^{-5}$.

This indicates that using the filter $|\mathbf{k}|^2 \hat{H}$ in the relaxation term is in fact analytically equivalent to the HPF model with constant ν_t. The results for turbulent channel flow indeed show this similarity, see figure 4.37. The relation between the ADM relaxation regularisation and other LES approaches is also discussed in *e.g.* Adams & Stolz (2002) and Müller *et al.* (2004).

4.7.4   Energy budget

For the LES presented in the previous sections, the turbulent energy budget has been evaluated (for notation see also appendix B.3). The turbulent production $\mathcal{P}$ is defined as

$$\mathcal{P} = \langle \overline{u}_i' \overline{u}_j' \rangle \langle \overline{S}_{ij} \rangle \; . \tag{4.20}$$

The total viscous dissipation $\langle \varepsilon_{\text{visc}} \rangle = -\frac{2}{Re} \langle \overline{S}_{ij} \overline{S}_{ij} \rangle$ is split into the part of the viscous dissipation arising due to the mean flow

$$\varepsilon_{\text{visc,mean}} = -\frac{2}{Re} \langle \overline{S}_{ij} \rangle \langle \overline{S}_{ij} \rangle \; , \tag{4.21}$$

and the viscous dissipation due to the velocity fluctuations

$$\varepsilon_{\text{visc,fluct}} = -\frac{2}{Re} \langle \overline{S}_{ij} \overline{S}_{ij} \rangle + \frac{2}{Re} \langle \overline{S}_{ij} \rangle \langle \overline{S}_{ij} \rangle \; . \tag{4.22}$$

Similarly, the total dissipation due to the SGS model contributions is defined as $\langle \varepsilon_{\text{SGS}} \rangle = \langle \tau_{ij} \overline{S}_{ij} \rangle$ and split accordingly into

$$\varepsilon_{\text{SGS,mean}} = \langle \tau_{ij} \rangle \langle \overline{S}_{ij} \rangle \; , \tag{4.23}$$

$$\varepsilon_{\text{SGS,fluct}} = \langle \tau_{ij} \overline{S}_{ij} \rangle - \langle \tau_{ij} \rangle \langle \overline{S}_{ij} \rangle \; . \tag{4.24}$$

Note that negative values of the dissipation correspond to a loss of kinetic energy.

Figure 4.39 shows the energy budget for the HPF-SF model. Note that these quantities are dependent on an accurate description of the velocity field in terms of velocity profiles and Reynolds stresses. The production and the two contributions to the viscous dissipation collapse onto one line for the different cutoff wavenumbers. However, a distinct influence of the cutoff wavenumber on the SGS dissipation is visible in the figure. Apart from the simulation using $\omega_c = 0$ (Schumann's model), both $\varepsilon_{\text{SGS,mean}}$ and $\varepsilon_{\text{SGS,fluct}}$ are decreasing with increasing ω_c. The contribution of $\varepsilon_{\text{SGS,fluct}}$ to the total SGS dissipation is also decreasing with ω_c, see $\int \varepsilon_{\text{SGS,fluct}} \mathrm{d}z / \int \langle \varepsilon_{\text{SGS}} \rangle \mathrm{d}z$ in table 4.6. Consistent results can also be found for the HPF Smagorinsky model. This behaviour indicates that the SGS dissipation acting only on smaller scales is more effective in terms of total dissipation, *i.e.* less dissipation is needed.

The energy budget for the different SGS models is shown in figure 4.40 together with the DNS data. The mean viscous dissipation
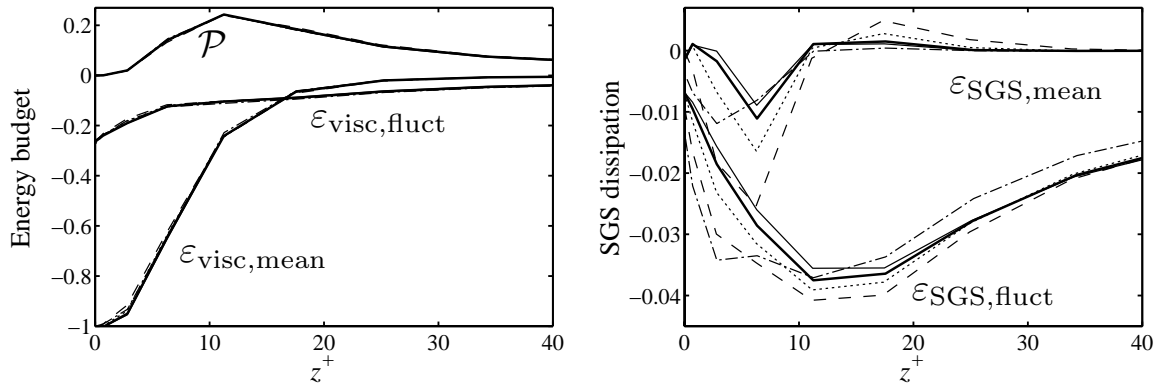
Figure 4.39: Energy budget for the HPF-SF model, normalised by viscous wall units, $(u_\tau^\circ)^4/\nu^\circ$: Left: Production $\mathcal{P}$, viscous dissipation due to mean-flow strain $\varepsilon_{\mathrm{visc,mean}}$, viscous dissipation due to strain of fluctuations $\varepsilon_{\mathrm{visc,fluct}}$. Right: SGS dissipation due to mean flow $\varepsilon_{\mathrm{SGS,mean}}$, SGS dissipation due to fluctuations $\varepsilon_{\mathrm{SGS,fluct}}$. —·—$\omega_c = 0$, ----$\omega_c = \pi/3$, ········$\omega_c = \pi/2$, ———$\omega_c = 2\pi/3$, ———$\omega_c = 3\pi/4$.

$\varepsilon_{\mathrm{visc,mean}}$ deviates from the data obtained from DNS for the FSF and the Smagorinsky model, which is primarly due to an incorrect mean velocity profile (see also figure 4.34). The turbulent production predicted by the Smagorinsky model peaks further away from the wall compared to the DNS and has a higher integral value. On the other hand, the FSF model slightly underpredicts $\mathcal{P}$. The HPF models and the dynamic Smagorinsky model are predicting $\mathcal{P}$ and $\langle \varepsilon_{\mathrm{visc}} \rangle$ quite accurately. The mean and fluctuating SGS contribution of the Smagorinsky model is much higher than that of the other models. The FSF model also has a strong contribution from $\varepsilon_{\mathrm{SGS,mean}}$ which is due to the full (non-HPF) strain-rate tensor. The dynamic Smagorinsky model predicts much lower values for both parts of the SGS dissipation, however, it still has a significant value of $\varepsilon_{\mathrm{SGS,mean}}$. On the other hand, for the HPF models, $\varepsilon_{\mathrm{SGS,fluct}}$ is much lower, see figure 4.39 (note the different scaling of the ordinate).

Classical eddy-viscosity models with positive model coefficient are strictly dissipative, *i.e.* they do not allow for any energy flux from the subgrid scales back to the resolved scales. This is obvious by looking at the SGS dissipation for eddy-viscosity models (see equation 2.21),

$$\varepsilon_{\mathrm{SGS}} = \tau_{ij}\overline{S}_{ij} = -2\nu_t\overline{S}_{ij}\overline{S}_{ij} = -\nu_t|\overline{S}| \leq 0 \;, \qquad (4.25)$$

which is always negative for positive eddy viscosity ν_t.
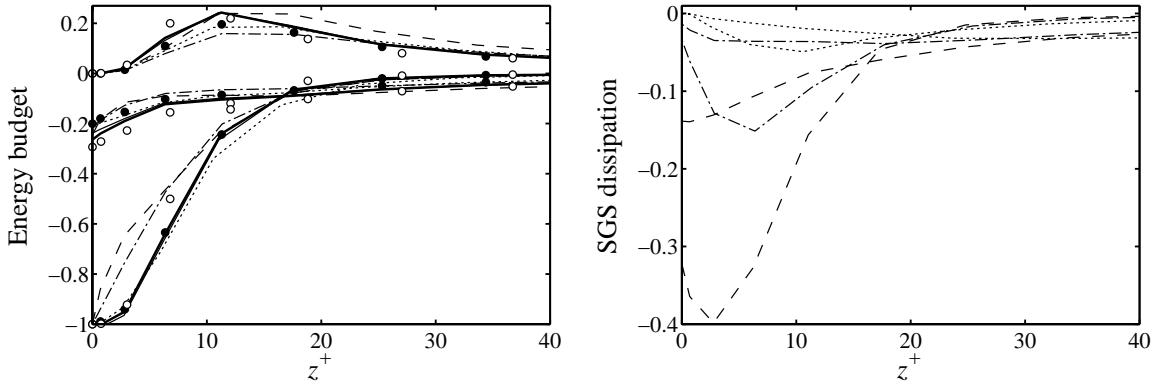
Figure 4.40: Energy budget for the different SGS models. Left: *Production* $\mathcal{P}$*, viscous dissipation due to mean-flow strain* $\varepsilon_{\text{visc,mean}}$*, viscous dissipation due to strain of fluctuations* $\varepsilon_{\text{visc,fluct}}$*.* Right: *SGS dissipation due to mean flow* $\varepsilon_{\text{SGS,mean}}$*, SGS dissipation due to fluctuations* $\varepsilon_{\text{SGS,fluct}}$ *for the classical eddy-viscosity models (note that for all models* $\varepsilon_{\text{SGS,mean}} > \varepsilon_{\text{SGS,fluct}}$ *close to the wall).* —— *HPF-SF (*$\omega_c = 2\pi/3$*),* - - - - *Smagorinsky model (*$C_S = 0.05$*),* ········ *dynamic Smagorinsky model,* —·— *FSF model (*$\omega_c = 2\pi/3$*),* —— *HPF Smagorinsky model (*$\omega_c = 2\pi/3$*),* • *DNS (evaluated on the LES grid),* ◦ *no-model LES.*

However, several studies have shown that for wall-bounded flows there is indeed an intermittent backscattering, *e.g.* Piomelli *et al.* (1991); Härtel *et al.* (1994) and Domaradzki & Saiki (1997). The SGS term of the HPF eddy-viscosity models does actually permit backscatter, since the SGS dissipation is not necessarily negative,

$$\varepsilon_{\text{SGS}} = \tau_{ij}\overline{S}_{ij} = -2\nu_t S_{ij}(H * \overline{\mathbf{u}})\overline{S}_{ij} \; . \tag{4.26}$$

In order to examine this effect in simulations of turbulent channel flow, a conditional averaging of the two quantities

$$\langle \varepsilon_{\text{SGS}}^{-} \rangle = \left\langle \frac{\varepsilon_{\text{SGS}} - |\varepsilon_{\text{SGS}}|}{2} \right\rangle \quad \text{and} \quad \langle \varepsilon_{\text{SGS}}^{+} \rangle = \left\langle \frac{\varepsilon_{\text{SGS}} + |\varepsilon_{\text{SGS}}|}{2} \right\rangle \tag{4.27}$$

has been performed, similar to Piomelli *et al.* (1991); Domaradzki & Saiki (1997). Here, $\langle \varepsilon_{\text{SGS}}^{-} \rangle$ is the forward dissipation and $\langle \varepsilon_{\text{SGS}}^{+} \rangle$ the backward dissipation (backscatter). The results for the HPF Smagorinky model ($\omega_c = 2\pi/3$) are shown in figure 4.41. Also shown is the total SGS dissipation obtained from DNS data interpolated onto the LES grid

$$\langle \varepsilon_{\text{SGS}}^{\text{DNS}} \rangle = \langle \tau_{ij} S_{ij}(\overline{\mathbf{u}}) \rangle = \langle (\overline{u_j u_i} - \overline{u}_i \overline{u}_j) S_{ij}(\overline{\mathbf{u}}) \rangle \; . \tag{4.28}$$
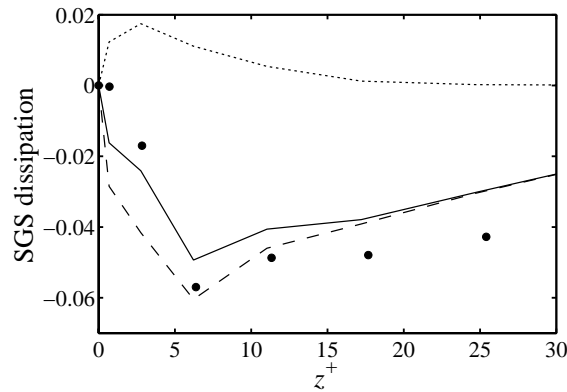
Figure 4.41: The SGS dissipation for the HPF Smagorinsky model ($\omega_c = 2\pi/3$). ——— *Total SGS dissipation $\langle \varepsilon_{\mathrm{SGS}} \rangle$,* ----*forward dissipation $\langle \varepsilon_{\mathrm{SGS}}^- \rangle$,* ········ *backward dissipation (backscatter) $\langle \varepsilon_{\mathrm{SGS}}^+ \rangle$,* ● *total SGS dissipation $\langle \varepsilon_{\mathrm{SGS}}^{\mathrm{DNS}} \rangle$ from DNS data.*

Note that the interpolation operation denoted by the overbar is performed as described in section 4.7.1. It can be seen that the plane-averaged total SGS dissipation $\langle \varepsilon_{\mathrm{SGS}} \rangle$ is always negative for the LES and the DNS data, showing an overall forward scatter in both cases. The total amount of SGS dissipation for the LES data agrees reasonably well with the DNS data, see also figure 4.40 for the other SGS models. Moreover, close to the wall, for the LES a significant amount of backscatter peaking at $z^+ \approx 3$ can be observed, which amounts to about 70% of the total SGS dissipation at this wall-normal position.

In order to correlate the locations at which backscatter is observed, wall-parallel slices of the flow domain are considered. In figure 4.42, an instantaneous LES velocity field indicating the positions of the low and high-speed streaks by the use of gray-scales is depicted. Although no two-point correlation data is shown, the typical streak spacing can be estimated from the plot as approximately 100 wall units. Superimposed in figure 4.42 are contours of $\varepsilon_{\mathrm{SGS}} = \tau_{ij} \overline{S}_{ij}$ of the same realisation. Note that positive values of $\varepsilon_{\mathrm{SGS}}$ represent backscatter. A close correlation between the regions of the intense backscatter and low-speed streaks can be observed.

Similarly, the same visualisation is given in figure 4.43 for the DNS data, however, of a different instantaneous realisation. Although not as conclusive as in figure 4.42, the correlation between backscatter regions and low-speed streaks can be anticipated also for the DNS data. It can therefore be concluded that the present LES based on the high-pass
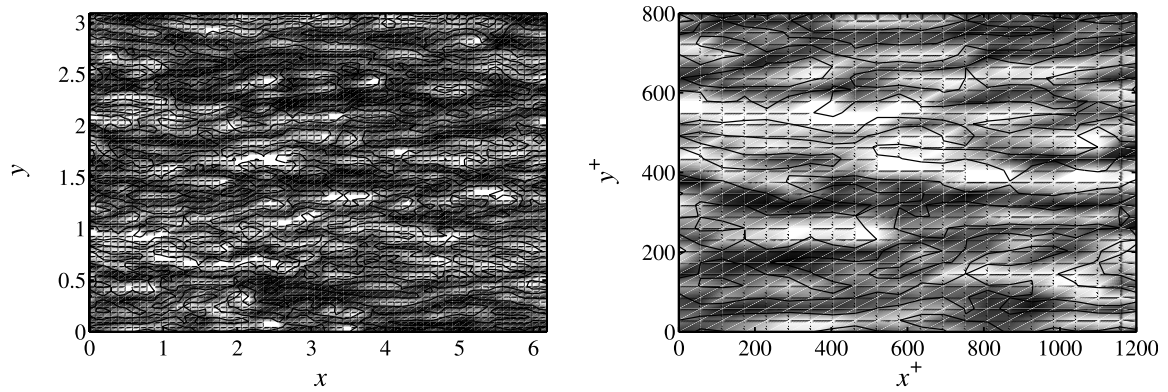
Figure 4.42: *Visualisation of the instantaneous velocity field $\overline{u}' = \overline{u} - \langle\overline{u}\rangle_{x,y}$ taken from LES with the HPF Smagorinsky model. Gray-scales ranging from $\overline{u}' = -0.05$ (black) to $\overline{u}' = 0.05$ (white) in a plane $z^+ = 2.8$. Superimposed are contours of $\varepsilon_{\mathrm{SGS}} = \tau_{ij}\overline{S}_{ij} = 0.00001$ (≈ 0.0004 in viscous scaling) showing backscatter regions of the same realisation.* Left: *Full computational domain.* Right: *Enlargement of region $[0,2] \times [0,1.4]$.*
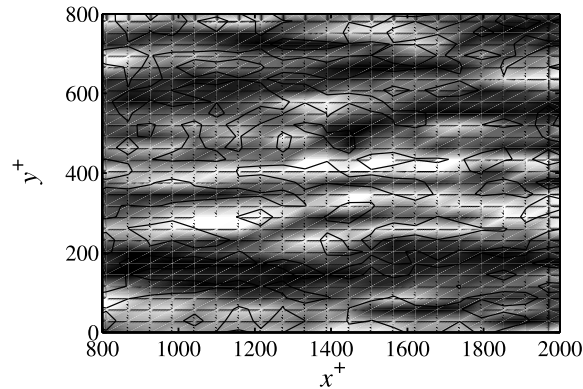
Figure 4.43: *Visualisation of a section of the instantaneous velocity field $\overline{u}' = \overline{u} - \langle\overline{u}\rangle_{x,y}$ taken from an evaluation of the DNS data. Gray-scales ranging from $\overline{u}' = -0.05$ (black) to $\overline{u}' = 0.05$ (white) in a plane $z^+ = 2.8$. Superimposed are contours of $\varepsilon_{\mathrm{SGS}} = \tau_{ij}\overline{S}_{ij} = 0.00001$ (≈ 0.0004 in viscous scaling) showing backscatter regions of the same realisation.*

filtered eddy-viscosity models predict a reasonably correct total SGS dissipation together with backscatter located at the same positions as found in the DNS data.

4.8   Comparison of the SGS models

To summarise the different results presented in this chapter, table 4.9 provides an qualitative assessment of the various SGS models used in this chapter. In particular, the variants of the approximate deconvolution model (ADM, section 2.2.3) are included, *i.e.* ADM-3D, ADM-2D and ADM-RT. Variants of the dynamic Smagorinsky (DS) model (section B.4) using different test filters are also considered, *i.e.* using the three-dimensional second-order filter (2.18), the sixth-order filter $Q_1 * G$ and the spectral cutoff filter. Additionally, classical eddy-viscosity models (section 2.2.1) including the Smagorinsky model, the structure-function (SF) model and the filtered structure-function (FSF) model are compared together with their high-pass filtered (HPF) counterparts, HPF Smagorinsky and HPF-SF model (see section 2.2.2).

Note that the conclusions summarised in the table 4.9 are limited to the flow cases, model implementations and resolutions used in this work and should not be mistaken as being generally valid.

Different criteria assessing the LES performance are compared in a qualitative way. In particular, for transitional channel flow the evolution of the integral quantities Re_τ and H_{12} and the prediction of the transitional vortical structures is assessed. For turbulent channel flow, the averaged skin friction and shape factor, the prediction of the Reynolds stresses and the mean velocity profiles are compared.

For the case of homogeneous isotropic turbulence (HIT, see chapter 6) the quality of the simulated compensated energy spectrum is evaluated.

The block entitled *Model Formulation* refers to details of the definition and implementation of the different SGS models. Specifically, it is noted whether the models are formulated in a three-dimensional way (*e.g.* three-dimensional filtering), whether an averaging of the model coefficient is needed in homogeneous directions, whether the model coefficients can be considered being generally valid for different flow types and Reynolds numbers, and what is the additional computational cost for the model terms compared to the no-model LES at the same resolution. Furthermore, the convergence towards the exact (DNS) solution with increasing grid resolution (grid refinement) and the ability of the SGS model to predict energy backscatter is compared.

As reported in section 4.4.1, using the standard formulation of ADM (ADM-3D) it was not possible to simulate the temporal transition at the coarse LES resolution chosen for this case (*i.e.* only 33 points in the

wall-normal direction, see section 4.1). However, with slighlty increased resolution the ADM-3D model is able to calculate through transition and predict the characteristic transitional quantities comparably well.

Model	Transition: Integral quantities Re_τ, H_{12}	Transition: Transitional vortical structures	Turbulence: Integral quantities Re_τ, H_{12}	Turbulence: Averaged Reynolds stresses	Turbulence: Velocity profile "Law of the wall"	HIT: Compensated energy spectra	Model Formulation: 3D model formulation	Model Formulation: Averaging of model coefficient C	Model Formulation: Generality of model coefficient C	Model Formulation: Computational cost	Model Formulation: Grid refinement	Model Formulation: Energy backscatter
No-model LES	+	-	--	--	--	--	n/a	n/a	n/a	++	+	--
FSF (3D)	++	-	+	+	-	+	+	+	-	+	+	-
SF	--	--	--	--	--	+	-	-	--	+	-	-
Smagorinsky	--	--	-	-	-	+	+	+	--	+	+	-
DS-2D (spec.)	+	-	++	++	++		-	-	++	-	++	-
DS-3D (Q_1G)	+	-	+	++	++		++	-	++	-	+	-
DS-3D (2nd)	++	--	--	-	-		++	-	++	-	--	-
HPF-SF	+	-	++	++	++	+	++	+	+	+	++	++
HPF-Smag.	+	-	++	++	++	+	++	+	+	+	++	++
ADM-RT (χ_{dyn})	+	++	-	++	++		++	-	--	-	++	++
ADM-RT (χ_{const})	+	++	++	++	++	+	++	+	-	+	++	+
ADM-2D (χ_{dyn})	+	-	-	+	+		--	-	+	-	+	+
ADM-3D (χ_{dyn})	[1]	[1]	-	+	++		++	-	+	-	+	+

Table 4.9: Comparison of the SGS model performance in LES of transitional and turbulent channel flow and homogeneous isotropic turbulence (HIT). The symbols + and - refer to good and bad results, respectively. ++ is better than +, similarly -- is worse than -. Note that the conclusions summarised in this table are limited to the flow cases, model implementations and resolutions used in this work.

[1] The ADM-3D model was not able to simulate transition at the chosen coarse grid resolution, see discussion in the text.

Chapter 5

Spatial transition and turbulence

The temporal simulations presented in the previous chapter 4 assume that the disturbance growth within one period of the primary Tollmien-Schlichting (TS) wave λ_{TS} is small. Based on this assumption, only one wavelength of the TS wave is considered and its growth is simulated in time, in a moving frame of reference, rather than in space, whereas in a physical experiment disturbances grow in space. The boundary conditions in the streamwise direction are thus chosen to be periodic, rendering the streamwise direction homogeneous. The main advantages of the temporal simulation approach are that the domain is much smaller in the streamwise direction than for a spatial simulation and, due to the periodic boundary conditions, neither inflow nor outflow need to be specified and efficient Fourier methods can thus be used.

During the first, weakly nonlinear and slowly evolving stages of transition, the temporal approach is well justified (Kleiser & Zang, 1991). Additionally, for the turbulent stages the similarity of the spatial and temporal approach is well-established and such simulations are commonly performed by the temporal approach (*e.g.* Moser *et al.* (1999)). However, there are differences during the highly intermittent later transitional stages concerning the evolution of the physical flow structures and, possibly, the appropriate subgrid-scale (SGS) modelling. For a discussion of various aspects of spatial simulations see Fasel (1990); Kleiser & Zang (1991).

In this chapter, the temporal large-eddy simulations presented in chapter 4 are extended to the spatial framework, see also Schlatter *et al.* (2005*d*). For boundary treatment, the fringe method (see Bertolotti *et al.* (1992); Nordström *et al.* (1999) and appendix A) has been implemented in the numerical simulation code (chapter 3).

5.1 Governing equations and SGS modelling

The governing equations for LES are the (spatially) filtered Navier-Stokes equations (2.5) for the non-dimensional velocity components

$\overline{u}_i$, $i = 1, 2, 3$ and the pressure $\overline{p}$,

$$\frac{\partial \overline{u}_i}{\partial t} + \frac{\partial \overline{u}_j \overline{u}_i}{\partial x_j} + \frac{\partial \overline{p}}{\partial x_i} - \frac{1}{Re_{CL}|_{\text{lam}}} \frac{\partial^2 \overline{u}_i}{\partial x_j \partial x_j} = -\frac{\partial \tau_{ij}}{\partial x_j} + F_i^F , \qquad (5.1)$$

complemented with the incompressibility constraint (2.6)

$$\frac{\partial \overline{u}_i}{\partial x_i} = 0 .$$

The non-dimensionalisation is similar to the temporal case, section 4.1.2. The effect of the non-resolved small scales enters through the SGS term $\tau_{ij} := \overline{u_i u_j} - \overline{u}_j \overline{u}_i$, which is not closed and must be modelled appropriately as detailed in section 2.2. The term F_i^F in equation (5.1) arises from the fringe forcing which will be discussed in the following section.

For the present results, a number of different SGS models have been examined. All of these models have already been tested in temporal K-type transition in plane Poiseuille flow (see chapter 4 and Schlatter *et al.* (2004*c*); Stolz *et al.* (2004); Schlatter *et al.* (2004*d*)) with the same spectral numerical method explained in chapter 3. We follow the nomenclature introduced in section 2.2 and briefly review the SGS models that will be used in the spatial simulations.

The *dynamic Smagorinsky model* is implemented according to Germano *et al.* (1991) and Lilly (1992) with a three-dimensional second-order test filter ($\omega_c = \pi/2$, equation (2.19)), with its transfer function shown in figure 2.3. The eddy viscosity is then defined as

$$\nu_t = (C_S \Delta)^2 |S(\overline{\mathbf{u}})| , \qquad (5.2)$$

with the dynamic model coefficient $C_S(x, z, t)$ where negative values were clipped. The averaging involved in the computation of the model coefficient (Germano *et al.*, 1991; Lilly, 1992) is performed in the spanwise direction y only, see section B.4 and equation (B.47). Note that in the temporal case the averaging is usually done in wall-parallel planes.

In the *filtered structure function (FSF) model* (Ducros *et al.*, 1996) the eddy viscosity is given by (see equation (2.25))

$$\nu_t = C_{FSF} C_K^{-3/2} \Delta \sqrt{F_2(H_0 * \overline{\mathbf{u}}, \mathbf{x}, \Delta)} , \qquad (5.3)$$

with $C_{FSF} = 0.0371$ (Schlatter *et al.*, 2004*b*) and the second-order velocity structure function F_2 computed in the three-dimensional six-point

formulation from the high-pass filtered velocity field $H_0 * \overline{u} = (I - G) * \overline{u}$. H_0 is defined in equation (2.12) (section 2.1.1, see also Stolz *et al.* (2001*a*)). The filter transfer functions $\hat{G}$ and $\hat{H}_0$ are shown in figure 2.2. The cutoff wavenumber ω_c, defined as $\hat{G}(\omega_c) = \hat{H}_0(\omega_c) = 1/2$, is set to $\omega_c = 2\pi/3$ for the results presented in this chapter. The filter is defined on an implicit five-point stencil in physical space, and it is assured that all moments in physical space up to second order are vanishing even for non-equidistant grids, as *e.g.* used in the the wall-normal direction of the channel. For this reason smooth (*i.e.* low-order polynomial) flow profiles are virtually invariant with respect to the filter operation with kernel G, and are small when high-pass filtered with the filter $H_N := (I - G)^{N+1}$, $N \geq 0$.

In contrast to classical eddy-viscosity models (section 2.2.1), the *high-pass filtered (HPF) eddy-viscosity models* (section 2.2.2, see Stolz *et al.* (2004)), compute both the strain rate and the eddy viscosity from the high-pass filtered velocities (see equation (2.26)), *i.e.*

$$\tau_{ij} - \frac{\delta_{ij}}{3}\tau_{kk} \approx -2\nu_t^{\mathrm{HPF}} S_{ij}(H_0 * \overline{\mathbf{u}}) \, , \tag{5.4}$$

with the corresponding eddy viscosity for the HPF-SF model (equation (2.29)),

$$\nu_t^{\mathrm{HPF}} = C_{SF}^{\mathrm{HPF}} C_K^{-3/2} \Delta \sqrt{F_2(H_0 * \overline{\mathbf{u}}, \mathbf{x}, \Delta)} \, , \tag{5.5}$$

and $C_{SF}^{\mathrm{HPF}} = 0.0405$ (Schlatter *et al.*, 2004*b*).

The *ADM-RT model* is based on the relaxation term (RT) of the approximate deconvolution model (ADM) (Stolz *et al.*, 2001*a*) presented in Stolz & Adams (2003) and Schlatter *et al.* (2004*d,c*). In this monograph, ADM and the ADM-RT model are discussed in section 2.2.3, equations (2.35) and (2.51). The model consists of a regularisation term $\chi H_5 * \overline{u}_i$ which is employed in the momentum equations (5.1),

$$\frac{\partial \tau_{ij}}{\partial x_j} = \chi H_5 * \overline{u}_i \, . \tag{5.6}$$

$H_5 = (I - G)^6$ is defined in equations (2.10) and (2.12) and denotes the high-order three-dimensional high-pass filter (Stolz *et al.*, 2001*a*) respecting the boundary conditions, see figure 2.2. χ is a model coefficient, which is set to a constant value herein. The ADM-RT model proved to be accurate and robust in predicting transitional and turbulent incompressible flows with spectral methods, see chapter 4 and Schlatter *et al.* (2004*d,c*).

5.2   Simulation method

The simulations use the standard Fourier-Chebyshev spectral method which is discussed in chapter 3. Periodic boundary conditions are imposed in the streamwise (x) and spanwise (y) directions together with no-slip conditions at the solid walls ($z = \pm 1$). The nonlinear convection terms are computed with full dealiasing employing the 3/2-rule in all spatial directions. No dealiasing has been used for the SGS model terms. The divergence-free condition is enforced exactly by an influence-matrix technique (Kleiser & Schumann, 1980). Time advancement is achieved by a semi-implicit Runge-Kutta/Crank-Nicolson scheme (Sandham & Kleiser, 1992; Wray, 1987).

To account for the spatially evolving flow a fringe region has been added to the flow domain in the streamwise direction similar to Bertolotti *et al.* (1992) and Nordström *et al.* (1999). Within this region, which accounts for 20% of the streamwise extent of the computational domain, the term

$$F_i^F = \lambda(x)(\mathcal{U}_i - \overline{u}_i) \tag{5.7}$$

in equation (2.1) forces the flow to return from the (turbulent) outflow profile upstream of the fringe region back to the prescribed inflow profile $\mathcal{U}_i$. The fringe function is defined as $\lambda(x) = \lambda_f \cdot F(x)$ with $F(x)$ given by Nordström *et al.* (1999); Lundbladh *et al.* (1999), see figure 5.1,

$$F(x) = S\left(\frac{x - x_{\text{start}}}{\Delta_{\text{rise}}}\right) - S\left(\frac{x - x_{\text{end}}}{\Delta_{\text{fall}}} + 1\right) , \tag{5.8}$$

with the smooth step function

$$S(x) \quad = \quad \begin{cases} 0 & , \; x \leq 0 \\ 1/[1 + \exp(\frac{1}{x-1} + \frac{1}{x})] & , \; 0 < x < 1 \\ 1 & , \; x \geq 1 \end{cases} . \tag{5.9}$$

The fringe function $\lambda(x) \geq 0$ and thus the forcing term F_i^F is non-vanishing only within the fringe region extending from $x_{\text{start}} = 80$ to $x_{\text{end}} = 100$ for the present setup. The shape of the fringe function is further defined by $\Delta_{\text{rise}} = 14$ and $\Delta_{\text{fall}} = 4$.

The inflowing disturbances are superimposed onto the laminar Poiseuille flow profile and forced within the fringe region as distributed boundary conditions $\overline{u}_i \; \leftarrow \; \mathcal{U}_i(x, y, z, t)$. They consist of a two-dimensional spatially evolving Tollmien-Schlichting (TS) wave and two
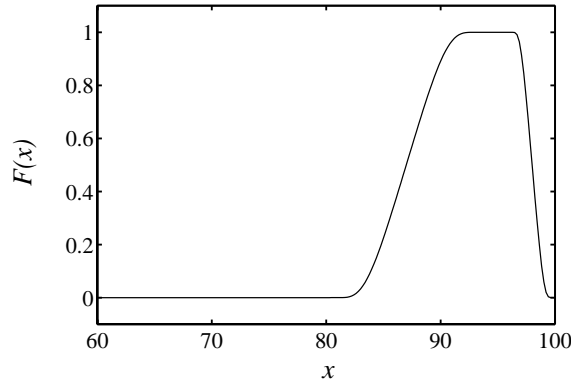
Figure 5.1: Fringe function $F(x)$ on the subdomain $[60, 100]$.

superimposed oblique three-dimensional waves with the same temporal frequency $\omega_{TS} = 0.3$ as the two-dimensional disturbances. The computation of the TS waves was performed similarly to the temporal case (see section 4.1.1) using a standard Chebyshev collocation method involving the solution to the Orr-Sommerfeld and Squire equations (see *e.g.* Schmid & Henningson (2001)). Note that in the coupled Orr-Sommerfeld/Squire equations the eigenvalue α appears up to fourth power (as opposed to the temporal eigenvalue ω which only appears linear). The resulting eigenproblem was solved using the companion matrix method. It was necessary to solve the eigenproblem using 128bit accuracy in the computer programme.

The eigenvalue spectra for the two-dimensional and three-dimensional waves are shown in figure 5.2. In figures 5.3 and 5.4, the eigenfunctions of the disturbances included in the initial conditions are displayed. The corresponding TS waves used in the temporal simulations have been described in section 4.1.1 and are depicted in figures 4.1-4.3.

The amplitude of these disturbances is set to 6% and 0.2% of the centre-line velocity, respectively, being twice as high as in the temporal reference simulation of Gilbert & Kleiser (1990) and Schlatter *et al.* (2004*c*) in order to trigger transition earlier and thus to allow for a shorter computational domain. These initial conditions excite standard K-type transition with an aligned pattern of Λ-vortices. The Reynolds number based on the bulk velocity and the channel half-width h is $Re_b = 3333$ (corresponding to $Re_\tau \approx 210$ in the fully turbulent regime). Statistical data has been averaged in y and in time from $t = 200$ to
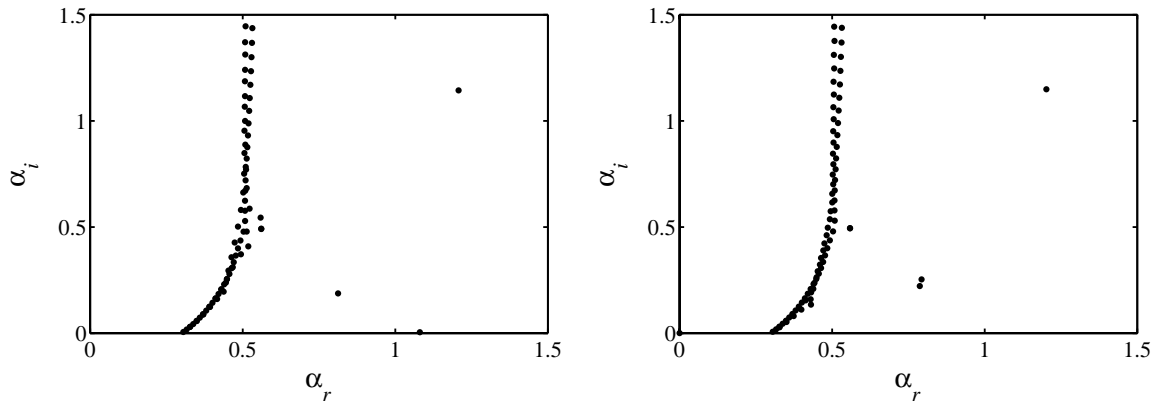
Figure 5.2: Spectrum of the eigenvalues $\alpha = \alpha_r + \alpha_i\mathrm{i}$ (streamwise wavenumber α) of the coupled Orr-Sommerfeld/Squire equations with parabolic base flow, $Re_b = 3333$, $\omega = 0.3$. Left: Two-dimensional waves, $\beta = 0$. Right: Three-dimensional waves, $\beta = \pm 2.0944$.
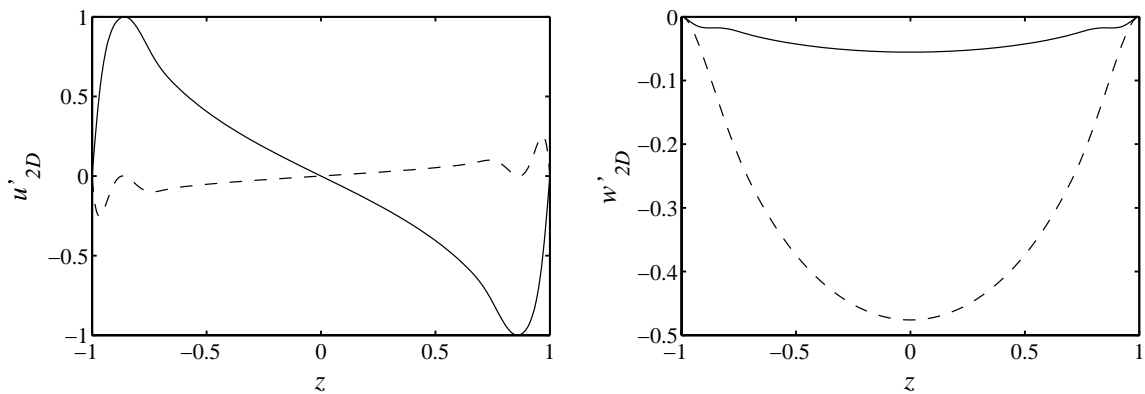
Figure 5.3: Two-dimensional eigenfunction for the eigenvalue $\alpha = 1.08 + 4.44 \cdot 10^{-3}\mathrm{i}$, $Re_b = 3333$, $\omega = 0.3$, $\beta = 0$. ——— Real part, ‐ ‐ ‐ ‐ imaginary part. Left: Streamwise velocity disturbance u'_{2D}. Right: Wall-normal velocity disturbance w'_{2D}.

$t = 410$, corresponding to 10 periods of the initial TS wave,

$$u_i = \langle u_i \rangle + u'_i = \langle u_i \rangle_{y,t} + u'_i \ . \tag{5.10}$$

At the beginning of the statistical sample ($t = 200$) the flow was found to be sufficiently settled. $t = 200$ corresponds to nearly three box through-flows. The dimensions of the computational box are $100h \times 3h \times 2h$. An overview of the flow development within the computational box is shown in figure 5.5.
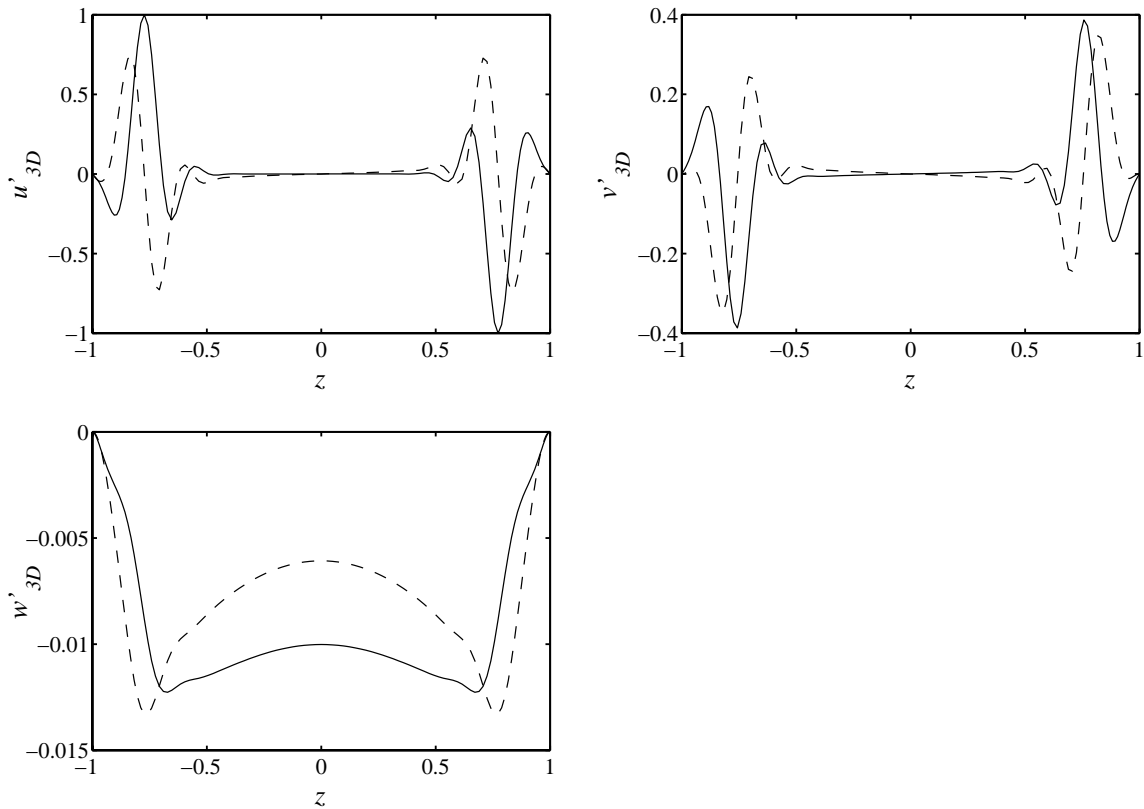
Figure 5.4: Three-dimensional eigenfunction for the eigenvalue $\alpha = 0.803 + 0.231i$, $Re_b = 3333$, $\omega = 0.3$, $\beta = 2.0944$. ——— *Real part,* - - - - *imaginary part. From* left *to* right *and* top *to* bottom*: Streamwise velocity disturbance u'_{3D}, spanwise velocity disturbance v'_{3D}, wall-normal velocity disturbance w'_{3D}.*
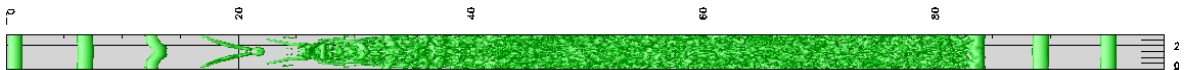
Figure 5.5: Visualisation of an instantaneous solution (isocontours of λ_2) within the entire computational domain in a (x,y)-plane. The inflow is located on the left, whereas the fringe domain $80 \leq x \leq 100$ is appended on the right-hand side (see also figure 2.2).

5.3   Results

As a first step, the application of the fringe method to the LES equations using an SGS model has to be examined. Several LES using the ADM-RT model have been performed varying both the fringe strength λ_f and the relaxation parameter χ. In figure 5.6, three simulations on a $768 \times 48 \times 49$ grid are compared for which λ_f was varied by a factor
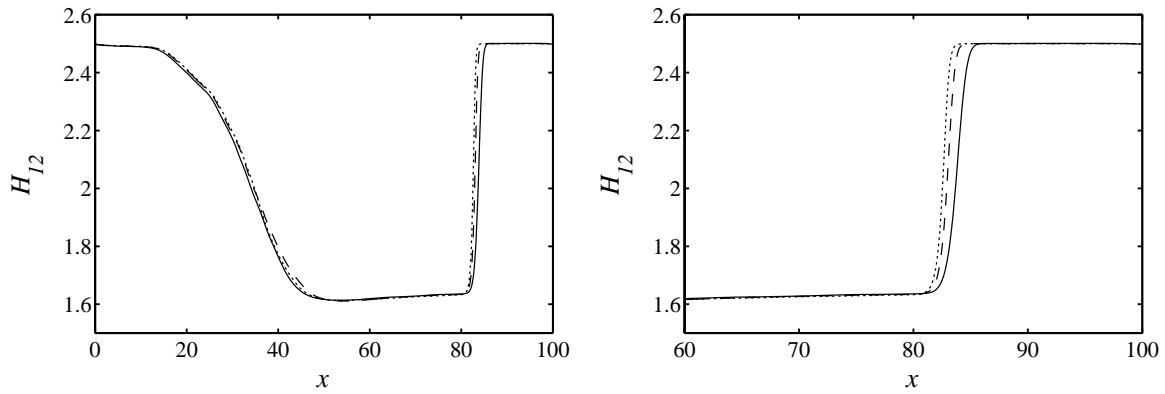
Figure 5.6: Evolution of the shape factor H_{12} during transition using ADM-RT on $768 \times 48 \times 49$ grid points, $\chi = 25$. —— $\lambda_f = 10$, - - - - $\lambda_f = 40$, ········ $\lambda_f = 100$. Left: *Full domain.* Right: *Enlargement of the fringe region.*
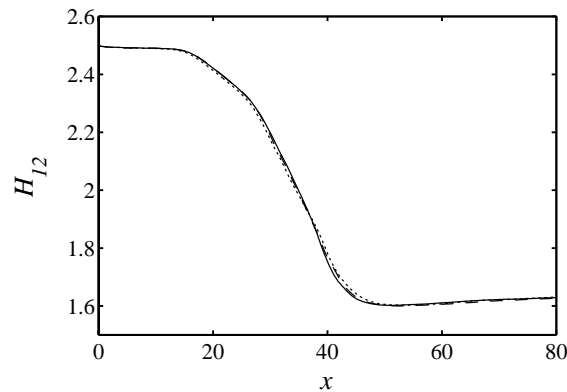
Figure 5.7: Evolution of the shape factor H_{12} during the transitional phase using ADM-RT on $512 \times 32 \times 33$ grid points. —— $\chi = 25$, $\lambda_f = 40$, - - - - $\chi = 50$, $\lambda_f = 40$, —·— $\chi = 25$, $\lambda_f = 10$.

of up to 10 with fixed $\chi = 25$. In the physically relevant subdomain $x \in [0, 80]$, the shape factor H_{12} nearly collapses for the different runs, whereas in the fringe region $x > 80$ a higher λ_f leads to slightly earlier (*i.e.* at earlier x) reestablishment of the laminar profile $H_{12} \approx 2.5$. At a lower resolution of $512 \times 32 \times 33$ grid points, figure 5.7 displays H_{12} for different combinations of χ and λ_f, again showing no significant discrepancies. For the remainder of the chapter, $\chi = 25$ was chosen. Additionally, tests have been conducted with gradually reducing the in-
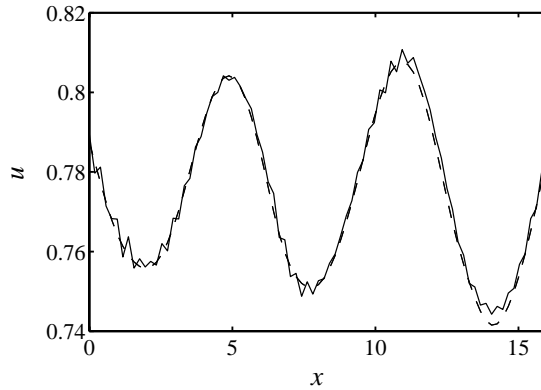
Figure 5.8: Streamwise velocity $\overline{u}$ close to the inflow at $z = -0.47$ computed using ---- ADM-RT and ——— no-model LES on $512 \times 32 \times 33$ grid points.

fluence of the SGS model within the fringe region by setting

$$\frac{\partial \tau_{ij}}{\partial x_j} = (1 - F(x))\chi H_5 * \overline{u}_i \ . \tag{5.11}$$

It was found that such a modification was not necessary for an accurate prescription of the inflow conditions.

On the other hand, the application of the fringe method without any SGS model (no-model LES) at the low LES resolution ($512 \times 32 \times 33$ nodes) caused the appearance of small wiggles in the instantaneous velocity as shown in figure 5.8. These wiggles are not present if an SGS model is used at the same resolution. They are most likely caused by the underresolution in the later stages of transition and in the turbulent part of the flow domain. These numerical instabilities are then able to affect the whole flow domain due to the global discretisation scheme. By increasing the resolution, these artefacts are reduced gradually and eventually vanish as soon as sufficient resolution is reached in the late transitional and turbulent parts of the domain. Conversely, in the LES these wiggles do not exist even at low resolution since they are effectively damped by the SGS model.

It can thus be concluded that the fringe method provides an accurate way to enforce inflow and outflow boundary conditions also in the presence of an SGS model. Moreover, it can be seen that the ADM-RT model is not very sensitive to the choice of the model coefficient χ (see also Schlatter *et al.* (2004*d*); Stolz *et al.* (2001*a*)).
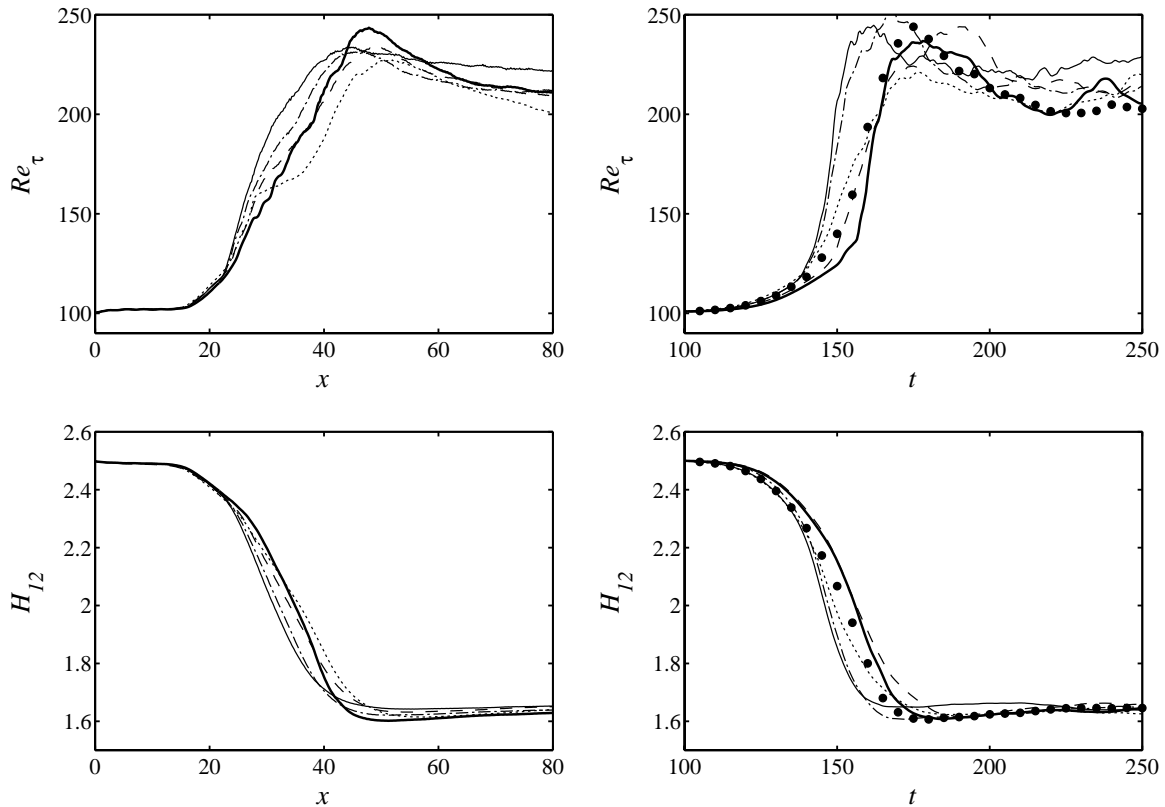
Figure 5.9: Evolution of Re_τ and H_{12} during the transitional phase computed on $512 \times 32 \times 33$ grid points in the spatial framework (left column, $\lambda_f = 40$) and in the temporal framework on $32 \times 32 \times 33$ grid points (right column). —— ADM-RT model with $\chi = 25$, ········ dynamic Smagorinsky model, – – – FSF model, –·– HPF-SF model, —— no-model LES, • temporal DNS (resolution $160 \times 160 \times 161$).

5.3.1   Transitional phase

In figure 5.9 the evolution of the Reynolds number based on the friction velocity and the channel half-width Re_τ and the shape factor H_{12} during transition from the slightly disturbed laminar flow to the turbulent state is shown for both the spatial and the temporal framework. The various spatial LES have been performed with a resolution of $512 \times 32 \times 33$ grid points, which corresponds to $32 \times 32 \times 33$ points for one period of the initial TS waves, similar to the temporal LES (Schlatter *et al.*, 2004c; Stolz *et al.*, 2004). It can be seen from the figure that all LES are able to predict transition to turbulence in both the temporal and spatial framework. Compared to the LES with an active SGS model and to the temporal DNS data, the no-model calculation undergoes transition

somewhat too early in both the temporal and the spatial simulations. At this resolution the no-model calculation is clearly underresolved, which can also be seen in visualisations of the instantaneous fields showing small wiggles in the velocities (see previous section and figure 5.8).

The qualitative behaviour of the different models is quite comparable between the temporal and spatial approach; *i.e.* the FSF model closely follows the no-model LES at lower x (earlier times in temporal LES), and during later stages it seems to be too dissipative. The same conclusion can be drawn for the dynamic Smagorinsky model, which however provides a more accurate description of the earlier transitional stages. It is interesting to note that in the spatial simulations the typical overshoot of Re_τ during transition is predicted only by the ADM-RT model with similar amplitude (approximately 15%) as in the temporal DNS and the corresponding temporal LES.

5.3.2   Transitional structures

Instantaneous streamwise velocity signals are displayed in figures 5.10 and 5.11 showing the typical low-velocity "spike" stages associated with the transitional breakdown (Nishioka *et al.*, 1975; Gilbert & Kleiser, 1990). From figure 5.10 it can be inferred that the one-spike stage is predicted accurately only by the ADM-RT model at the present low resolution. Both the no-model simulation and the data of the dynamic Smagorinsky model do not show this distinct early transitional stage at any time, which is associated with the appearance of the first hairpin vortex. However, by doubling the resolution to $1024 \times 64 \times 65$ grid points, the one-spike stage becomes also visible in the no-model computations (low-resolution DNS), nearly collapsing with the ADM-RT data (figure 5.10)

For the ADM-RT model, a sequence of velocity signals from the one-spike to the four-spike stage is shown in figure 5.11. Note that in this figure the velocity is shown as a function of the streamwise distance, in contrast to the time signal usually shown from experiments or temporal simulations (see also discussion below). All stages can be clearly identified and are qualitatively similar to those obtained by either temporal or spatial simulations at higher resolutions (see chapter 4 and Sandham & Kleiser (1992); Schlatter *et al.* (2004a)).

Visualisations of the instantaneous flow field by means of the negative-λ_2 vortex-identification criterion (Jeong & Hussain, 1995) are
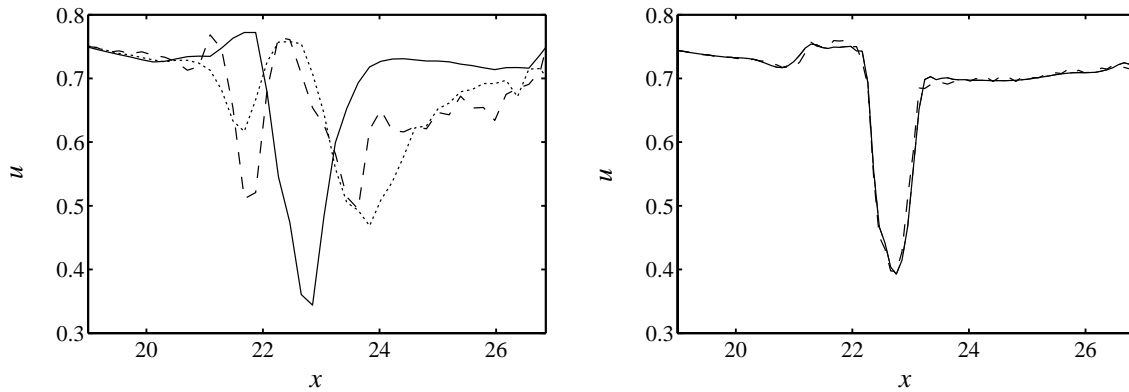
Figure 5.10: Streamwise velocity $\overline{u}$ for the one-spike stage at $z = -0.47$. Left: Resolution $512 \times 32 \times 33$, —— ADM-RT, ········ dynamic Smagorinsky model, ————no-model LES. Right: Resolution $1024 \times 64 \times 65$, ——high-resolution ADM-RT, ————no-model LES (low-resolution spatial DNS).

presented in figures 5.12–5.15 for different SGS models and resolutions. During the one-spike stage displayed in figure 5.12, only the ADM-RT model is able to predict the dominant single hairpin vortex (see also figure 5.10 and the corresponding discussion). At this time the no-model calculation already shows signs of (numerical) instability around the breakdown location ($x \approx 23$), which is also shown in figure 5.8.

At the two-spike stage (figure 5.13), for all models, the remainders (legs) of the Λ-vortices are visible at $x \approx 19$. The no-model data does not show the two typical hairpin vortices expected at this stage of development, and the flow field breaks down to turbulence too fast without the appearance of these distinct vortical structures. The data obtained with the ADM-RT model for both resolutions show the two distinct hairpin vortices with comparable downstream evolution of the structures and spreading of the turbulent region from the peak plane ($y = L_y/2$) towards the lateral boundaries of the domain. The dynamic Smagorinsky model also features some of these structures, however they are not as distinct as for the ADM-RT model. Especially further downstream ($x \approx 35$) the former model is too dissipative as indicated by an apparently coarser vortical structure present in the data. Note that with the chosen low LES resolution the spanwise extent of the hairpin vortex is resolved by approximately 5 grid points only.

The three-spike stage in figure 5.14 clearly shows the emergence of very fine structures for the high-resolution LES, which are naturally not resolved on the coarser LES grid. Similar to the visualisation at the
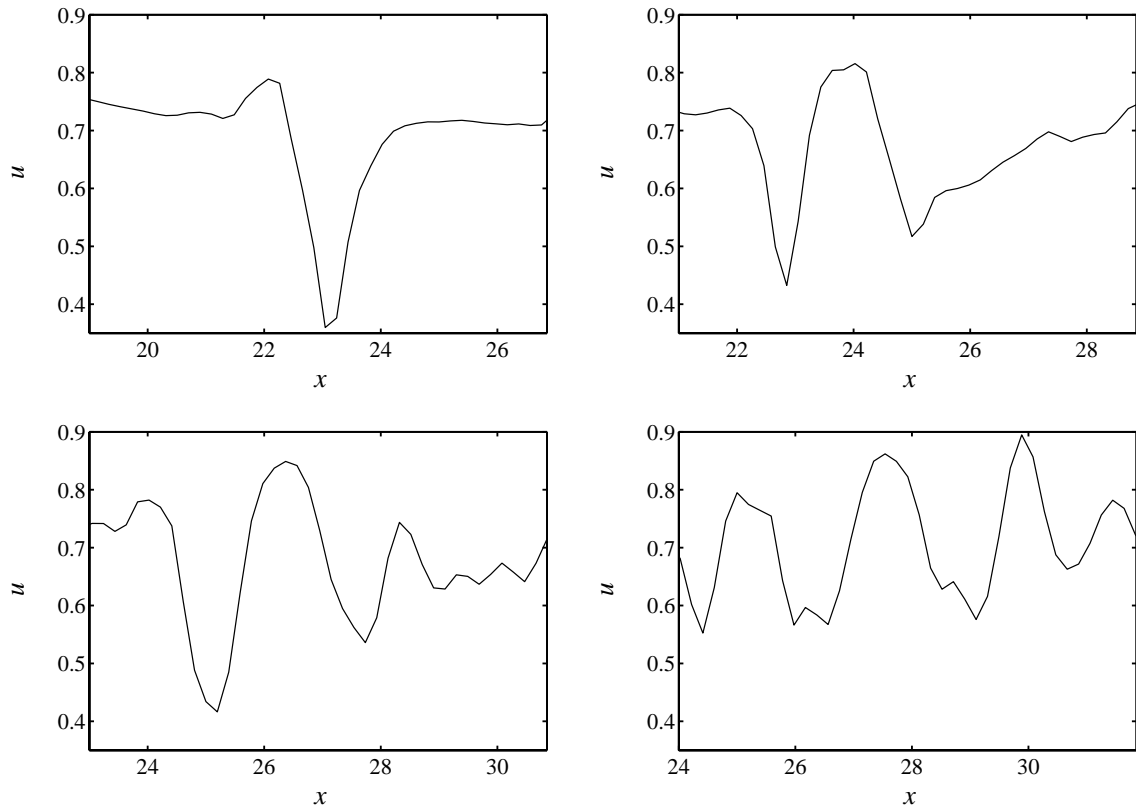
Figure 5.11: Streamwise velocity $\overline{u}$ for the various spike stages at $z = -0.47$ computed using ADM-RT on $512 \times 32 \times 33$ grid points. The streamwise extent of the plotted region corresponds approximately to the streamwise wavelength of the initial TS wave. From left *to* right *and* top *to* bottom*: one-spike stage, $t^* = 0$, two-spike stage, $t^* = 4$, three-spike stage, $t^* = 8$, four-spike stage, $t^* = 10$ (t^* relative time).*

four-spike stage (figure 5.15), the ADM-RT model is able to provide a detailed prediction of the vortical structures, whereas the data for the dynamic Smagorinsky seems to be less pronounced.

In figure 5.16 a comparison of the vortical structures between the temporal and the spatial simulation during the transitional breakdown is shown. For both cases, the data is obtained from LES using the ADM-RT model at resolution $32 \times 32 \times 33$ and $512 \times 32 \times 33$, respectively. The different stages of flow development of the temporal and spatial simulations which are compared have been chosen according to the appearance of spikes in the streamwise velocity signal, *i.e.* the times displayed in figures 4.29 and 5.11.

Up to the two-spike stage, a fairly close resemblance of the spatial

and temporal simulation results can be observed, *i.e.* the visual appearance of the vortical structures and their early transitional evolution is similar. However, during the three- and four-spike stages it is increasingly difficult to match the data between the two simulation methods, although both calculations feature the typical low-velocity spikes (figures 4.29 and 5.11) in the streamwise velocity signal which are closely connected to the roll-up of the shear layers into hairpin vortices.

This discrepancy in appearance is mainly caused by a different way of presenting the simulation data which was chosen for ease of data processing to alleviate manipulating the large amount of data. For the spatial simulation method the data is displayed at a fixed time t showing the evolution of the vortical structures in the streamwise direction x. The data of the temporal simulation, however, can be considered to be shown at a fixed streamwise location x displaying the (periodic) temporal evolution of the transitional structures (Kleiser & Zang, 1991). In order to obtain a closer comparison of the spatial and temporal simulations, the data should be shown for both methods at a fixed (physical) streamwise station, *i.e.* at a fixed x showing the evolution in time for the spatial simulation and at a fixed t for the temporal simulation (Alternatively, the results could also be compared at a fixed time t for the spatial simulation and a fixed location x for the temporal simulation data.). Note that the initial conditions for the spatial simulation were chosen to match a physical experiment (forced transition induced by *e.g.* a vibrating ribbon) by using the same temporal frequency ω_{TS} for the two-dimensional and the three-dimensional wave. In the temporal approach, on the other hand, the streamwise wavenumber α_{TS} was held constant for the two- and three-dimensional waves. It could be an interesting extension of the results presented in figure 5.16 to use the same initial conditions for both the spatial and temporal simulations and compare the data as detailed above.
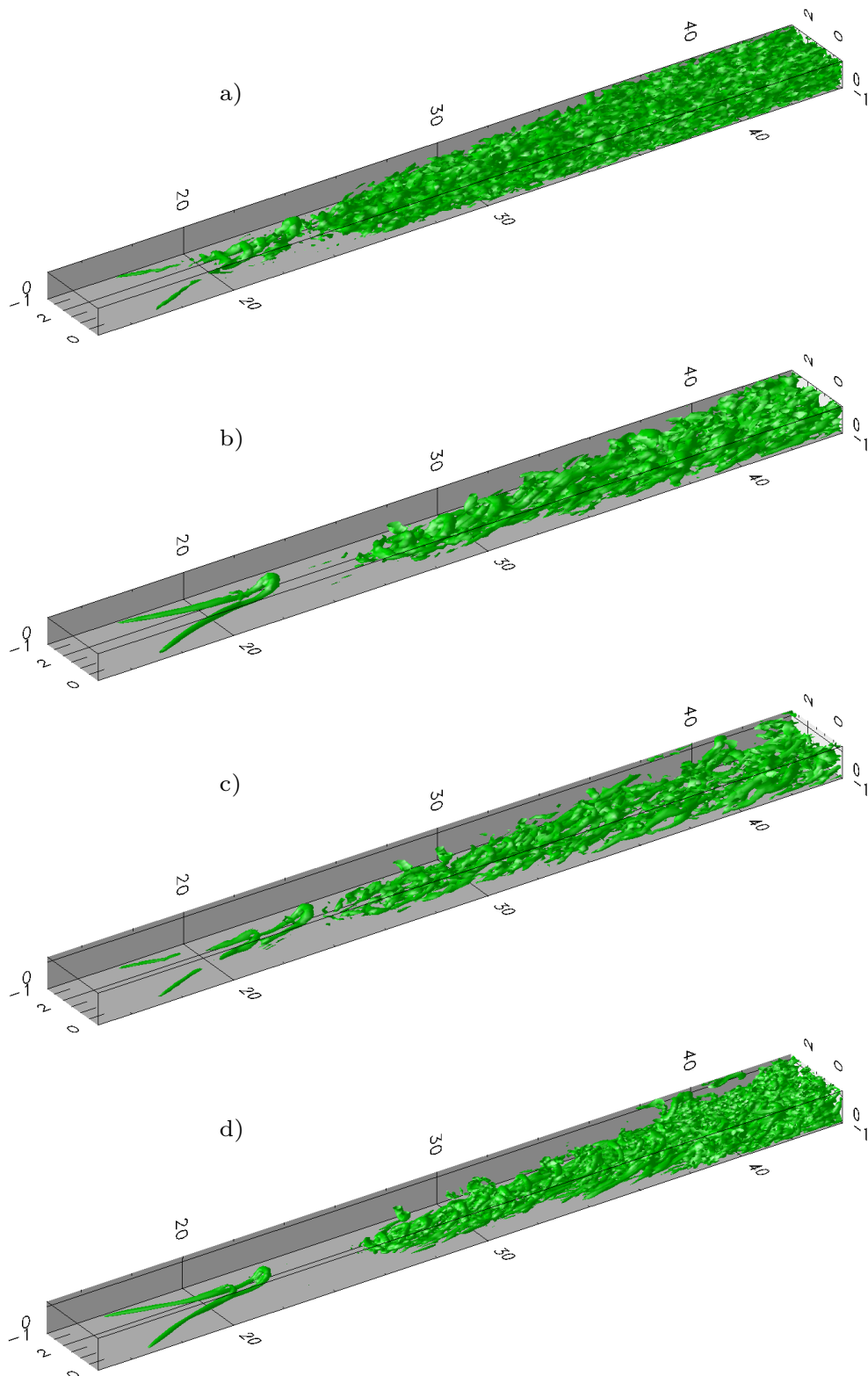
Figure 5.12: Visualisation of the instantaneous vortical structures at the one-spike stage at resolution $512 \times 32 \times 33$. (a) No-model LES, (b) ADM-RT model, (c) dynamic Smagorinsky model, (d) ADM-RT model on $1024 \times 64 \times 65$ grid (high-resolution LES).
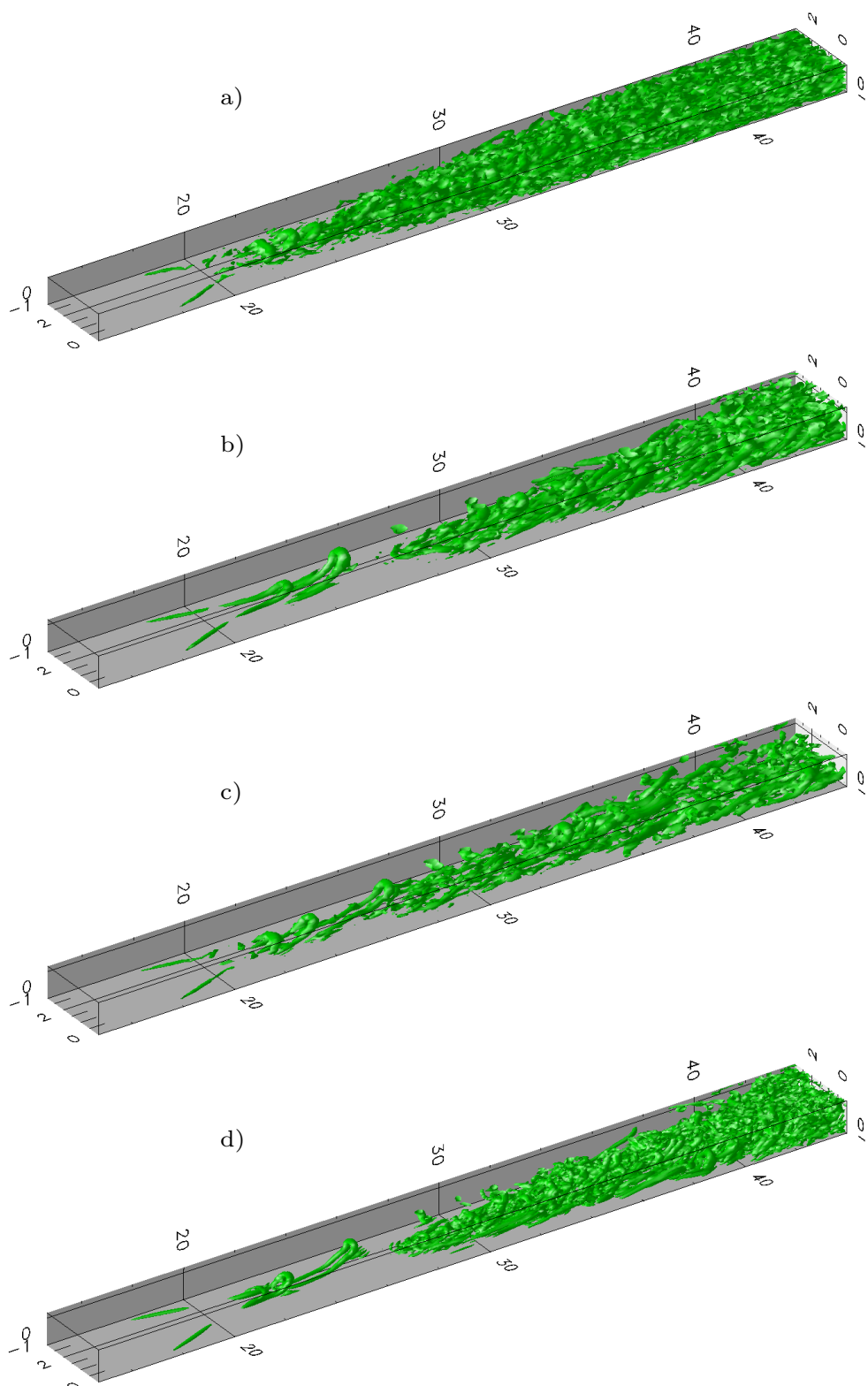
Figure 5.13: Visualisation of the instantaneous vortical structures at the two-spike stage at resolution $512 \times 32 \times 33$. (a) No-model LES, (b) ADM-RT model, (c) dynamic Smagorinsky model, (d) ADM-RT model on $1024 \times 64 \times 65$ grid (high-resolution LES).
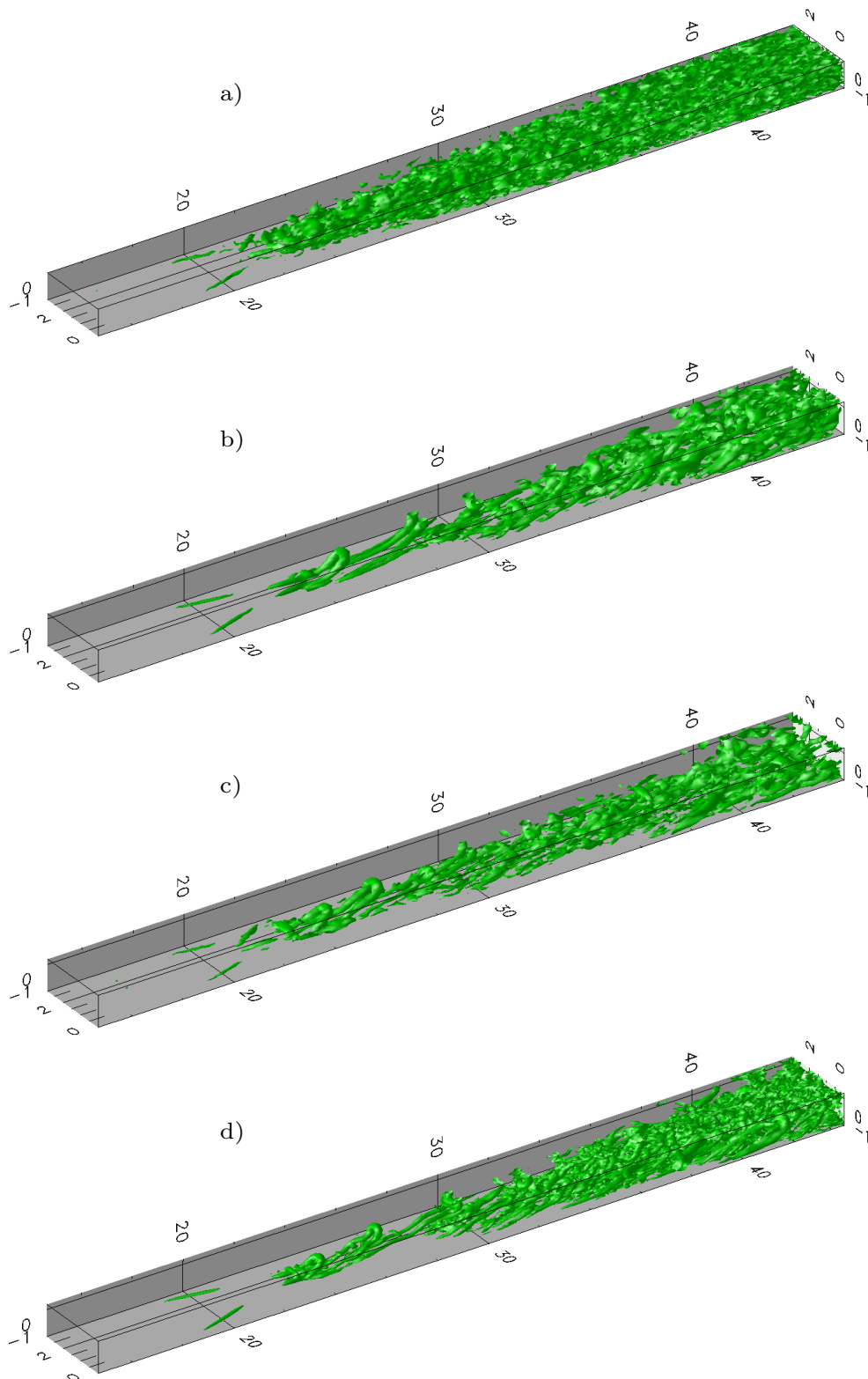
Figure 5.14: Visualisation of the instantaneous vortical structures at the three-spike stage at resolution $512 \times 32 \times 33$. (a) No-model LES, (b) ADM-RT model, (c) dynamic Smagorinsky model, (d) ADM-RT model on $1024 \times 64 \times 65$ grid (high-resolution LES).
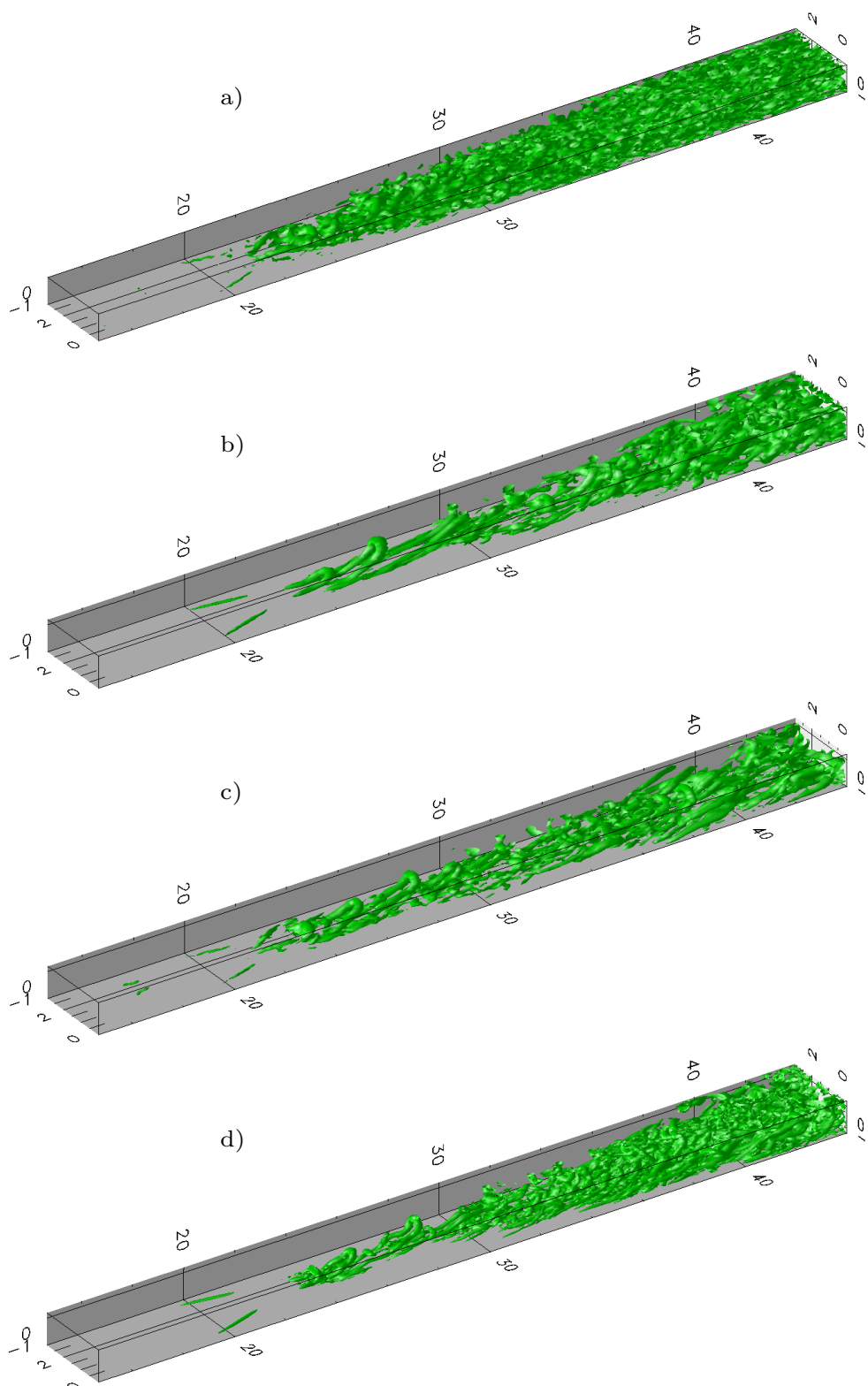
Figure 5.15: Visualisation of the instantaneous vortical structures at the four-spike stage at resolution $512 \times 32 \times 33$. (a) No-model LES, (b) ADM-RT model, (c) dynamic Smagorinsky model, (d) ADM-RT model on $1024 \times 64 \times 65$ grid (high-resolution LES).
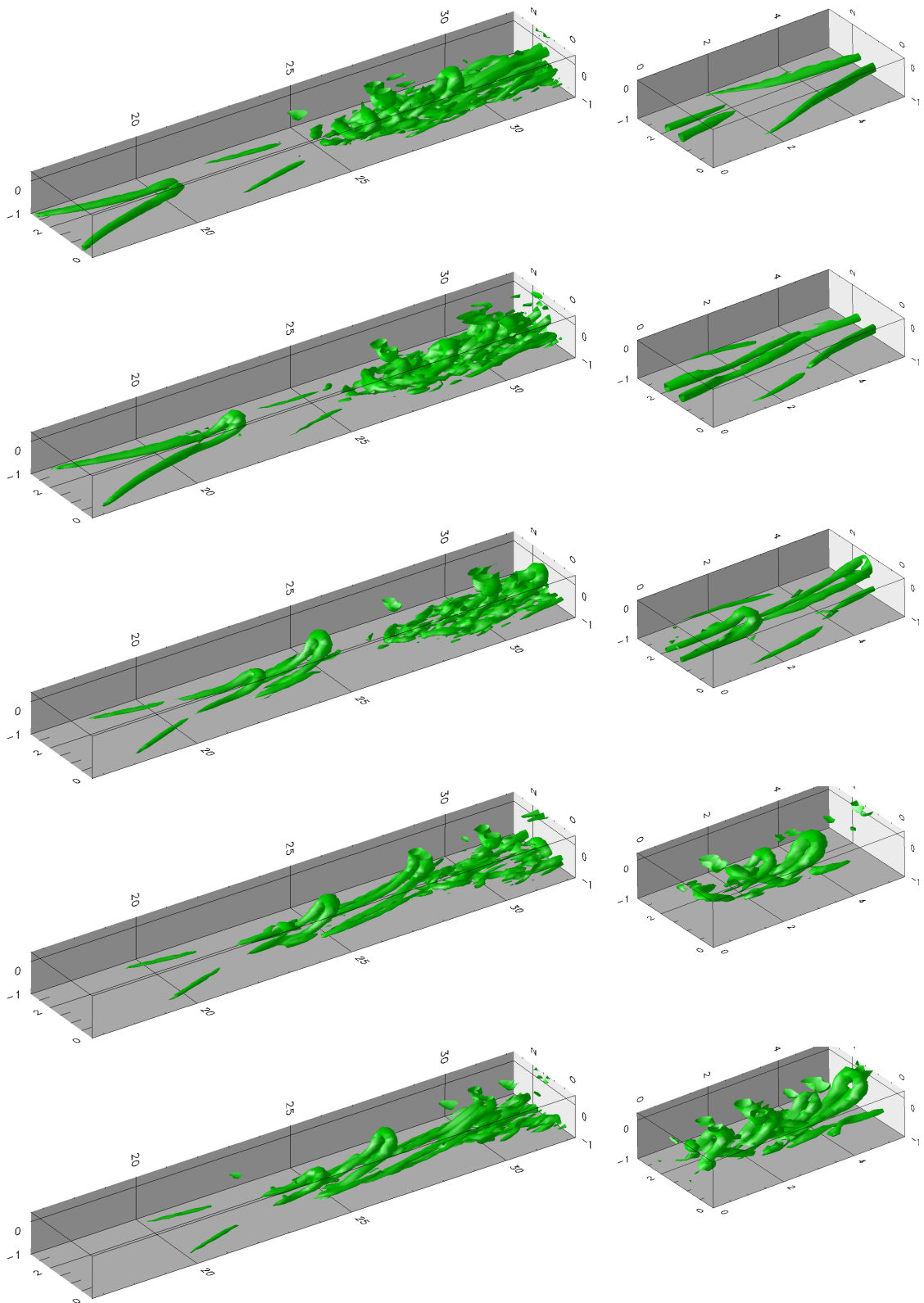
Figure 5.16: *Comparison of the transitional structures during transition for the spatial framework (*left column, *ADM-RT model on* $512 \times 32 \times 33$ *grid points) and the temporal framework (*right column, $32 \times 32 \times 33$ *grid points, ADM-RT model). From* top *to* bottom: *Zero-spike stage to four-spike stage.*

5.3.3   Turbulent channel flow

To confirm the accuracy of the LES in the turbulent phase, the spanwise and temporally averaged mean velocity profiles and Reynolds stresses are shown in figure 5.17 for the downstream position $x = 77$ close to the fringe region (which begins at $x = 80$). The temporal averaging was performed over at least 10 periods of the initial TS wave. As a reference, the corresponding data obtained from the temporal simulations are also shown. Although turbulence is not yet completely developed at that po-
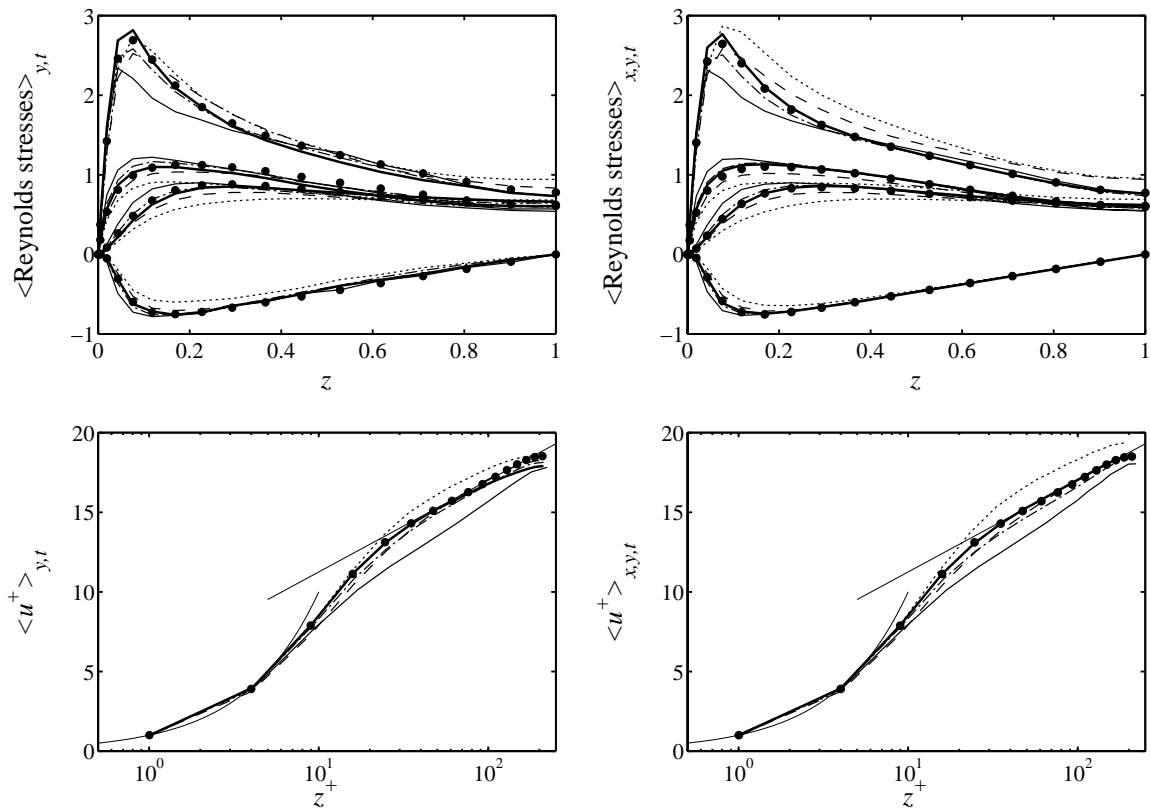
Figure 5.17: Averaged turbulent statistics: Reynolds stresses $\langle \overline{u}_1' \overline{u}_1' \rangle^{1/2}/u_\tau$, $\langle \overline{u}_2' \overline{u}_2' \rangle^{1/2}/u_\tau$, $\langle \overline{u}_3' \overline{u}_3' \rangle^{1/2}/u_\tau$, $\langle \overline{u}_1' \overline{u}_3' \rangle/u_\tau^2$ and the mean streamwise velocity profile $\langle \overline{u} \rangle^+$ in wall units computed on $512 \times 32 \times 33$ grid in the spatial framework (left column, $\lambda_f = 40$) and on $32 \times 32 \times 33$ grid in the temporal framework (right column). ——— ADM-RT model with $\chi = 25$, ········ dynamic Smagorinsky model, ———— FSF model, —·— HPF-SF model, ——— no-model LES, ● temporal DNS (resolution $160 \times 160 \times 161$).

sition, a close agreement between the temporal DNS and the ADM-RT model can be observed. Moreover, the same qualitative behaviour for the Reynolds stresses and the mean streamwise velocity profile can be estab-

lished for the various LES data obtained from the spatial and temporal simulations (Stolz *et al.*, 2004; Schlatter *et al.*, 2004*c*). This conclusion can also been drawn from the discussion of figure 5.9.

Chapter 6

Homogeneous isotropic turbulence

In general, an SGS model needs to compensate for the lack of energy transfer across the numerical cutoff frequency. Although the benefits of the high-pass filtering approach detailed in the previous section lie mainly in the treatment of wall-bounded flows (viscous sublayer) and for laminar-turbulent transition (filtering out mean shear), it is nevertheless important for any SGS model to correctly predict the SGS dissipation in the context of isotropic turbulence. It will therefore be shown in this section that the HPF models are equally well applicable for simulations of homogeneous isotropic turbulence, see also Schlatter *et al.* (2005*c*). Simulation results using the ADM-RT model are also provided.

6.1 Numerical method and initial conditions

The simulations of homogeneous isotropic turbulence (HIT) are performed in Fourier space on a periodic cubic domain with dimensions $L^3 = (2\pi)^3$ by a standard pseudospectral method solving the incompressible LES equations (2.5) (see *e.g.* Canuto *et al.* (1988)). The domain is discretised equidistantly with N grid points in each direction x_j. N is assumed to be even. The approximation of the velocities is thus given by

$$\overline{u}_i(x_1, x_2, x_3, t) = \sum_{k_1}\sum_{k_2}\sum_{k_3}\hat{\overline{u}}_i(k_1, k_2, k_3, t)e^{i(k_1 x_1 + k_2 x_2 + k_3 x_3)} , \quad (6.1)$$

with the spectral velocity $\hat{\overline{u}}_i$, the imaginary unit $i = \sqrt{-1}$, and the integer wavenumbers

$$k_j = -N/2 + 1, \ldots, N/2 - 1 . \quad (6.2)$$

Dealiasing using the 3/2-rule (see Canuto *et al.* (1988)) is applied in all spatial directions for the computation of the nonlinear convection terms. No dealiasing was employed for the SGS model terms. The odd-ball modes $|k_i| = N/2$, $i = 1, 2, 3$ arising from the use of even-numbered fast Fourier transforms (FFT) routines are explicitly set to

zero. Time advancement is achieved by an explicit third-order Runge-Kutta method (Williamson, 1980) for both the convective and viscous terms. The divergence-free condition is fulfilled exactly by a pressure projection.

Nearly 95% of the computer time is spent to evaluate the FFT. As in the channel flow simulation code described in chapter 3, the efficient FFTW library has been adopted (Frigo & Johnson, 1999) on scalar machines including the IBM SP-4 and Linux PCs. The calculations on vector computers were done using the FFT library by Temperton (1983, 1985). The FFT part of the code is parallelised by inserting OpenMP compiler directives (Dagum & Menon, 1998; Chandra *et al.*, 2001). On a single processor a maximum performance of 3.3 GFlops was obtained ($N = 120$) on the NEC SX-5 located at the Swiss National Supercomputing Centre (CSCS) in Manno (peak performance 8 GFlops). In parallel mode a sustained speed-up of 5.3 on 6 processors was reached with fixed problem size.

The simulations are started from a generic three-dimensional spectrum $E_0(k)$ with random phases for the Fourier coefficients (Chasnov, 1991),

$$E_0(k) \propto k^4 e^{-2(k/k_p)^2} \; , \tag{6.3}$$

with $k_p = 4$, normalised to unit kinetic energy. In order to obtain statistically stationary turbulence, a forcing of the flow is implemented by freezing the Fourier modes within the innermost spectral shells $|\mathbf{k}| < 2$. The turbulence is first allowed to decay until the forcing is started at $t = 0.5$. Although this forcing inhibits all dynamics at low wavenumbers, the results show that at higher wavenumbers homogeneous turbulence is generated.

6.2   Parameter settings

The SGS models have been implemented into the simulation code with the SGS model terms being computed without dealiasing procedure. For all the results, the high-pass filter $\hat{H}_0 = 1 - \hat{G}$ given by equations (2.12) and (2.10) with $\omega_c = 2\pi/3$ has been used. The transfer function of $\hat{H}_0$ is shown in figure 2.2. The model coefficients used for the simulations of isotropic turbulence are given in table 6.1. Compared to channel flow, the values had to be increased by a factor of approximately 3 for the structure-function-based models and by $\sqrt{3}$ for the Smagorinsky-based

Table 6.1: Parameters for LES of forced high Reynolds number homogeneous isotropic turbulence, $Re = 4 \cdot 10^5$, $Re_\lambda \approx 1100$, grid resolution of $N^3 = 32^3$. Data averaged from $t = 30$ to $t = 60$.

Case	Model	Re_λ	$10^4 \cdot \eta$	C, C_S
———	HPF-Smag.	1106	2.40	0.17
- - - -	HPF-SF	1129	2.42	0.13
———	Smag.	1180	2.56	0.12
········	SF	1138	2.53	0.05
—·—	FSF	1094	2.55	0.10
	ADM-RT	1044	2.38	0.75

Case	Model	$10^2 \cdot TKE$	$10^6 \cdot \varepsilon_{\mathrm{visc}}$	$\varepsilon_{\mathrm{SGS}}/\varepsilon_{\mathrm{visc}}$
———	HPF-Smag.	4.66	12.5	377
- - - -	HPF-SF	4.65	11.9	380
———	Smag.	4.37	9.08	402
········	SF	4.29	9.95	379
—·—	FSF	4.09	9.68	383
	ADM-RT	4.48	14.0	349

models. This is consistent with previous investigations of the classical models, see *e.g.* Lesieur & Métais (1996).

The energy spectrum is defined as

$$E(k) = 4\pi k^2 \left\langle \frac{1}{2}\hat{\bar{u}}_i(\mathbf{k})\hat{\bar{u}}_i^*(\mathbf{k}) \right\rangle_{\mathrm{shell}} , \qquad (6.4)$$

with the averaging performed over all modes in the spectral shell

$$k - \frac{1}{2} \le |\mathbf{k}| < k + \frac{1}{2}$$

of thickness $\Delta k = 1$. Additionally, all data has been averaged in time from $t = 30$ to $t = 60$ after statistically stationary conditions of forced isotropic turbulence have been reached. The total turbulent kinetic energy is thus given by

$$TKE = \int_0^{k_{\max}} E(k)\mathrm{d}k = \int_0^{k_{\max}} 4\pi k^2 \left\langle \frac{1}{2}\hat{\bar{u}}_i(\mathbf{k})\hat{\bar{u}}_i^*(\mathbf{k}) \right\rangle_{\mathrm{shell}} \mathrm{d}k . \qquad (6.5)$$

Table 6.2: Parameters for LES of forced high Reynolds number homogeneous isotropic turbulence, $N^3 = 32^3$.

Case	Re	Re_λ (approx.)
$\triangledown$	500	50
$\triangle$	10^4	200
$\square$	$4 \cdot 10^5$	1100
$\diamondsuit$	10^7	5500
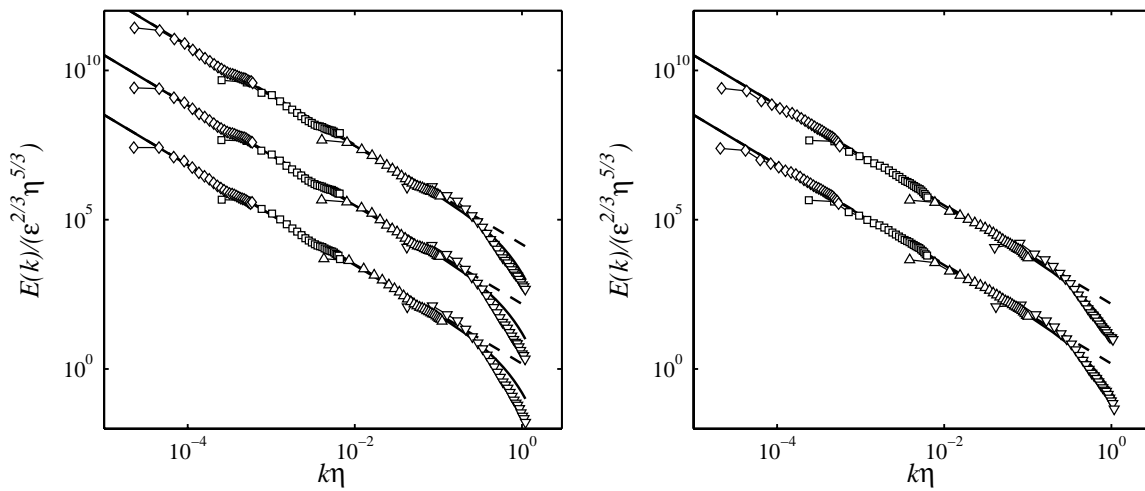
Figure 6.1: Normalised energy spectra of forced homogeneous isotropic turbulence for the different SGS models, at the Reynolds numbers of table 6.2. Left: Classical eddy-viscosity models: Smagorinsky model, SF model ($\times 10^2$), FSF model ($\times 10^4$). Right: HPF eddy-viscosity models. HPF Smagorinsky model, HPF-SF model ($\times 10^2$). ———— Pao spectrum (Pao, 1965), - - - - $C_K(k\eta)^{-5/3}$ ($C_K = 1.5$). Symbols see table 6.2.

The upper bound of the integral is $k_{\max} = \sqrt{3(N/2 - 1)^2}$, *i.e.* the diagonal of the cube with edge length $N/2 - 1$.

6.3   Results

In figure 6.1, normalised energy spectra obtained using the different SGS models for a range of Reynolds numbers are shown (parameters see table 6.2). The results are compared to the analytical spectrum of high-

Reynolds number turbulence (Pao, 1965)

$$E(k)/(\varepsilon Re^{-5})^{1/4} = C_K(k\eta)^{-5/3}\exp\left[-1.5C_K(k\eta)^{4/3}\right], \qquad (6.6)$$

where $\eta = (Re^3\varepsilon)^{-1/4}$ denotes the Kolmogorov length and C_K the Kolmogorov constant.

The dissipation $\varepsilon = \varepsilon_{\mathrm{visc}} + \varepsilon_{\mathrm{SGS}}$ can be decomposed into two components, *i.e.* the viscous dissipation,

$$\varepsilon_{\mathrm{visc}} = \int_0^{k_{\max}} \mathcal{E}_{\mathrm{visc}}(k)\mathrm{d}k = -\int_0^{k_{\max}} \frac{2}{Re}k^2 E(k)\mathrm{d}k, \qquad (6.7)$$

and the dissipation resulting from the SGS model,

$$\varepsilon_{\mathrm{SGS}} = \int_0^{k_{\max}} \mathcal{E}_{\mathrm{SGS}}(k)\mathrm{d}k \qquad (6.8)$$

$$= -\int_0^{k_{\max}} 4\pi k^2 \left\langle \frac{1}{2}\left(\hat{\bar{u}}_i^* \mathrm{i}k_j\hat{\tau}_{ij} + \hat{\bar{u}}_i(\mathrm{i}k_j\hat{\tau}_{ij})^*\right)\right\rangle_{\mathrm{shell}} \mathrm{d}k. \qquad (6.9)$$

It can be seen from figure 6.1 that the prediction of all LES for the normalised spectra is very close to the analytical reference, equation (6.6). For the case with the lowest Reynolds number $Re_\lambda \approx 50$, it can be inferred from the figure that the classical eddy-viscosity models are slightly too dissipative, which is due to an unphysically large SGS dissipation. It should be noted that for the highest Reynolds number $Re_\lambda \approx 5500$ the ratio $\varepsilon_{\mathrm{visc}}/\varepsilon_{\mathrm{SGS}}$ is approximately 10^{-4}, which can be considered to be close to the inviscid limit.

In figure 6.2 the energy spectra $E(k)$ and the dissipation spectra $\mathcal{E}_{\mathrm{visc}}(k)$ and $\mathcal{E}_{\mathrm{SGS}}(k)$ are depicted for $Re_\lambda \approx 1100$, see also table 6.1. The viscous dissipation follows the $k^{1/3}$ law according to equation (6.7) for all models considered. Similarly, the spectral slope of the subgrid-scale dissipation for the classical eddy-viscosity models is 1/3, which is due to the second-order derivatives involved in the computation of $\partial\tau_{ij}/\partial x_j$. On the other hand, $\mathcal{E}_{\mathrm{SGS}}(k)$ for the HPF models is significantly lower at small wavenumbers ($k\eta < 10^{-3}$) and rises approximately as $k^{3.5}$ for higher k. $\mathcal{E}_{SGS}$ saturates for $k\eta > 6\cdot 10^{-3}$. This behaviour is typical for the HPF models, as the large-scale fluctuations are filtered out prior to the calculation of the SGS terms. The strong rise of $\mathcal{E}_{\mathrm{SGS}}(k)$, similar to a hyperviscosity, is closely related to the filter transfer function $\hat{H}_0(\omega)$. The saturation of the SGS dissipation near $k_{\max}$ is caused by the slightly
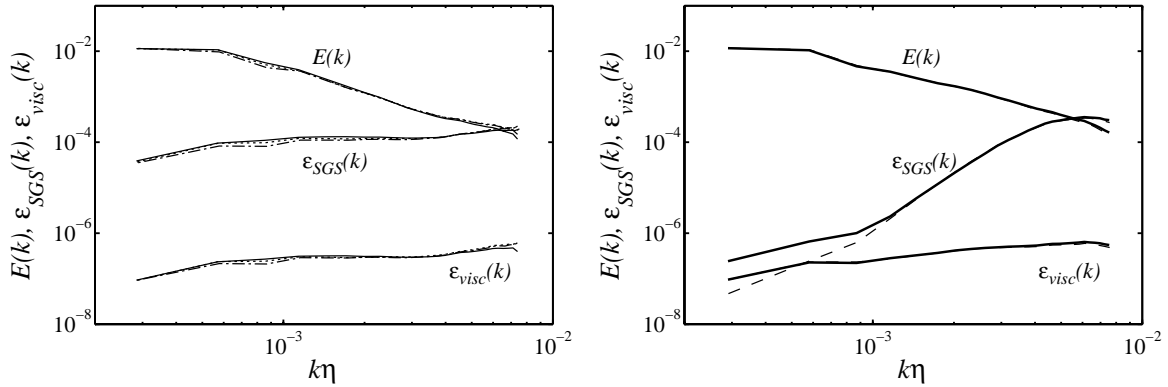
Figure 6.2: Energy and dissipation spectra for forced homogeneous isotropic turbulence ($Re_\lambda \approx 1100$, $N^3 = 32^3$) for the different SGS models. Left: *Classical eddy-viscosity models:* ———$Smagorinsky$ $model$, ········ SF $model$, —·—FSF $model$. Right: *HPF eddy-viscosity models.* ———HPF $Smagorinsky$ $model$, ----HPF-SF $model$ (see also table 6.1).

Figure 6.3: Compensated energy spectra $\varepsilon^{-2/3}k^{5/3}E(k) \approx C_K$ for forced homogeneous isotropic turbulence ($Re_\lambda \approx 1100$) for the different SGS models. ———HPF $Smagorinsky$ $model$, ----HPF-SF $model$, ———$Smagorinsky$ $model$ ········ SF $model$, —·—FSF $model$. Left: $N^3 = 32^3$, $k_{\max} = 26$ (see also table 6.1). Right: $N^3 = 120^3$, $k_{\max} = 102$, only the ———HPF $Smagorinsky$ $model$ and the ———$Smagorinsky$ $model$ are $shown$.

anisotropic three-dimensional filter evaluated as a tensor product of one-dimensional filters, equation (2.16).

Averaged compensated three-dimensional energy spectra $\varepsilon^{-2/3}k^{5/3}E(k) \approx C_K$ for the different SGS models are shown in figure 6.3 for two resolutions at $Re_\lambda \approx 1100$. Note that the slight kinks in the curves at $k \approx N/2$ and $k \approx \sqrt{2(N/2)^2}$ are artefacts due

Figure 6.4: Compensated energy spectra $\varepsilon^{-2/3}k^{5/3}E(k) \approx C_K$ for forced homogeneous isotropic turbulence ($Re_\lambda \approx 1100$), $N^3 = 32^3$. Left: Smagorinsky model, ——$C_S = 0.12$, - - - -$C_S = 0.096$, ········ $C_S = 0.144$. Right: HPF Smagorinsky model, ——$C_S = 0.17$, - - - -$C_S = 0.136$, ········ $C_S = 0.204$.

to the discrete wavenumber population according to the definition of the energy spectrum, equation (6.4). Qualitatively, the results for the classical eddy-viscosity models compare well with the compensated spectra shown in Lesieur & Métais (1996). An average value for the Kolmogorov constant $C_K \approx 1.4$ can be inferred, which is slightly less than the value given in recent publications, *e.g.* the high-resolution DNS of Kaneda *et al.* (2003). The HPF models, however, indicate a value of $C_K \approx 1.5 - 1.6$ with a flat spectrum, see also Schlatter *et al.* (2004b).

The sensitivity of the classical and the HPF Smagorinsky model to the choice of the (constant) Smagorinsky coefficient C_S, which has been varied by $\pm 20\%$, is displayed in figure 6.4. A higher C_S value results in increased dissipation and, consequently, in lower values for $\varepsilon^{-2/3}k^{5/3}E(k) \approx C_K$ near the numerical cutoff. Conversely, a lower model coefficient increases the slope of the compensated spectrum. Figure 6.4 also suggests a slightly decreased sensitivity to the model coefficient for the HPF Smagorinsky model.

Figure 6.5 presents results obtained using the ADM-RT model (see equation (2.51) in section 2.2.3) compared to data obtained by the HPF eddy-viscosity models (see figures 6.2 and 6.3). For ADM-RT a cutoff wavenumber for the filter G of $\omega_c = 2\pi/3$ was chosen together with $N = 5$, see equation (2.12). The fixed model coefficient was set to $\chi = 0.75$. The energy spectrum $E(k)$ and the dissipation spectrum $\mathcal{E}_{\text{visc}}(k)$ is similar for both the HPF models and ADM-RT. The com-
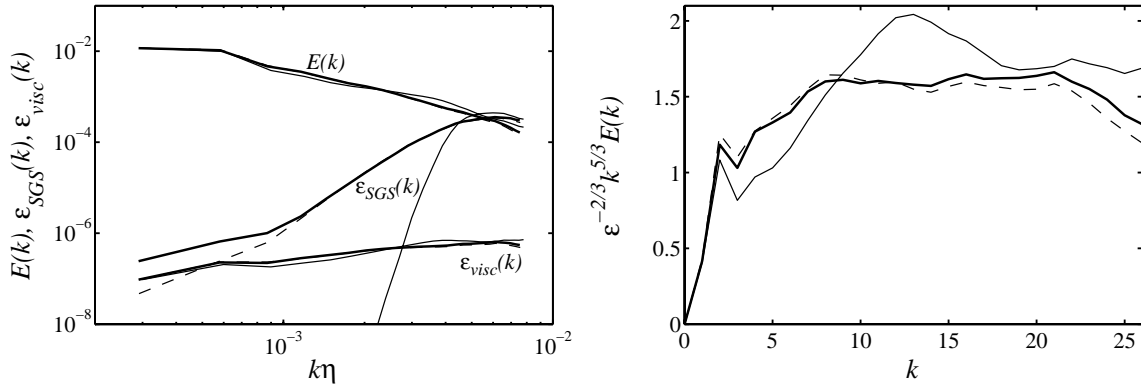
Figure 6.5: Results for forced homogeneous isotropic turbulence ($Re_\lambda \approx 1100$, $N^3 = 32^3$). Left: Energy and dissipation spectra. Right: Compensated energy spectra $\varepsilon^{-2/3}k^{5/3}E(k) \approx C_K$. ——— HPF Smagorinsky model, - - - - HPF-SF model, ——— ADM-RT model, $\chi = 0.75$ (see also table 6.1).

pensated energy spectrum $\varepsilon^{-2/3}k^{5/3}E(k) \approx C_K$ shows a plateau at $C_K \approx 1.7$, however not as flat as for the HPF models. Considering the SGS dissipation spectrum $\mathcal{E}_{\text{SGS}}(k)$ the model influence of the ADM-RT model is clearly visible. The relaxation term, which is based on the high-order high-pass filter H_N (equation (2.12)), acts only on the small-scale content of the velocity field. The SGS-dissipation is therefore vanishing for small wavenumbers, whereas a strong rise for higher wavenumbers is visible. The increase of $\mathcal{E}_{\text{SGS}}(k)$ is more pronounced than for the HPF models since for the relaxation term the filter H_5 has been applied as opposed to H_0 used for the HPF models. Note also the formal similarity of the ADM-RT and HPF models discussed in section 4.7.3.

In homogeneous isotropic turbulence, it is possible to further restrict the spectral range of wavenumbers to the sphere $|\mathbf{k}| \leq N/2 - 1$ ("spherical truncation") in order to improve the isotropy of the solution. In the present contribution, the whole range of wavenumbers $-(N/2 - 1) < k_i < N/2 - 1$ ("cubical truncation") was retained. Additionally, similar to the channel flow case the three-dimensional filter has been defined by a tensor product of one-dimensional operators, equation (2.16)

$$H_0 * \overline{u} = \overline{u} - G * \overline{u} = \overline{u} - G_1 * G_2 * G_3 * \overline{u} \,,$$

with G_i being the one-dimensional low-pass filter in the direction x_i. This evaluation of the filter results in a slightly anisotropic three-dimensional filter, mainly close to the numerical cutoff. However, tests
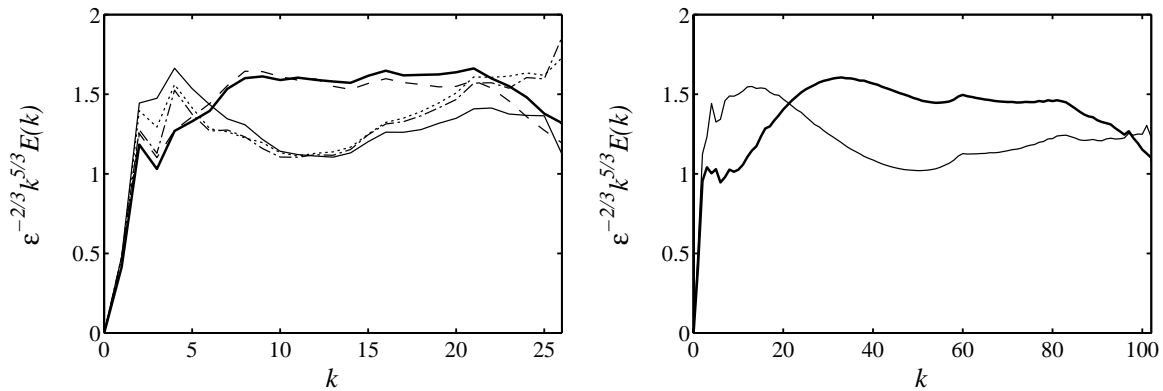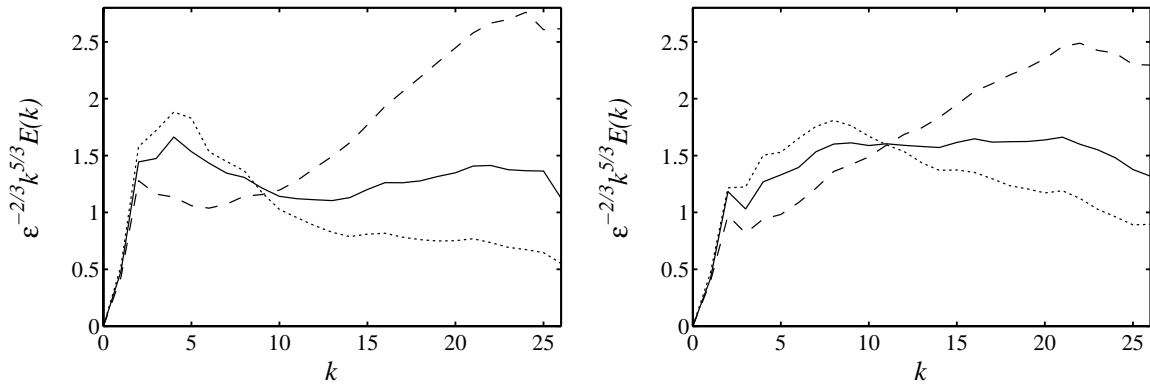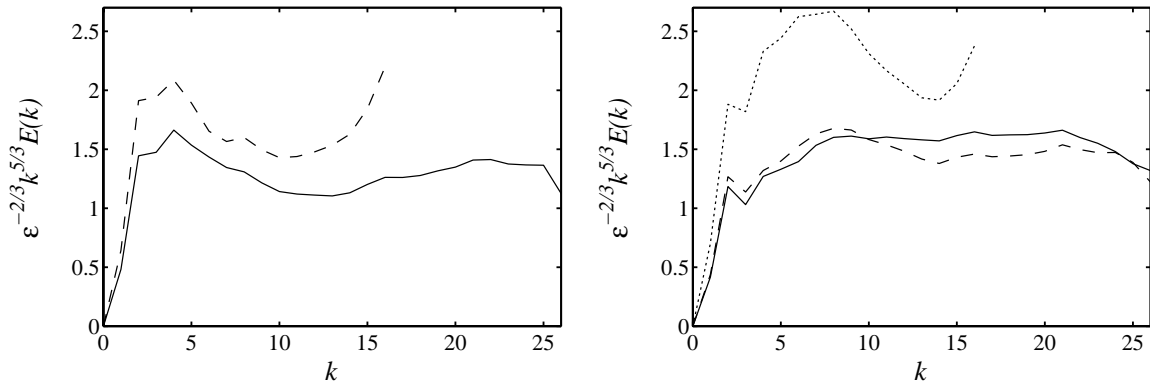
Figure 6.6: Compensated energy spectra $\varepsilon^{-2/3}k^{5/3}E(k) \approx C_K$ for forced homogeneous isotropic turbulence ($Re_\lambda \approx 1100$), $N^3 = 32^3$. Left: Smagorinsky model, —— cubical truncation, $C_S = 0.12$, ----spherical truncation, $C_S = 0.14$. Right: HPF Smagorinsky model, —— cubical truncation with non-isotropic filter eq. (2.16), $C_S = 0.17$, ----cubical truncation with isotropic filter eq. (6.10), $C_S = 0.16$, ⋯⋯ spherical truncation with isotropic filter eq. (6.10), $C_S = 0.23$.

have been performed using the above-mentioned spherical truncation together with the isotropic formulation of the filter

$$H(\mathbf{k}) = I - G(|\mathbf{k}|) \ . \tag{6.10}$$

Data obtained with these modifications are presented in figure 6.6. The results suggest that the respective model coefficients for both the classical and the HPF Smagorinsky model have to be increased by approximately 20-30% to account for the lower SGS energy transfer due to the reduced number of computational modes. Moreover, the compensated spectra shown in figure 6.6 using the spherical truncation are clearly not as flat as the respective spectrum using the cubical wavenumber space and, additionally, indicate a higher value for C_K. Additional calculations with higher resolution indicate that this result is not an artefact of the reduced number of computational modes.

Also shown in figure 6.6 are results of LES calculations using the HPF Smagorinsky model applying the isotropic version of the filter, equation (6.10). The results are similar to those obtained with the non-isotropic filter arising from the tensor product, equation (2.16), however with a slightly adapted model constant due to an effectively smaller ω_c.

To conclude, the results for forced isotropic turbulence presented in this section have shown that the high-pass filtered eddy-viscosity models

and the ADM-RT model work well for this basic flow type. An analysis of homogeneous isotropic turbulence using the approximate deconvolution model (ADM) has been presented in Müller *et al.* (2002), and using SGS models based on relaxation regularisation in Müller *et al.* (2004).

Chapter 7

Summary and conclusions

Flows undergoing transition to turbulence are of great practical importance. The ability to accurately simulate transitional flows using large-eddy simulation (LES) is a key problem that has to be solved before LES can routinely be applied in practical industrial applications. LES of transitional flows has become an active field of research only recently. Compared to studies of fully turbulent flows, there are only relatively few detailed LES results available by now for transitional flows (see also section 1.3.2). This thesis aims at further contributing to the development of appropriate subgrid-scale (SGS) modelling approaches suitable for large-eddy simulations of transitional and turbulent shear flows. An overview of the work is presented in section 7.1, the main conclusions are summarised in section 7.2. An outlook is given and open questions are discussed in section 7.3.

7.1 Summary

In the present work, results obtained by large-eddy simulation of transitional and turbulent incompressible channel flow and homogeneous isotropic turbulence are presented. The simulations have been performed using spectral methods in which numerical errors due to differentiation and aliasing are small. For the transition computations, both the temporal and the spatial simulation approach have been considered. Various classical and newly devised subgrid-scale models have been implemented and evaluated, including the approximate deconvolution model (ADM) (Stolz & Adams, 1999), the relaxation-term model (ADM-RT) (Stolz & Adams, 2003; Schlatter *et al.*, 2004*c*), and the new class of high-pass filtered (HPF) eddy-viscosity models (Stolz *et al.*, 2004; Schlatter *et al.*, 2005*c*).

As appropriate, comparisons to standard SGS models like the classical Smagorinsky model (Smagorinsky, 1963), the dynamic Smagorinsky model (Germano *et al.*, 1991) and the (filtered) structure-function model (Métais & Lesieur, 1992; Ducros *et al.*, 1996) have been made. For the dynamic Smagorinsky model and the filtered structure-function model, different definitions of the respective filters have been tested. Where

possible, high-resolution direct numerical simulations (DNS) have been performed to allow a detailed assessment of the performance of the respective LES. Moreover, no-model LES (*i.e.* coarse-grid DNS using the LES resolution) are provided for reference. Comparisons are made for turbulent statistics such as Reynolds stresses, mean velocity profiles, spectra, and energy budgets including the SGS model terms. As appropriate, resolution studies are performed to show the convergence of the LES towards the DNS results. Furthermore, visualisations of three-dimensional instantaneous transitional flow structures have been generated and analysed. A qualitative comparison of the various SGS models examined in this work is presented in figure 4.9.

In order to facilitate the use of deliberately chosen coarse LES grids, the standard ADM methodology has been adapted. This was necessary due to the observed destabilising properties of the deconvolution operation on such coarse grids in the wall-normal direction. In addition to the original ADM algorithm, new variants have been examined, in particular the SGS model based on a direct relaxation regularisation of the velocities (ADM-RT model) which uses a three-dimensional high-pass filtering of the computational quantities. This model is related to the spectral vanishing viscosity (SVV) approach by Tadmor (1989) and Karamanos & Karniadakis (2000).

A further study exploring various procedures for the dynamic determination of the relaxation parameter χ has been presented. The appropriate definition of the relaxation term causes the model contributions to vanish during the initial stage of transition and, approximately, in the viscous sublayer of wall turbulence. Moreover, the influence of aliasing errors on the LES results obtained with the ADM and ADM-RT models has been assessed.

The new high-pass filtered (HPF) eddy-viscosity models have been applied to incompressible forced homogeneous isotropic turbulence with microscale Reynolds numbers Re_λ up to 5500 and to fully turbulent channel flow at moderate Reynolds numbers $Re_\tau \approx 590$. The application of the HPF models to transitional channel flow was presented in Stolz *et al.* (2004, 2005). These models have been proposed independently in Vreman (2003) and Stolz *et al.* (2004), and are related to the variational multiscale method (Hughes *et al.*, 2000). Various high-pass filters with different cutoff wavenumbers have been considered.

The different SGS models have been tested in both the temporal and the spatial transition simulation approach. For the spatial simulations,

the fringe method has been used to obtain non-periodic flow solutions in the spatially evolving streamwise direction while employing periodic spectral discretisation. The combined effect of the fringe forcing and the SGS model has also been examined.

Additionally, a new inflow/outflow boundary treatment procedure has been described. The "windowing method" is based on a windowing of the computational variables to prescribe non-periodic inflow and outflow boundary conditions for numerical discretisations that rely on periodic spatial boundary conditions. Due to this periodicity, *e.g.* efficient and accurate Fourier discretisation schemes can be employed. Comparisons to the established fringe region technique have been given.

The computer codes used for the simulations presented in this thesis have all been parallelised explicitly based on the shared-memory approach. The codes have been optimised for modern vector and (super-)scalar computer architectures, running on different machines from desktop Linux PCs to the NEC SX-5 supercomputer.

7.2   Conclusions

The results obtained for transitional channel flow using the various SGS models show that it is possible to accurately simulate transition using LES on relatively coarse grids. In particular, the ADM-RT model, the dynamic Smagorinsky model, the filtered structure-function model and the different HPF models as well as the no-model LES were able to predict the laminar-turbulent changeover on the canonical case of incompressible channel-flow transition. For standard ADM, a slightly increased resolution in the wall-normal direction had to be employed, which is mainly attributed to reduced actual resolution due to the explicit filtering and the deconvolution operation. However, distinct differences in the performance of the various examined models concerning an accurate prediction of *e.g.* the transition location and the characteristic transitional flow structures could be observed.

During the early stages of K-type transition, the results of no-model LES calculations on coarse LES grids, which have sufficient resolution at that stage of flow development, are recovered by all considered models (except of course for the classical Smagorinsky and the structure-function model which both relaminarise the flow). This confirms that the SGS models are virtually inactive there, as they should. During the rapid mean-flow development, the model contributions begin to provide

additional dissipation. Since those initial stages of breakdown involve the formation of strong shear layers mostly in the wall-normal direction, SGS models that are defined three-dimensionally generally perform better than their two-dimensional counterparts. For three-dimensional models a coarser resolution in the wall-normal direction can therefore be chosen.

By examining instantaneous flow fields from LES of channel flow transition, distinct differences between the SGS models could be established. The dynamic Smagorinsky model fails to correctly predict the first stages of breakdown involving the formation of typical hairpin vortices on the coarse LES grid. The no-model calculation, as expected, is generally too noisy during the turbulent breakdown preventing the identification of transitional structures. In the case of spatial transition, the underresolution of the no-model calculation affects the whole computational domain by producing noisy velocity fluctuations even in laminar flow regions. On the other hand, the ADM-RT model, whose model contributions are confined to the smallest spatial scales, allows an accurate and physically realistic prediction of the transitional structures even up to later stages of transition. Clear predictions of the one to the four-spike stages of transition in the velocity signal could be obtained. Moreover, the visualisation of the vortical structures shows the appearance of hairpin vortices connected with those stages.

It has also been shown that the above SGS models behave similarly for both the temporal and the spatial transition simulation framework. Conclusions derived from temporal results transfer readily to the spatial, more physically relevant, but much more expensive, simulation method. It can thus be concluded that for the evaluation of LES for transitional flows the temporal framework is sufficient. Concerning the non-periodic boundary treatment, the combination of LES with the fringe method was assessed, and did not raise any difficulties even with an SGS model active within the fringe region. The fringe method allows an effective damping of the outflowing turbulent channel flow and provides an accurate prescription of the inflowing, weakly disturbed laminar flow.

In turbulent channel flow, the results obtained by the ADM-RT model nearly collapse onto the filtered DNS data, whereas a no-model LES is clearly not dissipative enough. Very accurate results were also obtained with the HPF eddy-viscosity models (see below) and, depending on the choice of the test filter, with the dynamic Smagorinsky model. The examination of different filters for use as test filter in the dynamic

Smagorinsky model showed that increasing the order of the filter leads to more accurate results. Very good results have been obtained using the three-dimensional sixth-order filter $I - H_1$ (see equation (2.12)). Unlike the spectral cutoff filter originally proposed by Germano *et al.* (1991), the sixth-order filter can also be used in general geometries since it is defined fully three-dimensionally.

The excellent results obtained for transitional and turbulent channel flow with the SGS model based on relaxation regularisation (ADM-RT model) on coarse grids demonstrate the applicability of subgrid models which provide dissipation based on a high-pass filtering approach. As shown in this thesis, the model contributions of the ADM-RT model virtually vanish in laminar or slightly disturbed flow regions. Due to the properties of the three-dimensional high-pass filter, the model provides an accurate description of the near-wall region, even permitting backscatter close to the walls. This SGS model is easy to implement and requires only a small computational overhead. Therefore, especially for coarse grids, the ADM-RT model should be preferred, whereas for higher resolution the standard ADM is also applicable, however with slightly less accurate results than the ADM-RT model. It is interesting to note that for LES of compressible boundary-layer flow using finite-difference discretisation, the deconvolution was found to be beneficial (Stolz & Adams, 2003). Note that the ADM formalism can be rewritten as a low-pass filter of the nonlinear convection terms and in fact damps the high-frequency content of those terms. For non-spectral numerical methods this provides a reduction of aliasing and differentiation errors in the high-frequency modes. Conversely, for spectral discretisations employed in the present work this additional filtering is not needed because the aliasing and differentiation errors are very small.

Additionally, numerical tests confirmed that LES using ADM and ADM-RT in channel flow are less sensitive to aliasing errors than DNS calculations and classical SGS models such as the dynamic Smagorinsky model. This property is very important for the widely-used numerical schemes for which full dealiasing is not straightforward or impossible. For spectral simulations additional computational effort can be saved by omitting dealiasing procedures. In other words, the relaxation-term based SGS models can be employed to reduce the effects of aliasing errors inherently present in most flow computations.

The ADM and ADM-RT models are also quite insensitive to the exact determination procedure of their model coefficient χ and its absolute

value. It turned out that even with a fixed (empirically determined) model coefficient both transition and turbulence could be predicted as accurately as when using more sophisticated determination procedures. Nevertheless, a robust and general dynamic procedure is eventually desirable, see section 7.3.

The results further demonstrate that a proper treatment of each spatial direction, in particular any inhomogeneous direction, should be included in the computation of the SGS model in order to faithfully represent the relevant physical features such as the local velocity gradients. By using a model that is defined three-dimensionally, usually a coarser grid can be chosen, *e.g.* in the wall-normal direction of channel flow. Moreover, the generality of the model with respect to complex geometries is certainly improved by using a three-dimensional model definition.

Very good results have been obtained with the HPF eddy-viscosity models for the energy and dissipation spectra in forced homogeneous isotropic turbulence up to $Re_\lambda \approx 5500$. The analysis of the SGS dissipation showed that the model contributions of the HPF models are virtually zero at low wavenumbers and increase rapidly for higher harmonics, similar to a hyperviscosity. The compensated energy spectra showed a flat plateau at $C_K \approx 1.6$. Using the same models, very accurate results have also been obtained for statistics of turbulent channel flow at $Re_\tau \approx 590$, including the mean flow, energy spectra and the Reynolds stresses. Furthermore, detailed analysis of the energy budget including the SGS terms revealed that the contribution to the mean SGS dissipation is nearly zero for the HPF models, while it is a significant part of the SGS dissipation for other SGS models. Moreover, unlike the classical eddy-viscosity models, the HPF eddy-viscosity models are able to predict backscatter. It has been shown that in channel flow locations with intense backscatter are closely related to low-speed turbulent streaks in both LES and filtered DNS data. In the near-wall region, significant backscatter occurs, *e.g.* at $z^+ \approx 3$ roughly 70% of the forward SGS dissipation is balanced by backscatter.

The HPF eddy-viscosity models provide an easy way to implement an alternative to classical fixed-coefficient eddy-viscosity models. The HPF models have shown to perform significantly better than their classical counterparts in the context of wall-bounded shear flows, mainly due to a more accurate description of the near-wall region. The results have shown that a fixed model coefficient is sufficient for the flow cases considered in this work. No dynamic procedure for the determination of the

model coefficient was found necessary, and no empirical wall-damping functions were needed.

The effect of the filter cutoff wavenumber ω_c on the performance of the HPF models has been studied and an empirical adaptation of the HPF model coefficient minimising the influence of ω_c has been proposed and employed successfully. Through the three-dimensional definition of the high-pass filter, the models are also applicable for general geometries, *i.e.* no special treatment of selected spatial directions is needed.

It has been demonstrated that the HPF eddy-viscosity models produce very accurate results even while using a constant eddy viscosity ν_t, *i.e.* without using the Smagorinsky or the structure-function eddy-viscosity closures. Moreover, a close relationship between the modelling approach of the HPF models and the relaxation term from ADM and ADM-RT could be established. By an accordingly modified high-pass filter, these two approaches become analytically equivalent for homogeneous Fourier directions.

A new boundary-treatment procedure ("windowing method") was developed and compared extensively to the well-established fringe method for a number of test cases. By properly designing the window function, spectral accuracy of a Fourier discretisation can be obtained. It is found that the accuracy of imposing the boundary conditions is similar for both techniques. Moreover, for flow problems with a spatially evolving base flow, the windowing method does not require the base flow to be periodic. It was further found that the performance of the fringe method strongly depends on the choice of the parameters: fringe strength, blending, start and length of the fringe region. While excellent results can be obtained for ideal parameters, the imprudent choice of those parameters can even lead to numerical problems due to the fringe forcing. The reduction of the time step in such cases is undesirable as it decreases the efficiency of the computation significantly. The windowing method, on the other hand, contains only a small number of tuning parameters and their influence is limited.

The windowing method provides an attractive alternative way to perform accurate simulations in non-periodic geometries using periodic discretisation schemes. Since it poses no restriction on the type of inflow conditions, its use for transitional and turbulent flows is perfectly possible.

7.3   Outlook

As discussed in the previous section, in this thesis a number of different investigations on large-eddy simulation of transitional and turbulent flows have been performed successfully. However, there are additional important flow types and modelling aspects that could not have been addressed in the course of this work. In the following an overview of these issues is given.

A natural continuation of the present work is the extension of the LES results to the flow case of transition and turbulence in boundary layers. Especially the spatially evolving nature of the mean flow and the need to impose well-posed free-stream boundary conditions are the main differences to the channel-flow case considered here. It is however believed that the main conclusions drawn in the previous section 7.2 transfer directly from channel to boundary-layer flow.

Additionally, more challenging transition scenarios could be considered, *e.g.* the simulation of free-stream turbulence induced transition in boundary layers (bypass transition, see *e.g.* the DNS by Brandt *et al.* (2004)). Another very interesting, and for technical applications important, flow case is a laminar boundary layer which separates due to an adverse pressure gradient, undergoes transition within the separation bubble and subsequently reattaches as a turbulent boundary layer. For this case detailed experimental data exist (Watmuff, 1999), which would serve well as reference data for LES.

Most SGS models assume that the turbulent flow is in energetic equilibrium between turbulent production and dissipation. It is however crucial for a successful LES strategy to faithfully cope with flows that depart from such equilibrium conditions, *e.g.* an impulsively started transverse pressure gradient (Moin *et al.*, 1990). The evaluation of different SGS models coping with non-equilibrium flows would certainly give further insight into future modelling strategies.

Transition in free shear flows, *e.g.* the formation and breakdown of Kelvin-Helmholtz vortices in developing mixing layers, could be an interesting extension of the present work on LES of transitional flows. This test case has already been considered by a number of other researchers in order to assess the performance of LES (see *e.g.* Lesieur *et al.* (1997)). The consideration of this flow case would allow the separation of the modelling aspects of transition in free shear flows from those involving solid walls. Results obtained by Rembold *et al.* (2002) using ADM for

the simulation of a transitional compressible rectangular jet flow are encouraging.

From a more technical point of view, a detailed examination of the combined influence of the numerical discretisation method and the SGS model is a very important issue. Despite recent development in that direction (see *e.g.* Adams *et al.* (2004); Grinstein & Fureby (2002); Kravchenko & Moin (1997)), there is still a need for deeper understanding of this coupling.

In particular, it would be instructive to recompute the present flow cases for incompressible transitional and turbulent channel flow with non-spectral discretisations such as finite differences of various orders and to compare those LES results to the ones obtained by spectral numerical methods. Finite-difference schemes are susceptible to a number of numerical errors including numerical dissipation, differentiation errors at high wavenumbers (modified wavenumber concept) and aliasing errors (see *e.g.* Lele (1992)), which are not present in spectral methods. The interplay of those errors with the SGS modelling strategy is of major importance, especially for industrial applications of LES.

The ADM-RT model presented in this work has been shown to produce very accurate results for both transitional and turbulent flows, in particular results that are more accurate than those obtained by the standard ADM model using the same resolution (see section 4.4). However, an investigation of compressible boundary-layer flow using finite-difference schemes (Stolz & Adams, 2003) showed that the deconvolution seems to be beneficial for the accuracy of the results, which is thought to be mainly due to a reduction of aliasing and discretisation errors. It would therefore be essential to investigate and quantify the detailed influence of the deconvolution operation used in the ADM model on the performance of an SGS model and to point out differences between the different flow cases and numerical methods.

For the ADM and the ADM-RT model, it has been shown *e.g.* in Schlatter *et al.* (2004*d*) that the exact determination procedure for the relaxation coefficient χ is of minor importance as long as its order of magnitude is adapted to the current flow situation. A similar conclusion could also be drawn from the HPF eddy-viscosity models in conjunction with a constant eddy viscosity ν_t (see section 4.7.3, Schlatter *et al.* (2005*c*)). Nevertheless, a robust dynamic procedure for the determination of the respective model coefficients within a model that is capable of predicting laminar, transitional, turbulent, and possibly non-equilibrium

flows is certainly a challenging task in any future SGS model and should therefore be investigated further.

Appendix A

Periodic boundary treatment of non-periodic flows

In this chapter, a new inflow/outflow boundary treatment procedure is described. The presentation is based on the publication Schlatter *et al.* (2005*a*) and the technical report Schlatter (2002). The boundary treatment method is applicable to the numerical computation of non-periodic flows which allows for the use of periodic spatial boundary conditions. Due to this periodicity, *e.g.* efficient and accurate Fourier spectral methods can be applied. The governing equations of the flow are modified using window functions as known from signal processing. Thereby, the windowed solution is forced to zero to high order at the artificial boundaries. The physical solution near the boundaries is obtained by a regularised dewindowing operation and boundary conditions are imposed with the help of a suitable base flow which needs to be defined only within the window-boundary regions. On the inner domain, the unmodified flow equations are solved. The base flow can contain spatially and temporally varying disturbances. Hence it is possible to employ transitional and turbulent inflow conditions using the windowing technique.

By properly designing the window function, spectral accuracy of a Fourier discretisation can be obtained. The performance of this scheme is analysed theoretically in this section. A numerical verification and comparisons to the more widely-used fringe region technique is given in Schlatter *et al.* (2005*a*) and Schlatter (2002). There, it is found that the accuracy of imposing the boundary conditions is similar for both techniques. Furthermore, for flow problems with a spatially evolving base flow, the windowing method does not require the base flow to be periodic.

The spatial simulations presented in chapter 5 of this thesis have been performed using the fringe region technique due to its simpler implementation. However, large-eddy simulation using the windowing method are also possible without problems.

In this chapter, only the theoretical foundation and a short summary of the implementation of the windowing method in a two-dimensional incompressible Navier-Stokes code is given. The full details and an extensive comparison to the fringe region technique are presented in Schlatter

et al. (2005*a*) and Schlatter (2002) for three test cases. In those references, the validity of the windowing method is first shown by applying the solution procedure to an ordinary differential equation. Using a two-dimensional Navier-Stokes solver, the convection of a localised vortical disturbance and a stationary, spatially evolving jet are then considered.

A.1   Introduction

For the numerical modelling of a flow problem in an Eulerian description the computational domain is usually a truncation of the real (physical) domain. At the computational domain boundaries the solution is often (partially) unknown, resulting in the need of *artificial boundary conditions* (see the reviews by Givoli (1991) and Colonius (2004)). The prescription of suitable conditions at an artificial boundary requires that some properties of the solution are known *a priori*. Since in most cases these properties are known only approximately or can only be guessed, differences between the approximate conditions and the proper physical solution are present near the boundaries. These regions, which are characterised by the changeover from the physical solution to the solution imposed by the (approximate) boundary condition, are commonly considered as "non-physical". At the artificial boundaries also the spatial discretisation has to be constructed such that the resulting numerical scheme is stable and reflections from the boundaries are suppressed.

For finite-difference schemes one usually needs to employ special boundary closures. This is avoided if periodic boundary conditions can be imposed at the artificial boundaries. Then the schemes used in the exterior of the domain can be extended across the artificial boundary and the solution algorithms usually gain robustness and efficiency. Since for the above reasons non-physical regions near artificial boundaries are practically unavoidable, one can exploit this fact by modifying the governing equations in such a way that near the artificial boundaries periodic boundary conditions can be assumed for the discretised spatial-derivative operators of the underlying flow equations without significantly increasing the size of the computational domain. The procedure has to ensure that away from the artificial boundaries the correct physical solution is recovered.

Reducing the effect of artificial boundary conditions by use of a forcing term was first applied by Israeli & Orszag (1981). They used a *sponge layer* to damp oscillations in the solution near the boundaries

before being treated by the artificial boundary conditions. In the *perfectly matched layer* (PML) approach (Bérenger, 1994), it is ensured that the damping layer is non-reflecting by changing the phase speed of the incoming waves such that they are damped. The PML approach has been extended to the treatment of non-uniform Euler flows (see *e.g.* Hagstrom & Nazarov (2003)).

The idea of obtaining non-periodic solutions on periodic domains is due to Spalart (1988), who modified the Navier-Stokes equations in "fringe regions" at the computational domain boundaries such that the solution was forced towards periodicity in these regions without affecting the physically meaningful solution in the valuable part of the domain. Spalart demonstrated that accurate results using the fringe method could be obtained. Some justification of the method was also given. The fringe method has found widespread use and was employed successfully in a number of publications involving transitional and turbulent flows, see *e.g.* Bertolotti *et al.* (1992), Lundbladh *et al.* (1999) and the references therein. The fringe method was further analysed in more detail by Nordström *et al.* (1999). These authors gave a justification of the method and showed quantitatively that for incompressible flow the inflow/outflow problem on the example of the spatially evolving Blasius profile can be simulated with high accuracy.

Here, we adopt a different approach, which was proposed for the simulation of transitional compressible boundary layer flow by Guo *et al.* (1994). The underlying idea is related to that of the spectral multidomain technique of Israeli *et al.* (1993) and is based on a windowing operation used for the spectral analysis of non-periodic data in signal processing (*e.g.* Otnes & Enochson (1978)). Colonius & Ran (2002) used a related approach to simulate flows on unbounded domains by employing a super-grid scale model to stretch the grid near the domain boundaries. In the present work, the method of Guo *et al.* (1994) is revisited and modified with respect to the treatment of the solution near the boundaries. It is then applied to incompressible flows and an extended analysis of its properties is performed.

In Schlatter *et al.* (2005*a*) both the windowing and fringe method and their application to flow problems are described. A model problem based on an ordinary differential equation is discussed to demonstrate the convergence properties of the windowing technique. Additionally, two numerical test cases involving the Euler and Navier-Stokes equations are presented. Test case 1 examines the ability of both methods to damp

out a single localised vortical disturbance as it travels out of the physical domain. Test case 2 considers a spatially evolving jet and assesses the performance of the fringe and the windowing method in simulating a spatially evolving flow.

A.2   Mathematical formulation

A.2.1   Problem description and governing equations

We consider incompressible fluid flow on a rectangular two-dimensional *physical domain* Γ_I with boundary $\partial\Gamma_I$. A Cartesian coordinate system is defined such that the streamwise (x_1 or x) and spanwise/cross-stream (x_2 or y) axes are aligned with the straight domain boundaries. The non-dimensional velocity vector with components $u_1 = u$ and $u_2 = v$ is denoted by $\mathbf{u}$. The non-dimensional density ρ and the non-dimensional dynamic viscosity μ are assumed to be constant. Non-dimensionalisation is such that the Reynolds number is given by $\mathrm{Re} = \rho/\mu$. The flow is then governed by the incompressible Navier-Stokes equations

$$\partial_t u_i + u_j \partial_j u_i + \frac{1}{\rho}\partial_i p = \frac{1}{\rho}\partial_j \mu(\partial_i u_j + \partial_j u_i) \, , \qquad \text{(A.1)}$$

and the continuity equation

$$\partial_k u_k = 0 \, . \qquad \text{(A.2)}$$

∂_i and ∂_t denote the partial derivatives with respect to x_i and time t, respectively. Unless stated otherwise, the summation convention over repeated indices applies.

Parts of the boundary $\partial\Gamma_I$ of the physical domain Γ_I can coincide with physical boundaries (*e.g.* walls), the remainder coincides with artificial boundaries (in particular inflow/outflow boundaries). For notational simplicity we assume that the entire boundary $\partial\Gamma_I$ is artificial. In an application where this is not the case (*e.g.* at solid walls) the boundary $\partial\Gamma_I$ has to be split accordingly and the following applies to the artificial parts of $\partial\Gamma_I$. Note that for well-posedness of the original problem formulation boundary conditions on the entire boundary $\partial\Gamma_I$ are necessary.

For the following considerations, periodic boundary conditions are assumed in the spanwise/cross-stream direction. In the streamwise direction x the flow is assumed to be spatially evolving. Therefore, the
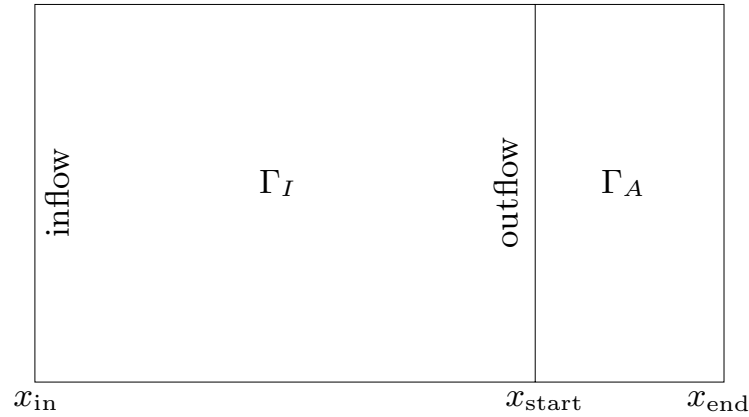
Figure A.1: Sketch of the computational domain Γ consisting of the physical domain Γ_I and the artificial boundary region Γ_A with $\Gamma = \Gamma_I \cup \Gamma_A$. The mean flow velocity is assumed to be from left to right. Periodic boundary conditions are applied in all directions.

inflow/outflow boundary treatment is imposed in the streamwise direction only. The subsequently described boundary treatment transfers directly to problems in three spatial dimensions and to periodic boundary treatment in more than one direction, but for simplicity we consider here only the two-dimensional case with one inhomogeneous direction.

For the boundary treatment, the physical domain Γ_I is enlarged in the streamwise direction forming the *computational domain* Γ (figure A.1). On Γ_I we would like to recover an accurate physical solution to the original flow problem according equation (A.1). The added subdomain $\Gamma_A = \Gamma \setminus \Gamma_I$, on the other hand, is responsible for the boundary treatment and is usually called fringe region. Here, we denote this region – to avoid confusion with the fringe region technique introduced in section A.2.2 – more generally *artificial boundary region*. The computational solution within Γ_A is not part of the physically relevant solution to the original flow problem. The boundary treatment thus modifies the underlying initial-boundary value problem (IBVP) on Γ_I to an IBVP with periodic boundary conditions in the x-direction on the enlarged domain Γ. For a unique solution of the periodic problem both the fringe and the windowing approach require distributed boundary data to be provided within the artificial boundary region Γ_A. The boundary conditions to the computational problem are thus assumed to be given on
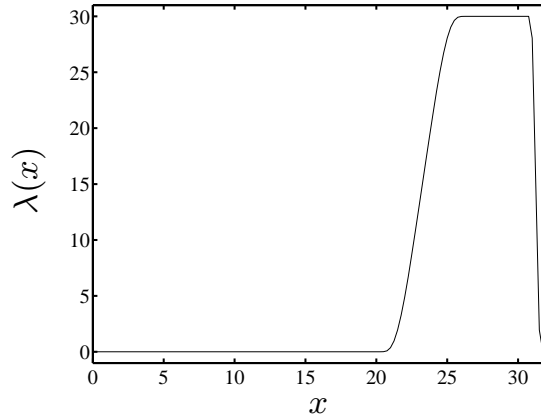
Figure A.2: Sample fringe function $\lambda(x)$ with parameters $\lambda_{\max} = 30$, $x_{\mathrm{start}} = 20$, $x_{\mathrm{end}} = 32$. $\Delta_{\mathrm{rise}} = 60\%$ and $\Delta_{\mathrm{fall}} = 10\%$ of fringe extent.

the subdomain Γ_A in the form of *distributed boundary conditions* $\mathcal{U}_i$,

$$u_i(\mathbf{x}, t) \to \mathcal{U}_i(\mathbf{x}, t) \ \text{ for } \ x \to \partial \Gamma_A \ . \tag{A.3}$$

The function $\mathcal{U}_i$ needs to be defined on Γ_A only and is usually referred to as (computational) base flow of the problem. $\mathcal{U}_i$ is allowed to vary both in space and time.

A.2.2 Fringe region technique

The following description of the fringe region technique is based on Lundbladh *et al.* (1999). The same form has been analysed in Nordström *et al.* (1999) and has been successfully applied in a number of cases, *e.g.* Brandt *et al.* (2004).

In order to be able to assume periodicity within the computational domain, the *fringe region* Γ_A is appended downstream of the physical domain Γ_I (see figure A.1). Within the fringe region, the flow is forced back to the desired inflow condition and possible disturbances are damped by adding a suitable volume force G_i to the right-hand side of the Navier-Stokes equations (A.1) which vanishes within Γ_I.

The general form of the fringe forcing is given by

$$G_i = \lambda(x)(\mathcal{U}_i - u_i) \ . \tag{A.4}$$

The fringe function $\lambda(x) \geq 0$ is non-vanishing only within the fringe region Γ_A, defined to extend from x_{start} to x_{end}. $\mathcal{U}_i$ is a prescribed flow

field, periodic in x, referred to as (computational) base flow, containing the inflow and outflow conditions (see Figure A.2).

If the physical base flow evolves in the streamwise direction x, the streamwise velocity component $\mathcal{U}_x$ of the computational base flow is a blending between inflow and outflow velocity and can be written as (Lundbladh *et al.*, 1999)

$$\mathcal{U}_x(x,y) = U(x,y) + [U(x - L_P, y) - U(x,y)]\, S\left(\frac{x - x_{\text{mix}}}{\Delta_{\text{mix}}}\right) \ . \quad \text{(A.5)}$$

$U(x, y)$ describes a solution to the Navier-Stokes (or boundary layer) equations in the absence of the periodic boundary treatment, *e.g.* the Blasius solution in the case of boundary layer flow. $L_P = x_{\text{end}} - x_{\text{in}}$ denotes the length of the periodic computational domain and the smooth step function $S(x)$ is given in equation (A.7) below. x_{mix} and Δ_{mix} define the properties of the blending and are explained in the following. Note that the blending (A.5) is only needed for a physical base flow U that is evolving in space, *e.g.* the simulation of spatially evolving boundary layers. For a base flow that is not dependent on x, $\mathcal{U} = U$ holds.

In two-dimensional flows, the other non-vanishing velocity component $\mathcal{U}_y$ of the base flow can be calculated using the continuity equation, especially in the blending region where the base flow is non-physically modified and $\mathcal{U}_y$ cannot be recovered otherwise. A natural choice for the parameters of the blending region for the coordinates introduced above is $x_{\text{mix}} = x_{\text{start}}$ and $\Delta_{\text{mix}} = x_{\text{end}} - x_{\text{start}}$. This choice ensures that the blending uses the maximum streamwise extent of the fringe region which is preferred for laminar or nearly laminar flows (Lundbladh *et al.*, 1999). Hereby it is assured that the effects on the valuable part of the flow domain are minimised.

It is perfectly possible to include temporally and/or spatially varying inflow disturbances into $\mathcal{U}_i$. Even completely turbulent inflow conditions can be employed in the fringe region, *e.g.* Brandt *et al.* (2004). Note that these superimposed disturbances should satisfy continuity in such a way that the entire base flow $\mathcal{U}_i$ is divergence-free (see details in Schlatter *et al.* (2005a)).

The form of the fringe function λ introduced in Lundbladh *et al.* (1999) is

$$\lambda(x) = \lambda_{\text{max}}\left[S\left(\frac{x - x_{\text{start}}}{\Delta_{\text{rise}}}\right) - S\left(\frac{x - x_{\text{end}}}{\Delta_{\text{fall}}} + 1\right)\right] \ . \quad \text{(A.6)}$$

The maximum strength of the fringe function is $\lambda_{\max}$ and its shape is defined by the function $S(x)$ and the parameters Δ_{rise} and Δ_{fall}. $S(x)$ is a smooth step function with $S(x) = 0$ for $x < 0$ and $S(x) = 1$ for $x \geq 1$. The following form of S has continuous derivatives of all orders for $x \neq 0$ and $x \neq 1$

$$
S(x) \quad = \quad \begin{cases} 0 & , \quad x \leq 0 \\ 1/[1 + \exp(\frac{1}{x-1} + \frac{1}{x})] & , \quad 0 < x < 1 \\ 1 & , \quad x \geq 1 \end{cases} \quad . \qquad \text{(A.7)}
$$

Note that the superposition given in equation (A.5) is continuously differentiable only for $x \neq x_{\text{mix}}$ and $x \neq x_{\text{mix}} + \Delta_{\text{mix}}$.

The application of the fringe method imposes an additional restriction on the maximum possible time step of the integration scheme. Straight-forward analysis of the linear temporal stability characteristics of the damping term G_i yields the condition

$$
\lambda_{\max}\Delta t \leq 2.51 \qquad \text{resp.} \qquad \lambda_{\max}\Delta t \leq 2.78 \qquad \text{(A.8)}
$$

for a third and a fourth-order Runge-Kutta scheme, respectively.

A.2.3   Windowing approach

Theoretical consideration

The windowing method has its roots in signal processing, where the windowing operation allows the spectral analysis of non-periodic signals (Otnes & Enochson, 1978; Harris, 1978). Similarly, the windowing operation in the present context can be understood as an artificial window through which the physical flow field is projected onto a computational domain.

As a window function on the domain $x \in [x_L, x_R]$ we define a function $w(x) \in C^\infty$ on $\mathbb{R}$ with the following requirements $(x_L < x_l < x_r < x_R)$

- **(R1)** $0 \leq w(x) \leq 1$ on the entire real axis $\mathbb{R}$,

- **(R2)** $\max\{1 - w(x)\} \leq \epsilon_2$ on the inner domain $[x_l, x_r]$,

- **(R3)** $w(x) \leq \epsilon_1 e^{-\alpha|x-x_L|}$ for $x < x_l$, $w(x) \leq \epsilon_1 e^{-\alpha|x-x_R|}$ for $x > x_r$ with some $\alpha > 0$, *i.e.* $w(x)$ decays at least exponentially for $x \to \pm\infty$. An implication of this requirement is $\max\{w(x_L), w(x_R)\} \leq \epsilon_1$.

Any bounded and continuous function $f(x)$ defined on $\mathbb{R}$ has a Fourier transform if it is multiplied with such a window function $w(x)$. Accordingly, we define the windowing operation by

$$\tilde{f}(x) := w(x)f(x) \; . \tag{A.9}$$

The Fourier transform of $\tilde{f}$ is then defined as

$$\hat{\tilde{f}}(k) = \int_{-\infty}^{\infty} \tilde{f} e^{-\mathrm{i}kx} dx \; , \tag{A.10}$$

and for $\tilde{f}^{(p)}$ integrable and $\tilde{f} \in C^{p-1}$ one can show by partial integration that

$$\left| \hat{\tilde{f}}(k) \right| = \mathcal{O}(|k|^{-p}) \; . \tag{A.11}$$

For $\tilde{f} \in C^{\infty}$ the inverse transform of $\hat{\tilde{f}}$ converges to $\tilde{f}$ spectrally.

The error introduced by performing the Fourier integral (A.10) only over a bounded domain $[x_L, x_R]$ according to

$$\hat{\tilde{f}}_{\delta}(k) = \int_{x_L}^{x_R} \tilde{f}(x) e^{-\mathrm{i}kx} dx \; , \tag{A.12}$$

instead of $(-\infty, +\infty)$ is estimated with (**R3**) as

$$\epsilon_{\delta}' = \max \left| \hat{\tilde{f}} - \hat{\tilde{f}}_{\delta} \right| \leq \left| \int_{-\infty}^{x_L} \tilde{f} e^{-\mathrm{i}kx} dx \right| + \left| \int_{x_R}^{\infty} \tilde{f} e^{-\mathrm{i}kx} dx \right| \leq 2\frac{M\epsilon_1}{\alpha} \tag{A.13}$$

with $M \geq \max |f(x)|$. Considering the band-limited inverse transform of equation (A.10)

$$\tilde{f}_N = \frac{1}{2\pi} \int_{-k_N}^{k_N} \hat{\tilde{f}}(k) e^{\mathrm{i}kx} dk \; , \tag{A.14}$$

where the cutoff wavenumber k_N is the Nyquist wavenumber $k_N = \pi/h$ with the grid spacing h, the estimate for the *truncation error*

$$\epsilon_N = \max \left| \tilde{f}_N - \tilde{f} \right| \leq \left| \frac{1}{2\pi} \left(\int_{-\infty}^{-k_N} + \int_{k_N}^{\infty} \right) \hat{\tilde{f}}(k) e^{\mathrm{i}kx} dk \right| \leq C |k_N|^{1-p}$$

$$\tag{A.15}$$

with a constant C decays at least as $\mathcal{O}\left(|k_N|^{1-p}\right)$. For band-limited $\tilde{f}_N$, it can be shown using Whittaker cardinal functions that the Fourier transform of $\tilde{f}_N$ is given as (Boyd, 2000)

$$\hat{\tilde{f}}_N(k) = h \sum_{j=-\infty}^{\infty} \tilde{f}(x_j)e^{-ikx_j} \qquad \text{with } x_j = j \cdot h; \quad h = \frac{\pi}{k_N} . \quad \text{(A.16)}$$

By a similar procedure as for the relation (A.13), the window truncation is imposed on $\hat{\tilde{f}}_N$ by terminating the summation in equation (A.16) at some integer lower and upper bounds j_L and j_R, respectively, where $x_L \leq x_{j_L} < x_L + h$ and $x_R - h < x_{j_R} \leq x_R$. For the resulting $\hat{\tilde{f}}_{N_\delta}$ one arrives at the estimate

$$\epsilon''_\delta = \max \left| \hat{\tilde{f}}_N - \hat{\tilde{f}}_{N_\delta} \right| \leq h \left| \sum_{j=-\infty}^{j_L} \tilde{f}(x_j)e^{-ikx_j} \right| + h \left| \sum_{j=j_R}^{\infty} \tilde{f}(x_j)e^{-ikx_j} \right|$$

$$\leq 2\epsilon_1 h M \left(1 + e^{-\alpha h}\right) , \qquad \text{(A.17)}$$

which is larger than ϵ'_δ of equation (A.13) only for $(\alpha h) \gtrsim 0.6590$, *i.e.* for coarse grids. The error $\left| \tilde{f}_{N_\delta} - \tilde{f}_N \right|$ can be estimated by taking the inverse Fourier transform of $(\hat{\tilde{f}}_N - \hat{\tilde{f}}_{N_\delta})$ and using equation (A.17) as

$$\epsilon_\delta = \max \left| \tilde{f}_{N_\delta} - \tilde{f}_N \right| \leq 2\epsilon_1 M \left(1 + e^{-\alpha h}\right) \leq 4\epsilon_1 M \qquad \text{(A.18)}$$

and is usually referred to as *window truncation error*. The overall error ϵ_w is then composed of both the truncation error and the window truncation error as

$$\epsilon_w = \max \left| \tilde{f}_{N_\delta} - \tilde{f} \right| \leq \epsilon_\delta + \epsilon_N . \qquad \text{(A.19)}$$

For $f(x) \in C^\infty$ in particular this means that the error ϵ_w decays exponentially until the window truncation error ϵ_δ is reached. ϵ_δ can be made as small as the machine precision by adjusting the value of ϵ_1 accordingly (see equation (A.13)).

For functions which are defined on a discrete grid, analogous derivations and estimates hold. In this case the Fourier transforms are replaced by discrete transforms and the integrals are replaced by summations using the trapezoidal rule.

The inverse windowing process is singular or at least ill-posed on the domain boundaries $x = x_L$ and $x = x_R$ since there $w \approx 0$. Retrieving the quantity f from the windowed value $\tilde{f}$ is ill-conditioned for any $x \in [x_L, x_l]$ and $x \in [x_r, x_R]$ for which w is small. Therefore, a regularised *dewindowing operation* is introduced as

$$\overline{f} = (1 - w)\mathcal{F} + \tilde{f} \ . \tag{A.20}$$

Here $\mathcal{F}$ is a function defined at least on $x \in [x_L, x_l]$ and $x \in [x_r, x_R]$ describing the distributed boundary data required for the solution of the periodic IBVP. In the context of a flow simulation, $\mathcal{F}$ is the base flow. The maximum regularisation error $|f - \overline{f}|$ on $x \in [x_l, x_r]$ is bounded by $(\epsilon_2 \cdot \max |\mathcal{F} - f|)$, whereas on $x \in [x_L, x_l]$ and $x \in [x_r, x_R]$ it is bounded by $\max |\mathcal{F} - f|$.

Different types of window functions can be designed. Since no window function used in signal processing (see Harris (1978)) directly suits the needs for the present application, different approaches were studied in Guo (1993). A window function satisfying the requirements (**R1**) to (**R3**) is

$$w(x) = 10^{-a^n |2(x - x_L)/(x_R - x_L) - 1|^n} \ , \tag{A.21}$$

which assumes that the window function describes a symmetric window ($x_l + x_r = x_L + x_R$). We refer to the window function (A.21) as an *exponential window* since it satisfies requirement (**R3**) and thus preserves spectral convergence of the Fourier series of a sufficiently smooth windowed function according to the above derivation. The parameters a and n can be calculated from the conditions that for some $x_L < x_l < x_r < x_R$

$$w(x_L) = w(x_R) \leq \epsilon_1 \quad \text{and} \quad w(x_l) = w(x_r) \geq 1 - \epsilon_2 \tag{A.22}$$

with small numbers ϵ_1 and ϵ_2, *e.g.* comparable to the machine precision.

Analytical relations for the derivatives $\partial_x w$ and $\partial_{xx} w$ can be derived easily. If desired, an extension to non-symmetric windows is straightforward by connecting two windows according to equation (A.21) with different parameters a and n in the middle of the domain $x = \frac{1}{2}(x_L + x_R)$.

An example of an exponential window function is shown in figure A.3 together with the spectrum of the windowed non-periodic function introduced in Guo *et al.* (1994) (scaled according to $x' = (x - x_L)/(x_R - x_L)$)

$$f(x') = \tanh(4x') + e^{-4x'} \sum_{k=0}^{4} \sin(2\pi 2^k x') \ , \qquad 0 \leq x' \leq 1 \ . \tag{A.23}$$
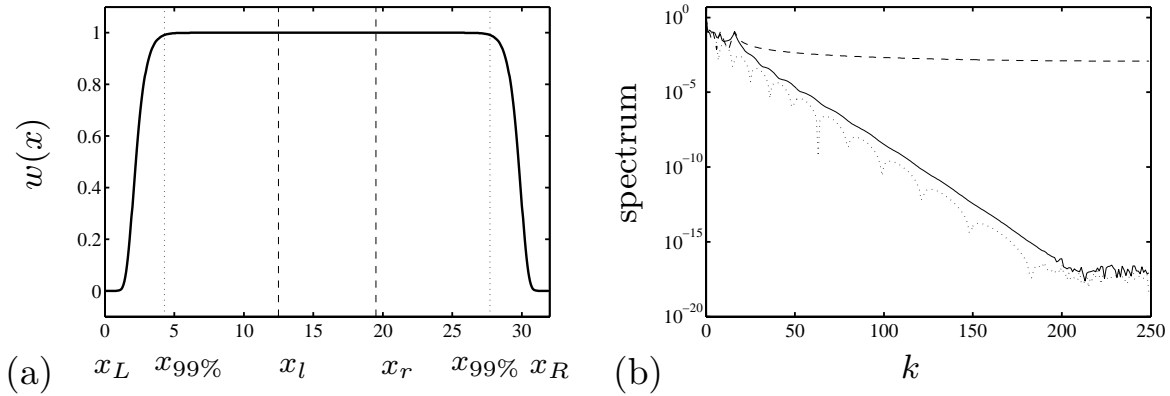
Figure A.3: Left: *Window function with parameters* $n = 27$, $a = 1.111$, $x_L = 0$, $x_R = 32$, $x_l = 12.5$, $x_r = 19.5$ *(vertical dashed lines)*, $w(x) = 0.99$ *at* $x = 4.3$ *and* $x = 27.7$ *(vertical dotted lines), spectral bandwidth* $k_w \approx 200$. Right: *Spectra of* ········ $w(x)$, ----- $f(x)$ *(equation (A.23))*, ——— $f(x)w(x)$.

It is evident from figure A.3b that this particular choice of the window function $w(x)$ preserves the spectral convergence of the Fourier representation of $f(x)w(x)$.

The efficiency of a window function can be estimated by the following consideration: The spectral bandwidth k_w of a window function $w(x)$ is defined by

$$|\hat{w}(k)| < \delta \quad \text{for} \quad |k| \geq k_w \tag{A.24}$$

with $\hat{w}(k)$ denoting the Fourier coefficients according to equation (A.10) and δ a fixed small error level. A harmonic function $g(x)$ with unit amplitude is given as (assuming $x_L = 0$)

$$g(x) = \sin\left(\frac{2\pi}{x_R} k_g x\right) \, . \tag{A.25}$$

The windowed function $\tilde{g}(x)$ is then, due to the convolution properties of the windowing process in Fourier space, resolved up to the error δ if at least

$$N \geq 2(k_w + k_g) \tag{A.26}$$

grid points are used in the discretisation of $w(x)$ and $g(x)$. For an exponential window the spectral bandwidth k_w is proportional to the physical extent of the domain divided by the extent of the windowing regions

$$k_w \propto \frac{x_R - x_L}{(x_l - x_L) + (x_R - x_r)} \, . \tag{A.27}$$
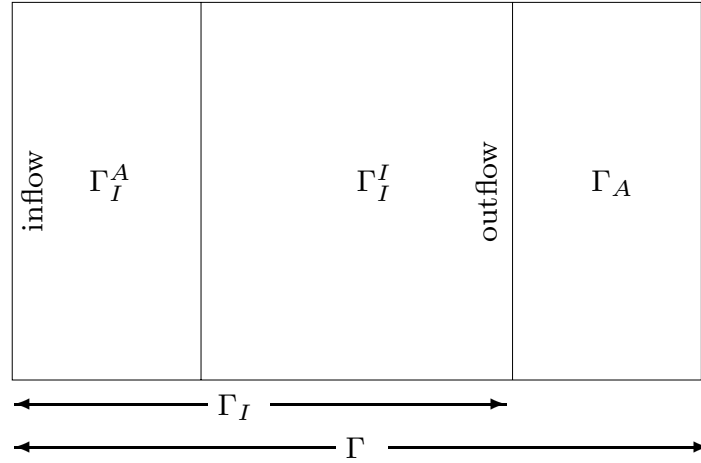
Figure A.4: Sketch of the computational domain Γ, adapted for the windowing technique, consisting of the physical domain Γ_I^I, the inflow domain Γ_I^A and the outflow domain Γ_A. $\Gamma = \Gamma_I \cup \Gamma_A$ with $\Gamma_I = \Gamma_I^I \cup \Gamma_I^A$.

Therefore, k_w is determined by the choice of the computational domain Γ alone. Equation (A.26) now shows that the overhead cost of the windowing process, *i.e.* the fraction k_w/N, will decrease with increasing resolution of the discretisation, *i.e.* with increasing k_g. The efficiency of the windowing methods lies thus in large N; moreover, the efficiency of a Fast Fourier Transformation (FFT) possibly used in the numerical algorithm also increases with N.

To apply the windowing procedure in the general case of $D > 1$ dimensions, the window function is extended tensorially by introducing functions $W_i(x_i)$ for each coordinate direction x_i analogously to $w(x)$ of equation (A.9). The window function is then defined as

$$W(\mathbf{x}) = \prod_{i=1}^{D} W_i(x_i) \tag{A.28}$$

and the windowing operation as

$$\tilde{f}_i(\mathbf{x}) = W(\mathbf{x})f_i(\mathbf{x}) \; , \; i = 1, \ldots, D \; , \tag{A.29}$$

for a D-component vector funtion $f_i(\mathbf{x})$.

Application to non-periodic flows

We again consider the flow in the domain Γ. Similarly to the fringe method, Γ_I denotes the subdomain of Γ in which we want to recover

the physically relevant solution (see sketch figure A.4). Γ_I consists of the domain Γ_I^I, where a solution of the unmodified equations (A.1) is sought, and the domain Γ_I^A, where physically correct inflow data are prescribed (distributed inflow conditions). The (normally not exactly known) outflow is treated in Γ_A, which is not part of the physical solution to the problem (distributed outflow conditions). The class of problems that can be treated with the windowing technique is summarised by the following properties:

- **(A1)** There exists a base flow $\mathcal{U}_i$ which is at least defined on Γ_I^A and Γ_A. This base flow is used as distributed inflow and outflow condition and therefore contains the boundary data for the flow problem. $\mathcal{U}_i$ can be constructed similar to equation (A.5) for the fringe method. It should satisfy continuity $\partial_i \mathcal{U}_i = 0$. For parts of section A.3.2 it will further be assumed that $\mathcal{U}_i$ is periodic in the flow direction x;

- **(A2)** The solution on Γ_I is subject to the distributed boundary data

$$u_i \to \mathcal{U}_i \ \text{ for } \ x \to \partial\Gamma_A \ . \tag{A.30}$$

  On the inflow boundary of the physical domain Γ_I the inflow condition $u_i = \mathcal{U}_i$ on the inflow portion of $\partial\Gamma_I$ is fulfilled exactly;

- **(A3)** The solution u_i is integrated according to the unmodified equations (A.1) only on Γ_I^I. The known solution on Γ_I^A is expected to provide accurate inflow data (solution to the Navier-Stokes equations). On Γ_A the outflow condition is imposed.

In analogy with the fringe technique, the base flow $\mathcal{U}_i$ on Γ_I^A can *e.g.* contain superimposed temporally and spatially varying disturbances. Again, it is advisable that these disturbances satisfy continuity. It should be noted that, since the inflow window is located within the physical domain Γ_I, there should be no non-physical energy feed into the flow and the velocities should follow physical evolution equations, *e.g.* in case of transition simulations results from linear stability theory.

The main difference of **(A1)-(A3)** to the properties of the fringe method is that Γ_I^A is assumed to be part of the physical domain Γ_I. This slight modification, however, does not pose a serious restriction on both the generality of problems that can be treated using the windowing method and the validity of the solution. Flow problems that are to

be treated with the windowing technique (and similarly with the fringe method) can be distinguished into two categories:

- Damping of outflowing disturbances together with an undisturbed inflow within an otherwise periodic base flow. In this case, perturbations of the base flow are usually introduced in the domain Γ_I^I and the *downstream* evolution is investigated, *e.g.* the flow around bodies or the spatial evolution of turbulent spots in a channel flow. For these cases, the base flow is usually independent of the streamwise variable x.

- A spatially evolving flow is examined. Here, the inflow on Γ_I^A is a valid solution to the Navier-Stokes equations. In this case the starting point of the physical domain is usually a matter of definition or its precise location is not important, *e.g.* boundary layer simulations starting downstream of the leading edge (Brandt *et al.*, 2004).

Windowed flow equations

In this section, the windowed evolution equation for the velocities u_i and pressure p are derived from the Navier-Stokes equations (A.1). Recall from equation (A.29) that the windowing operation is defined as

$$\tilde{u}_i(\mathbf{x}) = W(\mathbf{x})u_i(\mathbf{x}) \ , \tag{A.31}$$

and from equation (A.20) the definition of the dewindowing operation

$$\overline{u}_i = (1 - W)\mathcal{U}_i + \tilde{u}_i \ . \tag{A.32}$$

As mentioned earlier, the maximum regularisation error on Γ_I^I is bounded by $(\epsilon_2 \cdot \max|\mathcal{U}_i - u_i|)$, whereas on Γ_A and Γ_I^A it is bounded by $\max|\mathcal{U}_i - u_i|$, which is small by **(A2)**. The distributed boundary data of the solution are enforced by means of the dewindowing operation (A.32). From equation (A.31) follows that

$$\partial_j u_i = \frac{1}{W}(\partial_j \tilde{u}_i - u_i \partial_j W) \ , \tag{A.33}$$

which is singular on $\partial\Gamma$. Note that in equation (A.33) derivative operations are taken only on windowed variables and the window function.

Therefore, it is possible to use schemes assuming periodic boundary conditions to evaluate the derivatives, *e.g.* accurate global Fourier methods.

Similarly, we obtain for the gradient of the convective fluxes $F_{ij}^c = u_i u_j$

$$\partial_j F_{ij}^c = \frac{1}{W} \left(\partial_j \tilde{F}_{ij}^c - F_{ij}^c \partial_j W \right) = \frac{1}{W} \left(\partial_j \widetilde{u_i u_j} - u_i u_j \partial_j W \right) \ . \quad \text{(A.34)}$$

The diffusive fluxes become

$$F_{ij}^d = \mu(\partial_i u_j + \partial_j u_i) = \frac{1}{W} \mu(\partial_i \tilde{u}_j + \partial_j \tilde{u}_i - u_j \partial_i W - u_i \partial_j W) \ , \quad \text{(A.35)}$$

and the respective windowed flux is

$$\tilde{F}_{ij}^d = \mu(\partial_i \tilde{u}_j + \partial_j \tilde{u}_i - u_j \partial_i W - u_i \partial_j W) \ . \quad \text{(A.36)}$$

On taking the gradient of the diffusive flux one obtains by (A.33)

$$\partial_j F_{ij}^d = \frac{1}{W} \left(\partial_j \tilde{F}_{ij}^d - F_{ij}^d \partial_j W \right) \ . \quad \text{(A.37)}$$

Note that either form of F_{ij}^d in equation (A.35) can be inserted in (A.37). Depending on the numerical scheme it might be impractical to compute derivatives $\partial_i u_j$ on the non-windowed quantities. On the other hand, it is usually possible, depending on the window function W, to evaluate the term $\partial_j W/W$ despite the singularity of W^{-1} on $\partial \Gamma$ since $\partial_j W/W$ is bounded; *e.g.* for the exponential window (A.21) an analytical expression can be given. The second form in equation (A.35) is preferred in such cases.

On substitution of (A.34) and (A.37) into (A.1) and (A.2) one can derive the modified Navier-Stokes equations governing the evolution of $\tilde{u}_i$

$$\partial_t \tilde{u}_i + \partial_j \widetilde{u_j u_i} + \frac{1}{\rho} \partial_i \tilde{p} - \frac{1}{\rho} \partial_j \left[\mu(\partial_i \tilde{u}_j + \partial_j \tilde{u}_i) \right] =$$

$$= u_i u_j \partial_j W + \frac{p}{\rho} \partial_i W - \frac{1}{\rho} \partial_j \left[\mu(u_j \partial_i W + u_i \partial_j W) \right] - \quad \text{(A.38)}$$

$$- \frac{1}{\rho} \frac{\partial_j W}{W} \mu(\partial_i \tilde{u}_j + \partial_j \tilde{u}_i - u_j \partial_i W - u_i \partial_j W) \ ,$$

$$\partial_k \tilde{u}_k = u_k \partial_k W \ , \quad \text{(A.39)}$$

together with the dewindowing operation (A.32), which enforces the distributed boundary conditions.

The linear stability properties of the temporally discretised equation (A.38) have been analysed in Guo (1993). There, it is concluded that no additional time step restrictions are encountered.

Further refinements of the scheme just described are possible. Guo (1993) proposes for his compressible calculations the introduction of a *sponge region* close to the outflow and a *buffer domain* within the windowing region. However, for the present study, neither of these refinements were found to be necessary.

Formal comparison

It is instructive to compare the fringe and windowing techniques on a formal level by a simple analogy. Consider the fringe method applied to an evolution equation $\partial_t u_i + F_i(u) = 0$ in the following form (see section A.3.1)

$$\partial_t u_i + F_i(u) = \lambda(\mathcal{U}_i - u_i) \ . \tag{A.40}$$

Using a fractional step approximation in the framework of an Euler-forward integration, the discrete time step Δt is split into two substeps of length τ and τ'

$$\frac{u_i' - u_i^{(n)}}{\tau} = -F_i(u) \ , \tag{A.41}$$

$$\frac{u_i^{(n+1)} - u_i'}{\tau'} = \lambda(\mathcal{U}_i - u_i') \ . \tag{A.42}$$

The second equation can be rewritten as

$$u_i^{(n+1)} = (1 - \tau'\lambda)u_i' + \tau'\lambda\mathcal{U}_i \ . \tag{A.43}$$

The windowing approach enforces the boundary conditions via the dewindowing (A.32) at the end of each substep. Formally written

$$u_i^{(n+1)} = (1 - W)\mathcal{U}_i + W\overline{u}_i' \ , \tag{A.44}$$

where $\overline{u}_i'$ is calculated in a forward integration similar to (A.41). Comparing equations (A.43) and (A.44) yields the result

$$W = 1 - \tau'\lambda \ . \tag{A.45}$$

Without going into further details, equation (A.45) gives, except for the fractional step error, a formal framework to compare the fringe and the windowing techniques.

A.3 Implementation for 2D Navier-Stokes equations

In Schlatter *et al.* (2005*a*), the windowing and the fringe method were implemented into a two-dimensional Navier-Stokes code and compared for two different test cases. For the overview given here, only a schematic summary of the implementation details are given. The divergence-free condition (A.2) is enforced by a Helmholtz projection (Chorin, 1968). For an explicit Runge-Kutta time discretisation, it is sufficient to explain the numerical details of an Euler-forward time step. The updated velocity of a substep will be denoted by $u^{(n+1)}$. At time $t^{(n)} = n\tau$ the solution $\mathbf{u}^{(n)}$ on Γ is assumed to satisfy continuity, $\nabla \cdot \mathbf{u}^{(n)} = 0$.

A.3.1 Fringe method

For the fringe method, the forcing term G_i (see equation (A.4)) is evaluated and included into the Navier-Stokes equations according to (A.1). We proceed as follows:

- **(F1)** Using equation (A.1) and the abbrevation F_i including the nonlinear and viscous terms and the forcing term G_i

$$\partial_t u_i + \frac{1}{\rho}\partial_i p = F_i(\mathbf{u}^{(n)}) \ , \tag{A.46}$$

  we obtain for the first step of the algorithm

$$u_i^* = u_i^{(n)} + \alpha\tau F_i(\mathbf{u}^{(n)}) \ . \tag{A.47}$$

  The step size of the Runge-Kutta step is given by $\alpha\tau$ where τ is the full time step.

- **(F2)** The divergence-free condition on the intermediate solution $\mathbf{u}^*$ is enforced by a Helmholtz projection

$$u_i^{(n+1)} = u_i^{**} = u_i^* - \partial_i\phi \ . \tag{A.48}$$

  where ϕ is a scalar function and is determined from

$$\partial_k u_k^* = \partial_k\partial_k\phi \ . \tag{A.49}$$

The pressure can in principle be recovered directly from the fractional step algorithm, although the accuracy of the pressure solution is limited to first order in time (Brown *et al.*, 2001; Perot, 1993).

A.3.2   Windowing technique

For the windowing technique, equations (A.38) and (A.39) have to be solved. Basically, the same algorithm as for the fringe technique is used, although some modifications are appropriate. Instead of using the windowed quantity $\tilde{\mathbf{u}}$ as computational variable, the regularised dewindowed quantities $\overline{u}_i$ (see equation (A.32)) have been used in the code to minimise the code changes.

Similarly to section A.3.1, for each Runge-Kutta substep we proceed as follows:

- **(W1)** Using equation (A.38) we introduce $\tilde{F}_i$ according to

$$\partial_t \tilde{u}_i + \frac{W}{\rho} \partial_i p = \tilde{F}_i(\overline{\mathbf{u}}^{(n)}) \ . \tag{A.50}$$

  The forward projection is given for the windowed solution $\tilde{\mathbf{u}}$ as

$$\tilde{u}_i^* = \tilde{u}_i^{(n)} + \alpha\tau \tilde{F}_i(\overline{\mathbf{u}}^{(n)}) \ , \tag{A.51}$$

  or using the regularised dewindowed variables due to linearity

$$\overline{u}_i^* = \overline{u}_i^{(n)} + \alpha\tau \tilde{F}_i(\overline{\mathbf{u}}^{(n)}) \tag{A.52}$$

  for a stationary base flow. Alternatively, for non-stationary base flows $\mathcal{U}_i = \mathcal{U}_i(t)$, the time derivative of $\overline{u}_i$ (see equation (A.32)) has to be included, replacing equation (A.52) by

$$\overline{u}_i^* = \overline{u}_i^{(n)} + \alpha\tau \left(\tilde{F}_i(\mathbf{u}^{(n)}) + (1 - W)\partial_t \mathcal{U}_i \right) \ . \tag{A.53}$$

  Note that $(1 - W)\partial_t \mathcal{U}_i$ can alternatively be added in step **(W3)** since $\mathcal{U}_i$ is divergence-free by assumption.

  The test cases have shown (Schlatter *et al.*, 2005*a*) that an additional dewindowing operation at this point increases the accuracy of the results slightly

$$\overline{u}_i^{*+} = (1 - W)\mathcal{U}_i + W\overline{u}_i^* \ . \tag{A.54}$$

The reason for this is that the additional dewindowing enforces the boundary data on the intermediate solution $\overline{u}_i^{*+}$ and damps possible artefacts of $\tilde{F}_i$ in the windowing regions. A similar observation is also made by Colonius & Ran (2002), who found an additional filtering step in the fringe region to be beneficial.

- **(W2)** The divergence-free condition on the intermediate solution $\overline{\mathbf{u}}^*$ is enforced by a Helmholtz projection

$$\overline{u}_i^{**} = \overline{u}_i^* - \partial_i\phi \ . \tag{A.55}$$

Using (A.32) and the continuity equation one requires

$$\partial_k\overline{u}_k^{**} = \partial_k\tilde{u}_k^{**} - \mathcal{U}_k\partial_k W = 0 \ , \tag{A.56}$$

and applying the divergence operator to (A.55) using (A.56) we obtain

$$\partial_k\overline{u}_k^* = \partial_k\partial_k\phi \ . \tag{A.57}$$

- **(W3)** The final dewindowing is then performed as

$$\overline{u}_i^{(n+1)} = \overline{u}_i^{***} = (1 - W)\mathcal{U}_i + W\overline{u}_i^{**} \ . \tag{A.58}$$

The divergence error of the solution due to dewindowing at time $t^{(n+1)}$ is

$$\partial_i\overline{u}_i^{(n+1)} = (\overline{u}_i^{**} - \mathcal{U}_i)\partial_i W \ . \tag{A.59}$$

It is non-vanishing only in the windowing regions where, however, $(\overline{u}_i^{**} - \mathcal{U}_i)$ is small due to **(A2)**.

The Poisson equation (A.57) can be solved accurately by a Fourier transform only if $\overline{\mathbf{u}}^*$ is periodic on Γ. A non-periodic $\overline{\mathbf{u}}^*$ can be treated directly using a non-periodic Poisson solver of high order (*e.g.* Braverman *et al.* (1998)). Alternatively, $\overline{u}_k^*$ in equation (A.57) can be split into a periodic part and a non-periodic part. Formally assuming the additional dewindowing in **(W1)** given in equation (A.54), $\overline{u}_k^*$ can be written as

$$\overline{u}_k^* = (1 - W)\mathcal{U}_k + \tilde{u}_k^* \tag{A.60}$$

$$= \underbrace{\mathcal{U}_k}_{\mathrm{non-periodic}} \underbrace{-W\mathcal{U}_k + \tilde{u}_k^*}_{\mathrm{periodic}} \ . \tag{A.61}$$

Since the base flow $\mathcal{U}_k$ satisfies continuity, $\partial_k \mathcal{U}_k = 0$, equation (A.57) simplifies to

$$\partial_k \overline{u}_k^* = \partial_k \left(\mathcal{U}_k - W\mathcal{U}_k + \tilde{u}_k^* \right) = \partial_k \left(-W\mathcal{U}_k + \tilde{u}_k^* \right) = \partial_k \partial_k \phi_p \ , \quad \text{(A.62)}$$

which is a periodic problem on Γ and can thus be solved in Fourier space with periodic boundary conditions. The new solution is then given as

$$\overline{u}_i^{**} = \overline{u}_i^* - \partial_i \phi_p \quad \text{(A.63)}$$

with ϕ_p denoting the periodic part of ϕ.

The pressure is obtained from

$$\Delta p = -\rho \nabla \cdot (\mathbf{u} \cdot \nabla \mathbf{u}) \ . \quad \text{(A.64)}$$

with suitable boundary conditions (see *e.g.* Rannacher (1992)). If the pressure is not required on the entire domain, *e.g.*, a windowing operation can be employed to restrict the solution to the physically meaningful part of the domain and to allow for an efficient (spectral) solution.

A.4   Summary and conclusions

The windowing technique presented in Schlatter *et al.* (2005*a*); Schlatter (2002) has been summarised in this chapter. It was adapted from Guo *et al.* (1994) and refined by introducing a regularised dewindowing procedure, and proved to be successful in solving non-periodic problems governed by the Navier-Stokes equations while employing periodic Fourier discretisation. Analytical predictions on the convergence rate of the numerical solution can be made, which were confirmed by our numerical results. The convergence rate depends fundamentally on the choice of the windowing function. Properly designing this function allows for recovering spectral accuracy (Guo, 1993). An adaptation of the present algorithm to compressible flows is possible. The exact satisfaction of inflow conditions is ensured due to the dewindowing procedure even for base flows which do not accurately satisfy continuity. For this type of (non-physical) base flow the fringe method produces inferior results.

The accuracy of the windowing and the fringe method (see Nordström *et al.* (1999)) was compared in Schlatter *et al.* (2005*a*) for a number of parameters and three test cases. They cover essential requirements encountered in real applications, *e.g.* spatial laminar-turbulent transition

and turbulence simulations. Both methods were successful in providing an accurate inflow condition and an artificial outflow condition with limited upstream influence. The global errors of the windowing method were found to be at least as low as the errors of the fringe technique.

It was further found that the performance of the fringe method strongly depends on the choice of the parameters: fringe strength, blending, start and length of the fringe region. While excellent results can be obtained for ideal parameters, the imprudent choice of parameters can even lead to numerical problems due to the fringe forcing. The reduction of the time step in such cases is undesirable as it decreases the efficiency of the computation significantly. The windowing method, on the other hand, contains only a small number of tuning parameters and their influence is limited.

Implementing the fringe method into an existing simulation code does not pose any problems. For the windowing method, additional terms involving derivatives have to be included in the differential equation, which is more complicated. The cost of the additional calculations for the fringe forcing is negligible, and that for the evaluation of the windowed quantities and fluxes is small (increase of CPU time due to windowing operations around 5%). For both methods, the fraction of the computational domain needed for the treatment of the artificial boundary conditions is similar, typically of order 10% of the computational domain size. However, for spatially evolving, non-periodic base flows the fringe method relies on a blending to provide a periodic base flow. The windowing method, on the other hand, can be applied directly using a non-periodic base flow and does not necessarily need an extension of the domain by a blending region.

The influence of the fringe region on the accuracy is difficult to estimate. For the windowing technique, simple estimates can be used to assess the impact of the boundary treatment on the accuracy. These relations show that the accuracy can be increased with finer resolution of the window function.

The windowing method provides an attractive alternative way to perform accurate simulations in non-periodic geometries using periodic discretisation schemes. Since it poses no restriction on the type of inflow conditions, its use for transitional and turbulent flows is possible.

Appendix B

Summary of mathematical expressions

This section describes some important mathematical expressions for modelling and turbulent quantities used throughout this thesis. In particular, details of the structure function F_2, the strain rate S_{ij} and the transport equation for the turbulent kinetic energy (TKE) are discussed. The implementation of the dynamic Smagorinsky model is described in section B.4.

B.1   Structure function

The local second-order velocity structure function of the velocity field $\mathbf{u}$ at position $\mathbf{x}$ is defined as

$$F_2(\mathbf{u}, \mathbf{x}, \Delta) = \left\langle \|\mathbf{u}(\mathbf{x}) - \mathbf{u}(\mathbf{x} + \mathbf{r})\|^2 \right\rangle_{\|\mathbf{r}\| = \Delta} \tag{B.1}$$

with a length scale Δ and the Euclidian norm $\|\cdot\|$. If the flow is assumed to be one-dimensionally isotropic, Batchelor's formula (Batchelor, 1953) yields

$$F_2(\mathbf{u}, \mathbf{x}, \Delta) = 4 \int_0^\infty E(k) \left(1 - \frac{\sin(k\Delta)}{k\Delta} \right) \mathrm{d}k \ , \tag{B.2}$$

with $E(k)$ denoting the three-dimensional energy spectrum of the velocity $\mathbf{u}$. The actual implementation of F_2 given an equidistant cartesian grid $\mathbf{x}_{i,j,k} = (i\Delta, j\Delta, k\Delta)$ in six-point formulation is (Lesieur & Métais, 1996)

$$
\begin{aligned}
F_2(\mathbf{u}, \mathbf{x}_{i,j,k}, \Delta) = \frac{1}{6} \Big(&\ \|\mathbf{u}_{i+1,j,k} - \mathbf{u}_{i,j,k}\|^2 + \|\mathbf{u}_{i-1,j,k} - \mathbf{u}_{i,j,k}\|^2 \\
&+ \|\mathbf{u}_{i,j+1,k} - \mathbf{u}_{i,j,k}\|^2 + \|\mathbf{u}_{i,j-1,k} - \mathbf{u}_{i,j,k}\|^2 \\
&+ \|\mathbf{u}_{i,j,k+1} - \mathbf{u}_{i,j,k}\|^2 + \|\mathbf{u}_{i,j,k-1} - \mathbf{u}_{i,j,k}\|^2 \ \Big),
\end{aligned}
\tag{B.3}
$$

or written more compactly with $\mathbf{e}_i$ as unit vector in direction i

$$F_2(\mathbf{u}, \mathbf{x}, \Delta) = \frac{1}{6} \sum_{i=1}^3 \left(\|\mathbf{u}(\mathbf{x} + \Delta \mathbf{e}_i) - \mathbf{u}(\mathbf{x})\|^2 + \|\mathbf{u}(\mathbf{x} - \Delta \mathbf{e}_i) - \mathbf{u}(\mathbf{x})\|^2 \right) \ . \tag{B.4}$$

For the extension to non-equidistant grids, Kolmogorov's scaling law (Kolmogorov, 1991; Lesieur & Métais, 1996)

$$F_2(\Delta^*) \propto (\varepsilon\Delta^*)^{2/3} \tag{B.5}$$

can be used. For a grid with local mesh sizes Δx_i^- and Δx_i^+, this leads to

$$F_2(\mathbf{u}, \mathbf{x}, \Delta^*) = \frac{1}{6}\sum_{i=1}^{3}\left[\|\mathbf{u}(\mathbf{x}) - \mathbf{u}(\mathbf{x} + \Delta x_i^+\mathbf{e}_i)\|^2 \left(\frac{\Delta^*}{\Delta x_i^+}\right)^{2/3} + \right.$$
$$\left. \|\mathbf{u}(\mathbf{x}) - \mathbf{u}(\mathbf{x} - \Delta x_i^-\mathbf{e}_i)\|^2 \left(\frac{\Delta^*}{\Delta x_i^-}\right)^{2/3}\right] \tag{B.6}$$

with the averaged grid size assumed as $\Delta^* = (\Pi_{i=1}^3 \Delta x_i^+ \Delta x_i^-)^{1/6}$.

B.2   Strain rate

The strain rate of the velocity field u_i is defined as

$$S_{ij} = \frac{1}{2}\left(\frac{\partial u_i}{\partial x_j} + \frac{\partial u_j}{\partial x_i}\right) . \tag{B.7}$$

The norm $|S|$ is then written as

$$|S|^2 = 2S_{ij}S_{ij} = 2(S_{11}^2 + S_{22}^2 + S_{33}^2) + 4(S_{12}^2 + S_{13}^2 + S_{23}^2)$$
$$= 2\left(\frac{\partial u_1}{\partial x_1}\right)^2 + \left(\frac{\partial u_2}{\partial x_1}\right)^2 + \left(\frac{\partial u_3}{\partial x_1}\right)^2$$
$$+ \left(\frac{\partial u_1}{\partial x_2}\right)^2 + 2\left(\frac{\partial u_2}{\partial x_2}\right)^2 + \left(\frac{\partial u_3}{\partial x_2}\right)^2$$
$$+ \left(\frac{\partial u_1}{\partial x_3}\right)^2 + \left(\frac{\partial u_2}{\partial x_3}\right)^2 + 2\left(\frac{\partial u_3}{\partial x_3}\right)^2$$
$$+ 2\frac{\partial u_2}{\partial x_1}\frac{\partial u_1}{\partial x_2} + 2\frac{\partial u_3}{\partial x_1}\frac{\partial u_1}{\partial x_3} + 2\frac{\partial u_2}{\partial x_3}\frac{\partial u_3}{\partial x_2} . \tag{B.8}$$

From the definition of S_{ij} and $\omega = \nabla \times \mathbf{u}$ one can show that

$$2S_{ij}S_{ij} + \omega_i\omega_i = 2\frac{\partial u_i}{\partial x_j}\frac{\partial u_i}{\partial x_j} = 2\left[\ (\frac{\partial u_1}{\partial x_1})^2 + (\frac{\partial u_1}{\partial x_2})^2 + (\frac{\partial u_1}{\partial x_3})^2\right.$$
$$+ (\frac{\partial u_2}{\partial x_1})^2 + (\frac{\partial u_2}{\partial x_2})^2 + (\frac{\partial u_2}{\partial x_3})^2$$
$$\left.+ (\frac{\partial u_3}{\partial x_1})^2 + (\frac{\partial u_3}{\partial x_2})^2 + (\frac{\partial u_3}{\partial x_3})^2\right]. \text{(B.9)}$$

Alternatively, a first-order expansion of the differences in the definition of the structure function

$$\Delta^2 \left\|\frac{\partial \mathbf{u}}{\partial x_i}\right\|^2 \approx \|\mathbf{u}(\mathbf{x}) - \mathbf{u}(\mathbf{x} + \Delta\mathbf{e}_i)\|^2 \ , \tag{B.10}$$

yields the following relation for an equidistant grid with mesh size Δ (Lesieur & Métais, 1996)

$$F_2(\mathbf{u}, \mathbf{x}, \Delta) \approx \frac{1}{6}\Delta^2(2S_{ij}S_{ij} + \omega_i\omega_i) \ , \tag{B.11}$$

which can be extended to non-equidistant grids in a straightforward way.

B.3 Transport equation for the turbulent kinetic energy

The transport equation for the turbulent kinetic energy (TKE) is derived from the filtered LES equations (2.5),

$$\frac{\partial \overline{u}_i}{\partial t} + \frac{\partial \overline{u}_i\overline{u}_j}{\partial x_j} = -\frac{\partial \overline{p}}{\partial x_i} - \frac{\partial \tau_{ij}}{\partial x_j} + \frac{1}{Re}\frac{\partial^2 \overline{u}_i}{\partial x_j\partial x_j} \ , \tag{B.12}$$

by multiplication with $\overline{u}_i$. The velocity is split into a mean and a fluctuating part according to the Reynolds decomposition

$$\overline{u}_i = \langle \overline{u}_i \rangle + \overline{u}'_i \ , \tag{B.13}$$

where $\langle\cdot\rangle$ denotes a linear statistical average. Evolution equations for the total kinetic energy $E = \frac{1}{2}\overline{u}_i\overline{u}_i$, the kinetic energy of the mean flow $\overline{E} = \frac{1}{2}\langle \overline{u}_i \rangle \langle \overline{u}_i \rangle$ and the kinetic energy of the fluctuations $k = \frac{1}{2}\overline{u}'_i\overline{u}'_i$ can be readily derived. Note that $\langle E \rangle = \overline{E} + k$. The notation

$$\langle \overline{S}_{ij} \rangle = \frac{1}{2}\left(\frac{\partial \langle \overline{u}_i \rangle}{\partial x_j} + \frac{\partial \langle \overline{u}_j \rangle}{\partial x_i}\right) \ \text{ and } \ \overline{S}'_{ij} = \frac{1}{2}\left(\frac{\partial \overline{u}'_i}{\partial x_j} + \frac{\partial \overline{u}'_j}{\partial x_i}\right) \ , \tag{B.14}$$

is used. Then, the equations for the total kinetic energy read

$$\frac{\partial E}{\partial t} + \overline{u}_i \frac{\partial E}{\partial x_i} + \frac{\partial \overline{u}_i \overline{p}}{\partial x_i} - \frac{2}{Re}\frac{\partial \overline{u}_j \overline{S}_{ij}}{\partial x_i} + \frac{\partial \overline{u}_j \tau_{ij}}{\partial x_i} = -\frac{2}{Re}\overline{S}_{ij}\overline{S}_{ij} + \tau_{ij}\overline{S}_{ij} \ , \ \ (B.15)$$

for the kinetic energy of the mean flow

$$\frac{\partial \overline{E}}{\partial t} + \langle \overline{u}_i \rangle \frac{\partial \overline{E}}{\partial x_i} + \frac{\partial \langle \overline{u}_j \rangle \langle \overline{u}_i' \overline{u}_j' \rangle}{\partial x_i} + \frac{\partial \langle \overline{u}_i \rangle \langle \overline{p} \rangle}{\partial x_i}$$
$$-\frac{2}{Re}\frac{\partial \langle \overline{u}_j \rangle \langle \overline{S}_{ij} \rangle}{\partial x_i} + \frac{\partial \langle \overline{u}_j \rangle \langle \tau_{ij} \rangle}{\partial x_i} =$$
$$\langle \overline{u}_i' \overline{u}_j' \rangle \langle \overline{S}_{ij} \rangle - \frac{2}{Re}\langle \overline{S}_{ij} \rangle \langle \overline{S}_{ij} \rangle + \langle \tau_{ij} \rangle \langle \overline{S}_{ij} \rangle \ , \ \ \ (B.16)$$

and for the kinetic energy of the fluctuations

$$\frac{\partial k}{\partial t} + \langle \overline{u}_i \rangle \frac{\partial k}{\partial x_i} + \frac{1}{2}\frac{\partial \langle \overline{u}_i \overline{u}_j \overline{u}_j \rangle}{\partial x_i} + \frac{\partial \langle \overline{u}_i' \overline{p}' \rangle}{\partial x_i}$$
$$-\frac{2}{Re}\frac{\partial \langle \overline{u}_j' \overline{S}_{ij}' \rangle}{\partial x_i} + \frac{\partial \langle \overline{u}_j' \tau_{ij}' \rangle}{\partial x_i} =$$
$$-\langle \overline{u}_i' \overline{u}_j' \rangle \langle \overline{S}_{ij} \rangle - \frac{2}{Re}\langle \overline{S}_{ij}' \overline{S}_{ij}' \rangle + \langle \tau_{ij}' \overline{S}_{ij}' \rangle \ . \ \ \ (B.17)$$

The SGS contributions have been split into a mean and a fluctuating part,

$$\tau_{ij} = \langle \tau_{ij} \rangle + \tau_{ij}' \ . \ \ \ \ \ \ \ \ \ \ \ \ \ \ \ \ \ (B.18)$$

The turbulent production is defined as

$$\mathcal{P} = -\langle \overline{u}_i' \overline{u}_j' \rangle \langle \overline{S}_{ij} \rangle \ \ \ \ \ \ \ \ \ \ \ \ \ \ \ (B.19)$$

with $\mathcal{P} > 0$ denoting a net transport of energy from the mean flow to the fluctuating field.

The total viscous dissipation is given by

$$\varepsilon_{\text{visc}} = -\frac{2}{Re}\overline{S}_{ij}\overline{S}_{ij} \ . \ \ \ \ \ \ \ \ \ \ \ (B.20)$$

Note that negative values for the dissipation mean a net loss of energy. The viscous dissipation due to the mean flow and due to the fluctuating field are given as

$$\varepsilon_{\text{visc,mean}} = -\frac{2}{Re}\langle \overline{S}_{ij} \rangle \langle \overline{S}_{ij} \rangle \ , \ \ \ \ \ \ \ (B.21)$$

and

$$\varepsilon_{\text{visc,fluct}} = -\frac{2}{Re} \left\langle \overline{S}'_{ij} \overline{S}'_{ij} \right\rangle = -\frac{2}{Re} \left\langle \overline{S}_{ij} \overline{S}_{ij} \right\rangle + \frac{2}{Re} \left\langle \overline{S}_{ij} \right\rangle \left\langle \overline{S}_{ij} \right\rangle . \quad \text{(B.22)}$$

Similarly, the total dissipation due to the SGS model is

$$\varepsilon_{\text{SGS}} = \tau_{ij} \overline{S}_{ij} . \quad \text{(B.23)}$$

It can be split accordingly into

$$\varepsilon_{\text{SGS,mean}} = \left\langle \tau_{ij} \right\rangle \left\langle \overline{S}_{ij} \right\rangle \quad \text{(B.24)}$$

for the SGS dissipation acting on the mean field, and the dissipation of the fluctuating field

$$\varepsilon_{\text{SGS,fluct}} = \left\langle \tau'_{ij} \overline{S}'_{ij} \right\rangle = \left\langle \tau_{ij} \overline{S}_{ij} \right\rangle - \left\langle \tau_{ij} \right\rangle \left\langle \overline{S}_{ij} \right\rangle . \quad \text{(B.25)}$$

Some SGS models are directly acting on the velocity components by means of a forcing term, *e.g.* the ADM relaxation term

$$\frac{\partial \tau_{ij}}{\partial x_j} = \chi H_N * \overline{u}_i . \quad \text{(B.26)}$$

In this case, it is generally not possible to separate the SGS dissipation term from the transport part of the model contribution. The approximate SGS energy transfer terms thus read

$$\varepsilon^*_{\text{SGS}} = -\overline{u}_i \frac{\partial \tau_{ij}}{\partial x_j} . \quad \text{(B.27)}$$

The corresponding mean and fluctuating parts are

$$\varepsilon^*_{\text{SGS,mean}} = -\left\langle \overline{u}_i \right\rangle \frac{\partial \left\langle \tau_{ij} \right\rangle}{\partial x_j} , \quad \text{(B.28)}$$

and

$$\varepsilon^*_{\text{SGS,fluct}} = -\left\langle \overline{u}'_i \frac{\partial \tau'_{ij}}{\partial x_j} \right\rangle = -\overline{u}_i \frac{\partial \tau_{ij}}{\partial x_j} + \left\langle \overline{u}_i \right\rangle \frac{\partial \left\langle \tau_{ij} \right\rangle}{\partial x_j} . \quad \text{(B.29)}$$

B.4 Dynamic Smagorinsky model

The LES equations (2.5) for the filtered velocities $\overline{u}_i$ and pressure $\overline{p}$ are given by

$$\frac{\partial \overline{u}_i}{\partial t} + \frac{\partial \overline{u}_i \overline{u}_j}{\partial x_j} = -\frac{\partial \overline{p}}{\partial x_i} - \frac{\partial \tau_{ij}}{\partial x_j} + \frac{1}{Re} \frac{\partial^2 \overline{u}_i}{\partial x_j \partial x_j} \ , \qquad \text{(B.30)}$$

together with the filtered continuity equation (2.6)

$$\frac{\partial \overline{u}_i}{\partial x_i} = 0 \ . \qquad \text{(B.31)}$$

The filter operation denoted by the overbar $\overline{(\cdot)}$ is the primary LES filter G^P, equation (2.4). In the context of the dynamic Smagorinsky model, usually the implicit grid filter onto the coarse LES grid is assumed. The subgrid-scale stresses are given by (see equation (2.7))

$$\tau_{ij} := \overline{u_i u_j} - \overline{u}_i \overline{u}_j \ . \qquad \text{(B.32)}$$

The class of dynamic SGS models was first introduced by Germano *et al.* (1991). These models allow for a dynamic adjustment of the model coefficient to the local flow conditions, *e.g.* reducing the model contribution in the vicinity of walls or in laminar or transitional flow regions. The dynamic procedure, which will be described below, is based on the algebraic identity, known as the Germano identity, which relates the (known) subfilter stresses of a test filter to the corresponding (unclosed) subgrid-scale stresses of the grid filter. The cutoff wavenumber of the test filter is chosen lower than the primary LES filter, *e.g.* in Germano *et al.* (1991) half the filter width of the primary filter has been proposed, *i.e.* $\omega_c = \pi/2$ (see also section 2.1.1).

The LES equations are filtered by use of the test filter $\widetilde{(\cdot)}$ yielding

$$\frac{\partial \widetilde{\overline{u}}_i}{\partial t} + \frac{\partial \widetilde{\overline{u}}_i \widetilde{\overline{u}}_j}{\partial x_j} = -\frac{\partial \widetilde{\overline{p}}}{\partial x_i} - \frac{\partial T_{ij}}{\partial x_j} + \frac{1}{Re} \frac{\partial^2 \widetilde{\overline{u}}_i}{\partial x_j \partial x_j} \ . \qquad \text{(B.33)}$$

The subfilter-scale stresses at the test-filter level are then

$$T_{ij} := \widetilde{\overline{u_i u_j}} - \widetilde{\overline{u}}_i \widetilde{\overline{u}}_j \ . \qquad \text{(B.34)}$$

Following the presentation in Germano *et al.* (1991) and Lilly (1992) the resolved turbulent stresses are defined as

$$\mathcal{L}_{ij} := \widetilde{\overline{u}_i \overline{u}_j} - \widetilde{\overline{u}_i \overline{u}_j} \ . \qquad \text{(B.35)}$$

$\mathcal{L}_{ij}$ describes the turbulent stresses associated with the scales between the test and the grid scale. Note that $\mathcal{L}_{ij}$ can be computed from $\overline{u}_i$. By combining equations (B.32) and (B.34) the Germano identity (Germano *et al.*, 1991; Germano, 1992) is found

$$\mathcal{L}_{ij} = \widetilde{\tau}_{ij} - T_{ij} \ . \tag{B.36}$$

Using the Smagorinsky closure (see Smagorinsky (1963) and section 2.2.1) to model both the subgrid-scale stresses τ_{ij} and the subfilter stresses T_{ij}, one obtains

$$\tau_{ij} - \frac{\delta_{ij}}{3}\tau_{kk} = -2(C_S\overline{\Delta})^2|\overline{S}|\overline{S}_{ij} \tag{B.37}$$

$$T_{ij} - \frac{\delta_{ij}}{3}T_{kk} = -2(C_S\widetilde{\overline{\Delta}})^2|\widetilde{\overline{S}}|\widetilde{\overline{S}}_{ij} \ . \tag{B.38}$$

Note that for both filter levels the same constant Smagorinsky coefficient C_S has been assumed. $\overline{\Delta}$ and $\widetilde{\overline{\Delta}}$ denote a typical length scale of the respective filters. Employing the Germano identity (B.36) yields

$$\mathcal{L}_{ij} - \frac{\delta_{ij}}{3}\mathcal{L}_{kk} = \widetilde{\tau}_{ij} - \frac{\delta_{ij}}{3}\widetilde{\tau}_{kk} - T_{ij} + \frac{\delta_{ij}}{3}T_{kk} \tag{B.39}$$

$$= 2(C_S\widetilde{\overline{\Delta}})^2|\widetilde{\overline{S}}|\widetilde{\overline{S}}_{ij} - 2(C_S\overline{\Delta})^2\widetilde{|\overline{S}|\overline{S}_{ij}} \ . \tag{B.40}$$

By using the abbrevation

$$M_{ij} = \widetilde{\overline{\Delta}}^2|\widetilde{\overline{S}}|\widetilde{\overline{S}}_{ij} - \overline{\Delta}^2\widetilde{|\overline{S}|\overline{S}_{ij}} \ , \tag{B.41}$$

equation (B.40) is simplified to

$$\mathcal{L}_{ij} - \frac{\delta_{ij}}{3}\mathcal{L}_{kk} = 2C_{\mathrm{dyn}}M_{ij} \ . \tag{B.42}$$

C_{dyn} replaces the squared Smagorinsky coefficient C_S^2 and might be negative. In (B.42) six individual equations for the scalar coefficient C_{dyn} are formulated. In Germano *et al.* (1991) these equations were contracted with the resolved strain rate $\overline{S}_{ij}$ to yield a single equation for C_{dyn}. However, no physical justification for using $\overline{S}_{ij}$ has been given. Lilly (1992) suggested a least-squares approach to minimise the quadratic error of the individual equations, *i.e.* the residual

$$Q = (\mathcal{L}_{ij} - \frac{\delta_{ij}}{3}\mathcal{L}_{kk} - 2C_{\mathrm{dyn}}M_{ij})^2 \tag{B.43}$$

shall be minimal. C_{dyn} is then determined from

$$C_{\mathrm{dyn}} = \frac{1}{2} \frac{M_{ij}(\mathcal{L}_{ij} - \frac{\delta_{ij}}{3}\mathcal{L}_{kk})}{M_{lm}M_{lm}} \ . \tag{B.44}$$

If the filtered velocity fields $\overline{u}_i$ and $\widetilde{\overline{u}}_i$ are exactly divergence-free, equation (B.44) can be simplified to

$$C_{\mathrm{dyn}} = \frac{1}{2} \frac{M_{ij}\mathcal{L}_{ij}}{M_{lm}M_{lm}} \ , \tag{B.45}$$

since $M_{ij}\frac{\delta_{ij}}{3}\mathcal{L}_{kk} = \frac{1}{3}M_{ll}\mathcal{L}_{kk}$ and $M_{ll} = 0$ if $\partial\overline{u}_i/\partial x_i = \partial\widetilde{\overline{u}}_i/\partial x_i = 0$. This is only true for filters that commute with the numerical differentiation, *e.g.* the spectral cutoff filter applied in Fourier space. Numerical tests revealed, however, that only minor differences between the results obtained using equation (B.44) and (B.45) are present even for non-commuting filters. Additionally, these tests showed that C_{dyn} is fluctuating considerably in space and, occasionally, negative values were obtained (mainly during the laminar and transitional phases). Therefore, the determination equation for the Smagorinsky coefficient used throughout this thesis is given as

$$C_{\mathrm{dyn}} = \frac{1}{2} \frac{\langle M_{ij}\mathcal{L}_{ij} \rangle}{\langle M_{lm}M_{lm} \rangle} \ , \tag{B.46}$$

$$C_S = \begin{cases} \sqrt{C_{\mathrm{dyn}}} & , \quad C_{\mathrm{dyn}} > 0 \\ 0 & , \quad C_{\mathrm{dyn}} \leq 0 \end{cases} \ . \tag{B.47}$$

The averaging $\langle\cdot\rangle$ is performed over homogeneous directions, *i.e.* over wall-parallel planes in the temporal channel flow simulations and over the spanwise direction in the spatial channel flow simulations. It has been tested to use the spanwise averaging for the temporal channel flow simulations, however no significant differences have been observed.

In laminar or slightly disturbed transitional (*e.g.* low-amplitude Tollmien-Schlichting waves, see section 4.1.1) channel flow, the resolved stresses $\mathcal{L}_{ij}$ are virtually zero across the channel. On the other hand, M_{ij} is in general not vanishing except for the channel midplane ($z = 0$). Whereas a small $\mathcal{L}_{ij}$ assures a vanishing model coefficient for such flow types, a vanishing M_{ij} leads to a 0/0 problem for which, depending on the numerical discretisation scheme, special care has to be taken. In the present implementation a vanishing M_{ij} is trapped and equation (B.47) is replaced by $C_S = 0$.

Bibliography

ACKERMANN, C. & MÉTAIS, O. 2001 A modified selective structure function subgrid-scale model. *J. Turbulence* **2**.

ADAMS, N. A., HICKEL, S. & FRANZ, S. 2004 Implicit subgrid-scale modeling by adaptive deconvolution. *J. Comput. Phys.* **200**, 412–431.

ADAMS, N. A. & STOLZ, S. 2002 A subgrid-scale deconvolution approach for shock capturing. *J. Comput. Phys.* **178**, 391–426.

BARDINA, J., FERZIGER, J. H. & REYNOLDS, W. C. 1980 Improved subgrid models for large-eddy simulation. *AIAA Paper* **1980-1357**.

BARDINA, J., FERZIGER, J. H. & REYNOLDS, W. C. 1983 Improved turbulence models based on large eddy simulation of homogeneous, incompressible, turbulent flows. *Tech. Rep.* TF-19. Stanford University, USA.

BATCHELOR, G. K. 1953 *The theory of homogeneous turbulence*. Cambridge University Press, Cambridge, UK.

BÉRENGER, J.-P. 1994 A perfectly matched layer for the absorption of electromagnetic waves. *J. Comput. Phys.* **114** (2), 185–200.

BERLIN, S., WIEGEL, M. & HENNINGSON, D. S. 1999 Numerical and experimental investigations of oblique boundary layer transition. *J. Fluid Mech.* **393**, 23–57.

BERTOLOTTI, F. P., HERBERT, T. & SPALART, P. R. 1992 Linear and nonlinear stability of the Blasius boundary layer. *J. Fluid Mech.* **242**, 441–474.

BIRINGEN, S. 1987 Three-dimensional vortical structures of transition in plane channel flow. *Phys. Fluids* **30** (11), 3359–3368.

BORIS, J. P., GRINSTEIN, F. F., ORAN, E. S. & KOLBE, R. L. 1992 New insights into large eddy simulation. *Fluid Dynamics Research* **10**, 199–228.

BOYD, J. P. 1998 Two comments on filtering (artificial viscosity) for Chebyshev and Legendre spectral and spectral element methods: Preserving boundary conditions and interpretation of the filter as a diffusion. *J. Comput. Phys.* **143**, 283–288.

BOYD, J. P. 2000 *Chebyshev and Fourier spectral methods*, 2nd edn. Dover Publications, Mineola, USA.

BRANDT, L., SCHLATTER, P. & HENNINGSON, D. S. 2004 Transition in boundary layers subject to free-stream turbulence. *J. Fluid Mech.* **517**, 167–198.

BRAVERMAN, E., ISRAELI, M., AVERBUCH, A. & VOZOVOI, L. 1998 A fast 3D Poisson solver of arbitrary order accuracy. *J. Comput. Phys.* **144**, 109–136.

BROWN, D. L., CORTEZ, R. & MINION, M. L. 2001 Accurate projection methods for the incompressible Navier-Stokes equations. *J. Comput. Phys.* **168**, 464–499.

CALO, V. M. 2004 Residual-based multiscale turbulence modeling: Finite volume simulations of bypass transition. PhD thesis, Stanford University, USA.

CANUTO, C., HUSSAINI, M. Y., QUARTERONI, A. & ZANG, T. A. 1988 *Spectral Methods in Fluid Dynamics*. Springer, Berlin, Germany.

CHANDRA, R., DAGUM, L., KOHR, D., MAYDAN, D., MCDONALD, J. & MENON, R. 2001 *Parallel Programming in OpenMP*. Academic Press, San Diego, USA.

CHASNOV, J. R. 1991 Simulation of the Kolmogorov intertial subrange using an improved subgrid model. *Phys. Fluids A* **3** (1), 188–200.

CHORIN, A. J. 1968 Numerical solution of the Navier-Stokes equations. *Math. Comput.* **22**, 745–762.

CHOW, F. K. & MOIN, P. 2003 A further study of numerical errors in large-eddy simulations. *J. Comput. Phys.* **184**, 366–380.

COLONIUS, T. 2004 Modeling artificial boundary conditions for compressible flow. *Annu. Rev. Fluid Mech.* **36**, 315–345.

COLONIUS, T. & RAN, H. 2002 A super-grid scale model for simulating compressible flow on unbounded domains. *J. Comput. Phys.* **182**, 191–212.

DAGUM, L. & MENON, R. 1998 OpenMP: An industry-standard API for shared memory programming. *IEEE Computational Science and Engineering* **5** (1), 46–55.

DAVID, E. 1993 Modélisation des écoulements compressibles et hypersoniques: une approche instationnaire. PhD thesis, National Polytechnic Institute, Grenoble, France, in French.

DEARDORFF, J. W. 1970 A numerical study of three-dimensional turbulent channel flow at large Reynolds numbers. *J. Fluid Mech.* **41**, 453–480.

DOMARADZKI, J. A. & ADAMS, N. A. 2002 Direct modelling of subgrid scales of turbulence in large eddy simulations. *J. Turbulence* **3**.

DOMARADZKI, J. A., LOH, K. C. & YEE, P. P. 2002 Large-eddy simulation using the subgrid-scale estimation model and truncated Navier-Stokes dynamics. *Theoret. Comput. Fluid Dynamics* **15**, 421–450.

DOMARADZKI, J. A. & SAIKI, E. M. 1997 A subgrid-scale model based on the estimation of unresolved scales of turbulence. *Phys. Fluids* **9** (7), 2148–2164.

VAN DRIEST, E. R. 1956 On the turbulent flow near a wall. *J. Aero. Sci.* **23**, 1007–1011.

DUCROS, F., COMTE, P. & LESIEUR, M. 1996 Large-eddy simulation of transition to turbulence in a boundary layer developing spatially over a flat plate. *J. Fluid Mech.* **326**, 1–36.

EL-HADI, N. M. & ZANG, T. A. 1995 Large-eddy simulation of non-linear evolution and breakdown to turbulence in high-speed boundary layers. *Theoret. Comput. Fluid Dynamics* **7**, 217–240.

FASEL, H. 1976 Investigation of the stability of boundary layers by a finite-difference model of the Navier-Stokes equations. *J. Fluid Mech.* **78**, 335–383.

FASEL, H. 1990 Numerical simulation of instability and transition in boundary layer flows. In *Laminar-Turbulent Transition* (ed. D. Arnal & R. Michel), pp. 587–598. Third IUTAM Symposium 1989 (Toulouse, France), Springer, Berlin, Germany.

FASEL, H. & BESTEK, H. 1980 Investigation of nonlinear, spatial disturbance amplification in plane Poiseuille flow. In *Laminar-Turbulent Transition* (ed. R. Eppler & H. Fasel), pp. 173–185. First IUTAM Symposium 1979 (Stuttgart, Germany), Springer, Berlin, Germany.

FRIGO, M. & JOHNSON, S. G. 1999 *FFTW User's Manual 2.1.3*. Massachusetts Institute of Technology, USA, `http://www.fftw.org`.

GERMANO, M. 1992 Turbulence: the filtering approach. *J. Fluid Mech.* **238**, 325–336.

GERMANO, M., PIOMELLI, U., MOIN, P. & CABOT, W. H. 1991 A dynamic subgrid-scale eddy viscosity model. *Phys. Fluids A* **3** (7), 1760–1765.

GHOSAL, S. 1996 An analysis of numerical errors in large-eddy simulations of turbulence. *J. Comput. Phys.* **125**, 187–206.

GHOSAL, S., LUND, T. S., MOIN, P. & AKSELVOLL, K. 1995 A dynamic localization model for large-eddy simulation of turbulent flows. *J. Fluid Mech.* **286**, 229–255.

GILBERT, N. 1988 Numerische Simulation der Transition von der laminaren in die turbulente Kanalströmung. PhD thesis, Institut für theoretische Strömungsmechanik, Göttingen, Germany, in German.

GILBERT, N. & KLEISER, L. 1990 Near-wall phenomena in transition to turbulence. In *Near-Wall Turbulence – 1988 Zoran Zarić Memorial Conference* (ed. S. J. Kline & N. H. Afgan), pp. 7–27. Hemisphere, New York, USA.

GILBERT, N. & KLEISER, L. 1991 Turbulence model testing with the aid of direct numerical simulation results. In *Eighth Symposium on Turbulent Shear Flows*, pp. 26–1–1—26–1–6.

GIVOLI, D. 1991 Non-reflecting boundary conditions. *J. Comput. Phys.* **94**, 1–29.

GRINSTEIN, F. F. & FUREBY, C. 2002 Recent progress on MILES for high Reynolds number flows. *J. Fluids Eng.* **124**, 849–861.

GULLBRAND, J. 2003 Grid-independent large-eddy simulation in turbulent channel flow using three-dimensional explicit filtering. *CTR Annual Research Briefs* pp. 331–342.

GULLBRAND, J. & CHOW, F. K. 2003 The effect of numerical errors and turbulence models in large-eddy simulations of channel flow, with and without explicit filtering. *J. Fluid Mech.* **495**, 323–341.

GUO, Y. 1993 A new Fourier spectral method for the direct numerical simulation of three-dimensional, spatially growing compressible boundary layer transition. *Tech. Rep.* IB 221-93A16. DLR Göttingen, Germany.

GUO, Y., ADAMS, N. A. & KLEISER, L. 1994 Direct numerical simulation of transition in a spatially growing compressible boundary layer using a new Fourier method. In *Direct and Large-Eddy Simulation I* (ed. P. Voke, L. Kleiser & J.-P. Chollet), pp. 249–259. Kluwer, Dordrecht, The Netherlands.

HAGSTROM, T. & NAZAROV, I. 2003 Perfectly matched layers and radiation boundary conditions for shear flow calculations. *AIAA Paper* **2003-3298**.

HARRIS, H. F. 1978 On the use of windows for harmonic analysis with the Discrete Fourier Transform. *Proc. IEEE* **66** (1), 51–83.

HÄRTEL, C., KLEISER, L., UNGER, F. & FRIEDRICH, R. 1994 Subgrid-scale energy transfer in the near-wall region of turbulent flows. *Phys. Fluids* **6** (9), 3130–3143.

HERBERT, T. 1988 Secondary instability of boundary layers. *Annu. Rev. Fluid Mech.* **20**, 487–526.

HUAI, X., JOSLIN, R. D. & PIOMELLI, U. 1997 Large-eddy simulation of transition to turbulence in boundary layers. *Theoret. Comput. Fluid Dynamics* **9**, 149–163.

HUAI, X., JOSLIN, R. D. & PIOMELLI, U. 1999 Large-eddy simulation of boundary-layer transition on a swept wedge. *J. Fluid Mech.* **381**, 357–380.

Hughes, T. J. R., Calo, V. M. & Scovazzi, G. 2004 Variational and multiscale methods in turbulence. In *Proceedings of the XXI International Congress of Theoretical and Applied Mechanics (IUTAM)* (ed. W. Gutkowski & T. A. Kowalewski). Kluwer, Dordrecht, The Netherlands.

Hughes, T. J. R., Mazzei, L. & Jansen, K. E. 2000 Large eddy simulation and the variational multiscale method. *Comput. Visual. Sci.* **3**, 47–59.

Hughes, T. J. R., Oberai, A. A. & Mazzei, L. 2001 Large eddy simulation of turbulent channel flows by the variational multiscale method. *Phys. Fluids* **13** (6), 1784–1799.

Inagaki, M., Kondoh, T. & Nagano, Y. 2002 A mixed-time-scale SGS model with fixed model-parameters for practical LES. In *Engineering Turbulence Modelling and Experiments 5* (ed. W. Rodi & N. Fueyo), pp. 257–266. Elsevier, Amsterdam, The Netherlands.

Inagaki, M., Kondoh, T. & Nagano, Y. 2005 A mixed-time-scale SGS model with fixed model-parameters for practical LES. *J. Fluids Eng.* **127**, 1–13.

Israeli, M. & Orszag, S. A. 1981 Approximation of radiation boundary conditions. *J. Comput. Phys.* **41**, 115–135.

Israeli, M., Vozovoi, L. & Averbuch, A. 1993 Spectral multidomain technique with local Fourier basis. *J. Sci. Comput.* **8** (2), 135–149.

Jacobs, R. G. & Durbin, P. A. 2001 Simulations of bypass transition. *J. Fluid Mech.* **428**, 185–212.

Jeong, J. & Hussain, F. 1995 On the identification of a vortex. *J. Fluid Mech.* **285**, 69–94.

Kachanov, Y. S. 1994 Physical mechanisms of laminar-boundary-layer transition. *Annu. Rev. Fluid Mech.* **26**, 411–482.

von Kaenel, R., Adams, N. A., Kleiser, L. & Vos, J. B. 2003 The approximate deconvolution model for large-eddy simulation of compressible flows with finite volume schemes. *J. Fluids Eng.* **125**, 375–381.

VON KAENEL, R., ADAMS, N. A., KLEISER, L. & VOS, J. B. 2004 Large-eddy simulation of shock-turbulence interaction. *AIAA J.* **42** (12), 2516–2528.

KANEDA, Y., ISHIHARA, T., YOKOKAWA, M., ITAKURA, K. & UNO, A. 2003 Energy dissipation rate and energy spectrum in high resolution direct numerical simulation of turbulence in a periodic box. *Phys. Fluids* **15** (2), L21–L24.

KARAMANOS, G.-S. & KARNIADAKIS, G. E. 2000 A spectral vanishing viscosity method for large-eddy simulations. *J. Comput. Phys.* **163**, 22–50.

KIM, J., MOIN, P. & MOSER, R. 1987 Turbulence statistics in fully developed channel flow at low Reynolds number. *J. Fluid Mech.* **177**, 133–166.

KLEISER, L. 1982 Numerische Simulationen zum laminar-turbulenten Umschlagsprozess der ebenen Poiseuille-Strömung. PhD thesis, Kernforschungszentrum Karlsruhe, Germany, in German.

KLEISER, L., HÄRTEL, C. & WINTERGERSTE, T. 1998 There is no error in the Kleiser-Schumann influence matrix method. *J. Comput. Phys.* **141**, 85–87.

KLEISER, L. & SCHUMANN, U. 1980 Treatment of incompressibility and boundary conditions in 3-D numerical spectral simulations of plane channel flow. In *Proc. 3rd GAMM Conf. on Numerical Methods in Fluid Mechanics* (ed. E. H. Hirschel), pp. 165–173. Vieweg, Braunschweig, Germany.

KLEISER, L. & SCHUMANN, U. 1984 Spectral simulation of the laminar-turbulent transition process in plane Poiseuille flow. In *Spectral Methods for Partial Differential Equations* (ed. R. G. Voigt, D. Gottlieb & M. Y. Hussaini), pp. 141–163. SIAM, Philadelphia, USA.

KLEISER, L. & ZANG, T. A. 1991 Numerical simulation of transition in wall-bounded shear flows. *Annu. Rev. Fluid Mech.* **23**, 495–537.

KOLMOGOROV, A. N. 1991 The local structure of turbulence in incompressible viscous fluid for very large Reynolds numbers. *Proc. R. Soc. Lond. A* **434**, 9–13, first published 1941. Translated by V. Levin.

KRAICHNAN, R. H. 1976 Eddy viscosity in two and three dimensions. *J. Atmos. Sci.* **33**, 1521–1536.

KRAVCHENKO, A. G. & MOIN, P. 1997 On the effect of numerical errors in large eddy simulations of turbulent flows. *J. Comput. Phys.* **131**, 310–322.

KRISHNAN, L. & SANDHAM, N. D. 2004 Large eddy simulation of compressible turbulent spots. In *Advances in Turbulence X* (ed. H. I. Andersson & P.-Å. Krogstad), pp. 467–470. CIMNE, Barcelona, Spain.

LELE, S. K. 1992 Compact finite difference schemes with spectral-like resolution. *J. Comput. Phys.* **103**, 16–42.

LEONARD, A. 1974 Energy cascade in large eddy simulation of turbulent fluid flows. *Adv. Geophys.* **18** (A), 237–248.

LESIEUR, M., COMTE, P., LAMBALLAIS, E., MÉTAIS, O. & SILVESTRINI, G. 1997 Large-eddy simulations of shear flows. *J. Engng. Math.* **32**, 195–215.

LESIEUR, M. & MÉTAIS, O. 1996 New trends in large-eddy simulations of turbulence. *Annu. Rev. Fluid Mech.* **28**, 45–82.

LILLY, D. K. 1992 A proposed modification of the Germano subgrid-scale closure method. *Phys. Fluids A* **4** (3), 633–635.

LIU, S., MENEVEAU, C. & KATZ, J. 1994 On the properties of similarity subgrid-scale models as deduced from measurements in a turbulent jet. *J. Fluid Mech.* **275**, 83–119.

LUND, T. S. 1997 On the use of discrete filters for large eddy simulation. *CTR Annual Research Briefs* pp. 83–95.

LUNDBLADH, A., BERLIN, S., SKOTE, M., HILDINGS, C., CHOI, J., KIM, J. & HENNINGSON, D. S. 1999 An efficient spectral method for simulation of incompressible flow over a flat plate. *Tech. Rep.* TRITA-MEK 1999:11. KTH Stockholm, Sweden.

MAYLE, R. E. 1991 The role of laminar-turbulent transition in gas turbine engines. *J. Turbomachinery* **113**, 509–537.

MENEVEAU, C. & KATZ, J. 2000 Scale-invariance and turbulence models for large-eddy simulation. *Annu. Rev. Fluid Mech.* **32**, 1–32.

MENEVEAU, C., LUND, T. S. & CABOT, W. H. 1996 A Lagrangian dynamic subgrid-scale model of turbulence. *J. Fluid Mech.* **319**, 353–385.

MÉTAIS, O. & LESIEUR, M. 1992 Spectral large-eddy simulation of isotropic and stably stratified turbulence. *J. Fluid Mech.* **239**, 157–194.

MEYER, D. 2003 Large-Eddy Simulation transitioneller und turbulenter Kanalströmung mit gefiltertem Wirbelzähigkeitsmodell. Diploma thesis, Institute of Fluid Dynamics, ETH Zürich, Switzerland, in German.

MOIN, P. & KIM, J. 1982 Numerical investigation of turbulent channel flow. *J. Fluid Mech.* **118**, 341–377.

MOIN, P. & MAHESH, K. 1998 Direct numerical simulation: A tool in turbulence research. *Annu. Rev. Fluid Mech.* **30**, 539–578.

MOIN, P., SHIH, T.-H., DRIVER, D. & MANSOUR, N. N. 1990 Direct numerical simulation of a three-dimensional turbulent boundary layer. *Phys. Fluids A* **2** (10), 1846–1853.

MORKOVIN, M. V. 1969 On the many faces of transition. In *Viscous drag reduction* (ed. C. S. Wells), pp. 1–31. Plenum Press, New York, USA.

MOSER, R. D., KIM, J. & MANSOUR, N. N. 1999 Direct numerical simulation of turbulent channel flow up to $Re_\tau = 590$. *Phys. Fluids* **11** (4), 943–945.

MÜLLER, S. B., ADAMS, N. A. & KLEISER, L. 2004 Analysis of relaxation regularization as subgrid-scale model for large-eddy simulation. In *Direct and Large-Eddy Simulation V* (ed. R. Friedrich, B. J. Geurts & O. Métais), pp. 57–64. Kluwer, Dordrecht, The Netherlands.

MÜLLER, S. B., ADAMS, N. A., STOLZ, S. & KLEISER, L. 2002 Analysis of LES with ADM for forced and decaying isotropic turbulence. In *Advances in Turbulence IX* (ed. I. P. Castro, P. E. Hancock & T. G. Thomas), pp. 591–594. CIMNE, Barcelona, Spain.

NICOUD, F. & DUCROS, F. 1999 Subgrid-scale stress modelling based on the square of the velocity gradient tensor. *Flow, Turbulence and Combustion* **62**, 183–200.

Nishioka, M., Iida, S. & Ichikawa, Y. 1975 An experimental investigation of the stability of plane Poiseuille flow. *J. Fluid Mech.* **72**, 731–751.

Nordström, J., Nordin, N. & Henningson, D. S. 1999 The fringe region technique and the Fourier method used in the direct numerical simulation of spatially evolving viscous flows. *SIAM J. Sci. Comput.* **20** (4), 1365–1393.

Orr, W. M. F. 1907*a* The stability or instability of the steady motions of a perfect liquid and of a viscous liquid. Part I. A perfect liquid. *Proc. R. Irish Acad.* **27**, 9–68.

Orr, W. M. F. 1907*b* The stability or instability of the steady motions of a perfect liquid and of a viscous liquid. Part II. A viscous liquid. *Proc. R. Irish Acad.* **27**, 69–138.

Otnes, R. K. & Enochson, L. D. 1978 *Applied Time Series Analysis*. Wiley-Interscience, New York, USA.

Pacheco, P. 1997 *Parallel Programming with MPI*. Morgan Kaufmann, San Francisco, USA.

Pao, Y.-H. 1965 Structure of turbulent velocity and scalar fields at large wavenumbers. *Phys. Fluids* **8**, 1063–1075.

Péneau, F., Boisson, H. C., Kondjoyan, A. & Djilali, N. 2004 Structure of a flat plate boundary layer subjected to free-stream turbulence. *Int. J. Comput. Fluid Dynamics* **18** (2), 175–188.

Perot, J. B. 1993 An analysis of the fractional step method. *J. Comput. Phys.* **108**, 51–58.

Piomelli, U. 1993 High Reynolds number calculations using the dynamic subgrid-scale stress model. *Phys. Fluids A* **5** (6), 1766–1771.

Piomelli, U. 1999 Large-eddy simulation: Achievements and challenges. *Prog. Aerospace Sci.* **35**, 335–362.

Piomelli, U. 2001 Large-eddy and direct simulation of turbulent flows. In *CFD2001 - 9e conférence annuelle de la société canadienne de CFD*. Kitchener, Ontario, Canada.

PIOMELLI, U., CABOT, W. H., MOIN, P. & LEE, S. 1991 Subgrid-scale backscatter in turbulent and transitional flows. *Phys. Fluids A* **3** (7), 1799–1771.

PIOMELLI, U. & LIU, J. 1995 Large-eddy simulation of rotating channel flows using a localized dynamic model. *Phys. Fluids* **7** (4), 839–848.

PIOMELLI, U. & ZANG, T. A. 1991 Large-eddy simulation of transitional channel flow. *Comp. Phys. Comm.* **65**, 224–230.

PIOMELLI, U., ZANG, T. A., SPEZIALE, C. G. & HUSSAINI, M. Y. 1990 On the large-eddy simulation of transitional wall-bounded flows. *Phys. Fluids A* **2** (2), 257–265.

POPE, S. B. 2000 *Turbulent Flows*. Cambridge University Press, Cambridge, UK.

RANNACHER, R. 1992 On Chorin's projection method for the incompressible Navier-Stokes equations. In *Navier-Stokes equations II – Theory and numerical methods*, *Lecture Notes in Math.* 1530, pp. 167–183. Springer, Berlin, Germany.

REMBOLD, B., ADAMS, N. A. & KLEISER, L. 2002 Direct and large-eddy simulation of a transitional rectangular jet. In *Direct and Large-Eddy Simulation IV* (ed. B. Geurts, R. Friedrich & O. Métais), pp. 179–204. Kluwer, Dordrecht, The Netherlands.

REMPFER, D. 2003 Low-dimensional modeling and numerical simulation of transition in simple shear flows. *Annu. Rev. Fluid Mech.* **35**, 229–265.

RESHOTKO, E. 2001 Transient growth: A factor in bypass transition. *Phys. Fluids* **13** (5), 1067–1075.

REYNOLDS, O. 1883 On the experimental investigation of the circumstances which determine whether the motion of water shall be direct or sinuous. *Philos. Trans. R. Soc. London Ser. A* **174**, 953–982.

RICHTMYER, R. D. & MORTON, K. W. 1965 *Difference methods for initial-value problems*. John Wiley and Sons, New York, USA.

SAGAUT, P. 2002 *Large Eddy Simulation for incompressible flows*, 2nd edn. Springer, Berlin, Germany.

SAGAUT, P., COMTE, P. & DUCROS, F. 2000 Filtered subgrid-scale models. *Phys. Fluids* **12** (1), 233–236.

SANDHAM, N. D. & KLEISER, L. 1992 The late stages of transition to turbulence in channel flow. *J. Fluid Mech.* **245**, 319–348.

SCHLATTER, P. 2001 Direct numerical simulation of laminar-turbulent transition in boundary layer subject to free-stream turbulence. Diploma thesis, Institute of Fluid Dynamics, ETH Zürich, Switzerland, also published as *Tech. Rep.*, Department of Mechanics, KTH Stockholm, Sweden.

SCHLATTER, P. 2002 Periodic boundary treatment for non-periodic flow geometries. *Tech. Rep.* IFD-IB 02-02. Institute of Fluid Dynamics, ETH Zürich, Switzerland.

SCHLATTER, P., ADAMS, N. A. & KLEISER, L. 2005*a* A windowing method for periodic inflow/outflow boundary treatment of non-periodic flows. *J. Comput. Phys.* To appear.

SCHLATTER, P., STOLZ, S. & KLEISER, L. 2003*a* LES of transitional flows using approximate deconvolution. In *Turbulence and Shear Flow Phenomena 3* (ed. N. Kasagi, J. K. Eaton, R. Friedrich, J. A. C. Humphrey, M. A. Leschziner & T. Miyauchi), pp. 923–928.

SCHLATTER, P., STOLZ, S. & KLEISER, L. 2003*b* Numerical simulation of transitional and turbulent shear flows. In *CSE Annual Report 2002/2003* (ed. R. Jeltsch, K. Nipp & W. van Gunsteren), pp. 18–25. ETH Zürich, Switzerland.

SCHLATTER, P., STOLZ, S. & KLEISER, L. 2004*a* Applicability of LES models for prediction of transitional flow structures. In *Laminar-Turbulent Transition*. Sixth IUTAM Symposium 2004 (Bangalore, India), to appear.

SCHLATTER, P., STOLZ, S. & KLEISER, L. 2004*b* High-pass filtered eddy-viscosity models in incompressible high-Reynolds number flows. In *Advances in Turbulence X* (ed. H. I. Andersson & P.-Å. Krogstad), pp. 303–306. CIMNE, Barcelona, Spain.

SCHLATTER, P., STOLZ, S. & KLEISER, L. 2004*c* LES of transitional flows using the approximate deconvolution model. *Int. J. Heat Fluid Flow* **25** (3), 549–558.

SCHLATTER, P., STOLZ, S. & KLEISER, L. 2004*d* Relaxation-term models for LES of transitional/turbulent flows and the effect of aliasing errors. In *Direct and Large-Eddy Simulation V* (ed. R. Friedrich, B. J. Geurts & O. Métais), pp. 65–72. Kluwer, Dordrecht, The Netherlands.

SCHLATTER, P., STOLZ, S. & KLEISER, L. 2005*b* Computational simulation of transitional and turbulent shear flows. In *Progress in Turbulence* (ed. J. Peinke, A. Kittel, S. Barth & M. Oberlack), *Springer Proceedings in Physics*, vol. 101, pp. 207–214. Springer, Berlin, Germany.

SCHLATTER, P., STOLZ, S. & KLEISER, L. 2005*c* Evaluation of high-pass filtered eddy-viscosity models for large-eddy simulation of turbulent flows. *J. Turbulence* Accepted.

SCHLATTER, P., STOLZ, S. & KLEISER, L. 2005*d* LES of spatial transition in plane channel flow. In *Turbulence and Shear Flow Phenomena 4*. To appear.

SCHLICHTING, H. 1933 Zur Entstehung der Turbulenz bei der Plattenströmung. *Z. Angew. Math. Mech.* **13**, 171–174.

SCHMID, P. J. & HENNINGSON, D. S. 1992 A new mechanism for rapid transition involving a pair of oblique waves. *Phys. Fluids A* **4** (9), 1986–1989.

SCHMID, P. J. & HENNINGSON, D. S. 2001 *Stability and transition in shear flows*. Springer, Berlin, Germany.

SCHUBAUER, G. B. & SKRAMSTAD, H. K. 1947 Laminar boundary layer oscillations and the stability of laminar flow. *J. Aeronaut. Sci.* **14**, 69–78.

SCHUMANN, U. 1975 Subgrid scale model for finite difference simulations of turbulent flows in plane channels and annuli. *J. Comput. Phys.* **18**, 376–404.

SMAGORINSKY, J. 1963 General circulation experiments with the primitive equations. *Mon. Weath. Rev.* **91** (3), 99–164.

SOMMERFELD, A. 1908 Ein Beitrag zur hydrodynamischen Erklärung der turbulenten Flüssigkeitsströmung. In *Atti. del 4 Congr. Internat. dei Mat. III*, pp. 116–124. Rome, Italy, in German.

SPALART, P. R. 1988 Direct numerical study of leading edge contamination. In *Fluid Dynamics of Three-Dimensional Turbulent Shear Flows and Transition*, *AGARD* CP-438, pp. 5.1–5.13. AGARD, Neuilly-sur-Seine, France.

SPEZIALE, C. G. 1985 Galilean invariance of subgrid-scale stress models in the large-eddy simulation of turbulence. *J. Fluid Mech.* **156**, 55–62.

SQUIRES, K. D. 2004 Detached-eddy simulation: Current status and perspectives. In *Direct and Large-Eddy Simulation V* (ed. R. Friedrich, B. J. Geurts & O. Métais), pp. 465–480. Kluwer, Dordrecht, The Netherlands.

STOLZ, S. 2001 *Large-eddy simulation of complex shear flows using an approximate deconvolution model*. vol. 7/403, Fortschritts-Berichte VDI, Düsseldorf, Germany, PhD thesis, Institute of Fluid Dynamics, ETH Zürich, Switzerland.

STOLZ, S. 2004 High-pass filtered eddy-viscosity models for large-eddy simulations of compressible wall-bounded flows. In *Proceedings of HT-FED 2004, ASME Heat Transfer/Fluids Engineering Summer Conference*. Charlotte, USA, July 11-15.

STOLZ, S. 2005*a* Personal communication.

STOLZ, S. 2005*b* DNS and LES of subharmonic transition in supersonic boundary layers. *AIAA J.* Submitted.

STOLZ, S. 2005*c* High-pass filtered eddy-viscosity models for large-eddy simulations of compressible wall-bounded flows. *J. Fluids Eng.* To appear.

STOLZ, S. & ADAMS, N. A. 1999 An approximate deconvolution procedure for large-eddy simulation. *Phys. Fluids* **11** (7), 1699–1701.

STOLZ, S. & ADAMS, N. A. 2003 Large-eddy simulation of high-Reynolds-number supersonic boundary layers using the approximate deconvolution model and a rescaling and recycling technique. *Phys. Fluids* **15** (8), 2398–2412.

STOLZ, S., ADAMS, N. A. & KLEISER, L. 2001*a* An approximate deconvolution model for large-eddy simulation with application to incompressible wall-bounded flows. *Phys. Fluids* **13** (4), 997–1015.

Stolz, S., Adams, N. A. & Kleiser, L. 2001*b* The approximate deconvolution model for large-eddy simulations of compressible flows and its application to shock-turbulent-boundary-layer interaction. *Phys. Fluids* **13** (10), 2985–3001.

Stolz, S., Schlatter, P. & Kleiser, L. 2005 High-pass filtered eddy-viscosity models for LES of transitional and turbulent flow. *Phys. Fluids* Accepted.

Stolz, S., Schlatter, P., Meyer, D. & Kleiser, L. 2004 High-pass filtered eddy-viscosity models for LES. In *Direct and Large-Eddy Simulation V* (ed. R. Friedrich, B. J. Geurts & O. Métais), pp. 81–88. Kluwer, Dordrecht, The Netherlands.

Tadmor, E. 1989 Convergence of spectral methods for nonlinear conservation laws. *SIAM J. Numer. Anal.* **26** (1), 30–44.

Temperton, C. 1983 Self-sorting mixed-radix Fast Fourier Transforms. *J. Comput. Phys.* **52**, 1–23.

Temperton, C. 1985 Implementation of a self-sorting in-place prime factor FFT algorithm. *J. Comput. Phys.* **58**, 183–299.

Tollmien, W. 1929 Über die Entstehung der Turbulenz. *Nachr. Ges. Wiss. Göttingen* **1**, 21–44, in German.

Voke, P. & Yang, Z. 1995 Numerical study of bypass transition. *Phys. Fluids* **7** (9), 2256–2264.

Vreman, A. W. 2003 The filtering analog of the variational multiscale method in large-eddy simulation. *Phys. Fluids* **15** (8), L61–L64.

Vreman, A. W. 2004 An eddy-viscosity subgrid-scale model for turbulent shear flow: Algebraic theory and applications. *Phys. Fluids* **16** (10), 3670–3681.

Watmuff, J. H. 1999 Evolution of a wave packet into vortex loops in a laminar separation bubble. *J. Fluid Mech.* **397**, 119–169.

Wilcox, D. C. 1998 *Turbulence Modeling for CFD*, 2nd edn. DCW Industries, La Canada, USA.

Williamson, J. H. 1980 Low-storage Runge-Kutta schemes. *J. Comput. Phys.* **35**, 48–56.

WRAY, A. A. 1987 Very low storage time-advancement schemes. *Tech. Rep.* AA214a 4. NASA Ames Research Center, Moffett Field, USA.

ZANG, T. A., GILBERT, N. & KLEISER, L. 1990 Direct numerical simulation of the transitional zone. In *Instability and Transition, vol. 2* (ed. M. Y. Hussaini & R. G. Voigt), pp. 283–299. Springer, Berlin, Germany.

ZANG, Y., STREET, R. L. & KOSEFF, J. R. 1993 A dynamic mixed subgrid-scale model and its application to turbulent recirculating flows. *Phys. Fluids A* **5** (12), 3186–3196.

Curriculum vitae

Name	Philipp Christian Schlatter
Date of birth	May 21, 1975
Place of birth	Winterthur, Switzerland
Nationality	Swiss
October 2001 to April 2005	PhD student, research and teaching assistant under the supervision of Prof. L. Kleiser at the Institute of Fluid Dynamics, ETH Zürich, Switzerland
April 2001	Diploma (Dipl. Masch.-Ing. ETH, equivalent to Master's degree) in Mechanical Engineering, ETH Zürich, Switzerland
October 2000 to August 2001	Visiting graduate student at the Department of Mechanics, KTH Stockholm, Sweden
October 1996 to April 2001	Studies in Mechanical Engineering, ETH Zürich, Switzerland
September 1994	Matura (high-school graduation), Gymnasium Rämibühl, Zürich, Switzerland